Diagnosing the DARHT Electron Beam-Target Interaction and Hydrodynamic Expansion

by

Nicholas Ramey

A dissertation submitted in partial fulfillment
of the requirements for the degree of
Doctor of Philosophy
(Nuclear Engineering and Radiological Sciences)
in the University of Michigan
2022

Doctoral Committee:

Professor Ronald Gilgenbach, Co-Chair
Associate Professor Ryan McBride, Co-Chair
Dr. Joshua Coleman, Los Alamos National Laboratory
Associate Professor Eric Johnsen

Nicholas Ramey

nramey@umich.edu

ORCID iD: 0000-0001-5285-898X

ACKNOWLEDGMENTS

This work was supported by the U.S. Department of Energy through the Los Alamos National Laboratory. Los Alamos National Laboratory is operated by Triad National Security, LLC, for the National Nuclear Security Administration of the U.S. Department of Energy (Contract No. 89233218CNA000001).

LA-UR-22-27754

PREFACE

The purpose of this dissertation is to provide a roadmap for spectral diagnostic development and modeling of the electron beam-target interaction at the Dual-Axis Radiographic Hydrodynamic Test (DARHT) facility. This is motivated by the current lack of detailed knowledge of the beam-target interaction and the warm dense matter (WDM) generated during this process, along with the direct relevance to DARHT's main purpose in fulfilling its Stockpile Stewardship mission. Fully characterizing the beam-target interaction will improve the radiographic performance of the DARHT accelerators and can lead to a more advanced and optimized target design for minimizing the radiographic spot size. The phase space trajectory from cold metal to expanded plasma plume in an electron beam driven target is not known. Complicating this issue is the lack of validation of equation-of-state models in the WDM regime and under the vapor dome. The plasmas generated at DARHT span both regimes. Fully diagnosing this beam-target interaction can provide answers to many of these present unknowns. A critical part of solving these problems includes a full-scale, spectroscopic-quality radiation transport model to interpret the resulting spectroscopic measurements. This has been developed by linking together several codes, including atomic physics, radiation hydrodynamics, and radiation transport, and will continue to mature into the future.

TABLE OF CONTENTS

Chapter

LIST OF FIGURES

LIST OF TABLES

LIST OF APPENDICES

LIST OF ABBREVIATIONS

ATOMIC Another Theoretical Opacity Modeling Integrated Code

BBU Beam Breakup

BCUZ Beam CleanUp Zone

BPM Beam Position Monitor

CA Configuration Average

CATS Cowan’s ATomic Structure

CCD Charge-Coupled Device

CI Configuration Interaction

CSDA Continuous-Slowing-Down Approximation

DARHT Dual-Axis Radiographic Hydrodynamic Test

DOE Department of Energy

EOS Equation of State

EUV Extreme Ultraviolet

FESTR Finite-Element Spectral Transfer of Radiation

FS Fine Structure

FWHM Full-Width at Half-Maximum

GIPPER General Ionization Processes in the Presence of Electrons and Radiation

IPCRESS Independent of Platform and Can be Read by Existing Software Subroutines

ITS Integrated Test Stand

LANL Los Alamos National Laboratory

LBNL Lawrence Berkeley National Laboratory

LIA Linear Induction Accelerator

LIBS Laser-Induced Breakdown Spectroscopy

LLNL Lawrence Livermore National Laboratory

LSP Large Scale Plasma

LTE Local Theromdynamic Equilibrium

NIF National Ignition Facility

NIST National Institute of Standards and Technology

NNSA National Nuclear Security Administration

OTR Optical Transition Radiation

PFN Pulse Forming Network

PPT Prime Power Tank

SA Self Absorption

SSI Shearing and Shadowgraph Interferometer

WDM Warm Dense Matter

XFEL X-ray Free Electron Laser

XPS X-ray Photoelectron Spectroscopy

ABSTRACT

Quantitative electron beam-target interaction studies on the Dual-Axis Radiographic Hydrodynamic Test (DARHT) electron linear induction accelerators have only been performed recently. This includes characterization of the temperature, density, pressure, extent, and expansion velocity of the plasma plume. The results presented in this dissertation present a detailed and unified overview of the accelerator systems, target heating physics, beam transport, and diagnostic tools. Additional information includes calibration sources, radiation hydrodynamics, spectroscopic-quality radiation transport modeling, experimental measurements, and analyses of electron beam driven aluminum experiments.

The first set of spatially and temporally resolved spectroscopic measurements of electron beam driven aluminum are presented. Contamination quantification analyses are used to understand the origin of the strong Na-I 3p-3s lines that are observed in absorption within the aluminum plasma continuum. These results inform the creation of the first spectroscopic-quality radiation transport model that links several atomic physics codes to interpret the conditions from which the Na-I lines originate. A good agreement is found between the surface analysis results and the model which confirms the concentration of the sodium present within the aluminum alloy foil material. It also demonstrates, for the first time on electron beam-driven target experiments, the ability to interpret plasma conditions from measured absorption lines.

In a second experimental campaign which focuses on pure aluminum, the Al-I 3p-4s and 3p-3d doublets are both measured in emission. A detailed analysis of the Al-I 3p-4s doublet reveals that the lines undergo moderate self-absorption. A simple model of the self-absorption effect is successfully used to match measured spectra at various temperature/density/plasma scale length combinations. These measurements led to the realization of the minimum density that can be resolved by the spectrometers for the Al-I 3p-4s lines due to the large slit width required to observe a signal on aluminum. These measurements also demonstrate the sensitivity of visible and long wave UV spectroscopy to minor changes in both temperature and density. The simple self-absorption model will be useful for analysis of other beam-target interaction experiments with spectra exhibit-

ing either self-absorption or full self-reversal.

Substantial headway has been made on the modeling front by linking together several codes needed to model both the energy deposition, hydrodynamic motion, and atomic kinetics to produce synthetic spectral calculations that are compared with experimental measurements. There exists ample space for improvement, especially with benchmarking the hydrodynamics codes and equation-of-state tables with experimental measurements. The X-ray diagnostics required to make these new measurements along with the simulation capabilities required to interpret the results are under development and will be the subject of future studies.

CHAPTER 1

Introduction

Los Alamos National Laboratory (LANL) is the nation's premier nuclear weapons design laboratory. Operating under the purview of the National Nuclear Security Administration (NNSA) within the Department of Energy (DOE), LANL's primary mission is to ensure the safety, security, and effectiveness of the U.S. nuclear deterrent. Since 1992, the end of U.S. nuclear testing, this has become known as the Stockpile Stewardship Program. In addition to advanced computer codes dedicated to modeling the events happening inside a nuclear weapon, experiments are performed to acquire data from which computational models can be validated. The purpose of the Dual-Axis Radiographic Hydrodynamic Test (DARHT) facility at LANL is to support the Stockpile Stewardship Program by providing high-quality, multi-frame radiographic images of hydrodynamic (hydro) tests.

1.1 The DARHT Facility

The DARHT facility (Fig. 1.1) is used to study basic weapons physics. The facility consists of two accelerators, Axis-I and Axis-II. The axes of these two accelerators are orthogonal to one another and intersect at the firing point. The firing point is where the hydrodynamic tests are deployed and where the electron beams from the two accelerators are converted into X-rays for radiographing the hydrodynamic tests. The dual-axis nature of the facility provides the ability to extrapolate the resulting radiographs into three dimensional data. This was not possible with previous single-axis systems. As originally conceived in the early 1980s, DARHT was to have two identical single-pulse accelerators. The requirements, after the nuclear testing moratorium had begun, expanded to include a machine with the capacity to deliver multiple X-ray pulses in time. The single pulse machine, Axis-I, was commissioned in 1999 and continues to provide high quality radiographs. Axis-II, the multi-pulse machine, faced significantly more complex design challenges; a long-pulse electron Linear Induction Accelerator (LIA) had never before been constructed. After its full energy commissioning in 2008, a result of extensive inter-laboratory collaboration between

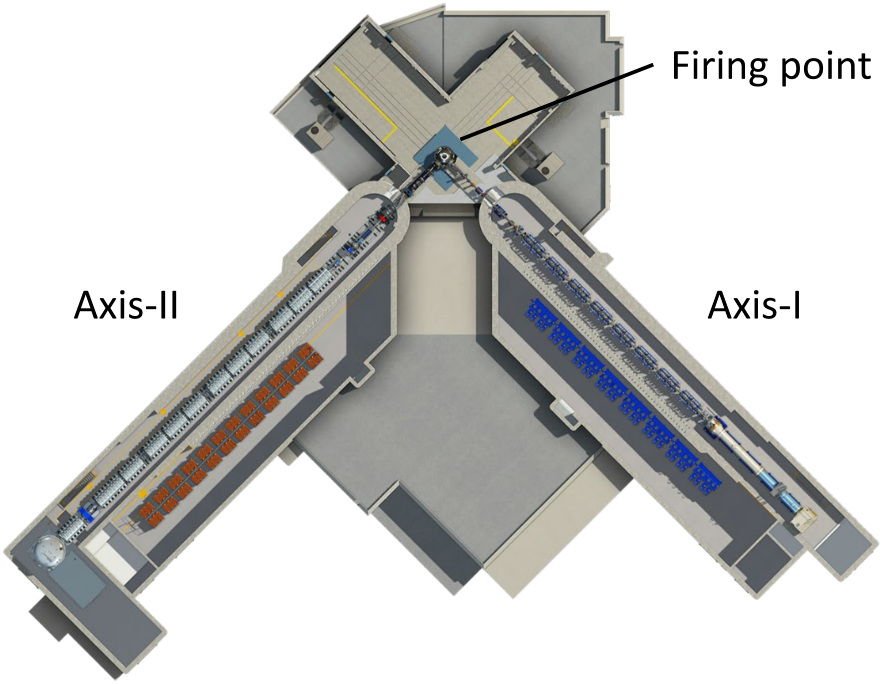

Figure 1.1: Top-down cutaway view of the DARHT facility at LANL. Axis-II is located on the left, and Axis-I on the right. The intersection of the two accelerators is the firing point.

LANL, Lawrence Livermore National Laboratory (LLNL), and Lawrence Berkeley National Laboratory (LBNL), DARHT successfully fired its first dual-axis hydro test in 2009. A description of both Axis-I and Axis-II follows, but more emphasis (and detail) is given to Axis-I as all of the experiments presented in this thesis were performed on Axis-I.

1.1.1 Axis-I

DARHT Axis-I (Figure 1.2) is a single pulse electron LIA. Developed by LANL, it began as the Integrated Test Stand (ITS) in 1991, which comprised the injector and the first set of 8 accelerator cells for initial electron beam generation and transport [13,14]. The injector consists of four major parts: a Prime Power Tank (PPT), Blumlein, transmission line, and diode. The PPT consists of a capacitor bank DC charged nominally to 112 kV [15,16]. This is switched through a Stangenes transformer to pulse charge a glycol Blumlein to 1.5 MV. The Blumlein is switched with a set of four laser-triggered spark gap switches in parallel into a set of three series transmission lines with increasing impedance to further step up the voltage. This voltage pulse arrives at the diode with a nominal voltage of 3.8 MV in a trapezoidal-like pulse, having 20 ns rise and fall times with a 60 ns flat top [17].

The cathode employed for electron production via field emission is a circular piece of velvet

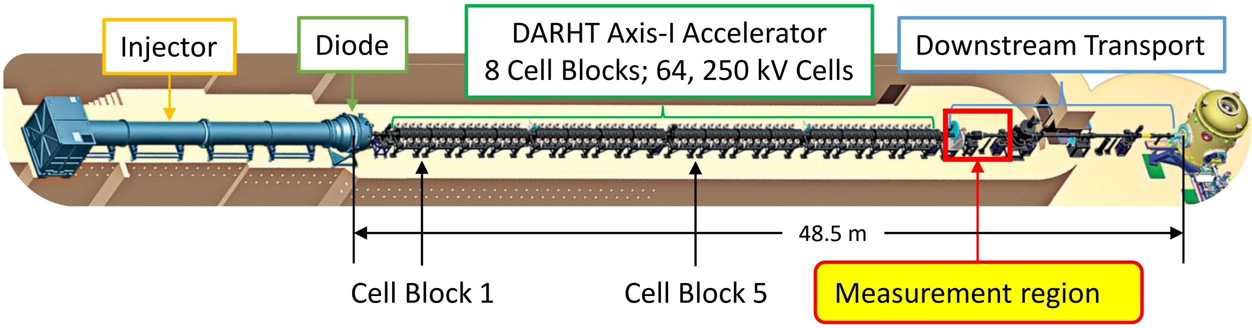

Figure 1.2: Axis-I of the DARHT facility. The confinement vessel used for hydrotests is located inside the containment chamber (yellow cylinder). Total length of the accelerator from the cathode surface to the converter target is 48.5 meters.

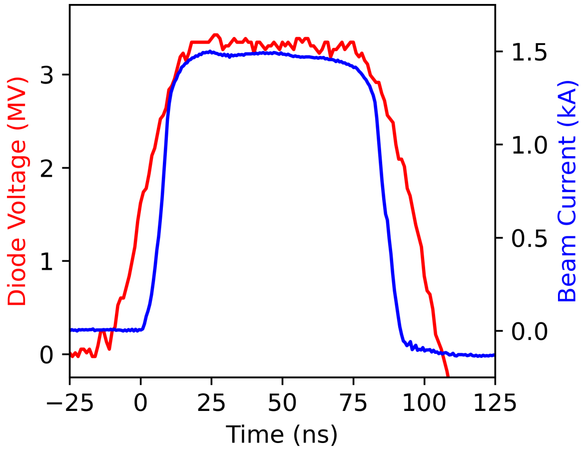

Figure 1.3: Example diode voltage (red) and beam current (blue) traces from Axis-I, shot 33925. The 3.5 MV voltage is due to operating the prime power tank at a charge voltage of 98 kV, which also results in a lower extracted and transported current of 1.5 kA.

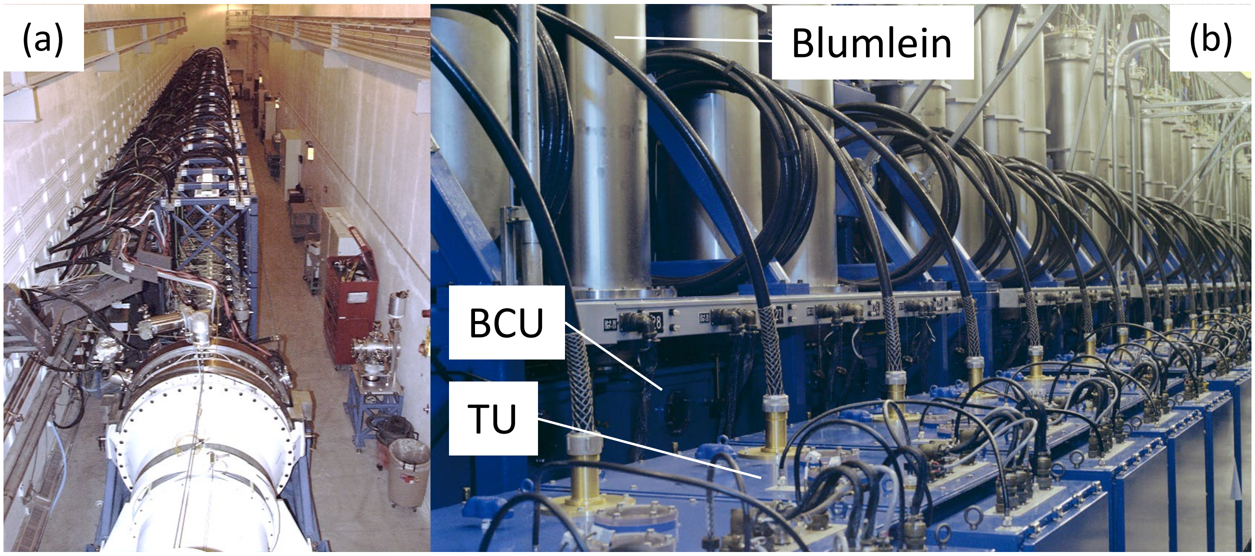

Figure 1.4: The Axis-I accelerator (a) and pulsed power (b) halls. Shown in (a) is the view looking downstream from the injector (white). The Blumleins (silver cylinders) and Blumlein charge units (BCUs) (blue, directly below Blumleins) along with the associated trigger units (TUs) (blue, foreground, with brass feedthroughs) can be observed in (b).

with a diameter of 50 mm [18]. The cathode size, and thus extracted current, can be varied from 19 mm to 70 mm to provide a range of space charge limited beam currents (200 A to 2.9 kA). The A-K gap is 17.8 cm. Example current and voltage pulses are shown in Figure 1.3.

The accelerator section of Axis-I is composed of 8 cell blocks, each of which contains 8 accelerator cells. Each individual cell is capable of imparting 250 kV to the beam across a 19.1 mm accelerating gap, including the effect of beam loading, for a net energy of 16 MeV added upon exiting the final cell block and entering the drift section of the accelerator. The pulsed power system used to drive the cells consists of 32 identical units, each of which contains a trigger unit, Blumlein charge unit, water-insulated Blumlein, and coaxial cables used to deliver the voltage to the cells. Each Blumlein drives two cells. The Blumleins are pulse charged to a nominal 250 kV in a similar fashion to the injector Blumlein. The voltage is fed out to four parallel 44 Ω coaxial cables (two for each individual cell) in a 70-ns pulse [19, 20]. See Figure 1.4 for representative photos of the accelerator and pulsed power halls.

The timing of the voltage delivery to the accelerator cells is critical. The length from the cathode surface to the final cell is approximately 34 meters, and since the electrons are born out of the diode with nearly 4 MeV, their speed is $> 99\%$ the speed of light, or roughly 1 ft/ns. Thus, the firing of Blumlein 32 (driving Cells 63 and 64) will be delayed about 100 ns later than the firing of Blumlein 1 (driving Cells 1 and 2) to provide the maximum accelerating voltage to the beam at the appropriate time as it traverses the accelerator.

Due to the short pulse length of the electron bunch, the accelerator cells are designed with a ferrite core containing a nested solenoid magnet. The ferrite core is made up of a stack of 11 oil-insulated nickel-iron-zinc toroids for a total of 27.93 mV-s per cell. A polystyrene insulator is used for vacuum voltage holdoff [21].

Included within each cell are a pair of nested dipoles that can be used to steer the beam. Beam position and current measurements are made by a Beam Position Monitor (BPM). There are two BPMs located in each cell block, in addition to two located between the injector and Cell Block 1 and the seven located downstream of Cell Block 8, in the downstream transport section of the accelerator. These BPMs are one of the primary beam diagnostics used every shot to ensure beam quality and repeatability.

1.1.2 Axis-II

DARHT Axis-II is an intense, long pulse, relativistic electron LIA [22, 23]. With a nominal pulse length of 2 μs, the Axis-II beam contains over 30× more charge than the Axis-I beam. This required duration and intensity necessitated many different design choices for the injector, cathode, pulsed power, accelerator cells, and downstream transport compared with Axis-I. LBNL was responsible for the design of the pulsed power and injector systems, while LLNL was responsible for the kicker design and downstream transport to produce the desired multiple radiographic pulses.

The injector system, to provide the required long pulse length, is an 88-stage Marx generator with each stage consisting of a type E Pulse Forming Network (PFN) architecture. Compared with a traditional Marx generator, a Marx PFN system uses lumped element PFNs to form each stage of the Marx instead of capacitors. The injector delivers a nominal 3.2 MV voltage pulse with a 400 ns rise time and 2 μs flat top to a 16.5-cm-diameter dispenser cathode [24]. A thermionic cathode is required for low emittance, long pulse, high current extraction as designated by the Axis-II beam parameters; research is ongoing to investigate the long pulse and multi pulse capability of field and photoelectron emitters.

A total of 74 induction cells add voltage to the beam after extraction through the diode. Six of these cells operate as a part of the injector and have a larger center bore and a lower operating voltage (175 kV) than the subsequent 68 cells operating at 200 kV that form the accelerator section [25]. The injector cells, combined with collimators and apertures, collectively form the Beam CleanUp Zone (BCUZ) [26]. The BCUZ is used to remove the off-energy electrons in the beam head due to the finite rise time of the voltage pulse. The tail of the pulse is sharp due to the use of a crowbar. Removing these off-energy electrons before the beam enters the accelerator helps prevent background X-ray production and beam charge deposition in undesired portions of the accelerator that could result in insulator flashover, cathode poisoning by backstreaming desorbed neutrals and ions, or other detrimental issues.

The Axis-II inductor cells have Metglas cores with a $\sim$0.50 V-s capacity. Each cell is individually driven by a 4-stage Marx PFN. The nonlinear magnetization current of the Metglas cores of the accelerator cells is compensated within the Marx PFNs by varying the inductance within each stage [27].

After exiting the beam transport section, the beam continues into the downstream transport section. Pulsed electromagnetic fields in the kicker divert portions of the large, 2-μs-long beam to the bremsstrahlung converter target, while the remaining parts of the beam are transported into a beam dump [28, 29].

1.1.3 The Beam-Target Interaction

While fundamentally different in how the electron bunches are accelerated, the end goals of both of DARHT's machines are clear; provide a quality X-ray pulse (or pulses, for Axis-II) for radiography of the hydrodynamic test object. The choke point of both of these radiographic systems is the point at which the X-rays are produced. This is known as the beam-target interaction. A detailed physics description of this in its entirety is left to Chapter 2, but an overview and motivation for its understanding will be laid out here.

The target used for X-ray production is made of tantalum, which has an atomic number, Z, of 73. The reason why a high-Z material such as Ta is desirable for X-ray generation is because the bremsstrahlung (braking) radiation cross-section scales as Z^2 [30]. A $\sim$20 MeV electron beam, when focused onto a bremsstrahlung converter target, will collisionally and radiatively deposit energy into the target material. This produces a spectrum of X-rays up to the beam endpoint energy, the precise details of which are dependent on target thickness [31, 32]. The bremsstrahlung generated along with the scattered electrons will also contribute to secondary energy deposition into the target material. This net energy deposition eventually will result in the heating and disassembly of the target material which can then adiabatically expand into the surrounding vacuum.

Less of a concern, but still non-negligible for the single pulse Axis-I accelerator, this expanding plasma plume can and will interact with subsequent electron pulses later in time and result in undesirable effects. First, this can lead to space charge neutralization of the beam which can pull the focal spot upstream and cause defocusing and an increase in spot size, degrading radiograph quality [33–37]. Second, the vaporized target material now exists in a lower density condition which, when subsequent electron beam pulses arrive later in time on Axis-II, lowers the bremsstrahlung production efficiency relative to the original solid target. This reduced dose may mean an inadequate radiographic pulse for the experimenters as it potentially would not provide the contrast required to resolve certain features of the test object under dynamic conditions.

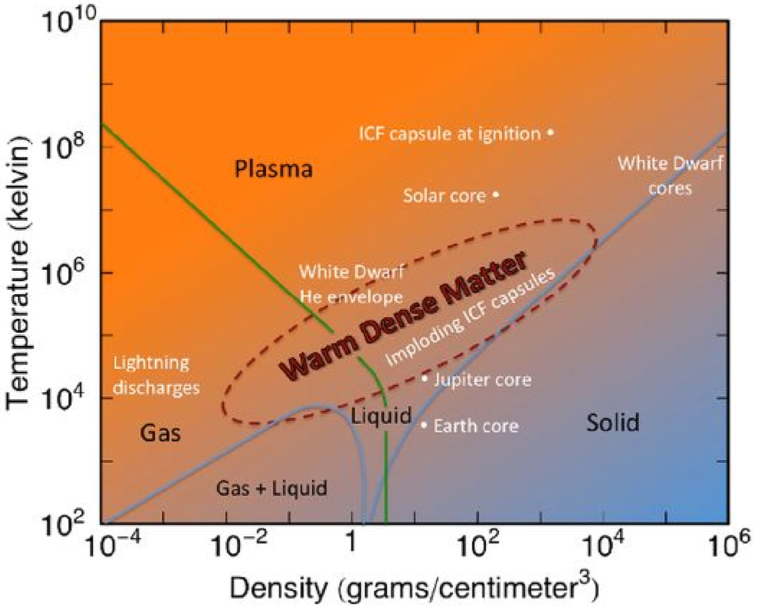

Figure 1.5: Phase space plot highlighting the region of WDM. Note that WDM spans nearly all four regular states of matter: solid, liquid, gas, and plasma. Figure from https://www.lanl.gov/.

Understanding this beam-target interaction is important both for DARHT and future multi-pulse flash radiography machines. Measurements of the Warm Dense Matter (WDM) evolution and late-time plume expansion using visible, EUV, and X-ray diagnostics to determine the temperature, density, pressure, velocity, and other relevant parameters are required to diagnose the beam-target interaction. In addition, mature computational models are required to interpret more complex experimental measurements. These experiments are key to uncovering potentially new physics concepts, validating hydrodynamics and Equation of State (EOS) models, and improving the radiographic performance of DARHT by realizing new bremsstrahlung converter target designs. Initial measurements on DARHT Axis-I have focused on low-Z materials because the electronic structure and resulting characterization is simpler compared with mid-Z and high-Z materials, while also minimizing undesired bremsstrahlung production acting as added background that reduces signal-to-noise ratio (S/N). The material of focus in this thesis is aluminum ($Z = 13$).

1.2 Warm Dense Matter

WDM is characterized by the strongly correlated nature of the ions in addition to the partially or fully Fermi degenerate electron population [38]. Occupying the region of phase space defined by $0.1\rho_0 < \rho < 10\rho_0$ and temperatures of 0.1 eV to 10 (or 100) eV, WDM is a theoretical no-man's land, presenting significant challenges to accurately model and predict its properties. It is con-

T_e (eV)	n_e (cm^{-3})	λ_D (nm)	N_{Debye} (# atoms)	ϵ_F (eV)	Θ	Γ
10	10^{16}	2.02×10^2	345	1.68×10^{-4}	59500	0.005
1	10^{23}	2.35×10^{-2}	0.005	7.80	0.13	1.22

Table 1.1: Calculated quantities from Equations 1.1–1.5 for a classical plasma (10 eV, 10^{16} cm^{-3}) compared with a warm dense plasma (1 eV, 10^{23} cm^{-3}).

jectured to be the makeup of some stellar interiors where pressure ionization dominates. Further, it is likely a transient state in inertial confinement fusion, which makes it relevant for harnessing fusion as a future power source. WDM is also formed in high-power pulsed radiography systems, where the plasma formed will expand upstream into the incoming electron beam and, due to the space charge neutralization of the beam, cause an over-focusing which degrades spot size and, subsequently, radiograph quality. WDM is a subsection in the field of high energy density physics defined by materials having an energy density greater than 1 MBar (see Figure 1.5). However, WDM can exist at lower pressures, particularly when not driven with shock compression. WDM is too dense for ideal plasma theory to apply, along with being too warm for condensed matter theory, which assumes zero temperature.

A classical plasma can be defined as a gas of quasi-neutral charged and neutral particles that exhibit collective behavior. A couple key assumptions of traditional plasma theory include the dominance of collective effects over collisions between individual particles, and a large number of particles contained within a Debye sphere $\mathrm{N}_{\mathrm{Debye}} \gg 1$. The Debye length, λ_D, is defined as the distance over which individual charges have their electric fields screened from the remainder of the plasma. The Debye sphere is a quantity that describes the number of particles within a sphere of radius λ_D. The Debye length is computed by the following expression:

$$\lambda_D = \sqrt{\frac{\epsilon_0 k_B T_e}{n_e e^2}}, \tag{1.1}$$

where ϵ_0 is the free space permittivity, k_B is the Boltzmann constant, T_e is the electron temperature, n_e is the electron density, and e is the electron charge. The Debye sphere can be calculated by the following:

$$\mathrm{N}_{\mathrm{Debye}} = \frac{4\pi}{3}\lambda_D^3 n_e. \tag{1.2}$$

The number of particles in the Debye sphere for a representative warm dense plasma of density 10^{23} cm^{-3} and temperature 1 eV is 0.005, with Debye length equal to 0.23 Å. It is clear that these values do not meet the condition of an ideal plasma.

Electron degeneracy and Coulomb coupling parameters are two metrics by which one can classify states of matter in the high energy density regime. WDM spans a wide range of both of these parameters. The degeneracy is given by the following expression,

$$\Theta = \frac{k_B T_e}{\epsilon_F}. \tag{1.3}$$

where the Fermi energy ϵ_F is defined as:

$$\epsilon_F = \frac{\hbar^2}{2m_e}(3\pi^2 n_e)^{2/3}. \tag{1.4}$$

If $\Theta < 1$, the plasma is considered degenerate. The Coulomb coupling is given by

$$\Gamma = \frac{q_e^2}{4\pi\epsilon_0(T_e + \epsilon_F)} \left(\frac{4\pi n_e}{3}\right)^{1/3}, \tag{1.5}$$

where q_e is the electron charge. The Coulomb coupling defines the collectiveness of the system, and is the ratio of the Coulomb energy to thermal energy. Typically, classical plasmas are weakly coupled (high T_e and low n_e), meaning $\Gamma \ll 1$; conversely, strongly-coupled plasmas have a coupling parameter around or greater than 1. Table 1.1 compares and contrasts these quantities between a classical plasma and a warm dense plasma.

Within the phase space range of WDM, the degeneracy and coupling range over several orders of magnitude: $0.05 < \Theta < 100$ and $0.1 < \Gamma < 2$. These values are calculated using an aluminum plasma ($n_{\text{solid}} \approx 6 \times 10^{22}$ cm^{-3}), and demonstrate the multi-physics nature of the WDM state; many effects need to be considered to accurately capture the interplay of the physical phenomena.

1.2.1 Drivers for WDM

Many platforms exist at this time to generate and probe the WDM state: laser driven shock heating, direct heating with X-ray free electron laser beams, magnetic compression of material using pulsed power, and collisional heating with particle beams. All of these techniques can vary significantly in the duration, size, repetition-rate, and temperature of the WDM generated. A brief overview of each technique is presented below.

Intense lasers focused onto a thin target foil surface results in the generation of strong electric and magnetic fields. These electric fields accelerate electrons from the target foil and cause them to reflex back and forth through the material. This results in rapid, isochoric heating of the material [39–43]. Lasers can also be used to indirectly drive targets into and through the WDM phase by using a hohlraum which creates an X-ray bath that subsequently drives the target, or by driving X-ray backlighters for probing the experimental volume. This is the method employed on the National Ignition Facility (NIF) for fusion-related experiments, where WDM is a transient state when investigating capsule implosions [44]. Note that the time resolution required for these experiments is very short (<1 ns) due to the relevant timescales for heating. An alternative X-ray drive is achieved through the use of an X-ray Free Electron Laser (XFEL). The monochromatic, intense X-ray pulse can both directly heat and probe WDM samples with extremely high spatial and temporal resolution [45–49].

Pulsed power is another controlled means of generating WDM samples [50, 51]. In cylindrical liner implosions, megaampere-class currents flowing axially along the cylinder walls generate strong magnetic fields that implode the liner and its contents via the $\vec{J} \times \vec{B}$ force. Single-wire, multiple-wire and tamped rod implosions can similarly generate states of WDM [52–55]. For many machines, the pulsed power driver can typically afford to act as both the drive and probe X-ray source by using X-pinches as backlighters. The Z machine at Sandia also has available a kilojoule-class laser for backlighting experiments [56].

Particle beam heating with ions has been demonstrated at several facilities. Both light [57–59] and heavy [60–62] ions have been used to heat thin foils, with the generating mechanism a particle accelerator. Laser driven ion heating through target normal sheath acceleration that can produce quasi-monochromatic beams has also been demonstrated [63–66]. The foil thicknesses are chosen taking into consideration the energies of the accelerated ions and the stopping power to ensure uniform, isochoric heating of the target material. One limitation of ion accelerators is the maximum charge that can be transported (10s of nC), which limits the sample volume that can be effectively heated, compared with electron LIAs which can contain on the order of 100s of μC of charge per bunch, without the need of drift compression to enhance intensity.

1.3 Electron Beam Driven WDM

As previously described, the DARHT facility at LANL consists of two fundamentally different electron accelerators with their beamlines oriented perpendicular to one another. The Axis-I LIA produces an intense, relativistic electron bunch with an 80-ns Full-Width at Half-Maximum (FWHM) at an energy of 19.8 MeV and a current of 1.5 kA. In these beam-target interaction experiments, the beam is incident upon range-thin low-Z metal foils and collisionally deposits energy in a two-stage heating process [3, 67–69]. Prior to hydrodynamic disassembly of the foil, the heating is isochoric. Once the foil begins to disassemble, the electron beam is depositing its energy into an expanding volume of WDM. The advantages of heating with relativistic electron beams include: (1) generating large volumes of WDM, (2) high reproducibility limited only by the quality of the linac, and (3) the "slow" timescales over which the WDM exists (100s of ns) compared to laser or X-ray driven WDM. The electron beam driven heating mechanism can be made purely isochoric, i.e. by forcing the foil disassembly time to coincide precisely with the end of the electron pulse. For example, this can be achieved by expanding the beam to a $\sim$1 cm diameter on the foil surface, yielding a lower fluence and heating the material through the vapor dome while only achieving pressures on the order of 10s of kBar.

Limitations of this technique, however, include the generation of background radiation and scattered electrons during the electron pulse, which can have endpoint energies up to the beam energy of 19.8 MeV. This is especially critical for quantifying the early time dynamics of the WDM during the electron beam pulse and must be accounted for in the design of X-ray diagnostics. As previously mentioned, this effect is presently mitigated by decreasing foil thickness and using lower-Z target materials. Further, the expanding plasma plume exhibits a strong density gradient, varying several orders of magnitude over millimeter scales. This limits visible diagnostic probes to surface measurements of the plume, rather than bulk measurements due to opacity and cutoff effects. This provides motivation for developing computational models to interpret and predict experimental measurements. Finally, DARHT is not a fundamental science facility like the NIF and the Z machine, or user facility like OMEGA; experimental time is governed by several competing resources, but is dominated by the mission need to support the Stockpile Stewardship Program. A more appropriate platform to study electron beam driven WDM with collisional heating would be a standalone facility with an endpoint energy of a few MeV – essentially a DARHT-I injector with a small transport lattice to focus the beam on target.

1.3.1 Outline of Present Work

This section outlines a brief summary of the remaining contents of this thesis. In Chapter 2, the details of the electron beam-target heating physics are given with relevant parameters and derivations needed to understand the context of the experiments presented in later chapters. In Chapter 3, an overview of the beam dynamics are provided to fully describe the electron beam and its generation, acceleration, transport, and focusing for the heating experiments described in later chapters. In Chapter 4, all the diagnostics for probing both the beam and plasma are presented, along with examples to illustrate their use in later chapters. Chapter 5 details the spectral calibration sources and measurements made for the utilized spectrometers. All computational modeling and simulation tools are explained in Chapter 6 and are subsequently used extensively to match and, in some cases, predict experimental measurements. Chapters 7 and 8 describe experimental measurements made on Axis-I, primarily focusing on temporally- and spatially-resolved visible emission and absorption spectroscopy and the supporting spectroscopic-quality radiation transport modeling required to interpret the measurements.

Conclusions are presented in Chapter 9 along with an attempt to coalesce and summarize the achievements from this body of work. Some notable firsts have been achieved here, including the development of a spectroscopic-quality radiation transport modeling capability interfacing with a

radiation hydrodynamics code for interpreting spectroscopic measurements. Diagnostic limitations illuminated from these models are provided along with recommendations for future diagnostic and modeling capabilities, some of which are already developing out of this thesis work.

CHAPTER 2

Electron Beam-Target Heating Physics

Electron beam-target heating is a complex process involving thermodynamics, particle beam energy deposition, and phase transitions, and can differ dramatically between different target materials. Figure 2.1 shows a general overview of the energy deposition process and subsequent target expansion. In this chapter, Sections 2.1–2.4 explain steps (1) and (2) in Fig. 2.1, Sections 2.5–2.6 explain step (3), and Section 2.7 explains step (4). This chapter will focus primarily on the heating of aluminum targets, but will also draw comparisons with other materials for comparing and contrasting the different processes. Throughout this chapter, the nominal beam parameters used for calculations, unless otherwise explicitly stated, are a beam energy of 19.8 MeV with a current profile as shown in Figure 1.3(b).

2.1 Energy Deposition

Energy deposition into solid targets by charged particle beams is calculated using the stopping power (dE/dx), which is a function of target material and particle energy and is typically given in units of $\mathrm{MeV\,cm^2/g}$. The stopping power is defined as the rate of energy loss per distance traveled within a medium. The total stopping power is composed of two separate contributions: collisional stopping (which involves Coulomb collisions with atomic electrons that result in ionization and excitation) and radiative stopping (which involves emission of bremsstrahlung). The collisional stopping power deals directly with the impinging charged particles (in this discourse, electrons) and their interaction with the target material via inelastic scattering cross sections [70, 71]. The radiative stopping power is evaluated with bremsstrahlung cross sections [72].

Another relevant quantity extracted from the total stopping power is the Continuous-Slowing-Down Approximation (CSDA) range R. This is calculated by integrating the total stopping power from starting energy E_0 to endpoint energy E_f:

$$R = \int_{E_f}^{E_0} \frac{dE'}{\left[dE/dx\right]_{\text{tot}}(E')}, \tag{2.1}$$

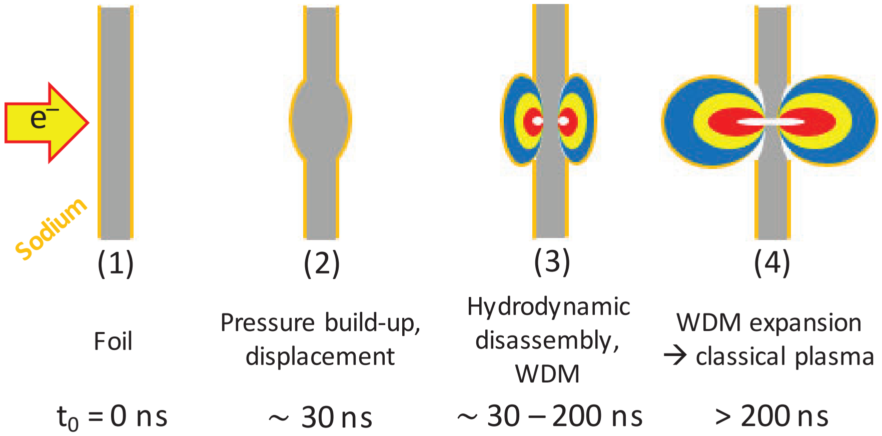

Figure 2.1: Electron beam driven WDM production. Approximate timescales for a 100-μm-thick target are given for reference, where t_0 is the start of energy deposition. (1) The intense, relativistic electron beam is focused down to a small spot on the Al foil (gray). (2) Energy deposition results in a pressure build-up and displacement of the foil. (3) Hydrodynamic disassembly and pressure release of the foil material; transition into the WDM stage, where the contours from blue to red represent roughly the increasing density gradient. (4) Adiabatic expansion of the WDM, which transitions later in time to a classical plasma.

where E' is the is the particle energy and $[dE/dx]_{\mathrm{tot}}$ is the total stopping power. This calculation is performed under the approximation that the continuous rate of energy loss by the particle in a material is equal to the total stopping power. Energy loss fluctuations due to the nature of the large angle scattering of electrons are also neglected. The CSDA range very accurately estimates the average depth reached within a material by a charged particle as it is decelerated. The National Institute of Standards and Technology (NIST) ESTAR stopping power tables are used to determine the stopping powers and CSDA ranges [73, 74].

Figure 2.2 plots the collisional, radiative, and total stopping powers for three different materials: aluminum ($Z = 13$), copper ($Z = 29$), and tantalum ($Z = 73$). Commonalities across all three materials include power law scaling of the radiative stopping power for electron energies $\gtrsim$ 1 MeV, and a minimum around 1 MeV for the collisional stopping power. It is clear from these plots that radiative stopping power scales with the Z of the material. Collisional stopping dominates the total stopping below 50 MeV for aluminum, below 25 MeV for copper, and below 10 MeV for tantalum. A plot of the CSDA range in Figure 2.3 is a more intuitive way to consider the electron beam interaction with the target material; it is apparent that the higher-Z material more quickly stops electrons (and thus deposits more energy) compared to a lower-Z material. In other words, the CSDA range demonstrates the correlation between increasing atomic number and the corresponding increase in stopping power (and thus a decrease in range).

The stopping power is used to calculate the energy deposited by an electron bunch with a radius

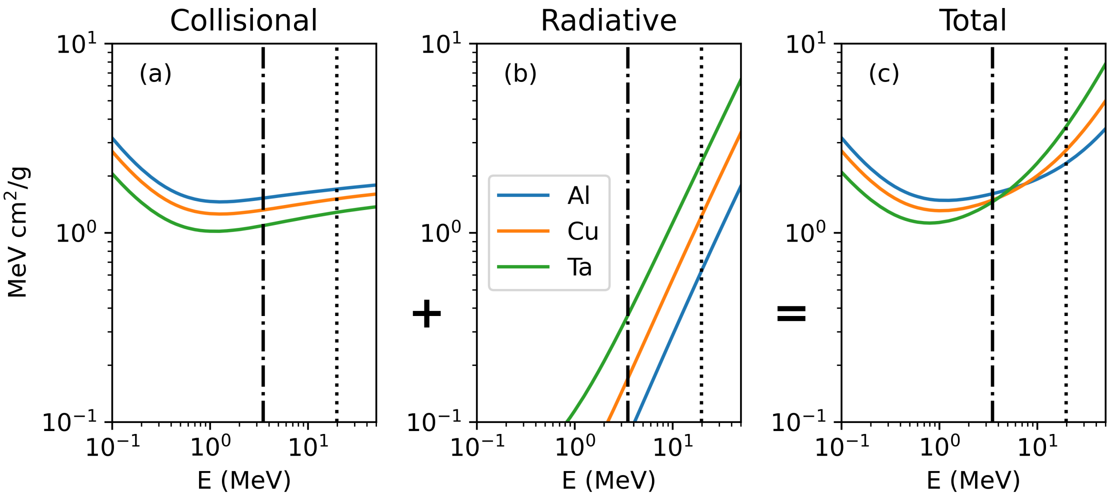

Figure 2.2: Stopping power calculations for aluminum, copper, and tantalum highlighting the relevant electron energies of 3.5 MeV (dash-dot, Axis-I injector only) and 19.8 MeV (dotted, Axis-I full accelerator). (a) Collisional stopping power; (b) radiative stopping power; (c) total stopping power.

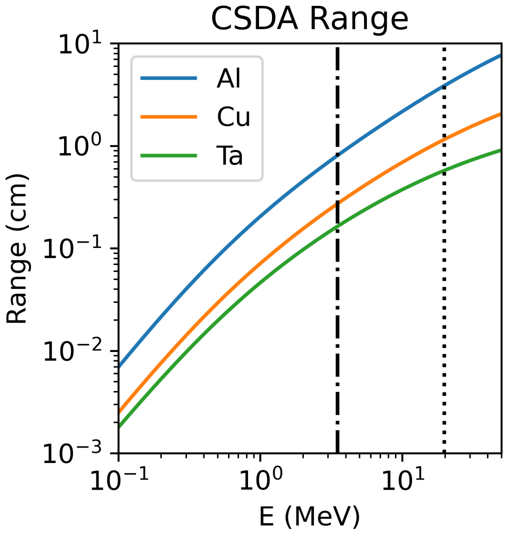

Figure 2.3: Electron CSDA range in aluminum, copper, and titanium with the relevant electron energies of 3.5 MeV (dash-dot, Axis-I injector only) and 19.8 MeV (dotted, Axis-I full accelerator) highlighted. At 19.8 MeV, the range in aluminum is 3.90 cm, compared with 1.16 cm in copper and 0.57 cm in tantalum.

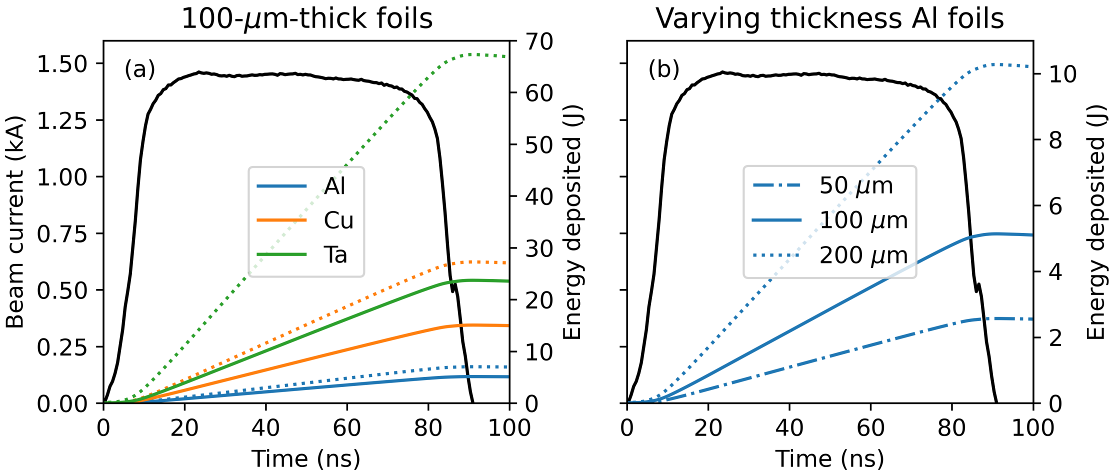

Figure 2.4: Time dependent energy deposition (right axis) by a 20 MeV electron beam into foils of varying Z and thickness calculated using Equation 2.2 (assuming no target expansion). (a) 100 μm aluminum, copper, and tantalum foils, where collisional energy deposited is shown in the solid traces, and the total (collisional + radiative) energy deposited is shown in the dotted traces. (b) Collisional energy deposition into aluminum foils with thicknesses of 50 μm (dash-dot), 100 μm (solid), and 200 μm (dotted). The current trace shown (left axis, same scale for each inset) is from BPM 19, shot 33909.

r_{beam} and time dependent charge $q(t)$ into a target foil of thickness Δz, density ρ_0, and mass m in the following equation:

$$\Delta E(t) = q(t)\frac{dE}{dx}\rho_0 \Delta z = \frac{q(t)}{\pi r_{\text{beam}}^2}\frac{dE}{dx}m. \tag{2.2}$$

This expression assumes a uniform distribution of electrons depositing energy and does not represent a Gaussian or Lorentzian spatial beam current profile, the latter of which is measured on target with near-field Optical Transition Radiation (OTR) and will be described further in Section 4.1.2. The accumulated charge $q(t)$ is found by integrating the current profile shown in Fig. 2.4 over time.

Figure 2.4 plots the time dependent energy deposition by a 20 MeV electron beam into different foil materials and thicknesses, assuming no foil expansion. Also highlighted is the difference when accounting only for collisional energy deposition compared to total (collisional + radiative) energy deposition. At ~20 MeV for aluminum, the change is not very significant (~20%). However, at modestly higher Z like copper, the radiative energy deposition is very nearly equal in contribution to the collisional energy deposition. At high Z (tantalum), the radiative energy deposition dominates the total energy deposition, accounting for almost 70% of the total.

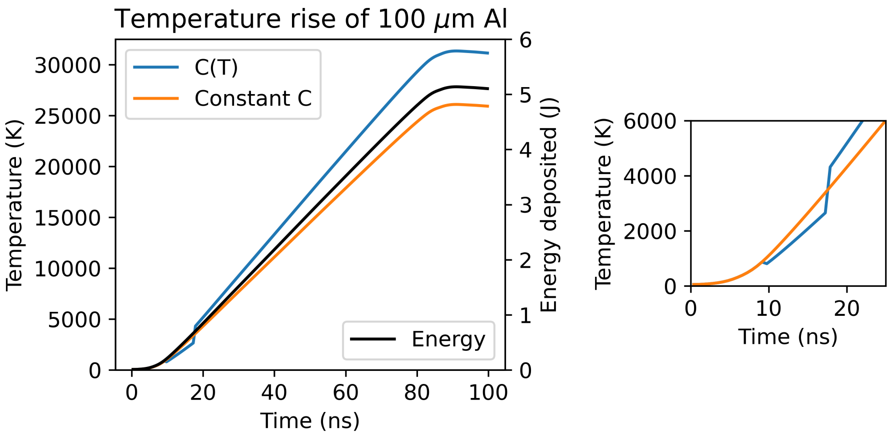

Figure 2.5: Temperature rise of a 100 μm Al foil heated by a 1-mm-diameter beam. The current profile used is that from Fig. 2.4. The deposited energy is shown in black, while the temperature rise due to the temperature-dependent heat capacity is shown in blue and the temperature rise due to the constant heat capacity in shown in orange. The inset to the right highlights the differences obtained when using the temperature (i.e., phase) dependent heat capacity versus a constant heat capacity for the duration of the heating.

2.2 Temperature Rise

The time dependent temperature rise of the heated material can be estimated using the first law of thermodynamics:

$$\Delta T(t) = \frac{E(t)}{mC}, \tag{2.3}$$

where C represents the phase-dependent heat capacity of the material. For aluminum, $C_{\text{solid}} = 0.925$ J/g/K and $C_{\text{liquid}} = 1.18$ J/g/K. An ideal gas heat capacity of $C_{\text{gas}} = 0.77$ J/g/K is assumed after the material is completely vaporized. Using Equation 2.3, the temperature as a function of time is plotted in Figure 2.5 for a 100-μm-thick Al foil heated by an electron beam with a diameter of 1 mm. Calculations are plotted using both a temperature dependent heat capacity as well as a constant heat capacity. The simple approximation of a constant heat capacity results in an underestimation of the final temperature by 17%. The temperature dependent heat capacity calculation compares reasonably well with Ref. [75], where it is within 4% of the calculated value.

One important note on the temperature rise is that it is relatively independent of foil thickness, due to the factor $\frac{E(t)}{m}$. The mass scales linearly with the increasing foil thickness ($m \propto r_{\text{beam}}^2 \Delta z$), as does the energy deposited, shown in Eq. 2.2. Increasing the foil thickness only prolongs the time to material disassembly and results in a higher pressure attained within the foil. This will be explained in more detail later in this chapter in Section 2.5.

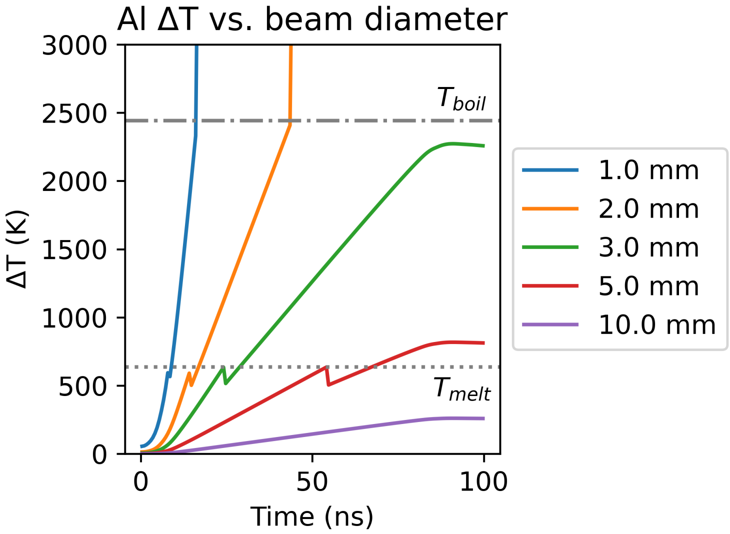

Figure 2.6: Temperature rise of a 100 μm Al foil heated by electron beams of various diameters. Also highlighted are the melting (dotted) and boiling (dash dot) temperatures of aluminum. With this model, beam diameters greater than 3 mm do not result in vaporization of the target material.

2.3 Gas Desorption

The energy deposition into the target material under high vacuum (10^{-7} Torr) can result in the desorption of contaminant monolayers on the surface of the target material. These monolayers usually consist of water molecules. The desorption process is described by three distinct steps: (1) desorption of the surface monolayers (H_2O) once a temperature threshold of 400° C is reached; (2) disassociation and ionization of the water molecules; and (3) acceleration of the ions upstream into the electron beam. This results in neutralization of the beam space charge, which can result in a pinching (or over-focusing) of the beam upstream of the target.

A temperature rise of only 400° C is sufficient to desorb loosely bound layers of atoms on the surface of the target and provide effectively space charge limited current emission [76, 77]. Depending on the beam size, this temperature can be achieved quite rapidly (< 50 ns). It has been demonstrated, however, that the target material itself does not have to undergo a phase change (melt) to release backstreaming ions that impact beam quality. In addition, the gas desorption process does not depend on target thickness. As shown in Figure 2.6, beam diameters less than 5 mm are sufficient to induce ion emission, while beam diameters greater than 3 mm do not result in vaporization of the aluminum target.

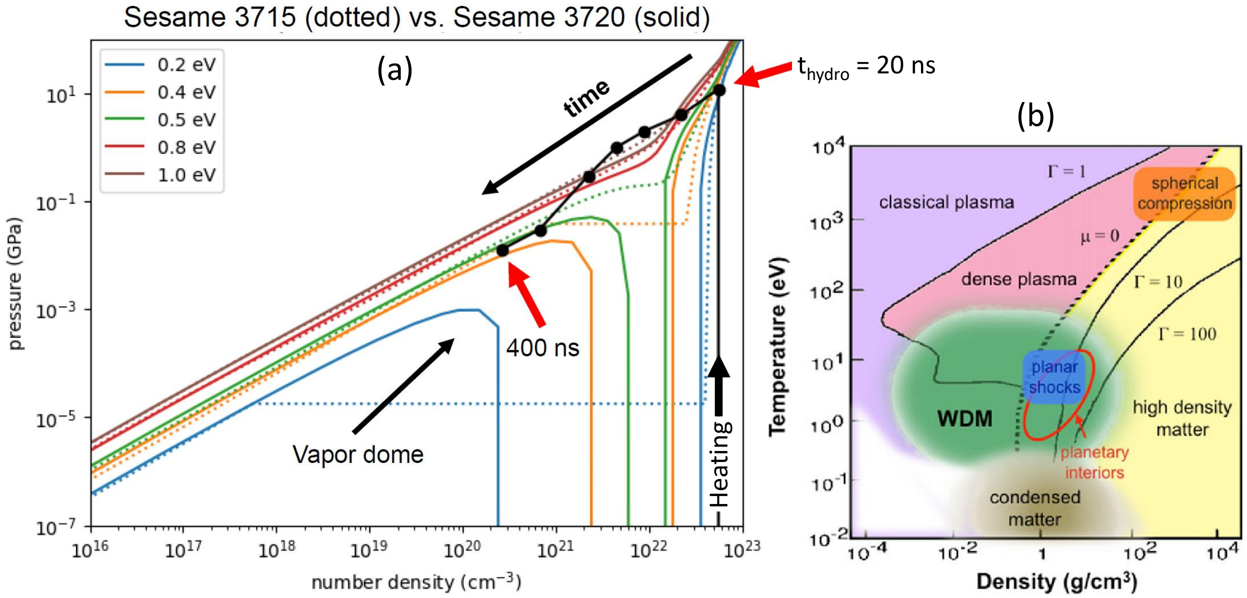

Figure 2.7: (a) SESAME EOS plot of aluminum showing relevant isotherms for 0.2–1.0 eV. The dotted lines correspond to the legacy EOS 3715, while the solid lines are the newer EOS 3720. The vapor dome is highlighted and is only accounted for in SESAME 3720. (b) General phase space plot highlighting the WDM phase along with other relevant states of matter such as traditional condensed matter and classical plasmas. Also shown are contours representing the coupling (Γ) and the onset of degeneracy (high-density side of $\mu = 0$, where μ is the chemical potential). Inset (b) is reproduced from Ref. [1].

2.4 Phase Dynamics

Isochoric heating is defined as uniform heating throughout the volume of a material before it has time to hydrodynamically expand. When tracing this heating profile as shown in Figure 2.7(a), the vertical line from $t = 0$ to t_{hydro} corresponds to the isochoric heating phase. The pressure points along with temperatures and densities as a function of time are from LASNEX simulations and will be further discussed in Chapter 6. The flexible range of fluence of the Axis-I beam (450 J/cm^2 for an expanded 1-inch-diameter beam to 300 kJ/cm^2 for a focused 1-mm-diameter beam) attained by changing the focusing field strength of the solenoid magnet DT#1 provides the ability to control both the peak temperatures and target disassembly times to reach various points within the phase diagram. Specifically, the vapor dome highlighted in Fig. 2.7(a) is of interest. This is relevant for benchmarking EOS tables; the legacy SESAME EOS 3715 does not account for this, while the new EOS 3720 does. As previously mentioned, an in-depth discussion of these EOS issues will be provided in Chapter 6.

2.5 Hydrodynamic Disassembly

Hydrodynamic disassembly of the target material occurs when the material can no longer contain the pressure buildup caused by the energy deposition. The hydrodynamic disassembly is influenced by several different parameters: beam energy density, material thickness and properties (i.e. equations of state), and target configurations. This peak pressure can be estimated using the ideal gas law:

$$P = n_e k_B T_e. \tag{2.4}$$

For example, aluminum at solid density and a temperature of 1 eV has a pressure of 9.6 GPa. This result can be used to calculate the ion acoustic sound speed c_s in the material in its given state:

$$c_s = \sqrt{\frac{\gamma Z P}{\rho_0}} = \sqrt{\frac{\gamma k_B T_e}{m_i}}, \tag{2.5}$$

where γ is the adiabatic index (under the ideal gas assumption, $\gamma = 5/3$), and Z is the charge state of the plasma. The second formulation from Equation 2.5 is used to infer roughly the electron temperature by measuring the expansion velocity $v_{\max}$. This can be obtained by performing a series of time-gated plasma plume expansion (Chapter 4, Section 4.2.1) or shadowgraph (Chapter 4, Section 4.2.4) measurements and then using the following relation [69, 78]:

$$c_s = \frac{\gamma - 1}{2} v_{\max}. \tag{2.6}$$

The hydrodynamic disassembly time corresponding to the pressure release for a planar foil can be estimated using the following equation [79]:

$$t_{\text{hydro}} = \frac{\Delta z}{2 c_o}, \tag{2.7}$$

where Δz is the foil thickness and c_o is the sound speed at ambient pressure. For aluminum, $c_o = 5.2$ km/s [80]. The factor of two accounts for expansion in both directions normal to the foil surface.

Using the 9.6 GPa calculated for a solid density aluminum plasma with a temperature of 1 eV, the ion acoustic sound speed is computed to be $c_s = 2430$ m/s. Equation 2.7 estimates a hydrodynamic disassembly time of $t_{\text{hydro}} = 10$ ns for a 100 μm aluminum foil. This is in reasonably agreement with the LASNEX results plotted in Figure 2.7, but the formulation in Eq. 2.7 does not include the effect of the energy density profile provided by the beam, so it is only treated as a rough approximation of t_{hydro}. Measurements presented in Table 4.5 in [81] on an 1100-series aluminum foil with a thickness of 100 μm determine a $t_{\text{hydro}} = 21$ ns with a pressure of 8.0 GPa (shot #28891) which is in good agreement with Fig. 2.7.

Note that $t_{\rm hydro}$ is not directly proportional to the incident energy density. The hydrodynamic disassembly time has been shown in simulations to be only slightly faster with twice the energy density, but the resulting expansion occurs twice as fast [82]. In short, reducing the spot size by a factor of two would increase the temperature and peak pressure by a factor of four: $P \propto T \propto 1/r_{\rm beam}^2$.

2.6 WDM

As the material heats up and builds up pressure, it transitions into the WDM state. WDM, previously defined in Section 1.2, exists in the temperature-density space from 0.1 to 10 (or 100) eV and $0.1\times$ to $10\times$ solid density. As shown in Fig. 2.7(b), WDM spans a complex space where the plasma varies strongly in both degeneracy (Θ) and coupling (Γ) , as defined by Equations 1.3 and 1.5. Collisional heating with electrons does not compress the target material, so the highest densities achieved correspond to the solid densities of the target materials. Radiation hydrodynamics simulations (see Section 6.1) predict the WDM state to exist out to 200 ns after initial heating of the target material by the electron pulse, after which it decays to below $0.1\times\rho_0$ into a dense, classical-like plasma.

WDM cannot be directly probed by existing diagnosics on the DARHT accelerators. Due to the low temperature and high density, traditional "passive" measurements, i.e. collecting, collimating, and dispersing the radiation produced by the plasma, do not work as the plasma is dominated by absorption effects and very low emissivity, relative to hot plasmas. Present measurements have recorded densities up to 10^{19} cm^{-3} with 532-nm interferometry [83], and visible spectroscopy via Stark broadening has measured densities up to 10^{18} cm^{-3} [3, 68, 69]. While these measurements do constrain and demonstrate the WDM state to be present, the WDM state has not been directly measured.

2.7 Expansion

The material disassembly and expansion results in the formation of a density and temperature gradient that exhibits roughly cylindrical symmetry. The bulk of the plasma, according to radiation hydrodynamics simulations, exists at a relatively uniform temperature and density, while the outer region exhibits a higher temperature and a severe density gradient. This gradient can span several decades of density in 100s of μm. The majority of the present plume measurements, especially for spectroscopy, are made well after the material has disassembled [3, 68, 69]. A consequence of measuring a plasma plume with a severe density gradient is the opacity effects and attenuation

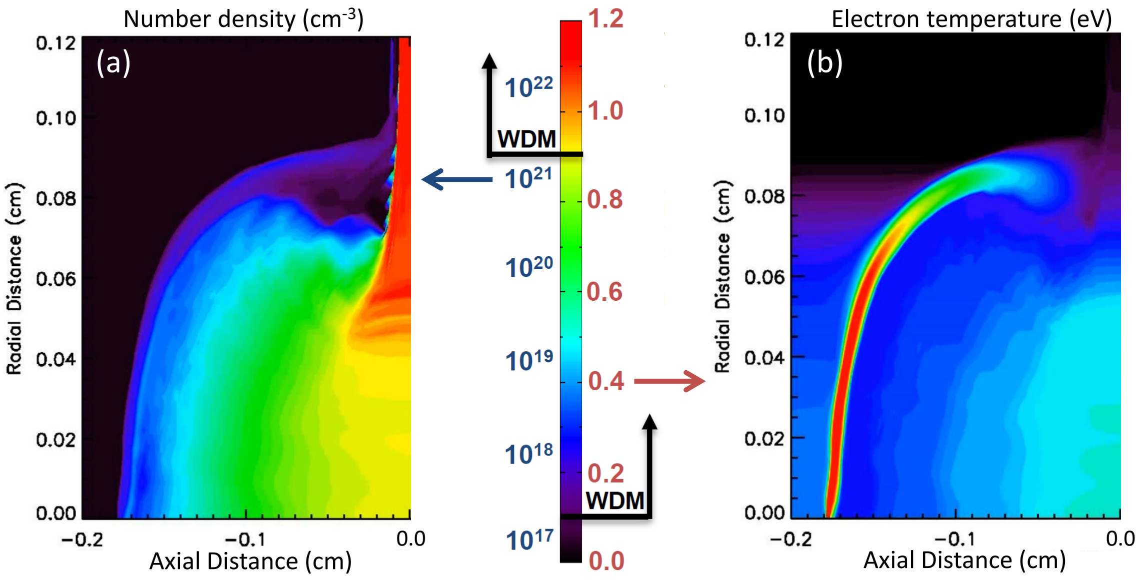

Figure 2.8: 2-D cylindrically-symmetric radiation hydrodynamics simulation results of the (a) density and (b) electron temperature at 250 ns for a representative beam heating a 100 μm aluminum foil. The results are symmetric about $R = 0$ and very nearly symmetric about $Z = 0$.

of the escaping (and/or probing) radiation. Thus, the majority the spectroscopic measurements are determined to be localized to a surface layer, as will be further detailed in Chapter 8, and can require radiation transport modeling to accurately interpret the lineshapes. A 2-D plot of the LASNEX-modeled temperature and density of a 100 μm aluminum foil at 250 ns after initial energy deposition is shown in Figure 2.8. Note the apparent presence of a shock signified by the enhanced temperature on the leading edge of the plume. The shock exists within the aluminum materials and not within the desorbed water vapor monolayers. In Figure 2.8, the water vapor exists in the low-temperature region to the left (upstream) of the shocked region (T$_e$ > 1 eV).

As the plasma plume expands, it radiatively cools, slowing its expansion velocity and reducing its temperature and density. The plume still exists over long timescales with respect to the electron beam timescales. In fact, the plume light can be measured nearly 10 μs after initial energy deposition [3, 67]. The plume leading edge position and velocity can be roughly approximated as a point source explosion and calculated using the Taylor–von Neumann–Sedov formulation [84–86]:

$$z(t) = \eta \left(\frac{Et^2}{\rho_0}\right)^{1/5}; \; v(t) = \frac{dz(t)}{dt} = \frac{2\eta}{5}\left(\frac{E}{\rho_0}\right)^{1/5} t^{-3/5}. \tag{2.8}$$

At 500 ns, the plume extent for a 100 μm aluminum target is roughly 5 mm with an expansion velocity of a few km/s. These time and space scales are directly relevant for multi-pulse radiography on Axis-II and, if unmitigated, this backstreaming plasma (in addition to the backstreaming desorbed ions) can induce a time-varying radiographic spot size. Ref. [37] documents early efforts on controlling the late-time behavior of the plasma plume.

2.7.1 Summary

This chapter describes the electron beam heating process of range thin metal foils. The collisional energy deposition by the relativistic electron beam into the target material and resulting temperature rise and gas desorption due to this temperature rise has been explained. The phase changes experienced by the heated material are explained, followed by the subsequent hydrodynamic disassembly of the target material into the WDM phase. Finally, the expansion and cooling of this plasma plume in space and time is given.

CHAPTER 3

DARHT Axis-I Beam Dynamics

3.1 Transverse Beam Envelope Equation

To describe the motion of a charged particle beam, simplifying assumptions can be made about the beam properties, in addition to generally decoupling the transverse and longitudinal forces acting on the beam. Specifically, it is usually sufficient to only consider averaged values across the beam cross section, in particular the beam radius R and the beam envelope angle. The key assumption made for developing the beam envelope equation is that the beam is paraxial, or the beam envelope angle $\langle x' \rangle \ll 1$. The implication of the paraxial assumption is that external transverse forces can be simplified and beam-generated forces can be approximated as forces generated by an infinite-length beam. In addition, external fields are treated as static and the axial beam kinetic energy is much larger than the transverse kinetic energy. The beam energy is also assumed to be constant within the beam envelope.

The beam envelope equation can be used to describe the Axis-I electron pulse because the beam length (~ 25 m) is much larger than the beam radius (< 1 cm). The derivation of the beam envelope equation is provided in Refs. [87, 88].

Below is the beam envelope equation for electrons, where $'$ denotes a derivative with respect to the axis of propagation ($\hat{z}$):

$$R'' = -\frac{\gamma' R'}{\beta^2 \gamma} - \frac{\gamma''}{2\beta^2\gamma} R - \left(\frac{qB_z}{2\beta\gamma m_e c}\right)^2 R + \frac{\epsilon^2}{R^3} + \left(\frac{q\psi_0}{2\pi\beta\gamma m_e c}\right)^2 \frac{1}{R^3} + \frac{K}{R}. \tag{3.1}$$

Here, $\beta = 1 - \frac{1}{\gamma^2}$ and $\gamma = 1 + \frac{E}{E_0}$, B_z represents an external applied magnetic field, and ψ_0 is the magnetic flux enclosed by the beam envelope at the birth of the particles (for Axis-I, this occurs at the planar velvet cathode):

$$\psi_0 = \int_0^{R_z} 2\pi R \, dR \, B_z(R, Z_S). \tag{3.2}$$

The term on the left side of Equation 3.1 is the second derivative of the beam envelope radius

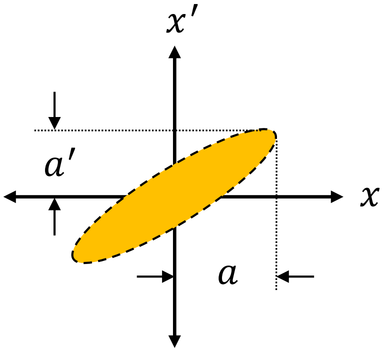

Figure 3.1: Transverse phase space representation. The area within the dotted line is quantified by the emittance.

with respect to z. On the right side are three negative terms that represent focusing (decreasing beam envelope size) processes, and three positive terms that represent defocusing (beam envelope growth) processes.

The first focusing term is a result of particle acceleration, typically arising from applied axial electric fields. The second focusing term arises from radially applied electric fields. The third focusing term arises from axially applied magnetic fields. On Axis-I, these are provided by the solenoid magnets located within the accelerator cells.

The first defocusing term is a result of the thermal energy spread of the beam, as quantified by the emittance, ϵ. The emittance quantifies the thermal energy spread of the beam, and is a measurement of the phase space distribution of the beam. The second defocusing term is a result of the beam particles being born with nonzero canonical angular momentum. This is typically negligible; on Axis-I a bucking coil is used to "buck out" (or zero) the magnetic field on the cathode face. The third defocusing term is due to the repulsion of the beam by its own space charge. This is quantified by the generalized perveance.

Transport of charged particle beams principally depends on two quantities: emittance (ϵ) and perveance (K). The emittance quantifies the thermal energy spread of the beam, and is a measurement of the phase space distribution of the beam. The phase space is a six-dimensional space in position (x, y, z) and velocity (v_z, v_y, v_z) that fully describes the state of the beam. A 2-D projection is shown in Figure 3.1, where $x' \equiv \frac{v_x}{v_z}$. In a well aligned and linear accelerator focusing system, the volume of phase space (area of the ellipse in Fig. 3.1) occupied by the beam is conserved. Emittance is typically given as a 4rms quantity and has units of $\pi \cdot$ mm $\cdot$ mrad:

$$\epsilon_{\text{4rms}} = 4\sqrt{\langle x^2\rangle\langle x'^2\rangle - \langle xx'\rangle^2}. \tag{3.3}$$

The quantities $\langle x^2 \rangle$ and $\langle x'^2 \rangle$ are the second moments of the distribution. The third term $\langle xx' \rangle^2$ describes the change of growth of the phase space ellipse shown in Fig. 3.1. The thermal energy spread of an electron beam produced from a cold cathode can be characterized by measuring the temperature of the plasma on the cathode surface through which the electrons are extracted [18]. It is described by the following expression:

$$a'_{\mathrm{th}} = \frac{v_{\mathrm{Tx}}}{v_z}. \tag{3.4}$$

The quantity v_{Tx} is the transverse thermal velocity which can be calculated using the transverse thermal beam temperature. The expression for the normalized emittance is useful because it is usually conserved for accelerating beams:

$$\epsilon_{\mathrm{n4rms}} = \beta\gamma\epsilon_{\mathrm{4rms}}. \tag{3.5}$$

Note that the expression for emittance used in Eq. 3.1 is ϵ_{4rms}, which is defined in Eq.3.3.

The generalized perveance is the ratio of the beam potential energy to kinetic energy, or the ratio of the space charge of the beam to the inertia of the beam with current I:

$$K = \frac{eI}{2\pi\epsilon_0 m_e (\gamma\beta c)^3}. \tag{3.6}$$

By definition, the expression in Equation 3.6 is unitless. This value is relevant for quantifying the beam quality as it is produced out of a diode, and is a measure of the space charge effects on the beam. Generally, beams with a high generalized perveance ($> 10^{-4}$) are difficult to transport due to extremely high space charge [89]. On Axis-I at nominal operations (50 mm cathode, 98 kV PPT charge, 1.45 kA), $K = 4.0 \times 10^{-4}$ at a beam energy of 3.38 MeV after extraction through the anode, and $K = 2.7 \times 10^{-6}$ after exiting the last accelerator cell at 19.8 MeV.

Another formulation of the perveance, known as the gun perveance, can be found from the 1-D Child-Langmuir law:

$$K_{\mathrm{gun}} = \frac{I}{V^{3/2}}. \tag{3.7}$$

The gun perveance for Axis-I operating at the same conditions assumed above for the generalized perveance is $K_{\mathrm{gun}} = 2.2 \times 10^{-7}$ A/V$^{3/2}$.

Equation 3.1 can be simplified to mimic a beam bunch traveling through a uniform focusing section by setting $\gamma' = 0$ and $\psi_0 = 0$, which corresponds to no applied accelerating electric field and zero canonical angular momentum:

$$R'' + k_0^2 R - \frac{\epsilon^2}{R^3} - \frac{K}{R} = 0. \tag{3.8}$$

The focusing term has been written in terms of the wavenumber $k_0 = \frac{qB_z}{2\beta\gamma m_e c}$. A special solution to this equation is when the beam radius is constant ($R = R_0$), which is known as the matched beam condition:

$$k_0^2 R_0 - \frac{K}{R_0} - \frac{\epsilon^2}{R_0^3} = 0. \tag{3.9}$$

This expression highlights the relationship between the roles of emittance and perveance in beam transport. If $KR_0^2 < \epsilon^2$, the beam is in an emittance-dominated regime. Conversely, if $KR_0^2 > \epsilon^2$, the beam is space-charge dominated.

3.2 Numerical Modeling

The beam envelope equation can be solved numerically, given initial beam conditions $a = 2\sqrt{\langle x^2 \rangle}$, $a' = 2\sqrt{\langle x'^2 \rangle}$, and ϵ, and used to propagate the beam through a solenoid lattice for analytic beam tuning. Here, a and a' represent the 2rms values of the beam radius and angle, respectively. From Eq. 3.3, when $\langle xx' \rangle^2 = 0$, $\epsilon_{\text{4rms}} = aa'_{\text{th}}$. These initial conditions are usually obtained from a finite element model of the diode region that accurately captures the geometry and static $\vec{E}$ and $\vec{B}$ field contours, such as TRAK [18, 90]. On DARHT Axis-I, one tool used for modeling beam transport in the LIA is the XTR code [91, 92]. The Large Scale Plasma (LSP) code developed by Voss Scientific is also used for particle-in-cell modeling of the beam transport.

Tuning the accelerator refers to optimizing the solenoid lattice for optimal beam envelope transport conditions, namely a smooth and generally decreasing beam envelope as the beam is accelerated. The increase in beam energy as it is accelerated corresponds to a higher beam rigidity, which is relevant for calculating the kick supplied to the electron beam by the steering dipole magnets. The linear increase in beam energy along the length of the accelerator is matched by imposing a linearly increasing magnetic field strength. In general, the increased applied $\vec{B}$ field along the length of the LIA is used to reduce the growth of the Beam Breakup (BBU) instability. Different accelerator tunes are required for different cathode sizes (and thus different beam currents); to minimize BBU, the a higher $\langle B \rangle$ is required for higher current beams compared with lower current beams [89, 93].

Figure 3.2 demonstrates a tune designed for stronger (smaller beam envelope) transport through Axis-I for a 50 mm cathode. The higher field tune is used to help minimize the scraping of off-energy electrons along the beam pipe present at the head and tail of the beam pulse due to the finite rise and fall times in the injector voltage. Figure 3.3 demonstrates a refined tune for a 19 mm cathode that minimizes envelope oscillations along the length of the LIA. For both Figures 3.2 and 3.3, the magnetic lattice plotted corresponds to that of the new tune (red).

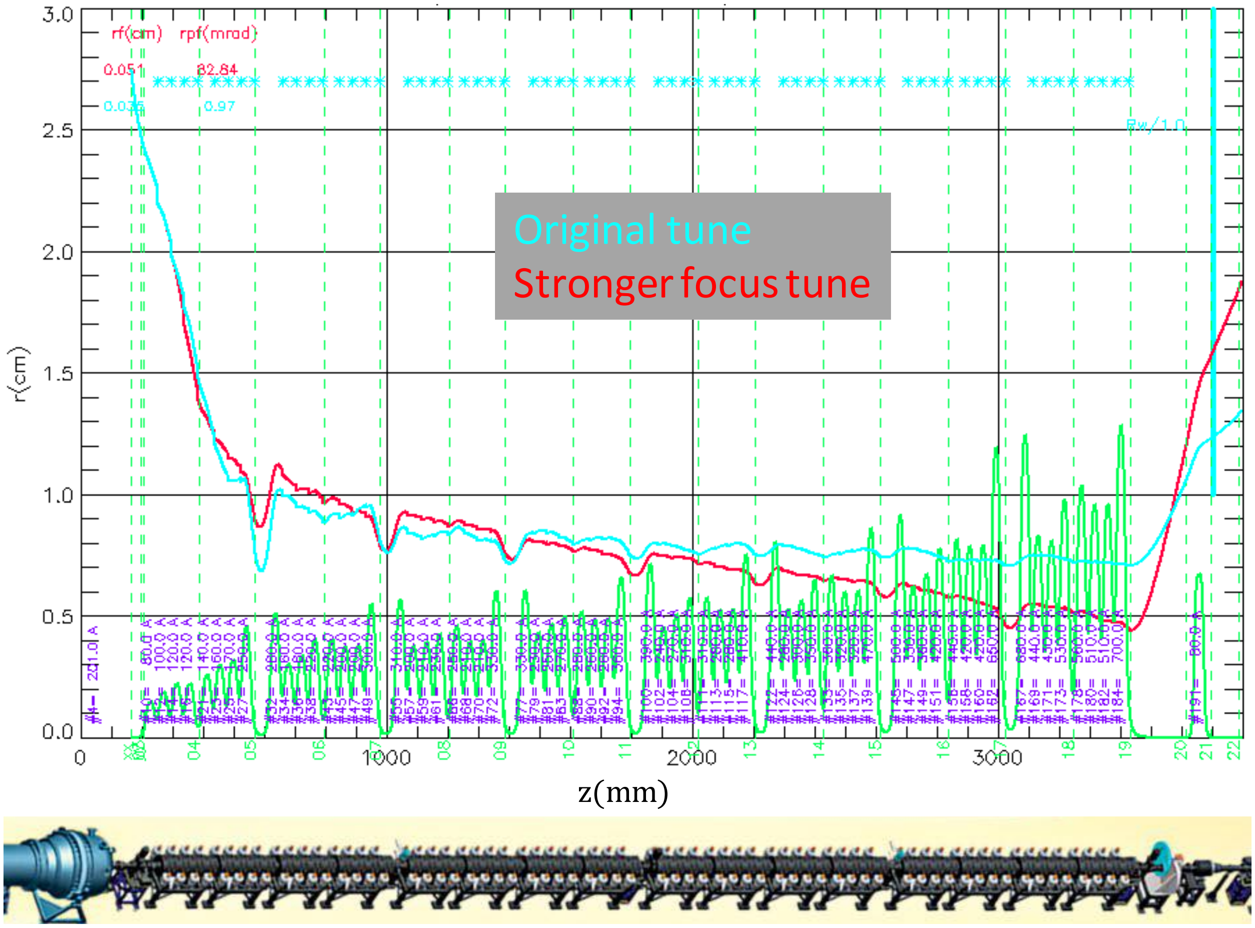

Figure 3.2: Comparison of two accelerator tunes for a 50 mm cathode on Axis-I. Shown in cyan is the original tune, with red being the new, stronger focused transport of the beam. The green curves are the magnetic field lattice provided by the accelerator solenoids, with the BPM numbers labeled at the bottom of the axis (also in green). The axial scale is shown next to an image of the accelerator for reference. Note that the $\vec{B}$ field does not return to a value of zero in between the cells.

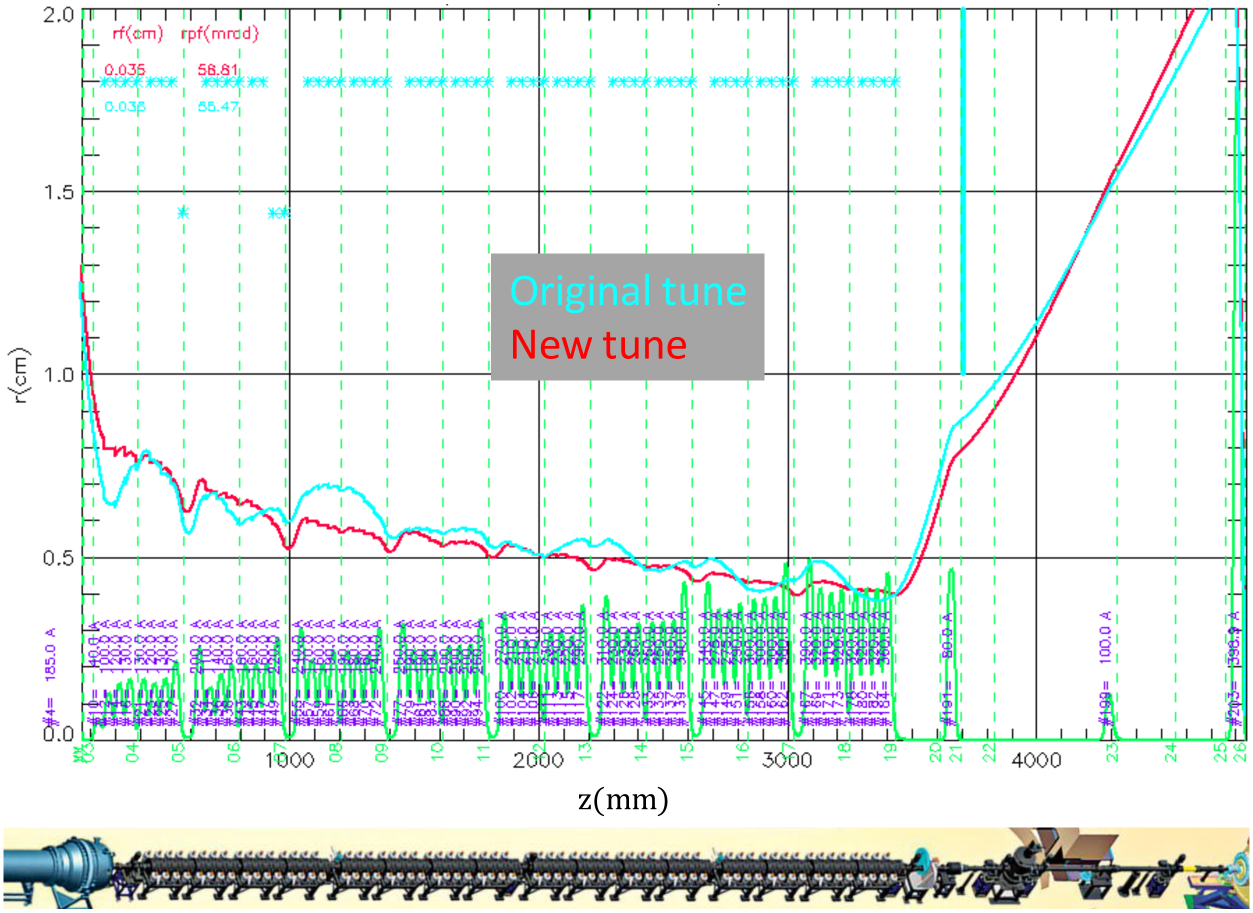

Figure 3.3: Comparison of two accelerator tunes for a 19 mm cathode on Axis-I. Shown in cyan is the original tune, with red being the refined transport of the beam that minimized beam envelope oscillations. The green curves are the magnetic field lattice provided by the accelerator solenoids, with the BPM numbers labeled at the bottom of the axis (also in green). The axial scale is shown next to an image of the accelerator for reference. Note this axial scale extends out to the final focus magnet located on the firing point. Similar to the previous figure, the $\vec{B}$ field does not return to a value of zero in between the cells.

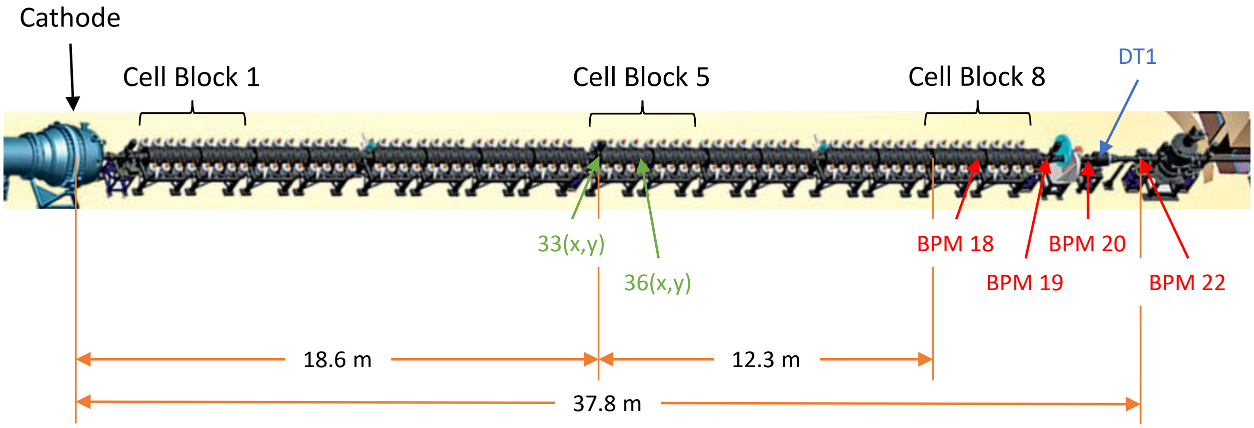

Figure 3.4: Detailed view of the Axis-I accelerator, including relevant distances in meters, referenced from the cathode surface. Each cell block contains eight accelerator cells, and BPMs (red) are located after every four cells. Beam steering is performed using the nested dipoles in Cells 33 and 36 (Cell Block 5, green), with BPM 18 (middle of Cell Block 8) and 19 (end of Cell Block 8) used for measurements of the beam centroid. Steering with these BPMs requires Cells 61–64, located in Cell Block 8, to be zeroed-out to approximate a field-free drift space.

3.3 Beam Steering

Steering and proper alignment of the beam is done using an alignment algorithm developed in Ref. [94] and first demonstrated on Axis-I in Ref. [93]. The goal of the steering is to have the beam centered within the bore of the accelerator to minimize beam instability growth, in particular BBU [89, 93]. The beam centroid can and will drift off-axis through the length of the accelerator due to cumulative misalignments of the individual components. These details are discussed and quantified in Ref. [93]. The time dependent motion of the beam centroid throughout the pulse, known as corkscrew, is a result the chromaticity of the beam (energy variation in time across the pulse) combined with cumulative misalignments of accelerator solenoids [95, 96]. Beam steering needs to be performed after changes to the accelerator configuration, and helps to minimize both corkscrew and keep the beam centered on-axis through the accelerator. Typically these changes are cathode changes, but they could also include cases when parts of the beamline are removed or replaced (i.e. an accelerator cell). A detailed view of the Axis-I accelerator with locations of dipoles and BPMs typically used for steering are highlighted in Figure 3.4.

The beam centroid position $(\langle x\rangle, \langle y\rangle)$ (mm) and angle $(\langle x'\rangle, \langle y'\rangle)$ (mrad) can be measured along the accelerator with BPMs. The position is directly measured, but the angle must be calcu-

	Shot	z (m)	$\langle x \rangle$ (mm)	$\langle x' \rangle$ (mrad)	$\langle y \rangle$ (mm)	$\langle y' \rangle$ (mrad)	$\langle r \rangle$ (mm)
Uncorrected	33834	32.47	0.36	0.16	−1.13	−0.02	1.25
Corrected	33839	32.47	0.17	0.11	0.01	0.09	0.28
Uncorrected	33834	34.32	0.66	0.58	−1.17	−0.18	1.42
Corrected	33839	34.32	0.38	0.55	0.17	0.07	0.53

Table 3.1: Measured time-averaged beam centroid corrections at the end of the accelerator at BPM 18 ($z = 32.5$ m) and BPM 19 ($z = 34.3$ m) using dipoles 33(x, y) and 36(x, y).

lated using a pair of BPMs along with a $\vec{B}$-field-free drift section. The steering algorithm,

$$\begin{pmatrix} N_x \\ N_y \\ M_x \\ M_y \end{pmatrix} = \begin{pmatrix} N_{xi} \\ N_{yi} \\ M_{xi} \\ M_{yi} \end{pmatrix} - D^{-1} \left[\begin{pmatrix} \langle x_i \rangle \\ \langle x'_i \rangle \\ \langle y_i \rangle \\ \langle y'_i \rangle \end{pmatrix} - \begin{pmatrix} 0 \\ 0 \\ 0 \\ 0 \end{pmatrix} \right], \tag{3.10}$$

solves for the correct dipole settings N_x, N_y, M_x, and M_y using the initial dipole settings N_{xi}, N_{yi}, M_{xi}, and M_{yi} and initial offsets $\langle x \rangle$, $\langle x' \rangle$, $\langle y \rangle$, and $\langle y' \rangle$ at the selected BPM. The transfer matrix, D, is defined as:

$$D = \begin{pmatrix} A_{xy,i} \; B_{xy,i} \; C_{xy,i} \; D_{xy,i} \end{pmatrix}, \tag{3.11}$$

where each component is defined by the following:

$$\begin{gathered} A_{xy,i} = \left. \begin{pmatrix} \frac{d\langle x \rangle}{dI} \\ \frac{d\langle x' \rangle}{dI} \\ \frac{d\langle y \rangle}{dI} \\ \frac{d\langle y' \rangle}{dI} \end{pmatrix} \right|_{N_x} ; \quad B_{xy,i} = \left. \begin{pmatrix} \frac{d\langle x \rangle}{dI} \\ \frac{d\langle x' \rangle}{dI} \\ \frac{d\langle y \rangle}{dI} \\ \frac{d\langle y' \rangle}{dI} \end{pmatrix} \right|_{N_y} ; \\ C_{xy,i} = \left. \begin{pmatrix} \frac{d\langle x \rangle}{dI} \\ \frac{d\langle x' \rangle}{dI} \\ \frac{d\langle y \rangle}{dI} \\ \frac{d\langle y' \rangle}{dI} \end{pmatrix} \right|_{M_x} ; \quad D_{xy,i} = \left. \begin{pmatrix} \frac{d\langle x \rangle}{dI} \\ \frac{d\langle x' \rangle}{dI} \\ \frac{d\langle y \rangle}{dI} \\ \frac{d\langle y' \rangle}{dI} \end{pmatrix} \right|_{M_y} . \end{gathered} \tag{3.12}$$

Each constituent term in Eq. 3.12 is calculated by individually changing each dipole current (33(x), 33(y), 36(x), and 36(y)—see Fig. 3.4) while holding the other three terms constant. This requires, at minimum, four shots, excluding the initial shot which populates the first term on the right hand side of Equation 3.10. The applied dipole $\vec{B}$ field must be sufficient to perturb the beam, but not cause it to scrape the beam pipe, or exceed the dynamic range of the BPM. Usually, a current change of ±1 A is adequate.

An example calculation using dipoles 33(x, y) and 36(x, y) located in Cell Block 5 and measuring the centroid at BPMs 18 and 19 located in Cell Block 8 is presented in detail in Appendix A. The results of the steering measurements are presented in Table 3.1. At BPM 18, the corrected radial centroid offset is reduced by nearly a factor of 5. Note that Cell Magnets 61–64 are turned off to provide a field-free drift section when steering with BPMs 18 and 19.

Note that the legacy algorithm used to steer the Axis-I beam inverts a 2×2 matrix (a single dipole pair) to steer the beam at a single point (or BPM). This steering method only corrects the beam centroid offset and not the angle offset. The proper steering and alignment using the 4×4 matrix detailed above simultaneously corrects both the beam centroid offset, $\langle x \rangle$, and angle offset, $\langle x' \rangle$.

3.3.1 Summary

This chapter introduces the relevant charged particle dynamics needed to model the transport of the relativistic electron bunch generated on DARHT Axis-I. The paraxial beam envelope equation is introduced, and each of the focusing and defocusing terms are explained. The intrinsic beam quantities, emittance and perveance, are defined. Example accelerator lattice tunes are presented and described. A steering algorithm which uses sets of dipoles located within accelerator cells, along with BPMs, is employed to steer the beam at selected points along the length of the accelerator.

CHAPTER 4

Diagnostics

This chapter introduces and explains the various diagnostics relevant to both measurements of the electron beam and plasma plume generated during the beam-target interaction.

4.1 Particle Beam

4.1.1 Beam Position Monitor

Beam Position Monitors (BPMs) along the length of Axis-I (shown in Figure 4.1) non-invasively monitor the electron beam current and position within the beam pipe. Figure 4.2 shows an Axis-I BPM with the relevant parts labeled. A total of eight inductive loops (B-dot probes) are placed around the beam azimuth every 45 degrees. B-dot probes are inductive voltage monitors that produce a signal proportional to the time rate of change of the beam-produced magnetic field passing through the area enclosed by the loop. The individual B-dot probes are formed using a type-N connector with the center conductor shorted to ground by a tab machined out of the inner diameter of the flange. The four B-dot probes located along the $\pm\hat{x}$ and $\pm\hat{y}$ axes make measurements of the beam centroid offset by differencing the $+x$ and $-x$ (as well as $+y$ and $-y$) signals to provide positions in x and y. The four B-dot probes located at 45° relative to $\hat{x}$ and $\hat{y}$ measure beam current.

A perfectly centered beam passing through an ideal BPM (i.e., no mechanical offsets, and each B-dot probe is identical) will produce an equivalent signal on each B-dot probe housed within the BPM. In practice, each BPM and, subsequently, each B-dot probe is individually calibrated. The position measurement extraction from a BPM measurement is a four step process: (1) properly scale the current, account for attenuation; (2) convert the signal from a voltage to an amperage by a factor of the form mV/kA; (3) subtract the offset; and (4) divide by the correction factor. The BPMs are limited to measuring small (several mm) offsets from the center of the beam pipe, with a minimum sensitivity to displacement of 100 μm. This limitation is a result of the S/N of the

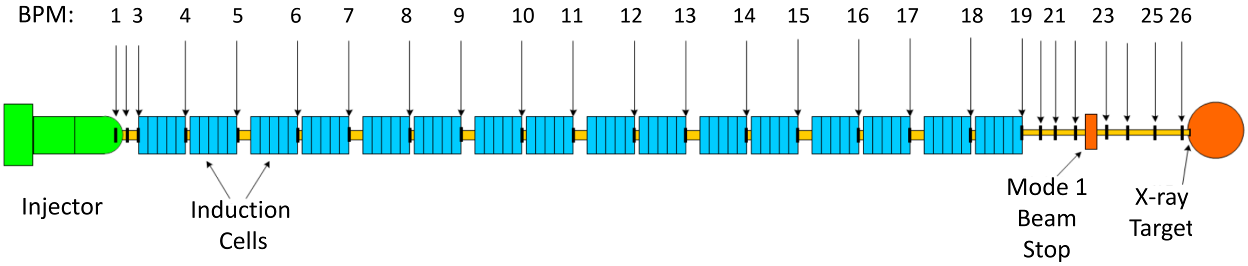

Figure 4.1: BPM locations on DARHT Axis-I. In the accelerator section (blue), there is a BPM located after every four accelerator cells. Three BPMs are located in the injector region, and seven BPMs are located in the downstream transport section. Note that for clarity, not every BPM is labeled; however, the location of each is highlighted by an arrow.

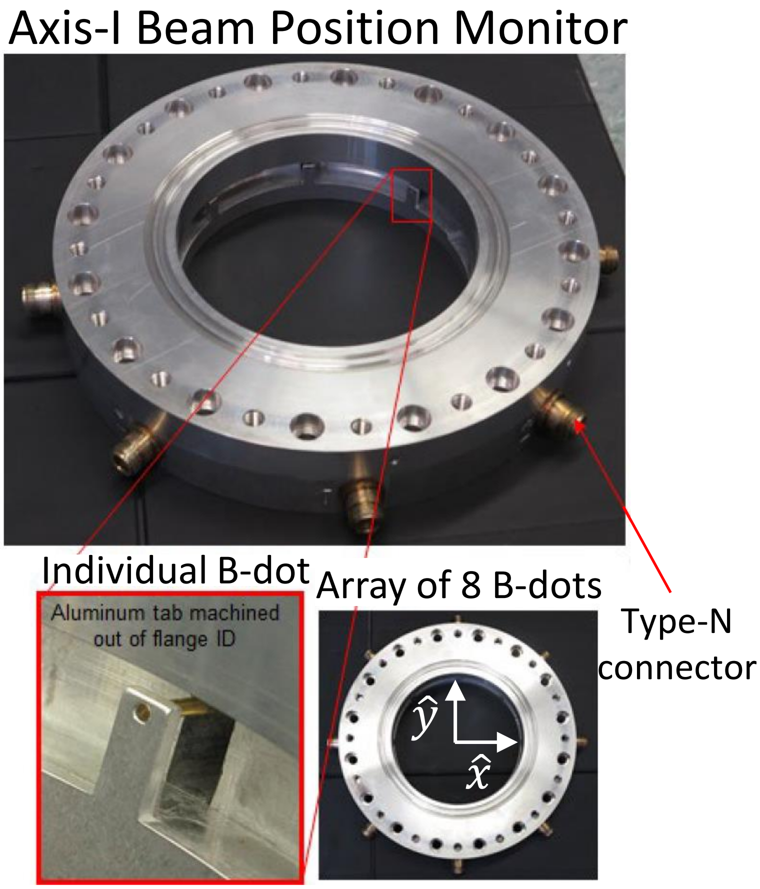

Figure 4.2: An Axis-I BPM with relevant parts labeled. Figure reproduced from [2].

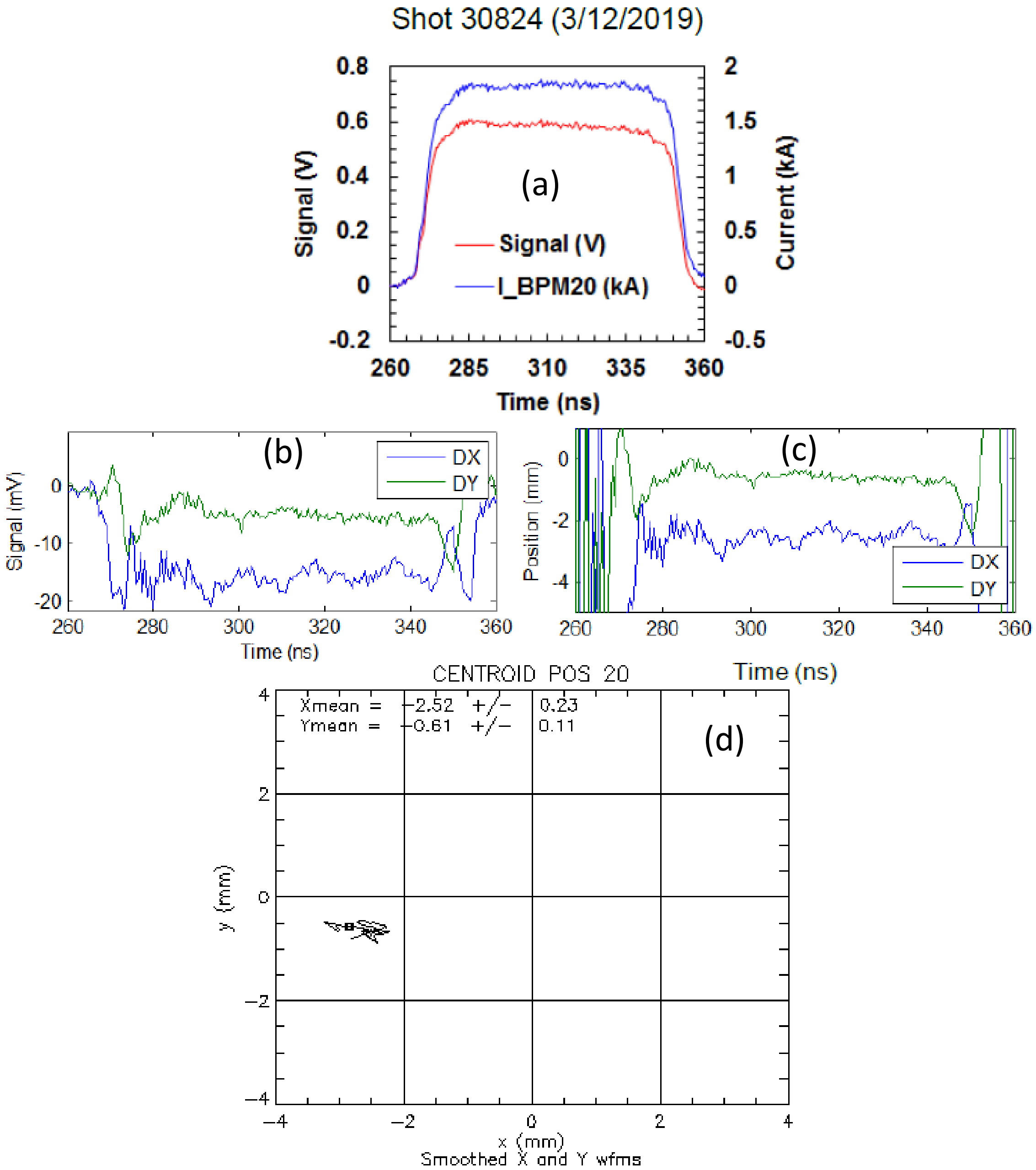

Figure 4.3: Example of Axis-I BPM data processing. (a) Measured signal (red) and corrected waveform to recover the beam current (blue). (b) Raw dx and dy BPM signals. (c) Processed dx and dy signals, according to the four steps discussed in the text. (d) Beam centroid location as displayed in the DARHT Axis-I beam analysis program.

differenced signal to determine the $\hat{x}$ and $\hat{y}$ offsets [97]. Figure 4.3 shows an example measurement of an Axis-I BPM from raw data to processed and visualized results.

4.1.2 Near-Field Optical Transition Radiation

Optical Transition Radiation (OTR) is the polarized continuum radiation produced due to a particle transiting through a vacuum-metal interface [98–100]. This effect is in contrast to Cherenkov radiation, which is produced by particles transiting a vacuum-dielectric interface where, within the material, the particles are traveling faster than the speed of light in that material. OTR measurements can be made either in the near-field or the far-field. Measurements in the far-field can resolve the characteristic radiation lobe peaks, as shown in Figure 4.4. The lobe intensity is proportional to γ^2, and the lobe separation is proportional to $1/\gamma$, where γ is the relativistic factor. This permits a direct measurement of the beam energy, angular dispersion, and beam emittance [**?**].

OTR measurements on DARHT are made in the near-field regime, where the polarization is not resolved. Instead, the OTR light provides a measurement of the beam spot on the target. This allows us to quantify the energy density $(\mathrm{J/m^3})$ deposited into the target foils. Figure 4.5 shows the diagnostic layout for measuring near-field OTR in the downstream barrel diagnostic region on DARHT Axis-I [68,69,83]. The light is captured by a PiMAX4 image intensified Charge-Coupled Device (CCD) camera [101]. Note that the line-of-sight is measuring 20° above the beam axis of propagation, so a correction factor of $1/\cos(20^\circ)$ must be applied to correct for the geometry as seen by the CCD. Figure 4.6 shows a calibration image with the fiducials used to determine image rotation and size.

The output light intensity varies with different foil materials; higher-Z materials like tin and gold are observed to have more light production compared with lower-Z materials like aluminum, as determined from the peak counts from the respective CCD images. The light is intense enough at peak focus, however, to permit 3 ns gating of the CCD camera to make time resolved measurements of the beam spot size throughout the beam pulse. Figure 4.7 illustrates an example OTR measurement and analysis for a 100 μm pure aluminum foil. A Lorentzian fit is used to match the peaked distribution of the emitted light.

4.2 Plasma

This section discusses diagnostics specific to the beam-target interaction studies performed in the DARHT Axis-I downstream transport measurement region. The measurement region is shown in Figure 4.8, which highlights the barrel diagnostic chamber and target paddle along with the focusing solenoid, debris blocker, and relevant BPMs. Figure 4.9 shows the legacy configuration

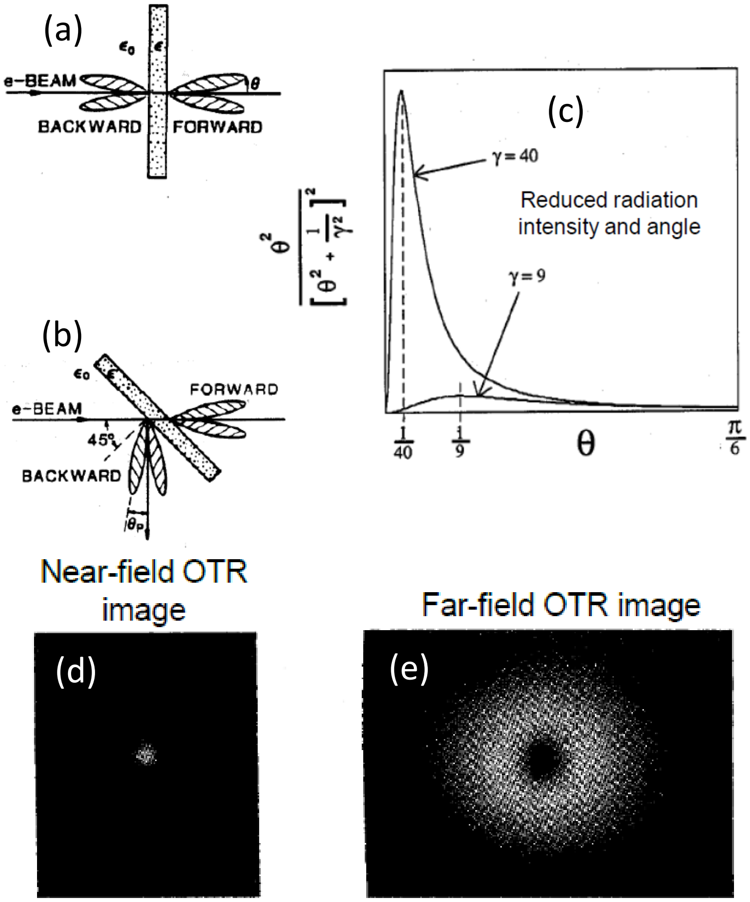

Figure 4.4: Details of OTR near-field and far-field measurements. (a) Radiation lobes for a target foil of permittivity ϵ normal to the beam. (b) Radiation lobes for a target foil at 45° relative to the beam. (c) Variation of lobe intensity and angle as a function of γ. The lower energy (γ = 9) case displays a reduced radiation intensity and angle compared with the higher energy (γ = 40) case. (d) Example near-field OTR image, where the distribution is representative of the beam size on target. (e) Example far-field (polarized) OTR image clearly demonstrating the radiation lobes. Figure reproduced from [2].

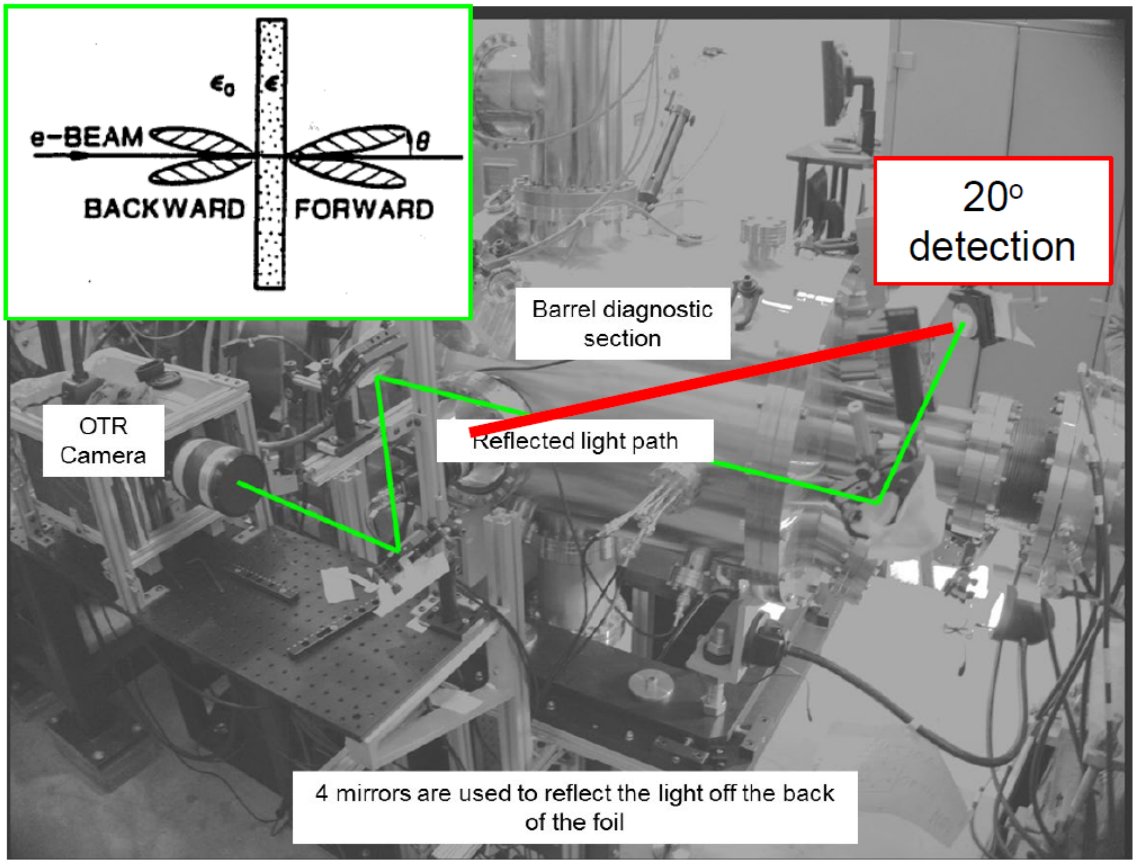

Figure 4.5: Near-field OTR diagnostic layout on DARHT Axis-I. Four turning mirrors are used to reflect the light from the back side of the foil surface to an image intensified CCD camera for time gated measurements. The red line roughly represents the path traveled by the light within the diagnostic barrel to the first turning mirror an angle of 20° above the beam axis of propagation. the green line represents the path of the light through the optics train external to the vacuum. Also see Figure 4.10, which shows the current configuration of all target diagnostics on Axis-I. Figure reproduced from [2].

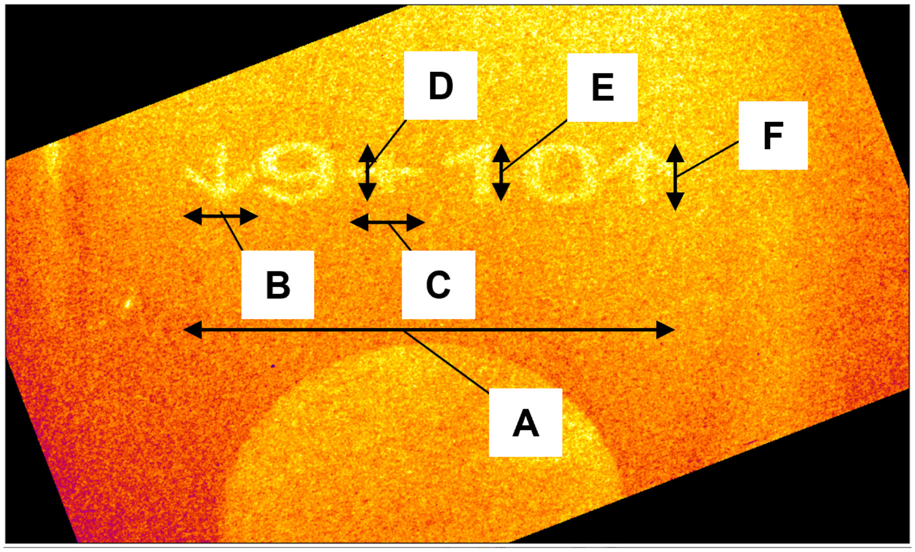

Figure 4.6: Calibration image for the Axis-I OTR diagnostic. A rotation of 21.1° counter-clockwise is required to properly vertically align the image. A calibration factor of 17.5 ± 1.7 pixels/mm is deduced based on the known sizes of dimensions A–F highlighted in the image. For reference, the length of A is 28.47 ± 0.05 mm.

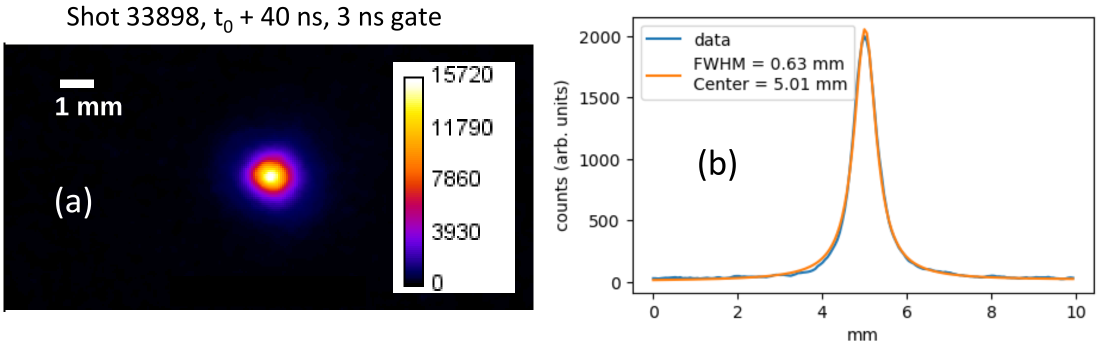

Figure 4.7: Example near-field OTR measurement. (a) Raw data with a spatial scale and a color bar indicating the counts. (b) 10-pixel-wide (in $\hat{y}$) lineout of the data with a Lorentzian fit, indicating a beam FWHM$= 0.63$ mm in $\hat{x}$.

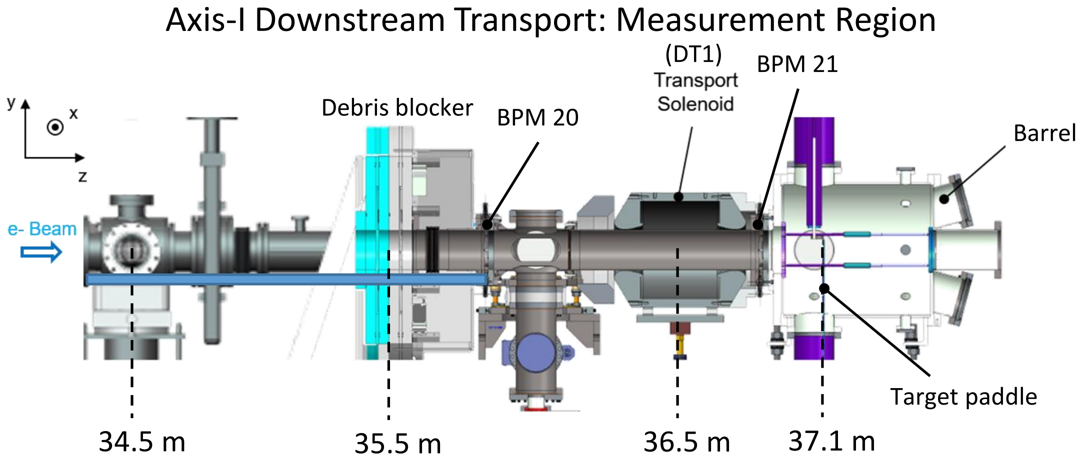

Figure 4.8: Part of the DARHT Axis-I downstream transport region within the accelerator hall. This is the measurement region labeled in Fig. 1.2 and is currently used for the electron beam-target interaction studies on Axis-I. The target paddle can hold ten, 1” square target foils. On average, each target foil is good for seven shots (for materials like aluminum, titanium, and copper) and will provide 100% diagnostic return. Diagnostic access via the side ports ($\hat{x}$) provides ~10 cm of viewing area on the upstream side of the target.

of target diagnostics used for the measurements described in Chapter 7. Figure 4.10 shows the current configuration of all target diagnostics used for the measurements described in Chapter 8.

4.2.1 Plume Imaging

Visible self-emission plume imaging using a gated intensified CCD camera provides qualitative measurements of the plasma plume size [3, 68, 69]. A series of time gated images yields a rough estimate of the plasma plume axial expansion velocity, subject to CCD sensitivity, dense plasma cutoff effects, and target paddle deflection in $\hat{z}$ (-12 mRad). The light output of the plasma determines the minimum gate time of the CCD. For example, a titanium plasma emitted sufficient light to permit 20 ns gated images [3], while plume imaging of an aluminum plasma required 50 ns gates [69].

Figure 4.11 shows example time gated measurements of an expanding titanium plasma plume. From these measurements, the axial expansion velocity is calculated by performing an axial lineout and picking off a threshold, typically 50% of the maximum value. The axial expansion velocity $v_{\max}$ is related to the ion sound speed $c_{\text{s,ion}}$ in the plasma by the following:

$$c_{\text{s,ion}} = \frac{\gamma - 1}{2} v_{\max} = \sqrt{\frac{\gamma k_B T_e}{m_i}}. \tag{4.1}$$

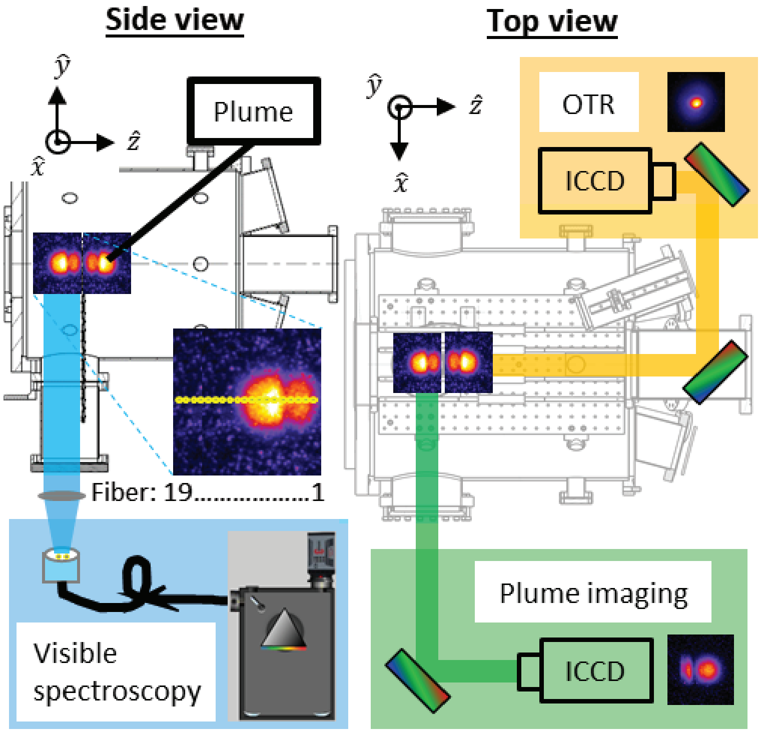

Figure 4.9: Legacy diagnostic configuration in the measurement region. This layout is representative of the measurements detailed in Chapter 7. Note that the side view described here is the same view displayed in Fig. 4.8. The plasma plume distribution shown for reference is an example measurement taken by the plume imaging diagnostic.

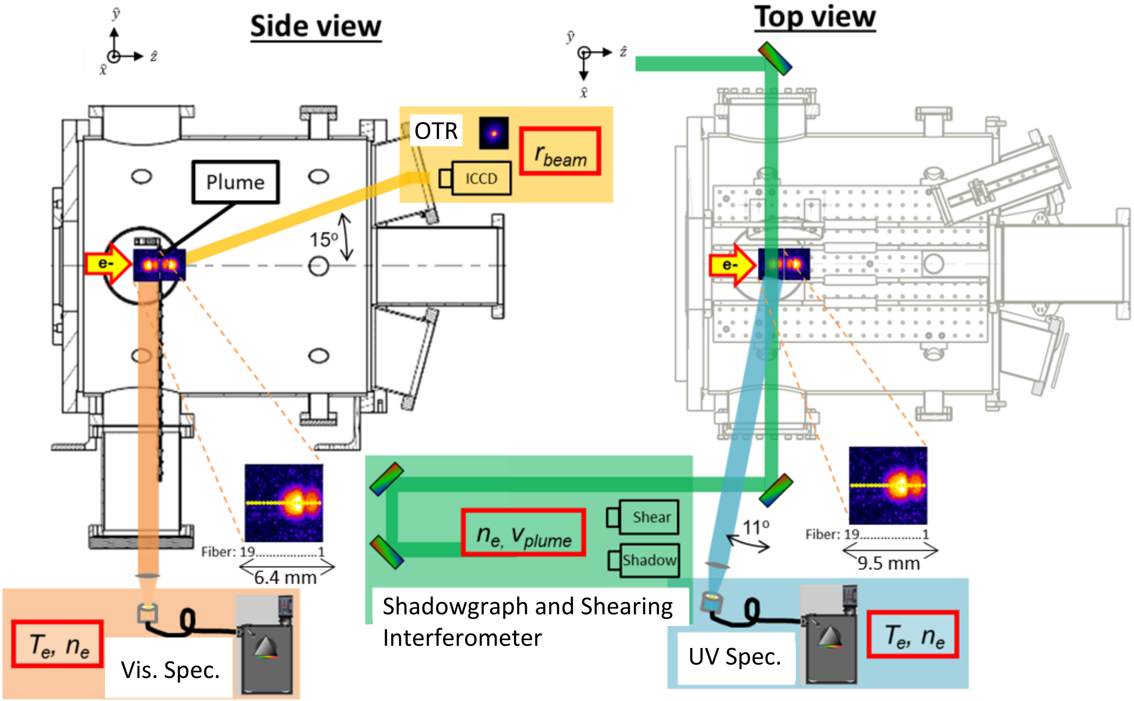

Figure 4.10: Present diagnostic configuration in the measurement region. This layout is representative of the measurements detailed in Chapter 8. Note that the side view described here is the same view displayed in Fig. 4.8. The plasma plume distribution shown for reference is an example measurement taken by the plume imaging diagnostic.

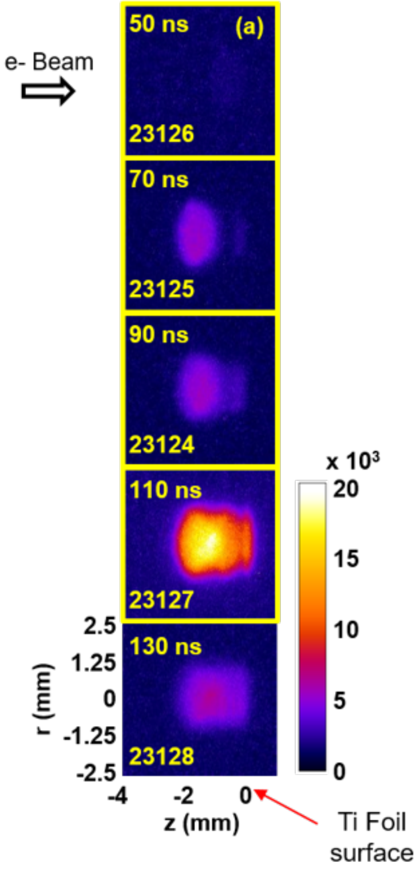

Figure 4.11: Example plume imaging measurement of an expanded titanium plasma. Figure reproduced from [3].

Here, m_i is the ion mass and γ is the adiabatic index. Thus, by approximating the plasma as an ideal gas, a measurement of the expansion velocity permits a rough estimation of the plasma electron temperature.

Limitations of the visible self-emission plume diagnostic are principally a result of cutoff effects of light escaping from the plasma plume. The CCD measuring the continuum light from the plasma is inherently a broadband measurement in the visible with a response defined by the quantum efficiency of the CCD intensifier. Thus, plasma densities must be low enough and temperatures high enough to ensure a sufficiently low (wavelength-dependent) opacity of the plasma for photons to escape and be measured. As will be described in Sec. 4.2.4, probing the plasma plume with a laser to produce a shadowgraph is inherently a more quantitative diagnostic because the opacity as a function of T_e and n_e at a single wavelength is easily calculated and folded in with the experimental measurements.

4.2.2 Visible Spectrometer

Visible spectroscopy is performed on the upstream side of the target using a lens-coupled 19×200-μm-diameter linear fiber array (0.22 numerical aperture, High OH (hydroxyl ion)) oriented orthogonal to the foil surface. A system magnification of 0.6 to 0.7× is achieved using a 180-mm focal length lens, resulting in a 7.7 to 6.4 mm axial coverage by the fiber array in the object plane. A 10-meter-long fiber bundle is fed into a 0.3-m focal length Czerny-Turner spectrometer (f/3.9) containing a triple-grating turret (150 grooves/mm, 500-nm blaze; 1800 grooves/mm, 500-nm blaze; 2400 grooves/mm, holographic) [102] and coupled with a PiMAX3 CCD containing a P43 phosphor [101]. The standoff distance of the visible fiber array from the target in Figure 4.10 is approximately 73 cm. All sensitive electronics (computers, CCDs, etc.) are staged approximately 2.4 meters away from the target diagnostic chamber to minimize potential radiation effects by the bremsstrahlung produced during the electron beam pulse.

This visible spectroscopy system is principally sensitive to photons with wavelengths greater than 340 nm and less than 700 nm, as shown in Figure 4.12. This quantum efficiency plot, however, does not take into account other losses present in the optical train, which is detailed in Figure 4.13. The plasma's output light is a function of emissivity ϵ and opacity κ and will be discussed in more detail in Chapter 6. Perfect vacuum is assumed with 100% transmission. All vacuum windows used for optical access are made of UV grade glass (fused silica, or, equivalently, quartz) and have excellent transmission down to 200 nm. The lens is the component that is varied in the experimental setups. The visible spectrometer uses a standard BK12 glass compound lens whose transmission is represented by the graph under the "Lens" block. Note the strong rolloff in transmission below 400 nm. In practice, this sets the lower bound on wavelengths measured by the visible spectrometer

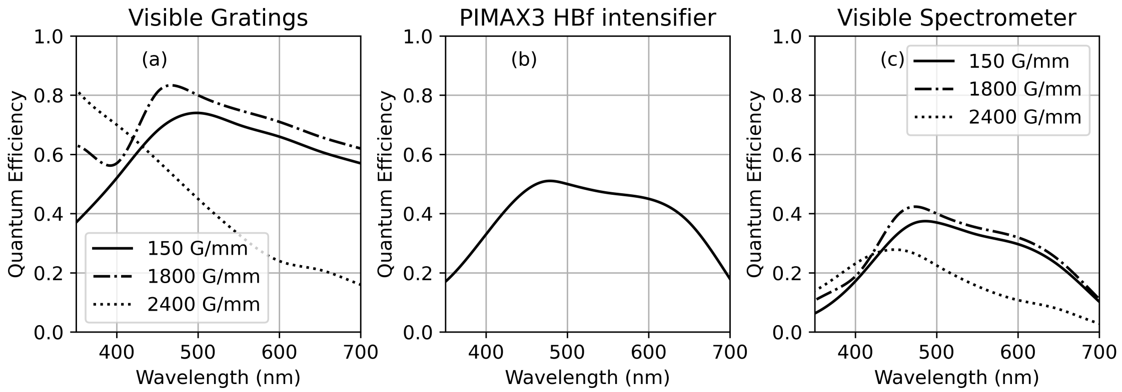

Figure 4.12: Quantum efficiencies of (a) the visible spectrometer gratings, (b) the PiMAX3 CCD intensifer, and (c) composite efficiency of the spectrometer as a whole (gratings and intensifier).

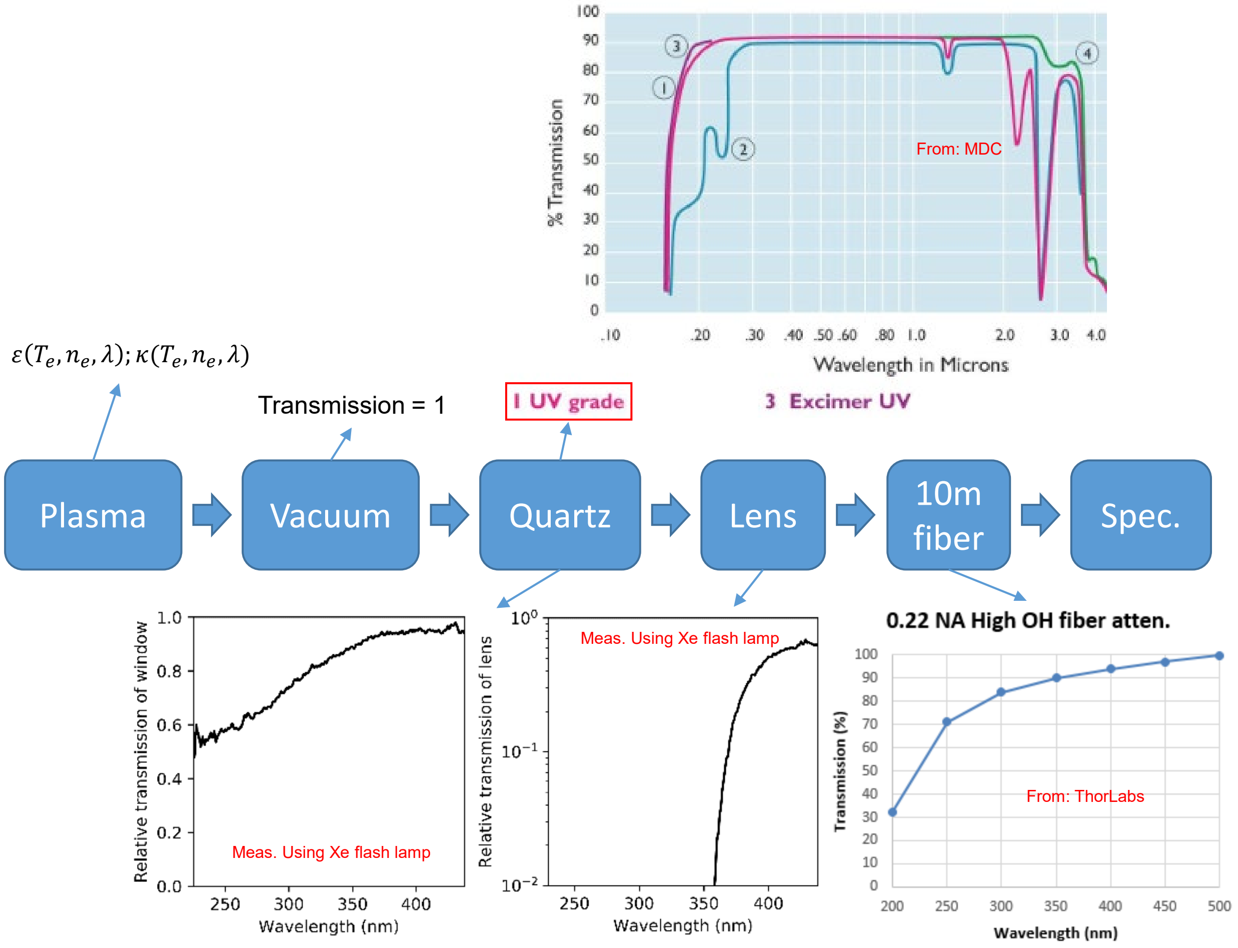

Figure 4.13: Layout of the optical train for spectroscopy measurements in the barrel on Axis-I. The measured transmission curves are shown for each individual component.

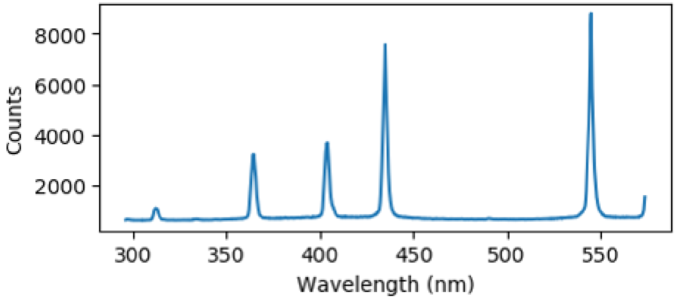

Figure 4.14: Visible spectrometer measurements of a Hg(Ar) DC pen lamp using the 150 grooves/mm survey grating centered at 435 nm with a 25 μs gate and 50× gain.

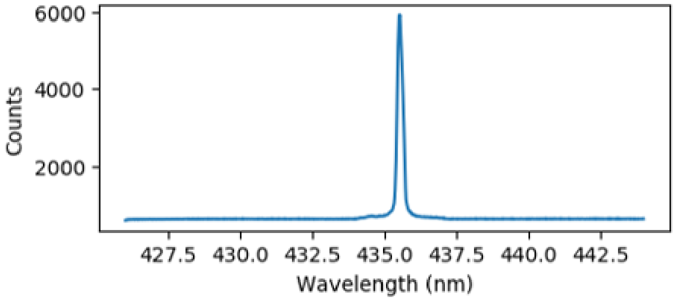

Figure 4.15: Visible spectrometer measurements of a Hg(Ar) DC pen lamp using the 1800 grooves/mm grating centered at 435 nm with a 25 μs gate and 50× gain.

to around 380 nm.

The visible spectrometer is only calibrated in these measurements for wavelength accuracy and not absolute intensity. The calibration source is a pencil lamp, described in Chapter 5, Section 5.1. This DC source provides a very stable source of mercury emission lines when using the Hg(Ar) lamp. Wavelength calibrations are performed within the Princeton Instruments LightField® software, which automatically calculates the pixel offset for each grating given two user-selected wavelengths. The Hg-I 435.834 and 546.075 nm lines are used for visible spectrometer calibration. In practice, only the 150 grooves/mm and 1800 grooves/mm gratings are used for spectroscopic measurements of the beam-target interaction; the minimal increase in resolution afforded by the 2400 grooves/mm holographic grating is offset by the more significant reduction in quantum efficiency. Example measurements are shown in Figures 4.14 and 4.15. Comparisons with the long wave UV spectrometer are shown in Figures 4.20 and 4.21.

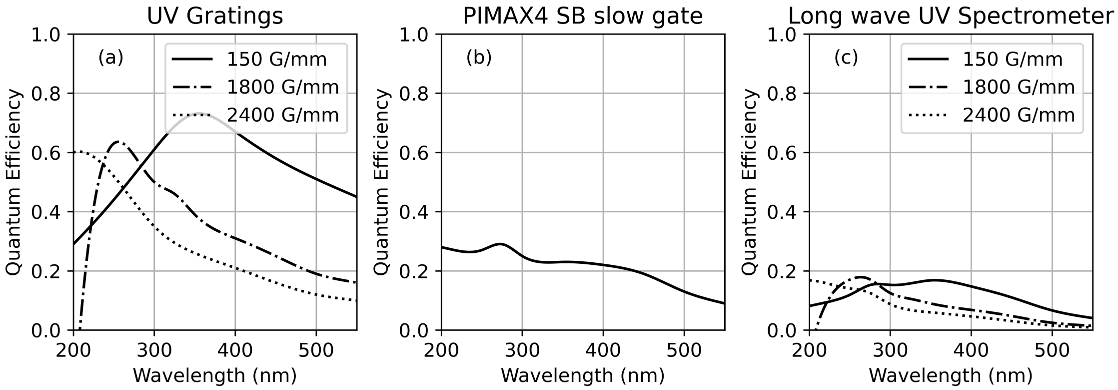

Figure 4.16: Quantum efficiencies of (a) the long wave UV spectrometer gratings, (b) the PiMAX4 CCD intensifer, and (c) composite efficiency of the spectrometer as a whole (gratings and intensifier).

4.2.3 Long Wave UV Spectrometer

Long wave ultraviolet (UV) spectroscopy provides measurements of photons down to nearly 200 nm, complimenting the visible spectrometer's range. The UV spectrometer also uses a lens-coupled 19×200-μm-diameter linear fiber array, but this array has a line-of-sight that is not quite orthogonal to $\hat{z}$; in this case, the line-of-sight is 11 degrees off orthogonal, on the upstream side of the foil (see Fig. 4.10). This is to accommodate the air-wedge shearing interferometer optics train. A system magnification of about 0.5× is achieved using a pair of fused silica lenses, providing a 9.5 mm near-axial coverage by the fiber array in the object plane. The lenses used are a 2" diameter plano-convex lens ($f = 100$ mm) and 1" diameter plano-concave lens ($f = -30$ mm), where the distance from the plano-concave lens to the fiber array is adjusted to vary the magnification. The 10-meter-long fiber bundle is fed into a 0.3-m focal length Czerny-Turner spectrometer (f/3.9) containing a triple-grating turret (150 grooves/mm, 300-nm blaze; 1800 grooves/mm, holographic; 2400 grooves/mm, holographic–UV optimized) and coupled with a UV-sensitive PiMAX4 CCD containing a P46 phosphor. The standoff distance of the UV fiber array from the target in Figure 4.10 is approximately 54 cm. The shorter standoff distance for the UV spectrometer was chosen to help compensate for the lower quantum efficiency of the system, as shown in Figure 4.16.

Figure 4.17 shows in detail why UV-grade focusing optics are required instead of traditional BK12 glass found in off-the-shelf compound lens systems. Preliminary UV spectrometer measurements of an aluminum plasma with identical focusing optics used on the visible spectrometer show significant absorption below 400 nm. Calibration measurements with a xenon flash lamp (Chapter 5, Section 5.2) show clearly the reduction of transmission with BK12 glass, compared with the transmission of fused silica. The principal thrust for deploying a UV spectrometer for beam-target

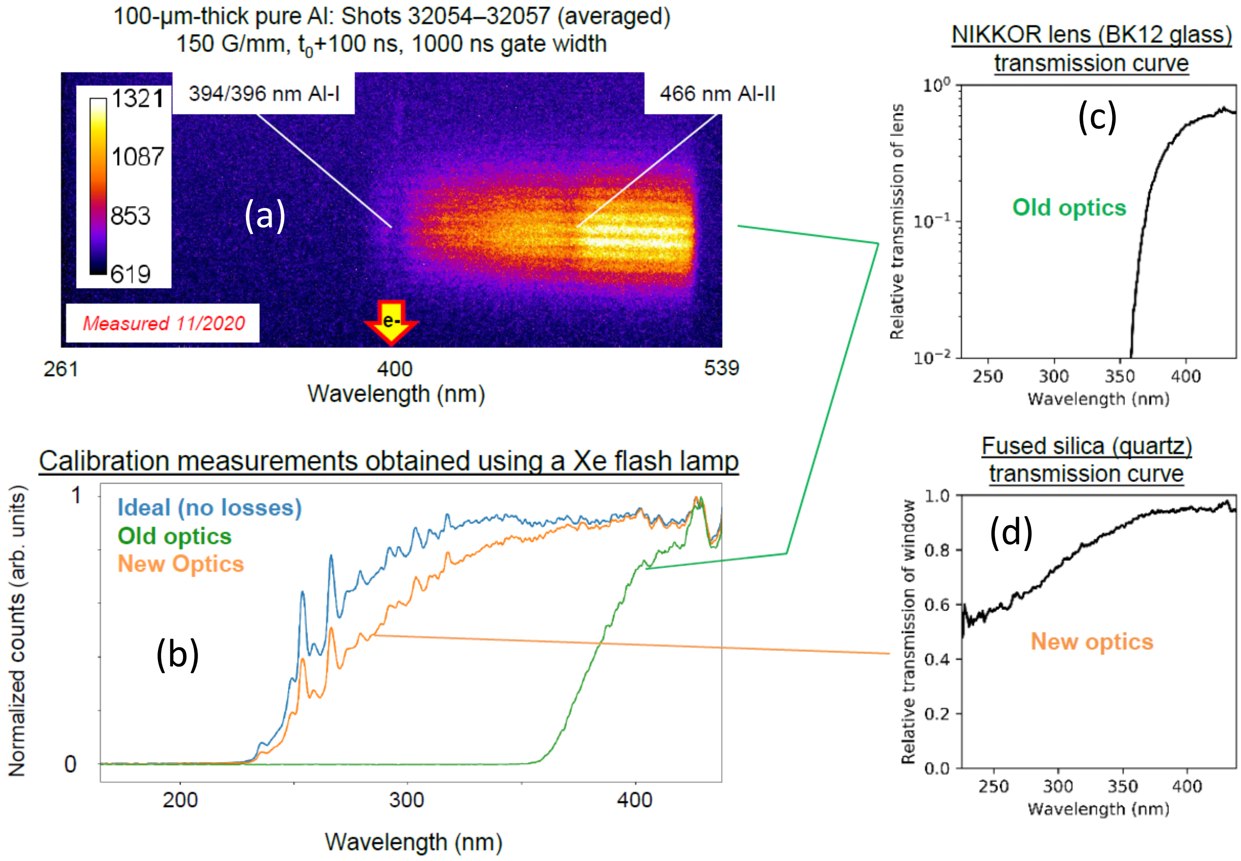

Figure 4.17: The effect of lens material on light transmission below 400 nm on UV spectrometer measurements. (a) Measurements of an aluminum plasma plume with original BK12 optics, with spectral features indicated. (b) Series of calibration measurements using a Xe flash lamp. (c) Calculated transmission curve for BK12 glass (old optics, note the logarithmic scale). (d) Calculated transmission curve for fused silica (new optics) (this curve is the same as what is shown in Fig. 4.13 for the quartz window).

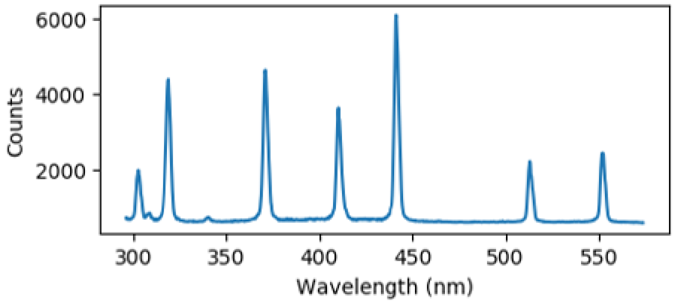

Figure 4.18: UV spectrometer measurements of a Hg(Ar) DC pen lamp using the 150 grooves/mm survey grating centered at 435 nm with a 25 μs gate and 50× gain.

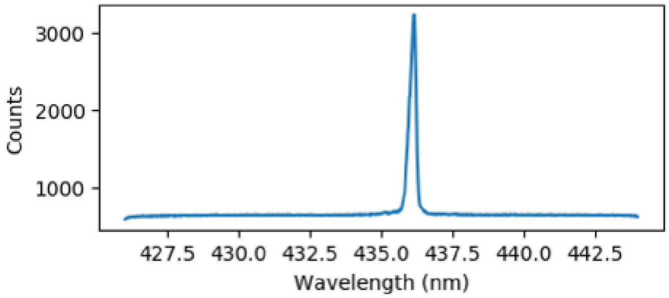

Figure 4.19: UV spectrometer measurements of a Hg(Ar) DC pen lamp using the 1800 grooves/mm holographic grating centered at 435 nm with a 25 μs gate and 50× gain.

interaction measurements arises from the general nature of emission lines produced by low-Z metals of interest. Many of these materials have copious emission lines in the 200–400 nm range, in particular titanium and copper, and to a lesser extent aluminum. Making measurements of these lines provides new insights into the plasma plume dynamics.

An example series of calibration measurements for the UV spectrometer using the Hg(Ar) pen lamp are shown in Figures 4.18 and 4.19. The same calibration procedure used for the visible spectrometer is also used here for the UV spectrometer, but with different lines due to the different measurement bandwidths. The Hg-I 253.652 and 435.834 nm lines are selected for wavelength calibration.

Figures 4.20 and 4.21 compare the spectrometer response and detection efficiency of both the visible and UV spectrometers. At a minimum slit width of 10 μm, the UV spectrometer has on average a 30% larger linewidth compared with the visible spectrometer. About 10% of this can be accounted for by the varying intensifier performance of each CCD from the factory (e.g. a larger grain size of the P46 phosphor compared with the P43 phosphor), while the remaining 20% may be due to variation across the intensifier face, intrinsic configuration of the spectrometer slit, or

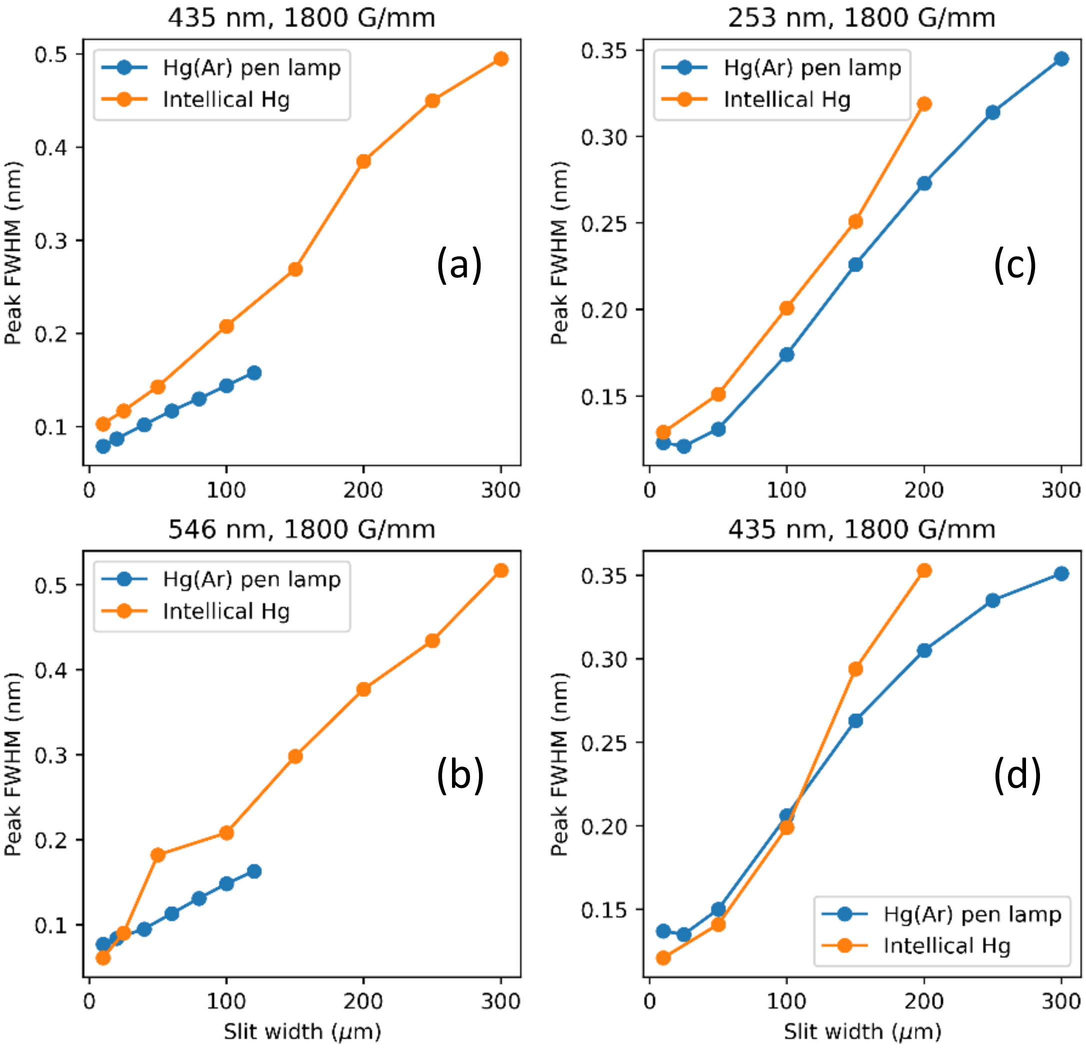

Figure 4.20: Comparison of spectrometer response as a function of slit width measured using a Hg(Ar) pen lamp (blue) and a Princeton Instruments mercury IntelliCal® source (orange) for the 1800 grooves/mm gratings. The visible spectrometer response is shown in (a) and (b). The long wave UV spectrometer response is shown in (c) and (d). The peak FWHMs correspond to the width of the measured line.

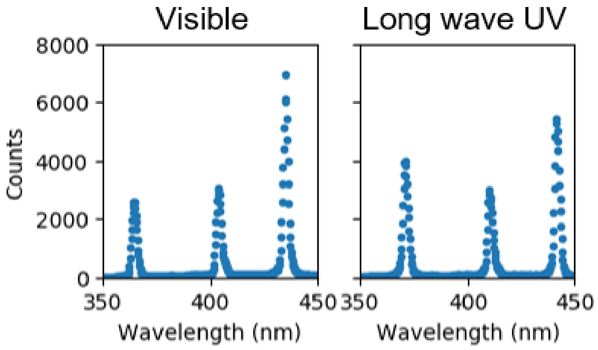

Figure 4.21: Comparison of the visible (Fig. 4.14) and UV spectrometer (Fig. 4.18) survey measurements from 350–450 nm. The Hg-I 404.656 nm line roughly has the same intensity on both spectrometers. The Hg-I 435.833 nm line has higher peak counts on the visible spectrometer, while the Hg-I 365.015 nm line has higher peak counts on the UV spectrometer. This agrees with the crossover in quantum efficiency when inspecting Figures 4.12 and 4.16, where below ~400 nm, the UV spectrometer has a higher quantum efficiency than the visible spectrometer.

aberrations such as coma or astigmatism within the spectrometer.

4.2.4 Shearing and Shadowgraph Interferometer

The Shearing and Shadowgraph Interferometer (SSI) has been developed and deployed on Axis-I for for the first ever spatially and temporally resolved density measurements of the electron beam-target interaction. The laser used to probe the plasma plume is a 532 nm Nd:YAG (2ω) with a pulse length of 5 ns and energy of 60 mJ. For a detailed description of this diagnostic, see Ref. [83, 103]. This section will focus on the general layout and resulting measurements as applied to Chapter 8.

A schematic of the SSI is shown in Figure 4.22. An example shadowgraph and sheared image is shown in Figure 4.23. The wrapped phase comes from summing the phase after processing the fast Fourier transform of the image. The Abel inversion then converts the phase shift to electron density. Figure 4.24 provides a more detailed view of the electron density and shadowgraph profile, including selected density contours relevant for spectroscopy. Figure 4.24(b) highlights the fidelity of the shadowgraph measurement compared with the sheared image; the shadowgraph corresponds to a density contour of about 10^{18} cm^{-3}.

The SSI is principally limited by the cutoff density n_c and the opacity of the plasma plume through which it passes. For 532 nm photons, $n_c = \frac{1.1\times10^{21}}{\lambda^2(\mu\mathrm{m})} = 4\times10^{21}$ cm^{-3}, but most interferometers are typically restricted to measuring a maximum of $0.1n_c$ due to opacity effects, fringe spacing, and S/N. Recent measurements with the SSI have resolved densities up to 10^{19} cm^{-3} [83]. A plot of the photon mean free path $\delta = 1/\kappa$ at relevant temperatures and electron densities at 532 nm

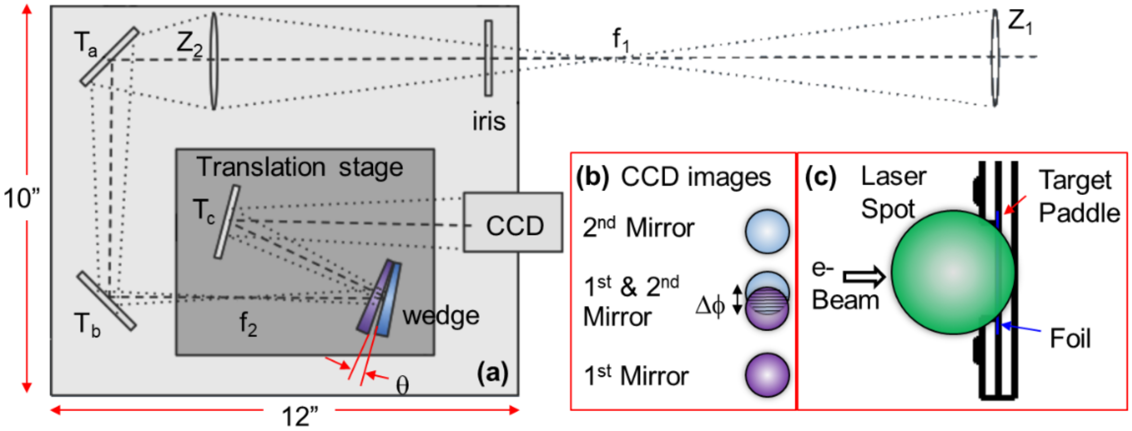

Figure 4.22: Experimental schematic of the SSI. (a) Optical layout of the system. Z_i and T_i indicate focusing lenses and turning mirrors, respectively. (b) Images produced by the interferometer. The 2^{nd} mirror reflection produces the shadowgraph image, and the overlap produces the sheared image. (c) Relative alignment of the laser spot on the target paddle. The beam diameter when it passes through the upstream plasma plume is 24 mm.

and the Al-I 3p-4s doublet 396.152 nm line center is shown in Figure 4.25. This further highlights the difficulty of probing dense, low temperature plasmas with visible light sources. However, the datasets obtained thus far have provided a powerful and previously unavailable capability for benchmarking the radiation hydrodynamics codes used to model the beam-target interaction and hydrodynamic expansion on DARHT. The measurements can also be spatially correlated with densities inferred from emission and absorption spectroscopy.

4.2.5 Summary

This chapter introduces and describes the suite of beam and plasma plume diagnostics deployed in the DARHT Axis-I measurement region. Near-field OTR is used as a spot size measurement of the focused beam on target to infer energy deposition into the target material. Plume imaging determines the plasma plume spatial extent, up to opacity limits, and permits an estimation of the plasma plume expansion velocity and electron temperature. The two spectrometers, visible and long wave UV, provide the capability to measure spectral lines over the wavelength range of 250–700 nm. The SSI diagnostic enables precise time-resolved 2-D electron density measurements, which can be spatially correlated with the 1-D axially-resolved spectroscopy measurements.

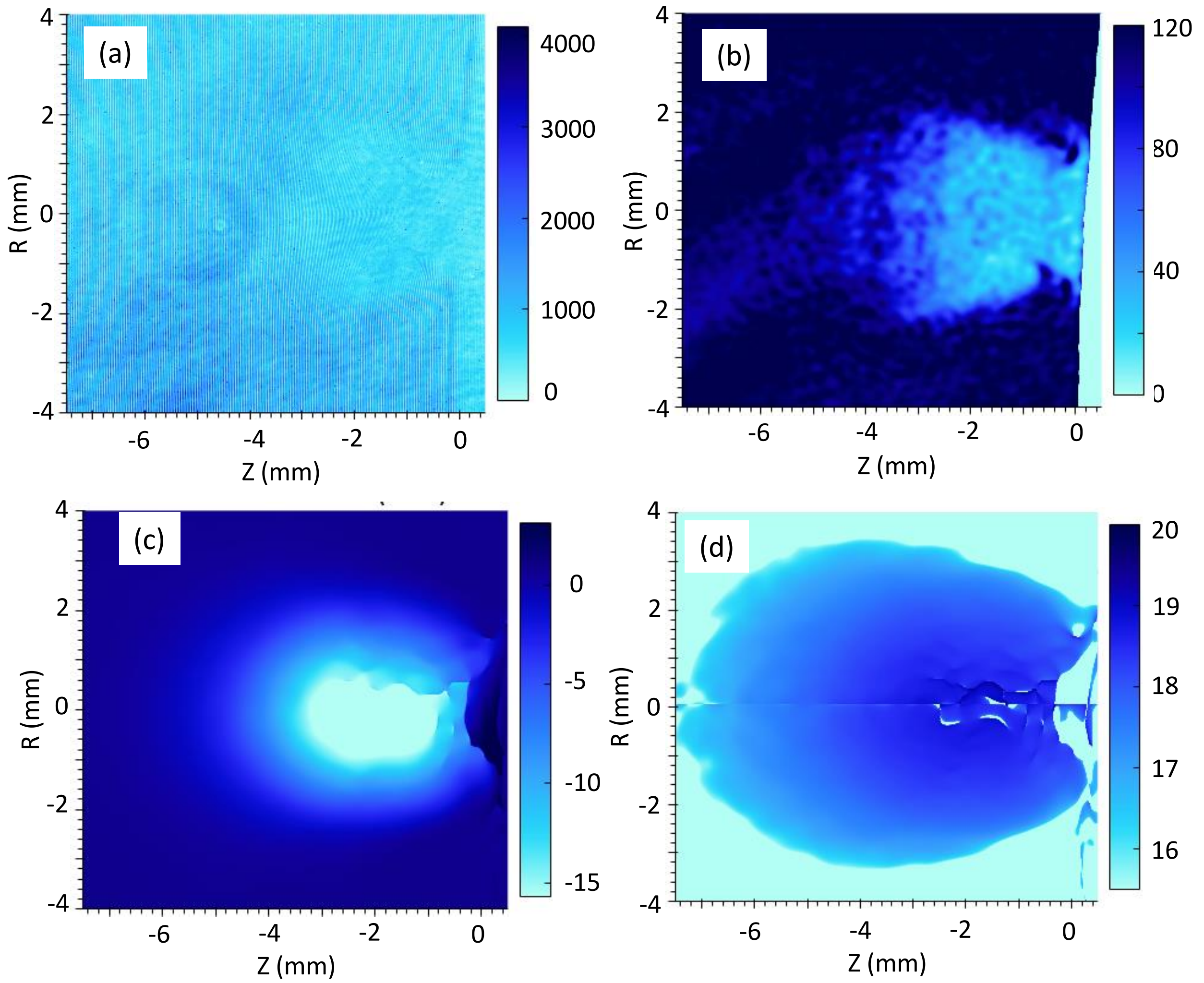

Figure 4.23: Shot 33909: SSI measurement and analysis of an electron beam heated 100 μm pure aluminum foil at $\mathrm{t}_0 + 500$ ns, where t_0 represents the start of electron beam energy deposition. (a) Raw sheared image (color bar represents percent transmission). (b) Raw shadowgraph image (color bar represents counts). (c) Phase unwrapped from the sheared image (color bar has units of radians). (d) Calculated electron density of the plasma plume (color bar represents $\log(\mathrm{n_e})$, where n_e is in units of cm^{-3}).

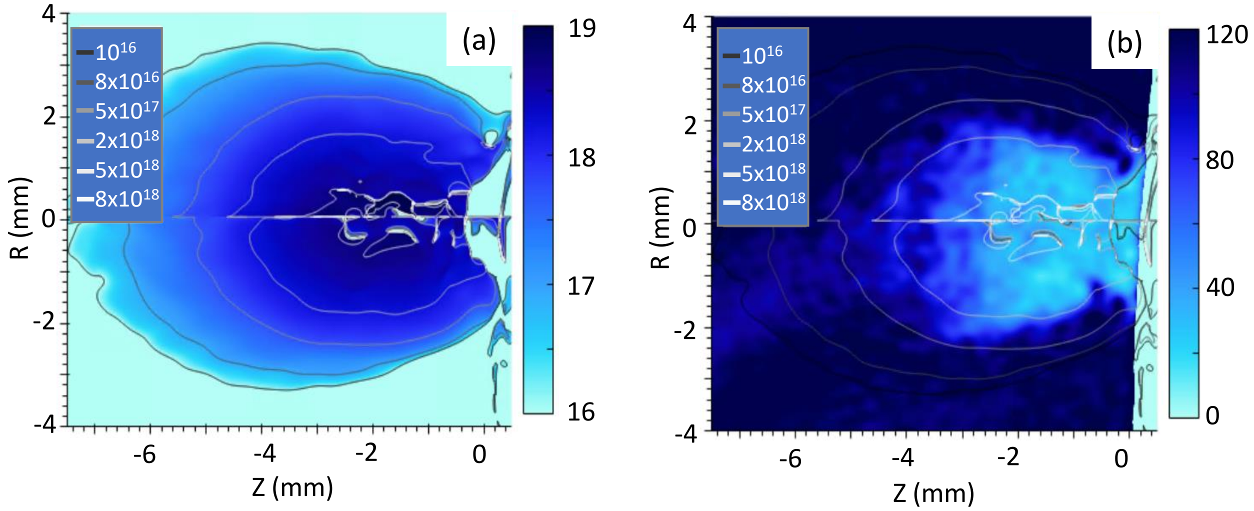

Figure 4.24: Detailed (a) electron density and (b) shadowgraph plot with contours from shot 33909 (100 μm pure aluminum, $\mathrm{t_0} + 500$ ns, where t_0 represents the start of electron beam energy deposition). The color bar for (a) represents $\log(\mathrm{n_e})$, where n_e is in units of cm^{-3}. The color bar for (b) represents percent transmission.

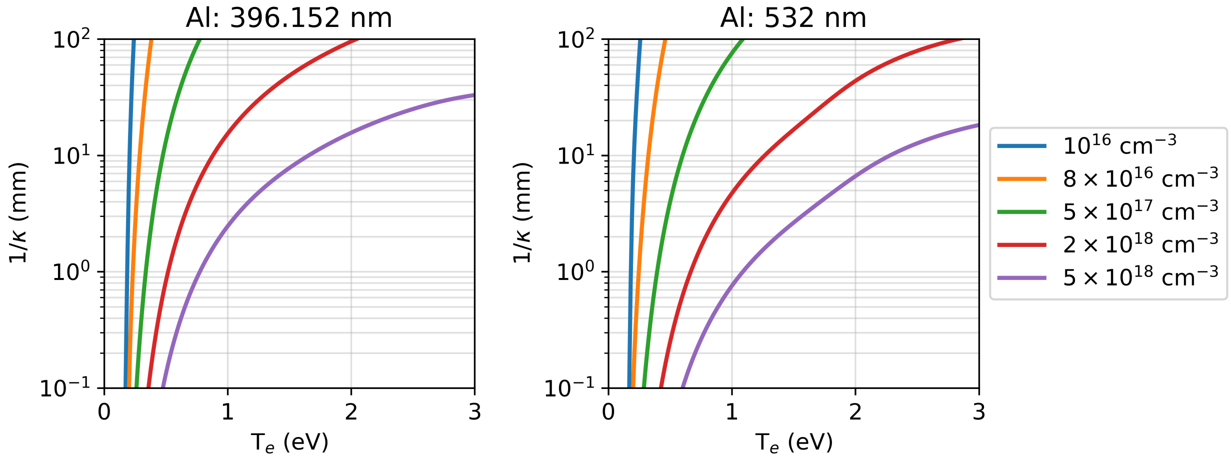

Figure 4.25: Opacity calculations at (a) 396.152 nm and (b) 532 nm for a pure aluminum plasma using the ATOMIC code over the electron densities highlighted in Fig. 4.24. The opacity is plotted as $1/\kappa$ in units of mm so it represents the mean free path of the photon. At all density and temperature combinations, the opacity is lower at 396.152 nm compared with 532 nm. In both cases, there is a rapid decrease in the photon mean free path below 0.5 eV.

CHAPTER 5

Spectral Calibration Sources and Measurements

This chapter explains the different spectral calibration sources used for spectrometer (visible and long wave UV) calibration both prior to deployment on DARHT Axis-I and *in situ* calibration once deployed. The DC pen lamps are principally used for wavelength calibration. The xenon flash lamps are used to confirm the single shot operations and temporal response of the spectrometer systems. The pulsed hollow cathode is an experimental source still under development for use as an Extreme Ultraviolet (EUV) photon source, but initial measurements of the discharge are presented using a long wave UV spectrometer.

5.1 DC Pen Lamp

Pen lamps are used as spectral calibration sources due to their low cost, small footprint, and reliable operation. These sources have been demonstrated to be simultaneous high-quality wavelength [9] and intensity [104] calibration sources. Mercury pen lamps operate as a low current discharge and are filled with a noble gas at a low-pressure along with a small mass of metallic mercury. The noble gas is used as a starter to ignite the discharge, but the mercury spectrum dominates the line

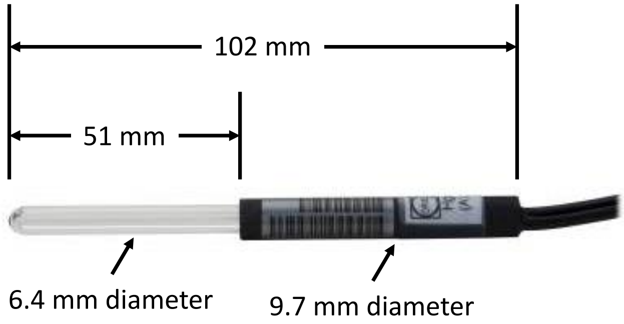

Figure 5.1: Dimensions of an Oriel pencil calibration lamp.

Wavelength (nm)	Intensity
253.6521	300,000
296.7283	2,600
312.5674	2,800
365.0158	5,300
404.6565	4,400
435.8335	10,000
546.0750	10,000

Table 5.1: Hg-I lines consistently measured from a Hg(Ar) pen lamp. Boldface indicates that these particular lines are used for wavelength calibration of the spectrometers: 253 nm and 435 nm for the long wave UV; 435 nm and 546 nm for the visible. The intensity is given with respect to the 435.8335 nm line, which has been scaled arbitrarily to 10,000. This data is from Ref. [9]. Note that this list is not inclusive of all Hg-I lines that can be measured from a Hg(Ar) pen lamp.

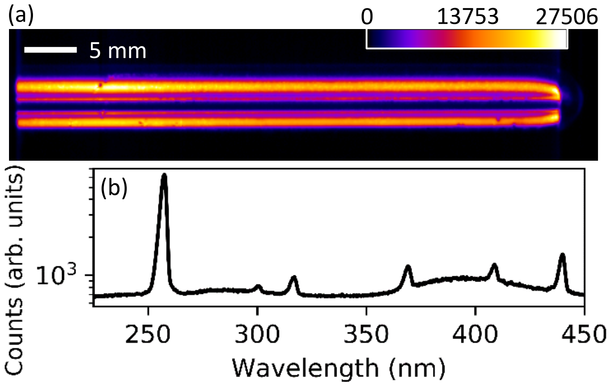

Figure 5.2: (a) Vacuum-based CCD image of the DC Hg(Ar) pen lamp discharge; 10 ms gate width. (b) Spectral survey (150 grooves/mm) of the emission lines and continuum produced by the Hg(Ar) lamp using a long wave UV spectrometer. The prominent Hg-I line at 253.65 nm dominates the spectra. Note the logarithmic counts scale in (b).

output of the lamp from 200–600 nm once stable operation is achieved. The Oriel 6035 Hg(Ar) pen lamp [105], shown in Figure 5.1, is the wavelength calibration source for both the visible and long wave UV spectrometers due to the strong and well characterized Hg-I lines produced in the UV and visible regimes. Table 5.1 shows the lines consistently observed, along with the lines used for wavelength calibration highlighted in bold.

A modified version of the Oriel lamp holder (#6058NS) that fits both a smaller 7×200 μm fiber bundle and the larger 19×200 μm linear fiber pack (used for the spectrometers introduced in Ch. 4) holds the pen lamp for spectrometer calibration measurements. Using this mount also provides a relatively light-tight enclosure to ensure the fiber bundle is only coupling in the light from the pen lamp, and not from ambient fluorescent lighting present in the laboratory. An example

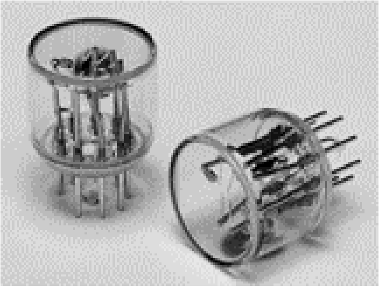

Figure 5.3: Hamamatsu xenon flash lamp, model L2187. The quartz cylinder which contains the electrodes has a diameter of 28 mm. The anode-cathode spacing, and thus the arc size, is 8 mm.

image and spectrum produced by the Hg(Ar) pen lamp is shown in Figure 5.2. A vacuum-based CCD [106] with a 10-ms gate is used to obtain the self-emission image. The broadband spectral survey showing the emission lines and continuum produced by the Hg(Ar) pen lamp is made using the long wave UV spectrometer described in Sec. 4.2.3.

5.2 Xe Flash Lamp

Xenon flash lamps (Figure 5.3) are excellent sources of intense light output from the UV to the near-infrared wavelengths. These sources provide a complimentary calibration measurement to the DC pencil lamps discussed in the previous section. Xe flash lamps are pulsed, providing enough light in the discharge to permit sub-μs gating, which is the relevant timescale for the beam-target interaction experiments. Furthermore, the light output is dominated by continuum-like emission down to $\sim$250 nm, in addition to featuring some characteristic xenon ion lines. This feature allows the xenon flash lamp to perform relative transmission measurements as a function of wavelength for different lens setups to optimize the optics train for the long wave UV spectrometer. This was previously shown in Figure 4.17.

Time gated images (10-ns gate width) using a UV-sensitive CCD [101] of the xenon flash lamp arc are shown in Figure 5.4. Separate measurements using a long wave UV spectrometer (described in Sec.4.2.3) yield a spectral survey, which shows the detailed spectrum of the output light from 200–450 nm. The spectrum is composed of continuum-like emission superimposed with Xe-II–IV emission lines inferred from comparison with the NIST tables [107]. Figure 5.5 shows the time history of the flash lamp discharge measured two independent ways: (1) integrated intensities from the images in Fig. 5.4(a); and (2) the response of a UV-sensitive GaP photodiode [4].

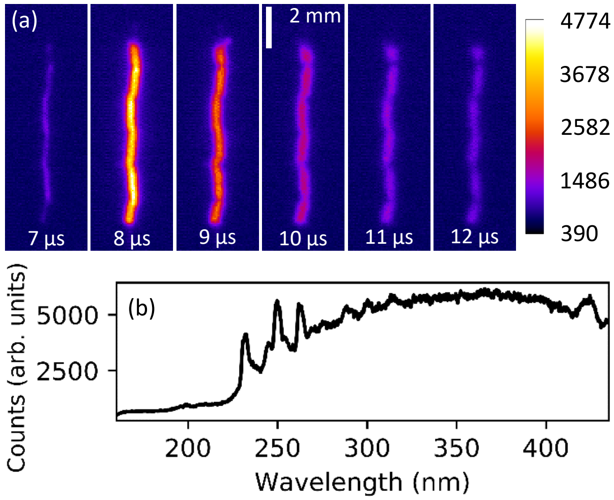

Figure 5.4: (a) Sequential images (10 ns gate width) of the Xe arc with a UV-sensitive CCD using a $OD = 1.0$ neutral density filter (10% transmission). Here, 7 μs is referenced to the t_0 of the pulser used to drive the Xe flash lamp. (b) Spectral survey (150 grooves/mm) using a long wave UV spectrometer (7 μs gate delay, 10 μs gate width, $10\times$ gain) that shows a strong continuum containing Xe ion emission lines.

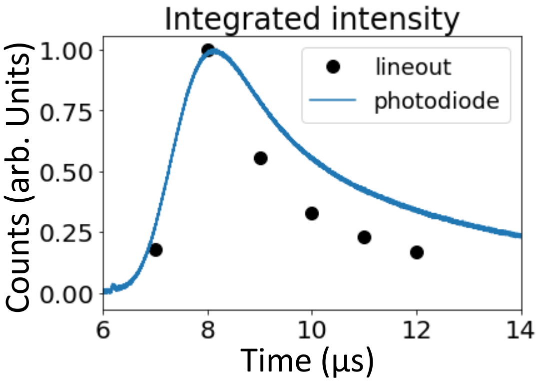

Figure 5.5: Plot of the xenon flash lamp discharge normalized intensity as a function of time. The black circles represent the integrated intensities from Fig. 5.4(a), and the blue curve is from a GaP photodiode sensitive to UV photons [4].

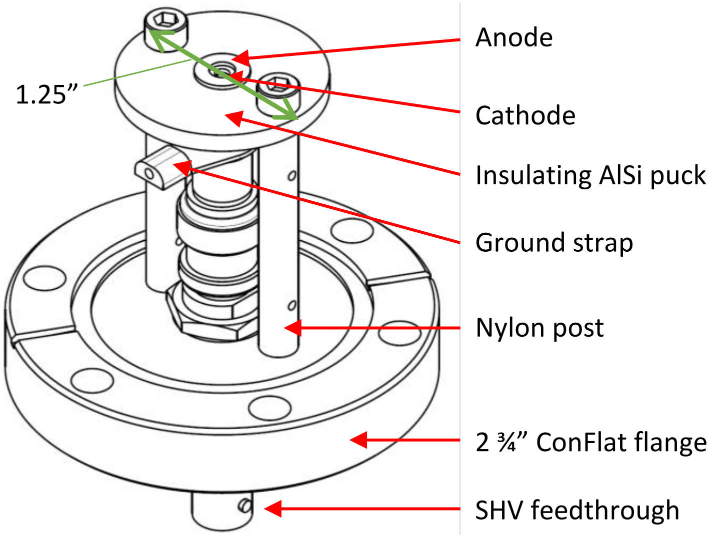

Figure 5.6: 3-D model of the pulsed hollow cathode source with relevant parts labeled. Not shown is the insulated wire connecting the ground strap to the anode. The wire is mated to the anode with a silver epoxy. In addition, the SHV feedthrough on the vacuum side (between the nylon posts) has been wrapped with Teflon tape to prevent corona.

5.3 Hollow Cathode

Hollow cathodes have been used as intense light sources for many decades [108, 109]. A custom pulsed hollow cathode has been designed, fabricated, and tested. It has potential as an EUV photon calibration source for next-generation beam-target interaction diagnostic development. The system is gas filled with either He, Ar, or atmospheric air, which is pressurized to 1–10 Torr. A 3-D model of the hollow cathode is shown in Figure 5.6. The relevant parts are labeled, but the insulating wire connecting the ground strap to the anode is not shown here for clarity. The wire is attached to the anode with a silver epoxy to provide a conductive current path. The SHV feedthrough, of which the conductor is the cathode, has been wrapped with Teflon tape to prevent corona and improve the discharge characteristics.

Figure 5.7 displays a hollow cathode assembly mounted to a vacuum assembly. The hardware shown includes a Convectron gauge for measuring the system pressure, a gas line used to provide a source gas (atmospheric air, argon, or helium), and a window for optical access to the discharge.

Figure 5.8 provides a cross-sectional illustration of the anode-cathode geometry. The cathode stalk fits within the insulating puck and has a cupped profile as shown. The brass washer anode has an inner diameter of 2.13 mm. The anode-cathode separation distance based on the distance of closest approach is approximately 2.5 mm.

A source that can operate either in a DC mode or a pulsed mode will generally produce a

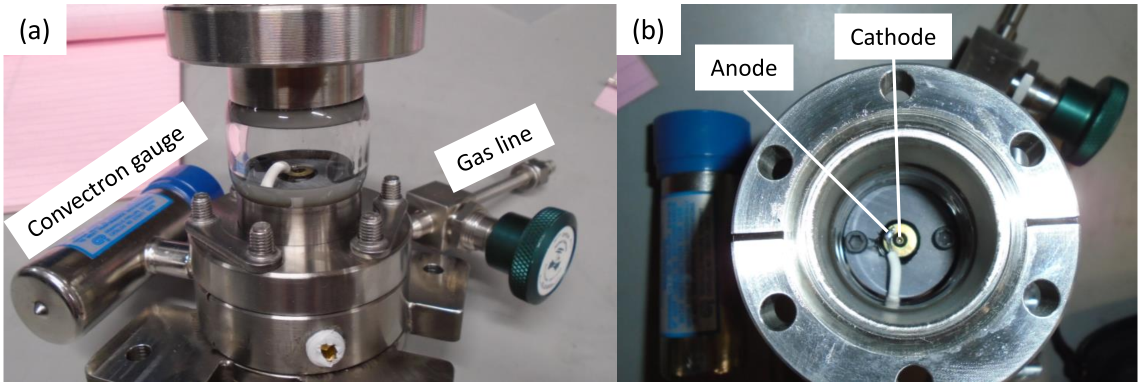

Figure 5.7: Images of the hollow cathode hardware. (a) The spool piece that mounts to the 2-3/4" flange includes ports for a gas line with an in-line flowmeter and a Convectron gauge for pressure measurements in the region of the hollow cathode. (b) End-on photograph of the anode-cathode region.

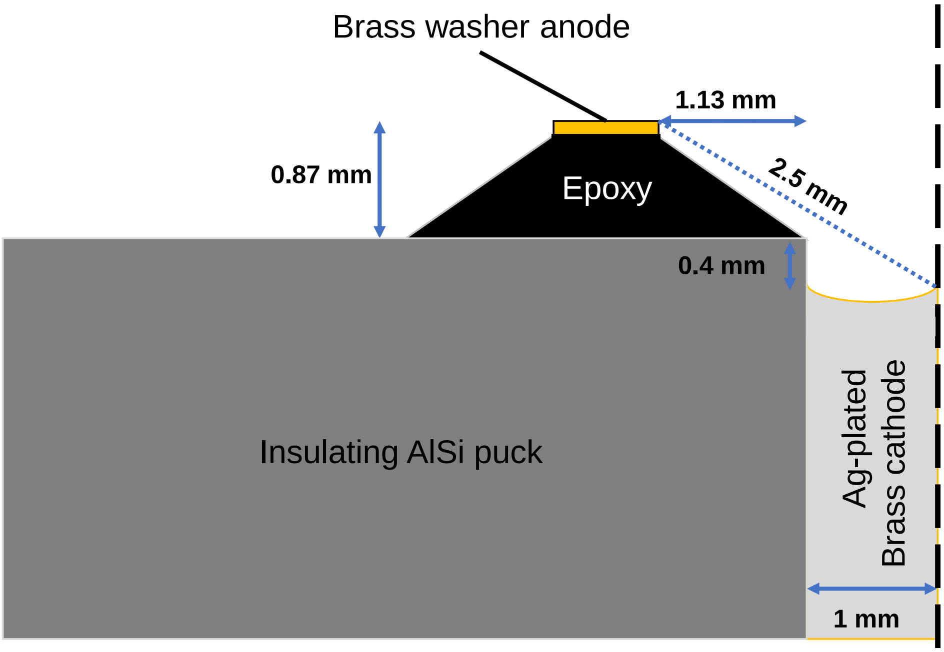

Figure 5.8: Cartoon diagram of the hollow cathode anode-cathode region with measured dimensions indicated. The dashed black line on the right denotes the (cylindrical) axis of symmetry. Note that the ground strap connection is not shown. The cathode is a part from Pasternack, part # PE44118 [5].

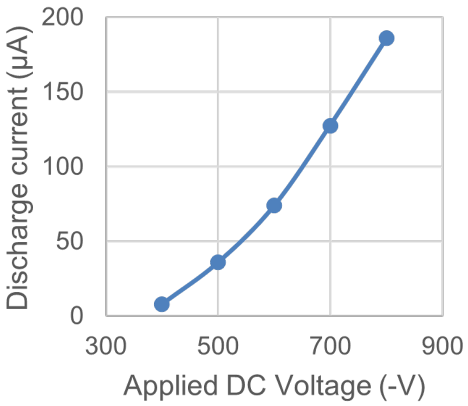

Figure 5.9: DC operations of the hollow cathode at 0.5 Torr showing measured discharge current as a function of applied voltage.

more intense discharge when operated in a pulsed mode. This hollow cathode system has been designed to operate in a pulsed mode. However, DC tests were conducted to ensure the discharge would operate normally and not breakdown. Figure 5.9 shows the discharge current at 0.5 Torr as a function of applied voltage using a high voltage DC power supply.

Pulsed operation is provided by a custom high voltage pulser using a nominal 5 kV solid-state MOSFET switch to drive the hollow cathode discharge. The circuit diagram of this pulser as modeled in LTSpice is shown in Figure 5.10, and the hardware is displayed in Figure 5.11. The simulated waveforms shown in Fig. 5.10(b) use a load resistance of 100 kΩ to simulate the impedance before the discharge is ignited. A high voltage power supply charges a capacitor ($\sim$3 nF) through a ballast resistor (1 MΩ). The solid-state MOSFET switch (powered by a 5 V DC supply) is triggered by a 5 V, 500 ns pulse that nominally defines the "on" time of the switch. The output pulse travels through an inductor (6.5 μH), a Pearson current transformer for a current measurement, and a current limiting resistor (50 Ω), respectively. A voltage divider ($10700{:}1$) then picks off the output voltage waveform.

The pulser was first tested for nominal operation and validation of the model by driving a 3.3 kΩ resistive load, which simulates an open circuit where the discharge is not ignited. Figure 5.12 shows the measured voltage and current waveforms when driving this resistive load both with and without an inductor on the pulser output. An inductor is included on the output of the pulser in addition to the 50 Ω resistance to help further limit the current draw through the solid-state switch to enhance its longevity, in addition to providing an inductive kick to the voltage. Note that the switch can be operated at a lower voltage (-3 kV) with the inductor in place compared with not using an inductor (-3.5 kV) and deliver both a higher voltage at a lower current.

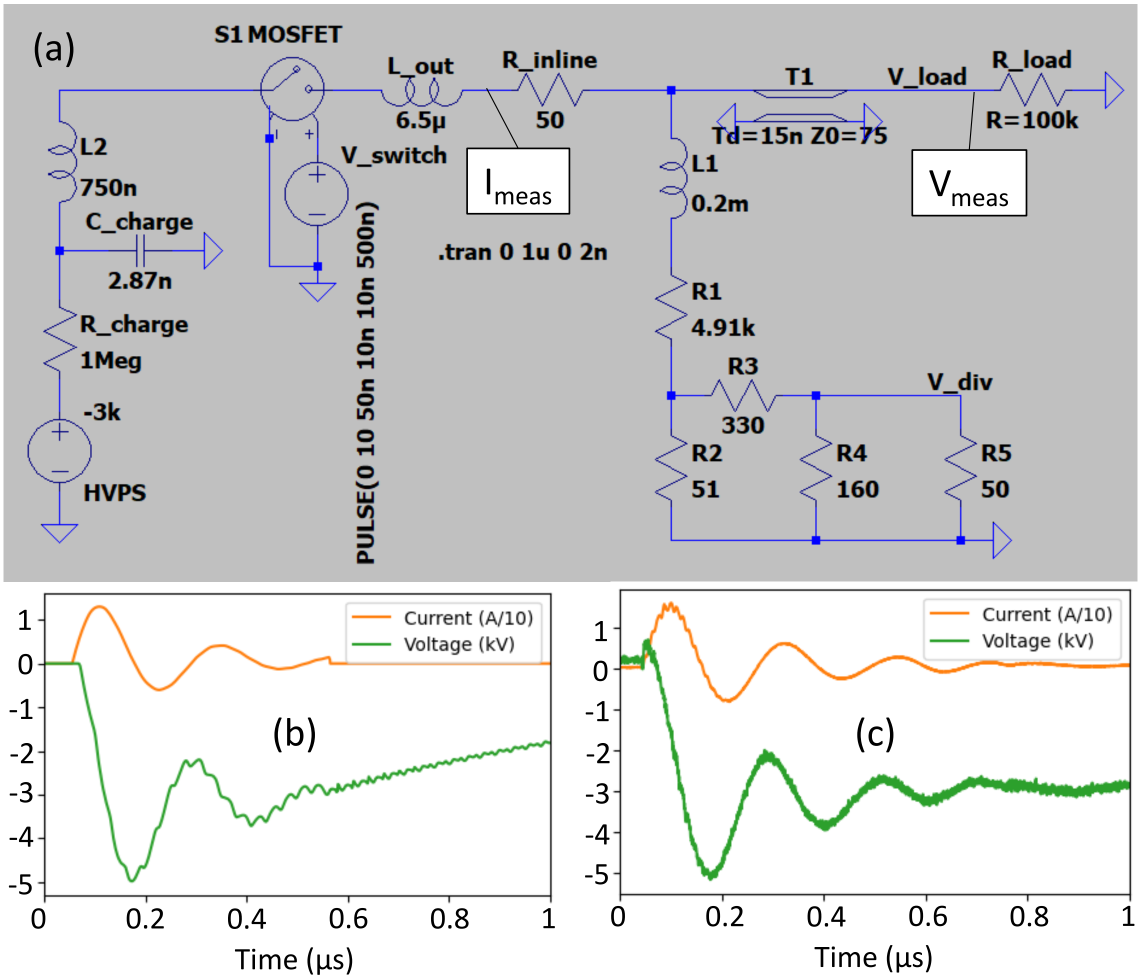

Figure 5.10: (a) Hollow cathode solid-state pulser circuit model. The load is represented by a 100 kΩ resistance which simulates the impedance before the discharge is ignited. (b) Simulated current (orange) and voltage (green) waveforms. (c) Measured current (orange) and voltage (green) waveforms. The voltage pulse is measured at V_{meas}, and the current pulse is measured at I_{meas} as shown in (a), which corresponds to both the physical location and the location in LTSpice where the measurements are made.

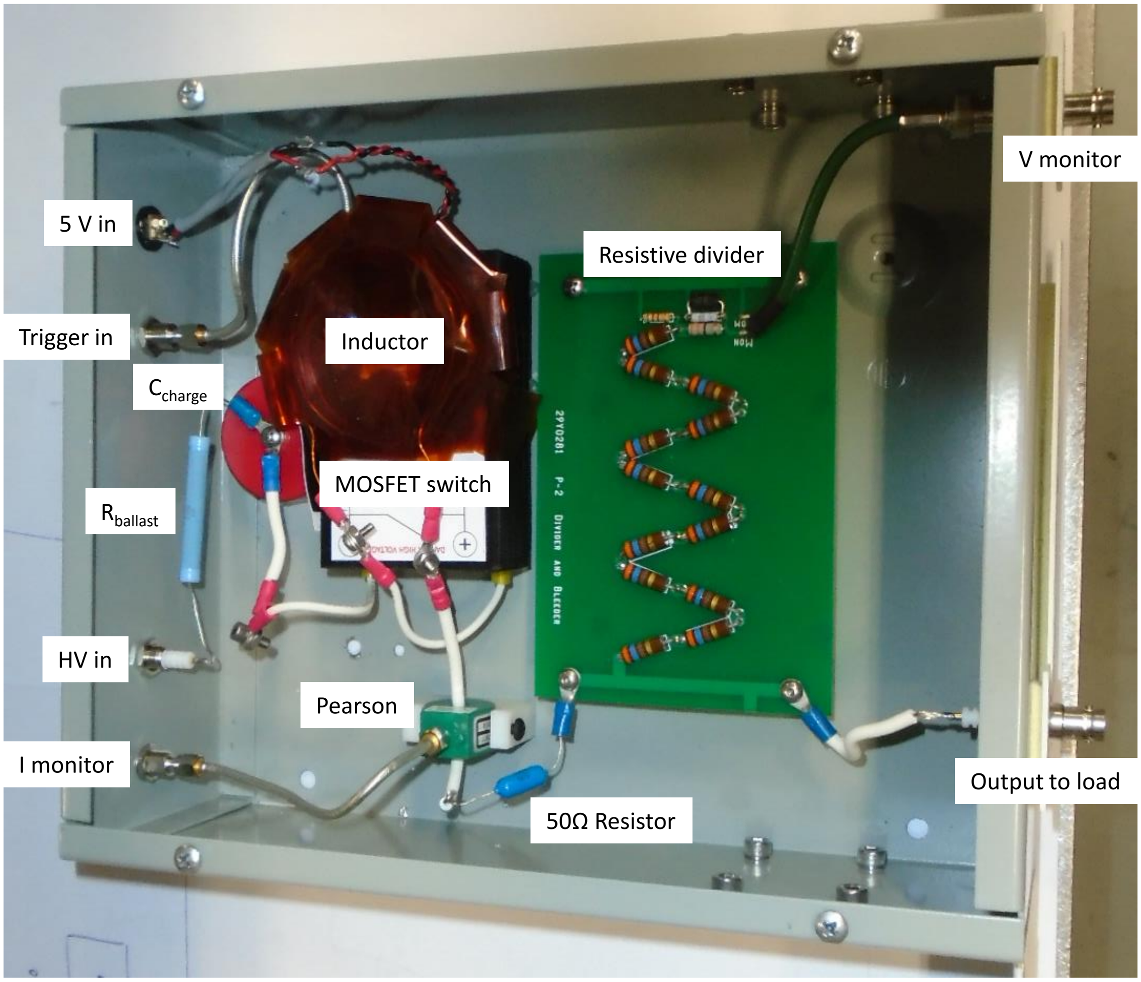

Figure 5.11: Hollow cathode pulser chassis with all parts labeled.

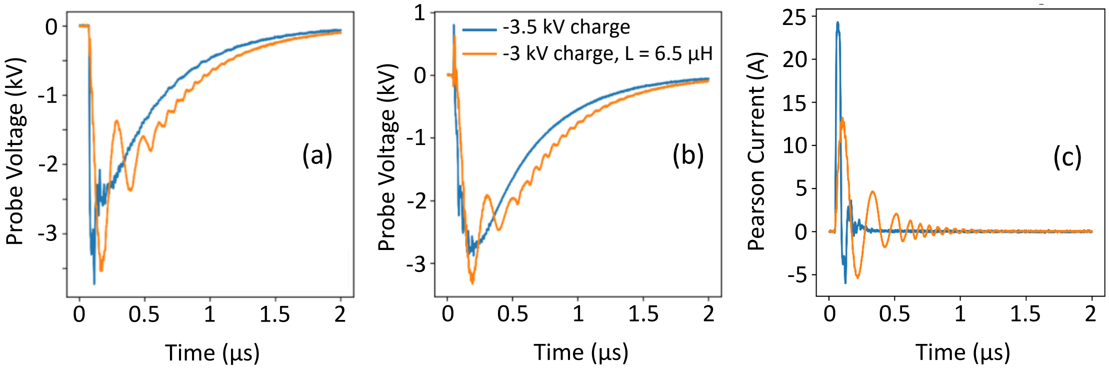

Figure 5.12: Voltage and current comparison of the custom solid-state pulser operating at a -3 kV charge driving a 3.3 kΩ resistive load without (blue) and with (orange) an inductor on the output of the switch. (a) Voltage measured across the load resistance using a Tektronix P6015A high voltage probe. (b) Voltage measured using the embedded resistive divider circuit within the pulser chassis. (c) Current measured using a Pearson current transformer located on the output of the pulser within the chassis.

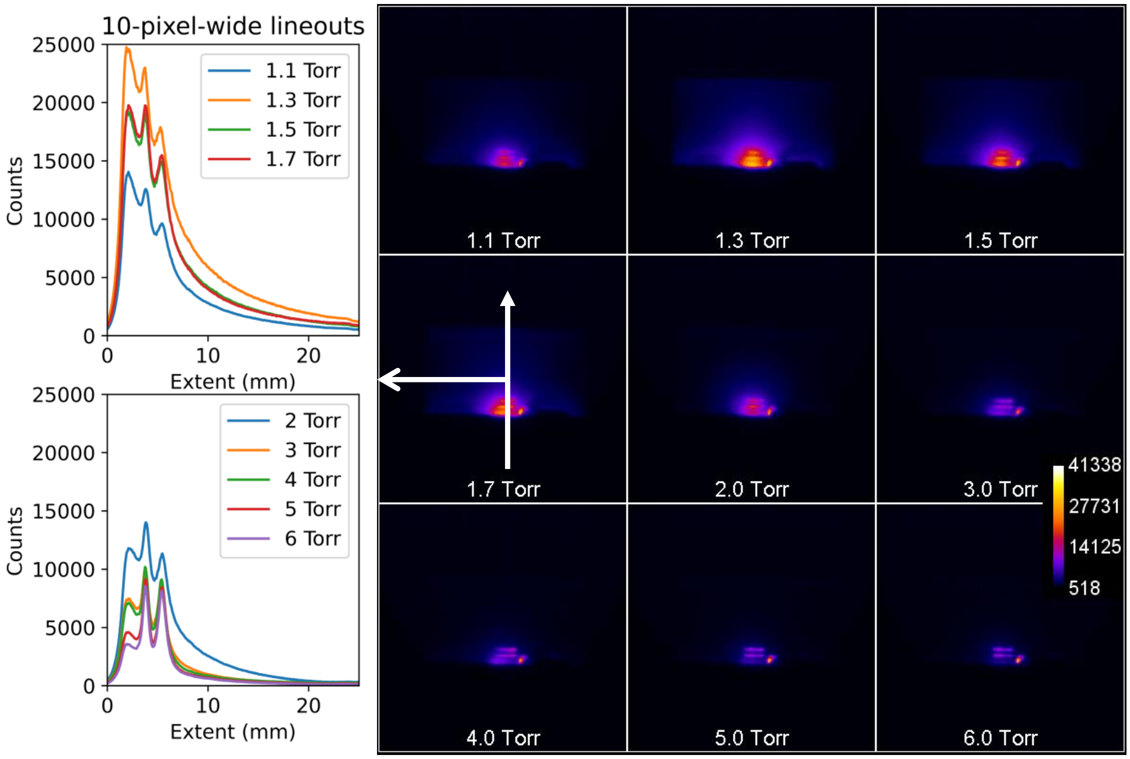

Figure 5.13: Imaging of the hollow cathode discharge at selected argon gas fill pressures (1 μs gate, 20× gain on a UV sensitive PiMAX CCD). Vertical lineouts (10 pixels wide) are also shown which illustrate the difference in discharge intensity versus pressure. A -3 kV charge was used to drive the hollow cathode.

Figures 5.13–5.15 provide a detailed overview of the operating space of the hollow cathode in argon from 1–6 Torr, using the drive circuit shown in Fig. 5.10(a). Images of the discharge are shown in Fig. 5.13, which highlight the effect of pressure on the spatial distribution and intensity of the discharge. An operating pressure of 1.3 Torr results in the highest counts measured by the UV sensitive PiMAX CCD.

Figure 5.14 shows the current and voltage profiles corresponding to different operating pressures that produce the discharges shown in Fig. 5.13. The breakdown time is defined as where the voltage pulse crosses zero; when the discharge is ignited, it provides a low resistance conductive path to ground. The selected pressures plotted from 1.1–5 Torr show the trends in the breakdown for different argon gas fill pressures. An increase in pressure results in a reduced amount of time required to ignite the discharge. The discharges at lower pressures exhibit substantially more RF oscillations superimposed on the voltage pulse. For increasing operating pressures, the collisionality of the plasma increases and attachment begins to dominate.

The effect of pressure on peak current and ignition delay time is shown in Fig. 5.15. Increasing the operating pressure results in an increased current draw during the discharge, a decrease in the delay time to discharge ignition, and a decrease in the spatial extent and intensity of the plasma. Additionally, at increased operating pressures, the variation in the breakdown jitter and the current drawn by the discharge is reduced.

Figure 5.16 shows an example high-resolution UV spectrum produced by the hollow cathode discharge operating at 3.5 kV in an argon background (2 Torr) with two different time gates. A linear 7×200 μm array is lens-coupled with a fused silica plano-convex lens ($f = 60$ mm) to provide a magnification of $0.3\times$. The array is looking head-on at the hollow cathode, with a line-of-sight similar to Fig. 5.7(b) and having a standoff distance from the cathode to the lens of $\sim$270 mm. Line emissions from several different species and ionization stages are observed and identified using the NIST tables [107]. The copper and zinc doublet lines are characteristic of the anode and cathode material, while the presence of the silver doublet is due to the use of a silver epoxy to attach the ground strap and provide a conductive path from the anode to ground. Both the Cu-I and the Ag-I doublet lines show a consistent intensity across the two time gates, while the Ar-II line and the Zn-I doublet show a reduced intensity in the later time gate.

5.3.1 Summary

The visible diagnostic calibration sources, including the DC pen lamp and Xe flash lamp, have been introduced and explained. The fabrication and testing of pulsed low-pressure hollow cathode is also described. The hollow cathode is measured initially with a long wave UV spectrometer to diagnose the spatial and temporal characteristics of the discharge. In addition, the solid-state pulsed power

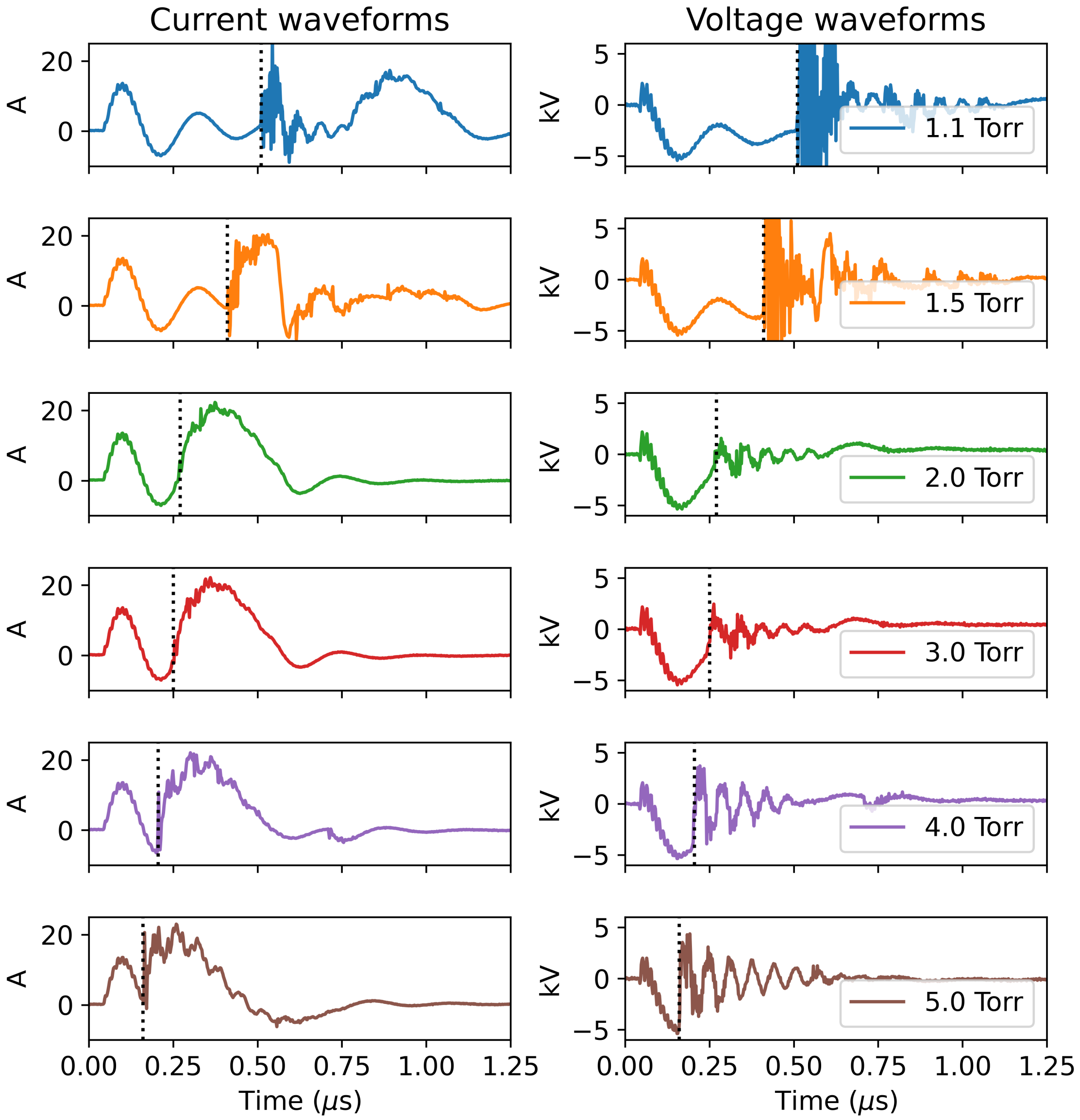

Figure 5.14: Measured voltage and current waveforms as a function of pressure for the hollow cathode discharge operating at a 3 kV charge with an argon gas fill. These selected plots show the trends in the breakdown (defined as where the voltage waveform crosses zero) for different argon gas fill pressures. An increase in pressure results in a reduced amount of time required to ignite the discharge, where the ignition time is indicated on the plots by the vertical dotted black lines.

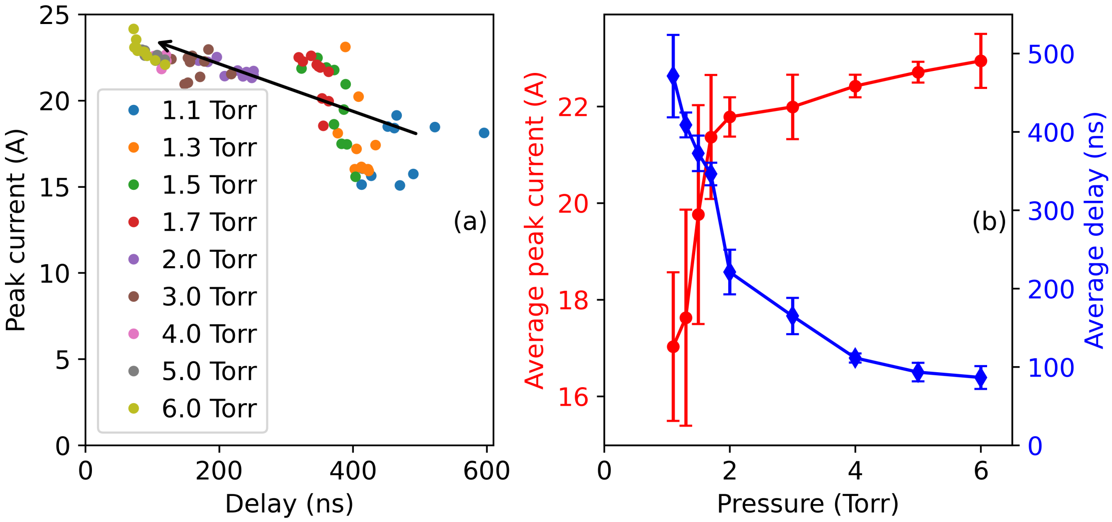

Figure 5.15: Operating space of the hollow cathode discharge operating at a 3 kV charge with an argon gas fill. The delay, or time to ignition, is determined by taking the difference in time of the driving current pulse peak (∼100 ns in Fig. 5.14) and the discharge current pulse peak. (a) Peak discharge currents and delays for a selected set of background gas pressures, with ∼10 shots at each pressure. The black arrow indicates the influence of increasing pressure. (b) Effect of pressure on the average peak current (red) and delay (blue) needed to ignite the discharge.

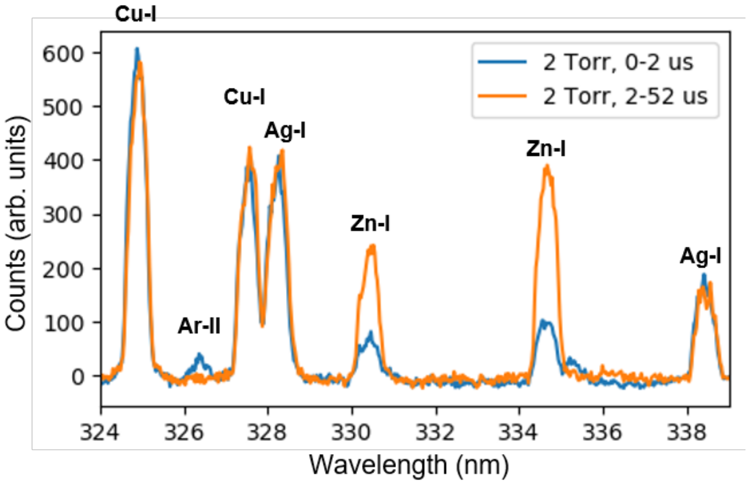

Figure 5.16: Long wave UV spectrometer measurement of a pulsed hollow cathode discharge operating at 2 Torr and a -3.5 kV charge under an argon gas fill. Lines are identified and labeled. The spectrometer is using a 1800 grooves/mm holographic grating centered at 329 nm with 40× gain, and the gate times (relative to the ignition of the discharge) are as indicated in the legend.

system required to drive this source was also designed, modeled, built, and successfully employed to produce a discharge.

CHAPTER 6

Numerical Simulation Tools

This chapter provides an overview of the modeling tools used in support of the DARHT beam-target interaction experiments. This discussion includes radiation hydrodynamics simulations of the beam-target interaction (Sec. 6.1) and the Los Alamos suite of atomic physics codes (Sec. 6.2) used to calculate the energy levels, cross-sections, and atomic kinetics required to generate the synthetic spectra generated by the spectroscopic-quality radiation transport model (Sec. 6.3). The explanations provided within the sections of this chapter are not to be considered standalone; instead, they are written to provide specific details and explain nuances on how they are used for this particular problem (the beam-target interaction, WDM, etc.). References to the primary sources for all codes are provided for further reading.

6.1 LASNEX

LASNEX is a 2-D Lagrangian radiation hydrodynamics code that historically has been used to model laser driven inertial confinement fusion experiments beginning in the 1970s [110]. It has been used for several years to model the DARHT beam-target interaction experiments, in particular the energy deposition by the electron beam and subsequent hydrodynamic expansion of the heated target material. The specific details of the implementation of the LASNEX model are given in [79], along with the first set of aluminum results presented in [69]. The electron beam parameters are drawn directly from experimental measurements; the near-field OTR measurements of the beam spot size during the peak focus are used to define the beam size in the simulation space. The LASNEX runs presented in Chapters 7 and 8 are performed from 0–400 ns with an output temporal resolution of 1 ns, and with variable spatial resolution over a mesh extending from $-5 < Z < +5$ cm, and $-0.5 < R < +0.5$ cm. Axial zone sizes vary from 1 cm far from the target foil down to $\sim$10 μm near and within the target foil. Similarly, radial zone sizes vary from 0.5 mm down to $\sim$20 μm.

The value of this hydrodynamic model is that it provides 2-D distributions of the T_e, n_e, n_i,

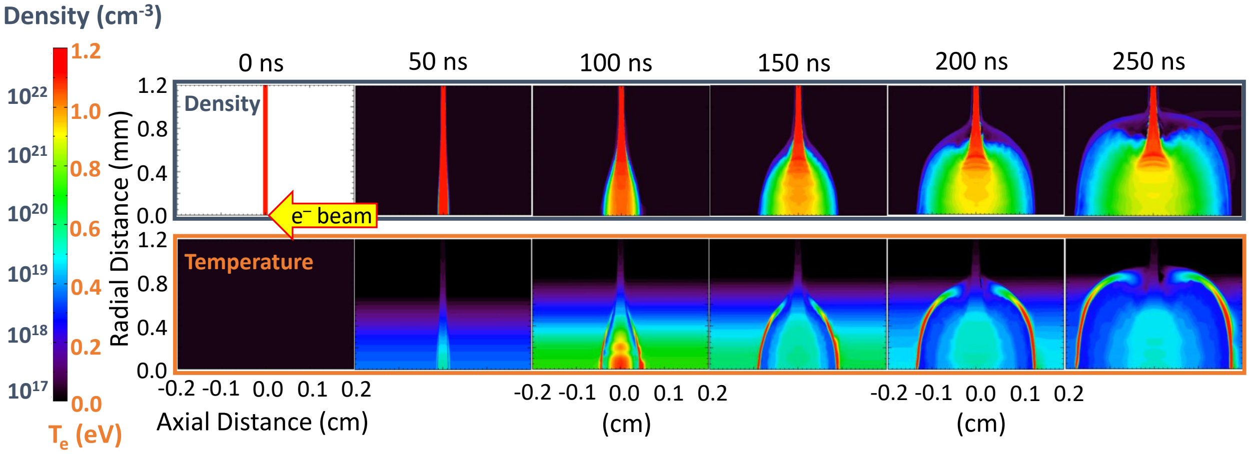

Figure 6.1: Example LASNEX 2-D n_e and T_e contour plots from 0–250 ns of a 100 μm aluminum foil (SESAME 3715) heated by a 19.8 MeV, 1.6 kA, 100 ns beam in a 0.89 mm FWHM Gaussian spot. The beam impinges on the foil on-axis from the $+Z$ direction.

and material stoichiometry. Figure 6.1 shows example contour plots of n_e and T_e at 50 ns intervals out to 250 ns. This information, contained within hydro dump files (outputs from the code), can be post-processed and fed into a spectroscopic-quality radiation transport model to generate synthetic spectra relevant to matching the real spectra measured from the visible and long wave UV spectrometers introduced in Chapter 4. This spectroscopic-quality radiation transport model will be discussed in detail later in this chapter in Section 6.3.

The relevant electron densities for visible emission and absorption spectroscopy are, very roughly, 10^{17}–10^{19} cm^{-3}. The grid resolution of the LASNEX model was improved in this region to sufficiently resolve in simulation space the T_e and n_e regions that contribute to forming the spectra measured by the spectrometers, specifically the density gradient from $\sim 10^{20}$ cm^{-3} down to $\sim 10^{16}$ cm^{-3}.

LASNEX interfaces with the SESAME [111,112] EOS tables for material properties, including temperature, density, pressure, and internal energy. Aluminum EOSs used for modeling the thin aluminum foils include the legacy SESAME 3715 [113] and the modern SESAME 3720 [114, 115]. Both tables have a minimum density of 10^{-6} g/cm^3 (2.2×10^{16} ions/cm^3). However, all the results presented in this chapter and subsequent chapters are runs of the legacy SESAME 3715 EOS because of issues associated with the vapor dome regime included in SESAME 3720. The hydrodynamic expansion of the target material from the beam-target interaction involves complex two-phase transitions. After the initial heating and hydrodynamic disassembly, the spatial density and temperature gradients likely straddle the two-phase mixture, where the vapor dome physics plays a role. It is unclear how well LASNEX is able to handle this.

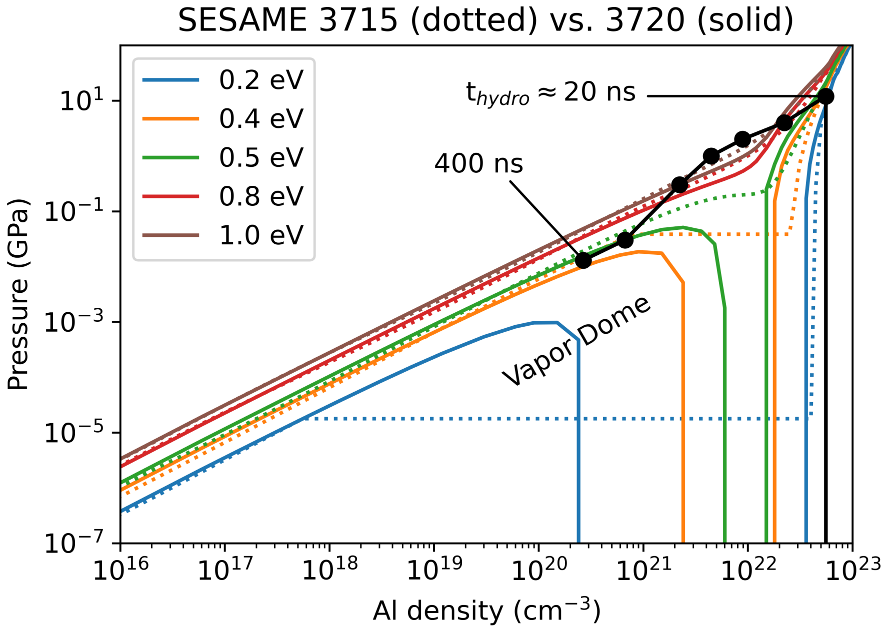

Figure 6.2: Comparison of SESAME EOS 3715 (legacy, dotted lines) and 3720 (new, solid lines) over the relevant pressure and density regimes at selected temperature contours from 0–1 eV. The black circles correspond to LASNEX calculated peak pressures and densities as a function of time out to 400 ns from the run displayed in Fig. 6.1. Note that SESAME 3715 and 3720 agree relatively well at higher temperatures. However, the vapor dome physics captured in SESAME 3720, including the negative pressure regime, is not included in SESAME 3715.

Figure 6.2 shows a comparison of SESAME 3715 and 3720, highlighting the difference in the pressure and density phase space relevant to electron beam driven aluminum target physics. The SESAME 3720 EOS, by construction, is allowed to have negative pressures when under tension, which is a mechanism for it to handle spallation models [116]. Turning tension on and off within the LASNEX model and comparing the results is not something that has been investigated up to this point. Further discussion of this is beyond the scope of this dissertation, but it is vital to future modeling efforts of electron beam driven aluminum.

6.2 Los Alamos Suite of Atomic Physics Codes

The Los Alamos suite of atomic physics codes provides an *ab initio* modeling capability for near-neutral and highly charged ions in both the semi-relativistic and fully relativistic regimes [117]. In addition, the codes are capable of performing either Configuration Average (CA) or Fine Structure (FS) calculations. CA runs are used to to provide a computationally efficient picture of relevant quantities before moving to the more intensive FS runs. For example, CA calculations can be used to accurately compute the ionization balance of the plasma and to ensure that a sufficient (converged) number of stages are included to model the plasma at a given temperature and density, while also providing a rough estimation of the relevant spectra over a defined photon energy range. After this verification procedure, FS calculations can then be used to provide high-resolution emissivity and opacity spectra over the defined photon energy range.

This dissertation applies the original suite of semi-relativistic codes to model the beam-target interaction physics, including the WDM state and classical-like plasmas that are best described as near-neutral systems. The Cowan's ATomic Structure (CATS) code is used to generate atomic structure data [10]. The General Ionization Processes in the Presence of Electrons and Radiation (GIPPER) code uses the levels from CATS to provide ionization cross section data [118]. The Another Theoretical Opacity Modeling Integrated Code (ATOMIC) code, using the results from both CATS and GIPPER, solves the collisional-radiative equations in either Local Theromdynamic Equilibrium (LTE) or non-LTE conditions to provide atomic level populations at given plasma conditions and calculate quantities like emissivity and opacity [117, 119]. When performing FS calculations, ATOMIC produces fully resolved fine-structure spectra that can be compared with experimental data. Detailed explanations and usage of the semi-relativistic capability in the Los Alamos suite of atomic physics codes for LANL employees is provided in Appendix B.

Ion	Configurations	Total Configurations	Total Levels
Al-I	Base: [Ne] $3s^2$ $3p^1$ $3s^2$ nl^1 through $n = 8$ $3s^1$ $3p^1$ nl^1 through $n = 8$ $3s^1$ $4s^1$ nl^1 through $n = 8$ $3p^3$ $3s^1$ nl^2 through $n = 4$	76	708
Al-II	Base: [Ne] $3s^2$ $3s^1$ nl^1 through $n = 10$ $3p^1$ nl^1 through $n = 4$ $3p^2$	40	174
Al-III	Base: [Ne] $3s^1$ nl^1 through $n = 9$ $2p^5$ $3s^1$ nl^1 through $n = 8$ $2p^5$ $3s^2$ $2p^5$ $3p^2$	60	562
Al-IV	Base: [Ne] $2p^5$ nl^1 through $n = 9$ $2p^4$ $3s^2$ nl^1 through $n = 5$	43	673

Table 6.1: CATS *nl*-type configurations for aluminum ions, where a noble gas configuration of [Ne] ($1s^2$ $2s^2$ $2p^6$) is implied for all configurations. The base (zero energy) configuration for each ion stage is given for reference. Note that for Al-III and Al-IV, the configurations deviate from the filled $2p^6$ subshell.

6.2.1 CATS

The CATS code was originally developed from R. D. Cowan's atomic structure programs and requires only simple inputs that specify the element, ion stage, and electronic configurations. It can be run in either CA or the detailed FS mode and outputs wavefunctions, energy levels, and oscillator strengths. For FS calculations, the output data are appropriately labeled to allow subsequent recall of the calculated configurations and fine structure levels [10]. This design allows the GIPPER and ATOMIC codes to efficiently use these calculated quantities for further atomic physics modeling.

CATS takes a user defined list of configurations particular to an element in a certain charge state and solves the Hartree-Fock equations. For all aluminum runs presented in this dissertation, configuration lists for ion stages I-IV (neutral to 3+) are generated. For modeling this near-neutral-like system, the inclusion of these charge states is sufficient to ensure a converged charged state distribution. Configurations in CATS are provided in an *nl*-type format and are used to generate *LS*-coupled basis states. Table 6.1 shows the configurations used for each ion stage, along with the total number of configurations and resulting number of levels.

	No inner-shell vacancies		Single inner-shell vacancy ($n = 2$)	
Ion	**Configurations**	**Levels**	**Configurations**	**Levels**
Al-I	76	708	144	4361
Al-II	40	174	88	2366
Al-III	60	562	63	725
Al-IV	43	673	38	575

Table 6.2: Comparison of CATS configurations and calculated levels containing no inner-shell vacancies, representative of runs for data shown in Chapters 7–8, compared with a single inner-shell vacancy ($n = 2$, L-shell hole) relevant for EUV spectroscopy.

Building configuration decks is not an exact science; it relies heavily on the users experience and intuition to include the appropriate configurations that will be relevant for modeling the experiment. The spectra that are ultimately generated with these runs for electron beam driven target plasmas are similar in character to a Laser-Induced Breakdown Spectroscopy (LIBS) plasma [120]. High-lying lines (nl > 8d, also known as Rydberg states) are generally never observed in LIBS-type plasmas. However, while these high-lying states may not be spectroscopically significant, they still can contribute to the level populations and can help to improve the convergence of such quantities. These configuration lists are usually truncated at $n = 10$. Furthermore, when using the CATS capability to match calculated level energies and gf values with measured values from the NIST databases, knowledge of the transitions of interest (initial and final levels and the corresponding energies) helps with the proper labeling of these transitions of interest. This issue becomes important when, in strongly mixed levels, the dominant configuration label is not always useful since two (or potentially several) configurations can contribute strongly to that level [121]. It can also be relevant when considering configurations involving inner-shell vacancies to model K-shell and L-shell spectra, where the resulting number of levels can increase by a factor of 10 due to the larger number of accessible states resulting from angular momentum coupling. This behavior is shown in Table 6.2.

6.2.2 GIPPER

The GIPPER code performs ionization cross section calculations between the levels of adjacent ion stages provided by the CATS outputs [118]. With atomic structure calculations performed for aluminum ion stages I–IV, a total of three GIPPER runs (I–II, II–III, and III–IV) are needed to generate the ionization cross sections required by ATOMIC. GIPPER calculates photoionization, scaled-hydrogenic collisional ionization, distorted-wave collisional ionization, and autoionization cross sections. For the runs that generate the data contained within this dissertation, all of these cross sections are calculated except for the distorted-wave collisional ionization cross section. The

Transition	$c_{\mathrm{i,min}}$	**Run time ($n = 2$ vacancy)**	**Run time (no inner-shell vacancy)**
I–II	0.001	did not finish	3 minutes
	0.01	31.5 hours	n/a
	0.1	46 minutes	n/a
II–III	0.001	50.3 hours	$<$ 1 minute
	0.005	11.5 hours	n/a
	0.01	4.8 hours	n/a
	0.05	10 minutes	n/a
	0.1	5 minutes	n/a
III–IV	0.001	1.3 hours	2 minutes
	0.005	12 minutes	n/a
	0.01	5 minutes	n/a
	0.05	$<$ 1 minute	n/a
	0.1	$<$ 1 minute	n/a

Table 6.3: The effect of configuration interaction on the GIPPER calculation run times involving full inner shells and single inner-shell vacancies. These runs used the CATS files corresponding to those shown in Table 6.2. Note that the value of $c_{\mathrm{i,min}} = 0.001$ is the default value set for all GIPPER runs. The runs with no vacancies were performed only with the default value as they completed in a reasonable period of time.

energies over which these cross sections are calculated are given in threshold units, defined as incident energies relative to the relevant transition energies. For calculations involving a large number of configurations, or configurations that spawn a large number of levels (i.e., including inner-shell vacancies described by K-shell and/or L-shell holes), CA mode is useful to complete calculations in a reasonable period of time, identify ion contributions, and understand the dominant features in a spectrum. The run time is, in general, less of a concern for low-Z elements, due to their simpler electronic structure, but it can quickly become the only option for higher-Z element calculations where the number of calculated levels can be very large ($\sim 10^6$).

As previously mentioned, the inclusion of inner-shell vacancies in a CATS calculation, even for a low-Z material like aluminum, can significantly increase the number of generated levels. This increased complexity can significantly increase run times, especially in GIPPER where the ionization cross sections are obtained by evaluating matrix elements between these levels. This behavior is shown in Table 6.3, where the minimum value of the mixing coefficient, $c_{\mathrm{i,min}}$, is varied to control the number of *LSJ* basis states used to construct each FS level:

$$|LSJ_{\mathrm{FS}}\rangle = c_1\,|LSJ_{1,\mathrm{basis}}\rangle + c_2\,|LSJ_{2,\mathrm{basis}}\rangle + \cdots\,. \tag{6.1}$$

Furthermore, in near-neutral systems, which are described by lower charge states, there can be substantially more Configuration Interaction (CI), or mixing, for the levels compared to higher charge states. This effect is due to the tendency, in near-neutral systems, of pure *LSJ* basis states to be closer in energies. The closeness in these energies typically results in stronger mixing in the corresponding FS levels. Hence, there are more matrix elements for GIPPER to calculate. The level of mixing can be controlled by the user when running GIPPER, which decreases the number of matrix elements considered, and thus the run time, at the expense of potentially decreased accuracy in the results. An overview of this concept is provided in Table 6.3. Note that CI is only important for FS runs, as CA mode, by definition, considers individual configurations to the fundamental states of interest [122]. A plot is provided in the following section of the effect of FS mixing and CA calculations on the generated spectra from an aluminum warm dense plasma.

6.2.3 ATOMIC

The ATOMIC code was developed at LANL out of a requirement for new, more accurate, and more extensive opacity tables for low-Z elements ($Z < 31$) [119]. It can be run with either an LTE or non-LTE solver. For all applications in this dissertation, the LTE solver is used. ATOMIC solves the collisional-radiative rate equations, given the inputs of electron temperature and electron density, and calculates the ion density and corresponding ion level populations. Given a user-defined photon energy grid, quantities such as emissivity and opacity can be calculated using either fine-structure levels (FS mode) or configurations (CA mode).

As discussed earlier, the atomic structure and cross section data from CATS and GIPPER runs that are fed into ATOMIC must also have been computed within the FS or CA mode. CA calculations are useful because they are less computationally expensive, can be used to see if the spectral features of interest are being produced, and to check for proper (converged) ionization balance, before proceeding with the more detailed FS runs. Figure 6.3 shows a comparison of CA with FS runs of a spectrum from an aluminum plasma with an electron temperature of 3 eV and electron density of 10^{21} cm^{-3}. It is clear that, in going from CA to FS mode, and with an increasing amount of CI (decreasing values of $c_{\mathrm{i,min}}$), the emissivity exhibits richer spectral features.

ATOMIC is used to generate the spectroscopic-quality databases of emissivity, opacity, and ionization balance across a range of user-defined temperatures and densities for the Finite-Element Spectral Transfer of Radiation (FESTR) code. The temperature and density ranges and resolutions, along with the corresponding photon energy grid, are determined by several factors. These include: (1) ensuring that the upper bound of temperature and density from the radiation hydrodynamics model is captured; (2) the temperature and density resolution is of sufficient quality to map to the mesh and maintain reasonably well its structure; (3) the photon energy grid is fine enough to resolve the line transitions of interest and the total size (number of points) is small enough to

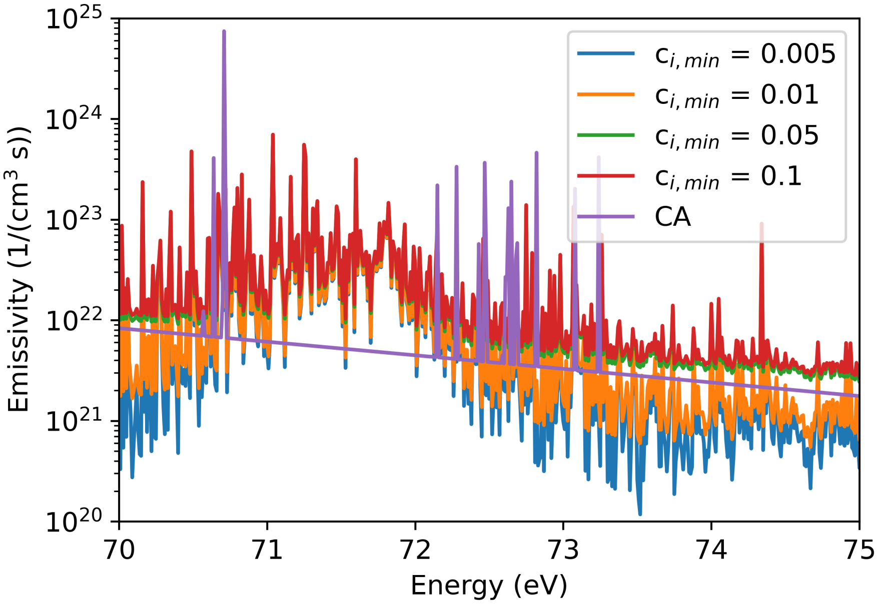

Figure 6.3: The effect of CA and FS modes on the calculation of plasma emissivity. The FS calculations are performed using four different minimum values of the mixing coefficient, $c_{\mathrm{i,min}}$, discussed in Eq. 6.1 and Table 6.3. The ATOMIC calculations are performed for an aluminum plasma with an electron temperature of 3 eV and electron density of 10^{21} cm^{-3} over an energy range of 70–75 eV (16.5–17.7 nm) with a resolution of 0.01 eV.

ensure a reasonable serial run time; and (4) the lower bounds are mostly captured within the EOS parameter space. For example, the databases generated for the pure aluminum runs presented in Chapter 8 have a temperature resolution of 0.01 eV from 0.1 to 2 eV, and a density resolution of 10 logarithmically spaced points per decade from 10^{14}–10^{22} cm^{-3}. The photon energy grid contains 501 points evenly spaced from 390–400 nm (inclusively), providing a resolution of 0.02 nm.

Line broadening mechanisms are also included as a capability within the ATOMIC code. Lines can be modeled with: (1) no additional broadening (natural line width); (2) Doppler, or thermal, broadening; (3) collisional broadening, in addition to Doppler broadening; (4) advanced collisional broadening using the D-K broadening routine [123], in addition to Doppler broadening; (5) Stark broadening for H- and He-like ions. For these near-neutral plasmas modeled in this dissertation, (5) is not applicable. Calculations using Doppler broadening only are most frequently calculated, as they typically proceed more quickly than calculations that also include collisional broadening. Turning on collisional broadening has value for LIBS-like plasmas where density gradients are minimal, as shown in [123], but has less utility for the beam-target interaction plasmas due to the extreme density gradient. In short, the lines tend to be significantly over-broadened to the point where spectral features are completely washed out, which is counter to the experimental results presented in both Chapters 7 and 8.

Parallelized runs of ATOMIC for generating single point (single energy) opacity tables across a grid of temperatures and densities is also useful for further post-processing of experimental data. This capability is discussed in more detail in Appendix B.

6.3 Finite-Element Spectral Transfer of Radiation (FESTR)

This section will discuss in detail the steps involved in building, running, and analyzing the results from the radiation transport model used to interpret the spectroscopic measurements made on the beam-target interaction plasmas. The FESTR code [6] is used to sample the 2-D structure of the LASNEX simulation via a ray-trace method to generate synthetic spectra and other relevant quantities, such as accumulated optical depth along the path traversed by a photon. The Los Alamos suite of atomic physics codes [117] is used to generate spectral databases that are accessed by FESTR during its process of calculating synthetic spectra.

6.3.1 FESTR Inputs and Outputs

The FESTR code is written in C++ and includes a number of different classes (formatted as mono spaced text) that define various objects relevant to the calculation of the synthetic spectral outputs. The details of these classes are explained in [6], but some highlights of the selected classes will be

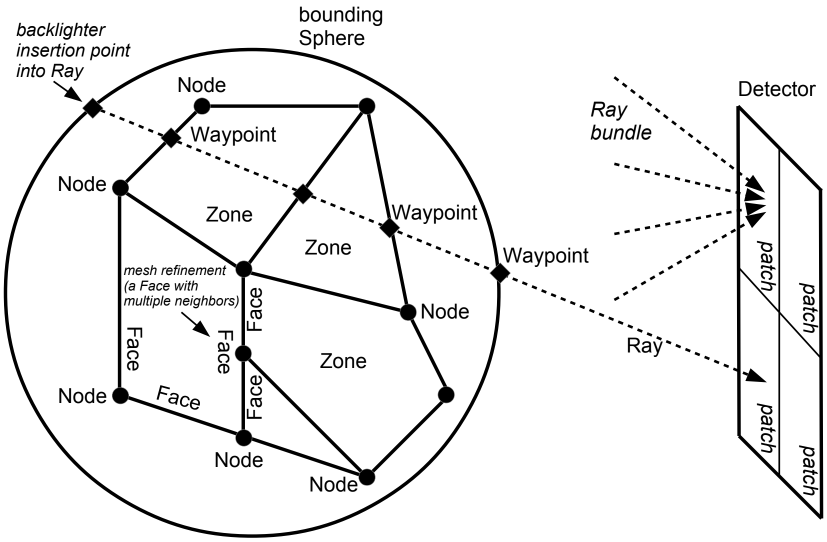

Figure 6.4: Schematic illustration of the three-dimensional geometric data structure of FESTR. Figure reproduced with permission from [6].

given here. The `Mesh` class consists of `Zones`, each of which is characterized by a uniform temperature, density, and material stoichiometry. `Hydro` holds material conditions within all `Zone` objects in the `Mesh`. A `Zone`, defined by its `Faces`, knows its neighbors which allows for the passing of the `Ray` between `Zones` during raytracing. The `Ray`, as it traverses the `Mesh`, knows its position and velocity vectors and carries with it the specific intensity (in units of W/cm^2/sr/eV) of its spectrum. The `Diagnostics` class defines a collection of `Detector` objects that define how the `Ray` is launched through the `Mesh`. A `Detector` can be defined to have several spatial patches that correspond to different lines of sight and, subsequently, will launch their own `Rays` to map their path through the `Mesh` until hitting the bounding sphere, at which point the direction is reversed and the spectrum is then accumulated as the `Ray` walks through the `Mesh` toward the `Detector` (as shown in Fig. 6.4). FESTR can also be run in tracking mode (turned on by an option when defining a `Detector`), where the spectrum accumulated by the `Ray` as it passes through each `Zone` along its trajectory through the `Mesh` will be printed to an output file. This powerful capability allows for the identification of the plasma conditions that contribute most strongly to the spectrum ultimately "seen" by the `Detector`.

The input deck for FESTR is relatively simple; it defines paths to all the relevant directories containing the material, hydro, database, diagnostics, and outputs, in addition to specifying the

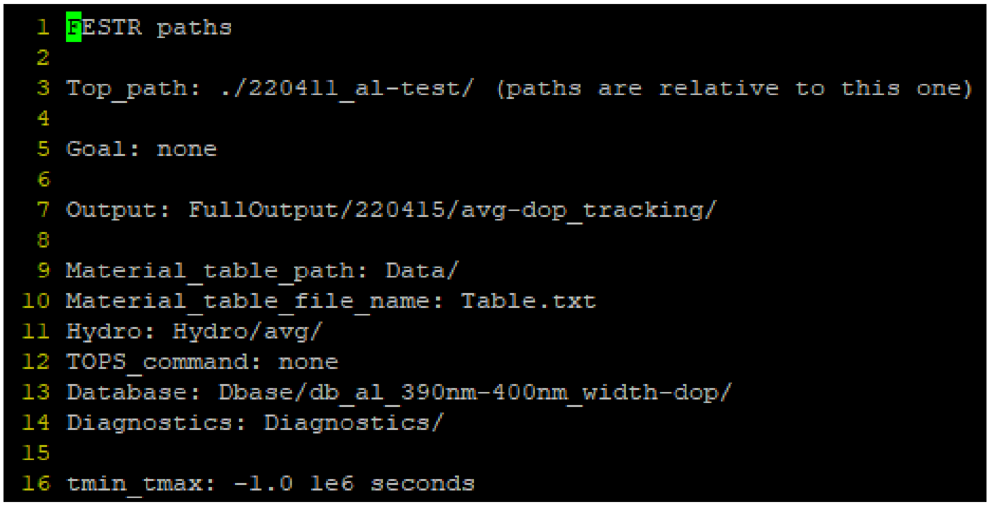

```
FESTR paths

Top_path: ./220411_al-test/ (paths are relative to this one)

Goal: none

Output: FullOutput/220415/avg-dop_tracking/

Material_table_path: Data/
Material_table_file_name: Table.txt
Hydro: Hydro/avg/
TOPS_command: none
Database: Dbase/db_al_390nm-400nm_width-dop/
Diagnostics: Diagnostics/

tmin_tmax: -1.0 1e6 seconds
```

Figure 6.5: Example FESTR input deck showing the paths and parameters defined by the user.

time window over which the model is run. An example input deck is shown in Figure 6.5. The simulation volume is contained within the bounding sphere. In short, the plasma lives fully within the bounding sphere at all times, and the `Detector` objects are created outside of the bounding sphere. Figure 6.4 shows a schematic illustration of the three-dimensional geometric data structures of FESTR. Note that, with the LASNEX data used in this dissertation, there does not exist the mesh refinement shown in Fig. 6.4; each `Face` of each `Zone` is uniquely neighbored with a `Face` from an adjacent `Zone`. The only exception to this rule is the construction of the bounding sphere, whose inner composite face consists of all the outermost-facing `Faces` that do not border any other material-containing `Zones` (i.e. the perimeter of the `Zones` nearest the bounding sphere in Fig. 6.4).

Along each `Ray`, FESTR solves the 1-D steady-state radiation transfer equation, which is expressed by the following:

$$\frac{dI_\nu(x)}{dx} = \epsilon_\nu(x) - \kappa_\nu(x)I_\nu(x), \tag{6.2}$$

where x is a spatial coordinate, $I(x)$ is the specific intensity, $\epsilon(x)$ is the emissivity, and $\kappa(x)$ is the opacity. The subscript ν denotes the fact that these quantities are all a function of wavelength. The general solution of Eq. 6.2 is:

$$I_\nu(x) = I_{B,\nu}e^{-\tau_\nu(B,x)} + \int_B^x \epsilon_\nu(t)e^{-\tau_\nu(t,x)}dt, \tag{6.3}$$

where the first term represents the specific intensity of the spectrum at the starting point B reduced by the optical depth by $e^{-\tau(B,x)}$, and the second term represents the accumulated spectrum over the path from B to x, also reduced by the optical depth. The optical depth τ is a unitless quantity

Ion	Configurations	Total Configurations	Total Levels
Na-I	Base: [Ne] $3s^1$ nl^1 through $n = 8$ $2p^5$ $3s^1$ nl^1 through $n = 5$ $2p^5$ $3p^1$ nl^1 through $n = 5$ $2p^5$ nl^2 through $n = 3$	43	478
Na-II	Base: [Ne] $2p^5$ nl^1 through $n = 9$ $2p^4$ $3s^1$ nl^1 through $n = 5$ $2p^4$ nl^2 through $n = 3$	41	649
Na-III	Base: $1s^2$ $2s^2$ $2p^5$ $2s^1$ $2p^6$ $2s^2$ $2p^4$ nl^1 through $n = 7$	21	419

Table 6.4: CATS *nl*-type configurations for sodium ($Z = 11$) ions, where a noble gas configuration of [Ne] ($1s^2$ $2s^2$ $2p^6$) is implied for all configurations unless otherwise shown. The base (zero energy) configuration for each ion stage is given for reference.

defined as the integral of the opacity (in units of cm^{-1}) along a path length ds:

$$\tau(t,x) = \int_t^x \kappa(s)ds. \tag{6.4}$$

The final accumulated spectrum, when running FESTR normally, is what the `Detector` object "sees" once the `Ray` finishes traversing the `Mesh`. When run in tracking mode, the outputs are the `Zone`-by-`Zone` evaluated results of the special uniform 1-D solution to Eq. 6.2, given by the following for a uniform medium of length L:

$$I_\nu = I_\nu^0 e^{-\kappa_\nu L} + \frac{\epsilon_\nu}{\kappa_\nu}\left(1 - e^{-\kappa_\nu L}\right). \tag{6.5}$$

6.3.2 ATOMIC Database Generation

The Los Alamos suite of atomic physics codes is used to generate spectral databases for use by the FESTR code. The spectral databases consist of emissivity, absorption, scattering, and degree of ionization values as a function of a user defined wavelength range across a grid of temperatures and densities. FESTR accesses these databases by first determining the T_e and n_e of the Zone under interrogation, then finds the corresponding nearest match to the T_e and n_e in the databases.

The configurations shown in Table 6.1 are used to generate the spectral databases for aluminum used in both Chapters 7 and 8. Table 6.4 shows the configuration list for sodium, used to generate the results shown in Chapter 7.

The following database generation details apply to the radiation transport model used in Chapter 7. A photon energy grid is used consisting of 2001 linearly spaced points ranging in wavelength from 585–595 nm, providing a resolution of 0.005 nm. Spectral databases for both aluminum (Al I–IV) and sodium (Na I–III) are generated over a temperature range of 0.25–1.5 eV (0.05-eV step). The aluminum runs use an electron density range of 10^{16} to 9×10^{21} cm^{-3} with nine points per decade for a total of 1404 runs. Here, each run represents a calculation at each unique T_e and n_e pairing. Doppler broadening is turned on, but there is no collisional broadening included for the aluminum runs as there are no spectroscopic lines of aluminum in this wavelength range of interest. The sodium runs use an electron density range of 10^{16} to 9×10^{18} cm^{-3} with nine points per decade for a total of 702 runs. Two sets of these runs for sodium are performed: one with Doppler broadening only, and the other with both Doppler broadening and the D-K collisional broadening routine [123].

The following database generation details apply to the radiation transport model used in Chapter 8. A photon energy grid is used consisting of 501 linearly spaced points ranging in wavelength from 390–400 nm, providing a resolution of 0.02 nm. Spectral databases for aluminum (Al I–IV) are generated over a temperature range of 0.1–2 eV (0.01-eV step). The runs use an electron density range of 10^{14} to 7.7×10^{22} cm^{-3} with nine points per decade for a total of 15,471 runs. Two sets of these runs for aluminum are performed: one with Doppler broadening only, and the other with both Doppler broadening and the D-K collisional broadening routine.

6.3.3 Oz, a LASNEX to FESTR Translator

FESTR is built to handle a 3-D unstructured mesh, allowing it to be flexible and use inputs from a variety of hydro codes. A pre-processor is used to format the hydro code dump files into a format that can be read by FESTR. In this case, the LASNEX radiation hydrodynamics simulations are performed with 2-D cylindrical symmetry, so the output files only include values in $+\hat{r}$ and $\pm\hat{z}$. So, this mesh from LASNEX along with its associated quantities (T_e, n_e, material stoichiometry, etc.) must be revolved about $\hat{z}$ to generate a fully three-dimensional mesh consisting of `Zones` bounded by `Faces` in the shape of conical ribbons that can be interpreted by FESTR's `Cone` objects (derived from the abstract class `Face`). The translator Oz is written for this purpose.

Figure 6.6 shows the general flow of data into and out of Oz. As stated, LASNEX outputs a hydro dump initially processed with a Yorick script [124] containing a grid of temperatures, densities, and material stoichiometry at multiple timeslices. The Python pre-processor code `pyReadMulti.py` reads and formats these files into text `t` files with a header that contains detailed information about the grid structure. A file called `times.txt` is also created that lists all the timeslices. This file is required by FESTR. Oz then uses these `t` files to produce the range of input files required by FESTR. These files include the following:

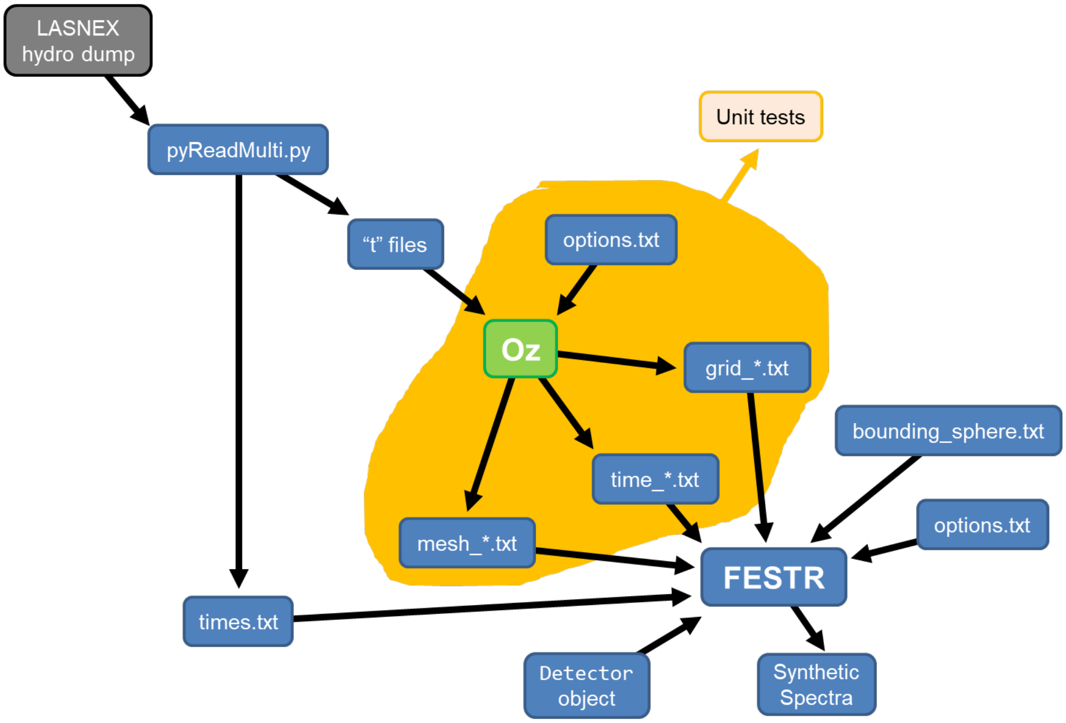

Figure 6.6: Oz flowchart.

1. `time_*.txt`: lists the plasma and material properties for each `Zone` at every time.
2. `grid_*.txt`: lists the locations (3-D vectors of position and velocity) of all of the `Nodes` (that define the `Zones`) at every time.
3. `mesh_*.txt`: defines the logical structure (`Zones` and `Faces`) of the `Mesh`; this mesh connectivity information is how all of the `Zones` will communicate with each other and pass `Rays` from one `Zone` to the next.

Here, the wildcard * indicates the time. FESTR then takes all of these files, in addition to some other files that are shown in Fig. 6.6, to actually perform the spectroscopic-quality radiation transport calculations.

Oz is a standalone code also written in C++ that uses many of the already existing classes written for FESTR. A new class, `OptionsParser`, is written to handle the commands contained within the input deck, the format and contents of which are shown in Figure 6.7. When running Oz, the user specifies which materials to include and a density floor that treats all `Zones` with densities less than this value as empty, to help speed up computational time.

The class `Mesh`, recycled from FESTR, is where the majority of the processing is done to properly format the `t` files into the time, grid, and mesh files discussed above. Figure 6.8 visualizes the

```
Oz paths and input parameters


========== P A T H S ==========         ================ D E S C R I P T I O N S ================

Top_path: ./al-na/                      All paths are relative to this one

Hydro_path: Hydro_pt89_1/               Path where all output files for FESTR will be written
                                        NOTE: must contain bounding_shpere.txt before running

T_file_path: t/                         All "t" files from pyReadMulti.py must be located here

Material_table_path: Data/              This should usually remain unchanged


===== P A R A M E T E R S =====

T_file_naming: Foil3715_100             Automatically adds "_*.t" to filenames

Hydro_type: lasnex_2Dcyl                Must be this

Number_of_materials: 4                  Equivalent to the variable nmat in pyReadMulti.py

Materials_of_interest: 0 0 1 1          Boolean list of materials to include from materials.txt

Density_floor: 1.0e14                   All densities less than this value will be set to 0.0

Number_of_timesteps: 415                Assuming starting timestep is 0 and is ++1 iterated
                                        NOTE: this value should be equal to the maximum timestep
                                          so it is actually equal to ONE LESS THAN the total
                                          number of timesteps

Material_table_file_name: Table.txt     This should usually remain unchanged
```

Figure 6.7: Example Oz input deck showing the paths and parameters defined by the user, along with their descriptions.

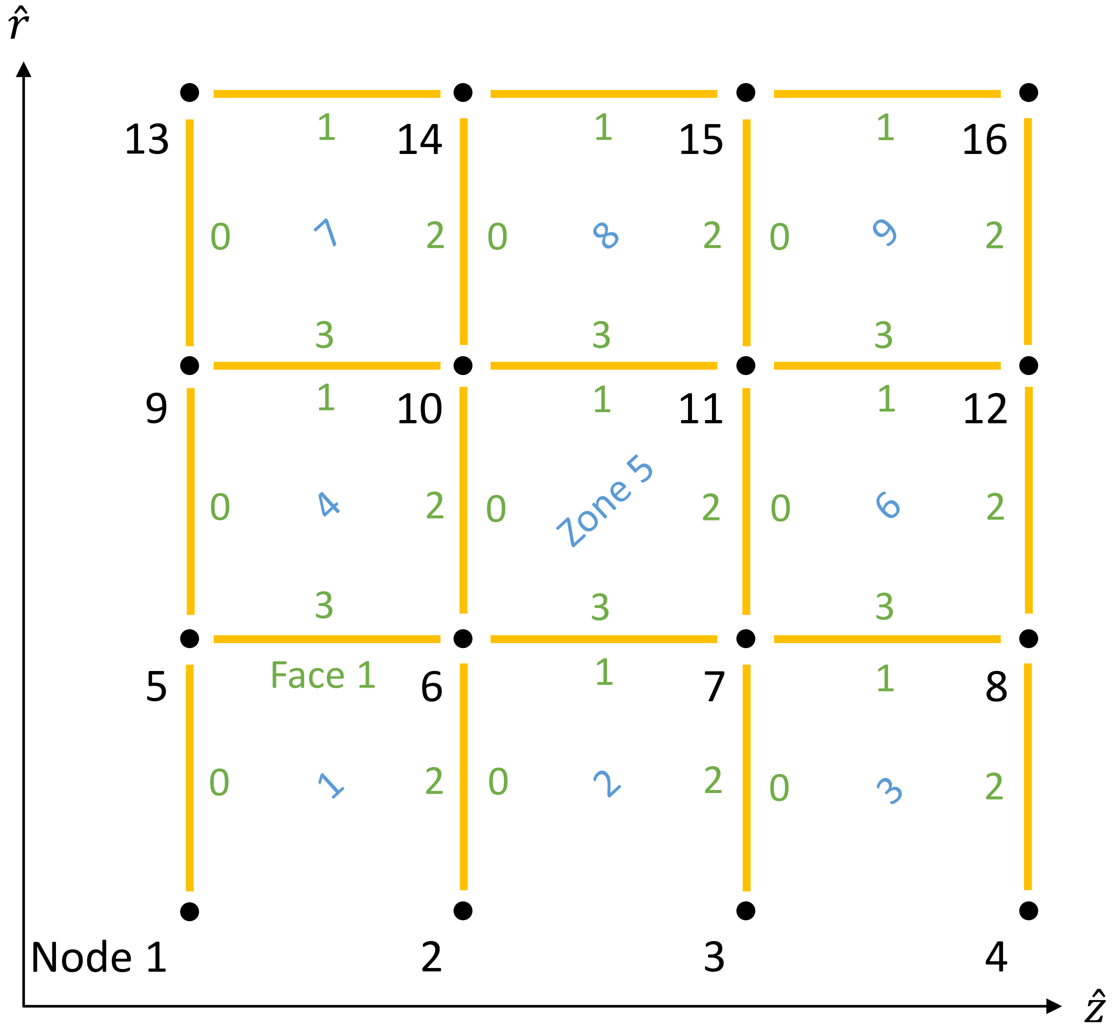

Figure 6.8: Illustration of the 2-D cylindrically symmetric geometry contained within the `t` files generated from pre-processing LASNEX dump files. `Nodes`, numbered as shown, are in black; `Faces` are shown in green; and `Zones` are labeled in blue. The volume enclosed by each `Zone` forms the shape of a toroid with a quadrilateral cross section. The bounding sphere, known as `Zone` 0 (not shown), is a sphere centered at the origin with a radius sufficient to fully enclose the spatial extent of the `Nodes`. The nomenclature for building the `mesh_*.txt` files from this geometry follows what is given in Fig. 6 of Ref. [6]. For example, the FaceID for `Zone` 4, `Face` 1 would read: (4, 1).

logic contained with Oz's `Mesh` class that allows it to translate the 2-D array of nodes from LASNEX into a fully 3-D mesh. Note that the `Zones` nearest the z-axis only have three `Faces` while all the other `Zones` have four `Faces`. In addition, the `Zones` are assigned their material properties based on the contents of the upper-right `Node` in the `t` files. In the `Mesh` class, the bounding sphere inner composite `Face` is first built by walking the perimeter of the `Zones` counterclockwise, accumulating the set of FaceIDs that uniquely identify the `Zone` label and `Face` label within its `Zone` (see Ref. [6], Fig. 6). Then, the code will iterate over the `Node` numbers, knowing *a priori* their spatial structure (total number of `Nodes`, number of rows, number of columns, etc.) based on the content of the `t` files. A `Zone` is created, followed by assigning the `Face` type (`Cone`), adding the `Nodes` that permit the definition of the `Face`, and telling that `Face` who its neighbor is. For example, as shown in Fig. 6.8, `Zone` 4 has four neighbors; three of its neighbors are other `Zones`, while the fourth is the inner composite `Face` of the bounding sphere, which is denoted as `Zone` 0, `Face` 1. The `Zone` is defined by `Nodes` 5, 9, 10, and 6. `Faces` are similarly labeled in a clockwise fashion. Written using the FaceID shorthand, where the first FaceID corresponds to `Zone` 4 and the second FaceID corresponds to its neighbor, the relationships are as follows:

1. (4, 0) ↔ (0, 1)
2. (4, 1) ↔ (7, 3)
3. (4, 2) ↔ (5, 0)
4. (4, 3) ↔ (1, 1)

Appendix C shows the README file for the Oz code, including usage and descriptions for all Oz-specific files and routines not found in FESTR. As illustrated in Fig. 6.6, a suite of Unit Tests is implemented to insure proper operation of the Oz code upon compilation.

6.3.4 Optical Depth Tracking Modification

Spectroscopic analysis of lines that requires measurements of the line widths and intensities are typically performed under the assumption that the lines originate from an optically thin plasma. As shown by Equation 6.3, the optical depth acts as an attenuation factor to the specific intensity of the spectrum. Opacity, and by extension the optical depth, is not only a function of temperature and density, but also a function of wavelength. For example, emission lines from the same element but from different ionization stages can have different optical depths; in short, at the same plasma conditions, one line may be optically thin while another is optically thick.

When a spectral line becomes optically thick, the intensity at the line center becomes reduced due to the SA of the emitted radiation by the other surrounding atoms due to the high opacity at

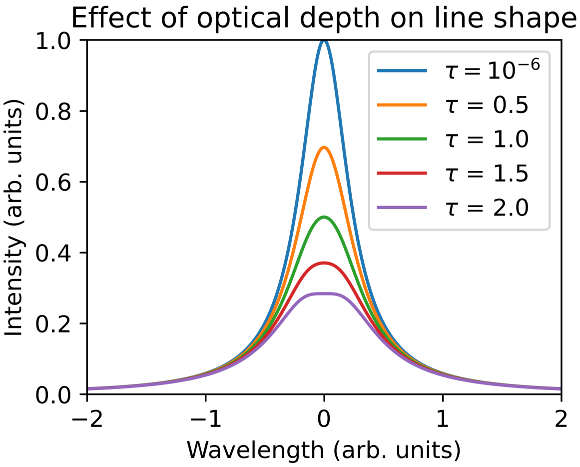

Figure 6.9: The effect of optical depth on line shape and height. $\tau = 10^{-6}$ is representative of an optically thin condition.

the line center. Figure 6.9 shows the effect of increasing optical depth on line shape and height. At an optical depth of $\tau = 1$, the line intensity is reduced by a factor of 2c, while the width is increased by a factor of $\sqrt{2}$. In extreme situations, this can result in a complete self-reversal of the spectral line, appearing as an absorbed line within a continuum [125]. These measurements are discussed in Chapter 7, where a sodium contaminant layer near the outer regions of the expanding beam-target interaction plasma plume produces D-line absorption features at 590 nm within an aluminum plasma continuum.

However, emission lines can still be measured from optically thick plasmas. Chapter 8 analyzes the measurements of the Al-I 394/396 nm resonance doublet from beam-target interaction experiments. The lines are observed almost always in emission, but due to the non-negligible optical thickness at the center of these lines, a simple Stark analysis of the line width in an attempt to determine n_e will significantly overestimate the actual value of n_e due to the reduction in intensity illustrated by Fig. 6.9. The smoking gun that these lines are exhibiting SA is the deviation of the doublet lines from their normal 2:1 ratio when optically thin; the stronger line (396 nm) exhibits more SA due to the higher opacity at that line center.

To uncover the correct n_e from the measurement, either a separate measurement of an optically thin line must be made to infer the effect of SA on the optically thick line, or the optical depth must be determined to then correct the inferred n_e from the optically thick line. The authors of Ref. [126] developed a method to correct for the effect of SA by simultaneously measuring both an optically thick line (Al-I 396 nm) and an optically thin line (H-α) via the SA coefficient SA using

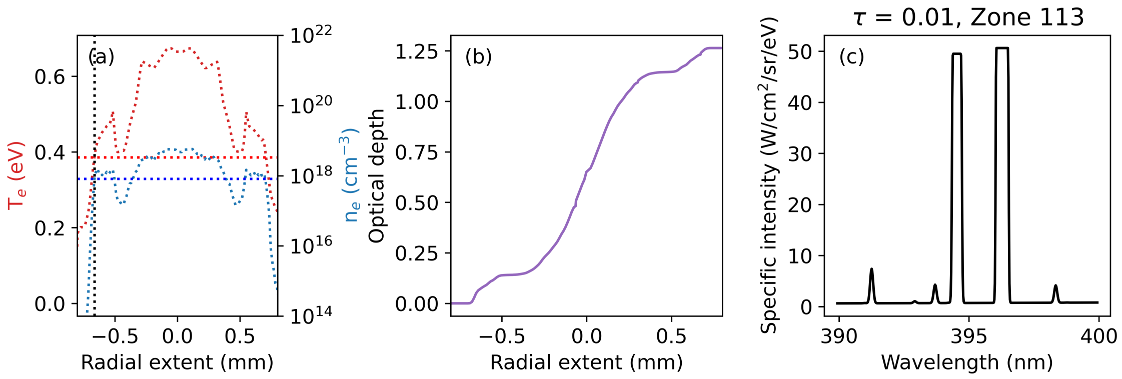

Figure 6.10: Optical depth tracking results and resulting spectrum from an aluminum plasma at a threshold optical depth value at the 396.152 nm line center of $\tau = 0.01$. The detector is located at a distance of $z = 4$ mm and is looking at the plasma parallel to $\hat{r}$. The `Ray` is traveling from $-r$ to $+r$. (a) Plasma T_e and n_e along the path of the `Ray`, with dotted lines marking the temperature (red), density (blue), and radial location (black) at which the user-defined optical depth threshold is reached. (b) Accumulated optical depth along the path of the `Ray`. (c) Accumulated spectrum corresponding to the threshold optical depth value.

the following relations:

$$SA \equiv \frac{1 - e^{-\kappa(\lambda_0)l}}{\kappa(\lambda_0)l} \tag{6.6}$$

and

$$\frac{\Delta\lambda}{2w_s} = \frac{n_e}{(SA)^{-\alpha}}, \tag{6.7}$$

where $\kappa(\lambda_0)l$ is the optical depth at the line center, $\Delta\lambda$ is the measured (uncorrected) line width, w_s is the Stark half-width, $\alpha = 0.54$, and n_e is the true electron density. By definition, $SA = 1$ for an optically thin plasma, and $SA \to 0$ for increasing optical thickness. In effect, the right hand side of Eq. 6.7 can be treated as an equivalent electron density n_e^*, which would be (incorrectly) inferred from a simple Stark broadening analysis. By applying the correction factor $(SA)^{-\alpha}$, the true n_e can be recovered.

For the sets of measurements presented in the subsequent chapters, no optically thin lines were able to be measured. Instead, the FESTR radiation transport model is used to determine the SA coefficient. As previously discussed, FESTR can be run in tracking mode, which provides spectra corresponding to each `Zone` traversed by the `Ray` as it crosses the `Mesh`. A simple modification of the output file contents from FESTR, when run in tracking mode to include the `Zone` values of T_e and n_e, allows for *a posteriori* calculation of the optical depth. A set of high resolution single-point (single energy) opacity databases generated for aluminum looking at the Al-I 3p-4s doublet line centers (3.1427 and 3.1288 eV) are generated (see Table B.5). These are used as look-up tables to infer the opacity for each `Zone` traversed by the `Ray` while in tracking mode. Then, knowing the spatial information contained within the `Ray` (i.e., path length), the accumulated optical depth is calculated. Figure 6.10 shows an example of the results for a pure aluminum plasma plume at a time of 300 ns. Even at the relatively low optical depth of $\tau = 0.01$ at $\lambda = 396.152$ nm shown here, the synthetic spectra is already showing features of SA, as seen by the line ratio no longer being 2:1. Another important note is the spatial origin of the spectrum; these lines are coming from the outermost region of this plasma and are not representative of the bulk plasma. The `Zone` at which the threshold optical depth value of 0.01 is reached has a temperature of 0.39 eV and an electron density of 8.1×10^{17} cm^{-3}.

At present, this calculation is only valid for 2-D, cylindrically symmetric plasmas with the `Ray` traversing along either $\hat{r}$ at a fixed z, or $\hat{z}$ at a fixed r. The proper modification, made within the raytracing routine of FESTR, will be completed in the near future and will be applicable to any arbitrary three-dimensional geometry. This will not affect the results of these calculations, and is instead intended as a generalization for any future applications of FESTR to other problems where optical depth tracking is of value.

6.3.5 Summary

This chapter describes the numerical simulation tools used to model the electron beam-target interaction experiments. The radiation hydrodynamics code LASNEX is used to model the energy deposition by the electron beam into the target foil and the hydrodynamic expansion of the plasma. LASNEX dump files provide information of the 2-D distributions of temperature, density, and material stoichiometry. The Los Alamos suite of atomic physics codes is used to perform *ab initio* calculations of the atomic physics processes relevant for generating spectral quantities like emissivity and opacity. These outputs, along with the hydro information, are used by FESTR to perform spectroscopic-quality radiation transport modeling of the spectra emitted by the synthetic plasma plume. The results of this model are compared directly with experimental measurements.

CHAPTER 7

Na Tracer Measurements

7.1 Introduction

Electron beam driven WDM production on an electron LIA results in a strong bremsstrah-lung and scattered electron background, and diagnostics are being actively developed to perform measurements in the warm dense phase. The diagnostics presented in this chapter are in the visible regime and are measuring the plasma after it hydrodynamically expands into a dense, classical-like plasma with a coupling of $\Gamma \approx 0.2$ and a degeneracy of $\Theta \approx 270$ [3,68]. Visible measurements are limited by opacity effects, and thus they only quantify the surface, rather than the bulk, plasma conditions. These measurements are therefore sensitive to any spectroscopically significant contaminants that may be present on the foil surface, most notably sodium.

In this chapter, we present measurements of sodium absorption lines (D-lines) present within the continuum generated by an expanded dense aluminum plasma plume. The plasma is generated by focusing an intense, relativistic electron pulse with a kinetic energy of 19.8 MeV, beam current of 1.45 kA, and FWHM of 80 ns to a 1-mm-diameter spot on target [69, 89, 93]. The heating and hydrodynamic transitions from solid density, to dense plasma, and eventual classical plasma are shown in Figure 7.1. The beam deposits a small fraction (5.4 J) of its total energy (2.3 kJ) into a range-thin 100-μm-thick Al foil. This low efficiency is due to the electron range (3.9 cm) being more than 300× the foil thickness. A simplified 2-D spectroscopic-quality radiation transport model has been constructed to interpret the plasma conditions based on the intensities and ratio of the absorbed Na 3p-3s lines. X-ray Photoelectron Spectroscopy (XPS) and Laser-Induced Breakdown Spectroscopy (LIBS) analysis techniques are used to verify and quantify the sodium contaminants on the aluminum foils.

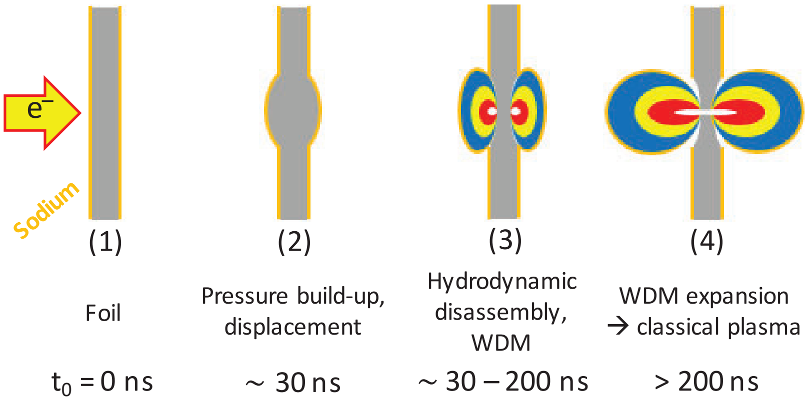

Figure 7.1: Electron beam driven WDM production. Approximate timescales for ∼100-μm-thick foils are given for reference, where t_0 is the start of energy deposition. (1) The intense, relativistic electron beam is focused down to a small spot on the Al foil (gray) containing a surface contaminant (Na, orange). (2) Energy deposition results in a pressure build-up and displacement of the foil. (3) Hydrodynamic disassembly of the foil material and transition into the WDM stage. (4) Vacuum expansion of the WDM, which transitions later in time to a classical plasma. Spectroscopy measurements are presently being made temporally in and around (4).

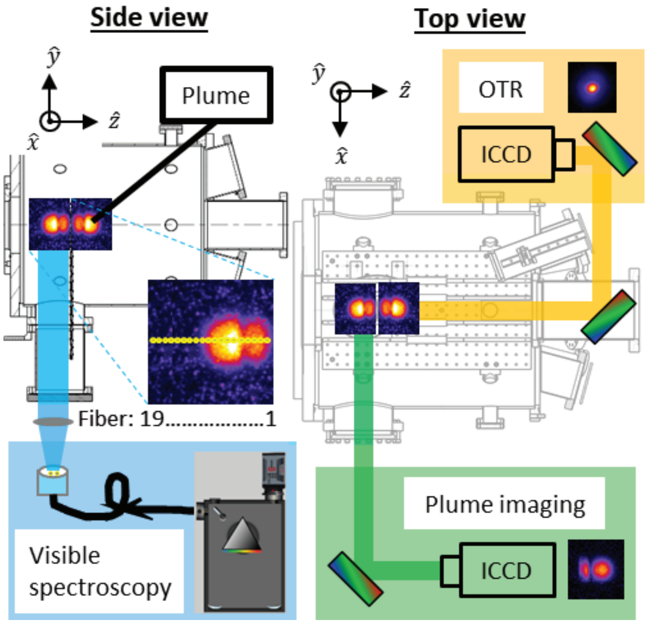

Figure 7.2: Two views of the target diagnostic chamber configuration for visible absorption spectroscopy (blue), plume self-emission imaging (green), and near-field OTR imaging (orange). The target foil lies in the $\hat{x}$–$\hat{y}$ plane and the electron beam travels in the $\hat{z}$ direction. The OTR turning mirror sits 15° above the beam axis. Note that the coordinate system is left-handed. This configuration is the legacy configuration shown in Fig. 4.9.

7.2 Experimental Configuration

These experiments are conducted using an electron beam to heat 100-μm-thick Al 1100 alloy foils [127]. As illustrated in Figure 7.1, the energy deposited into the foil causes the material to heat, undergo phase transitions from the solid-state to the plasma state, and expand hydrodynamically into the surrounding vacuum. The expanding plasma initially near solid density is opaque to visible light, which limits visible spectroscopy to later-time measurements, when the plasma begins to transition to $n_e < 10^{19}$ cm^{-3}.

Three separate beam and plasma diagnostics are shown in Figure 7.2, corresponding to the legacy configuration shown in Fig. 4.9. More detailed information on each diagnosic is provided in Chapter 4. Near-field OTR is used to measure the beam spot size at peak focus for energy density quantification. This is required for comparison with a hydrodynamics code, as described in Section 7.3. Visible plume self-emission imaging using a gated intensified CCD camera provides measurements of the plasma plume size [3, 68]. A series of time-gated images yields a rough estimate of the plasma plume axial expansion velocity, subject to CCD sensitivity, dense plasma cutoff effects, and target paddle deflection in $\hat{z}$ (12 mrad).

Visible spectroscopy is performed on the upstream side of the target using a lens-coupled 19×200-μm-diameter linear fiber array oriented orthogonal to the foil surface (parallel to $\hat{z}$). A system magnification of 0.6 is achieved using a 180-mm focal length lens, resulting in a 7.68 mm axial coverage by the fiber array in the object plane. The 10-meter-long fiber bundle is fed into a 0.3-m focal length Czerny-Turner spectrometer (f/3.9) containing a triple-grating turret (150 grooves/mm, 500-nm blaze; 1800 grooves/mm, 500-nm blaze; 2400 grooves/mm, holographic) [128]. All sensitive electronics (computers, CCDs, etc.) are staged approximately 2.4 meters away from the target diagnostic chamber to minimize potential radiation effects by the bremsstrahlung produced during the electron beam pulse.

7.2.1 Measured Spectra

The energy density throughout the duration of the beam is quantified with near-field OTR. Figure 7.3 shows a 5-ns gated image of the flat-top beam distribution on the aluminum target, 30 ns after the beginning of the beam pulse. The FWHM = 0.62 mm corresponds to a fluence of 190 kJ/cm^2. This results in isochoric heating of the solid foil until the pressure releases and the material begins to hydrodynamically disassemble [79]. The heated material is now a dense plasma and the electron beam continues to deposit energy into the expanding plasma plume.

Figure 7.4 details the plasma expansion using orthogonal visible self-emission plume imaging. The plume imaging shows cutoff effects from 50–150 ns likely due to the dense plasma that is opaque to visible photons. Plume ion expansion velocities and electron plasma temperatures are

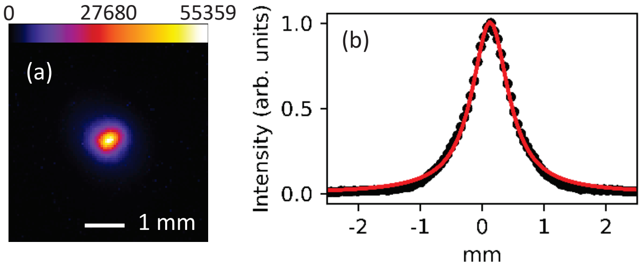

Figure 7.3: Near-field OTR measurement on shot 28891. (a) Raw image with a color bar for the counts. (b) A Lorentzian fit of the spot shown in (a) provides a beam spot FWHM = 0.62 mm. The CCD resolution of the target is 54 μm/pixel.

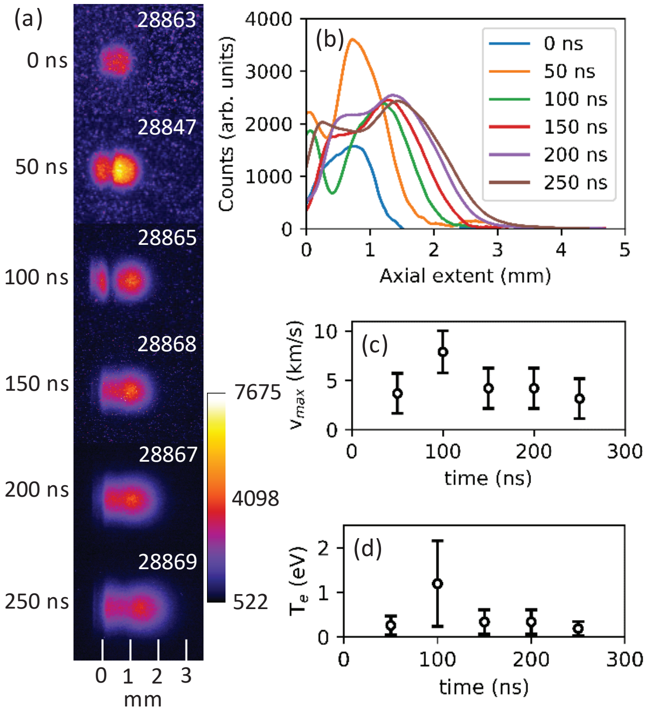

Figure 7.4: Plume imaging sequence of shots showing plasma expansion and SA. (a) The 50-ns gated image series beginning at t_0 = 0 ns. (b) The integrated axial intensities for the images shown in (a). (c) The axial expansion velocity of the plume ions. By treating the expanding plume as an ideal gas, the temperature can be inferred and is shown in (d).

estimated by treating the plume as an ideal gas ($\gamma = 5/3$) expanding into a vacuum [3, 78]. The leading-edge velocity is calculated using the FWHMs in Fig. 7.4(b), from which the electron temperature (T_e) is calculated using the relation given in Eq. 2.6: $c_s = \frac{\gamma-1}{2}v_{\max} = \sqrt{\frac{\gamma k_B T_e}{m}}$, where m is the mass of the aluminum atom and c_s is the ion sound speed. We wish to emphasize that these $v_{\max}$ and T_e measurements are treated as rough order-of-magnitude estimations: we can say with certainty that the plasma plume has a $T_e \approx 1$ eV, based on previous measurements of other low-Z materials [3, 68, 79]. As previously mentioned, new diagnostics to more accurately assess plume extent (up to opacity limits) are actively being developed and will be used in lieu of this self-emission plume imaging diagnostic for future measurements.

Three separate Al 1100 alloy foils were used as targets, with an average of seven shots per foil. Pilot desorption shots were first taken on each foil by defocusing the electron beam on the target face, which resulted in an incident fluence less than the melt phase transition. Subsequently, a spectral survey was performed and showed the presence of the Na D-lines absorbed on the Al continuum. Sodium absorption lines were clearly observed on 12 separate shots across the three different foils, confirming the reproducibility of the dataset.

A spectral survey of the plasma plume, shown in Fig. 7.5(a), shows strong continuum emission in the visible, perturbed by the Na D-lines near 590 nm. Figure 7.5(b) shows the absorbed D-lines beginning 200 ns after the start of energy deposition, where several fibers are clearly illuminated, with Fiber 6 and Fiber 10 located 2.1 ± 0.4 mm and 3.8 ± 0.4 mm upstream of the aluminum target face, respectively. The speckle present on the CCD for both Figs. 7.5(a) and (b) is due to charge deposited on the detector from the radiation background, and it is enhanced due to the increased gain. The increasing plasma density toward the foil surface results in decreased continuum levels (nearly 3× from Fiber 10 to Fiber 6), as shown in Fig. 7.5(c). The set of illuminated fibers is in reasonable agreement with the plume self-emission imaging data presented in Fig. 7.4(b), which has a FWHM of approximately 2.2 mm beginning 1 mm from the foil surface (note that fibers at axial distances ranging from 1.3–4.6 $\pm$ 0.4 mm have some level of continuum emission present).

Stark broadening is used to quantify the local surface plasma density using the absorbed Na 3p-3s doublet. Stark broadening is the dominant line broadening mechanism as the instrument width is < 0.20 nm and the Doppler width at 1 eV is 0.01 nm. In addition, the line profiles are not measurably Doppler shifted by the plasma motion. A total of six shots are fully analyzed to determine Stark widths as a function of axial distance from the foil surface. The following timeslices are referenced to the amount of time elapsed from the beginning of energy deposition: ($t_0 + 100$ ns) shots 28891 and 28894 illuminated Fibers 6–10, ($t_0 + 200$ ns) shots 28847, 28890, and 28895 illuminated Fibers 6–11, and ($t_0 + 300$ ns) shot 28889 illuminated Fibers 6–10. Stark widths of w_m = 0.180 and 0.185 Å/10^{17} cm^{-3} measured at a temperature of 15000 K are used for the 588.995 and 589.592 nm lines, respectively [7, 8]. In Figure 7.6, the data show that, as

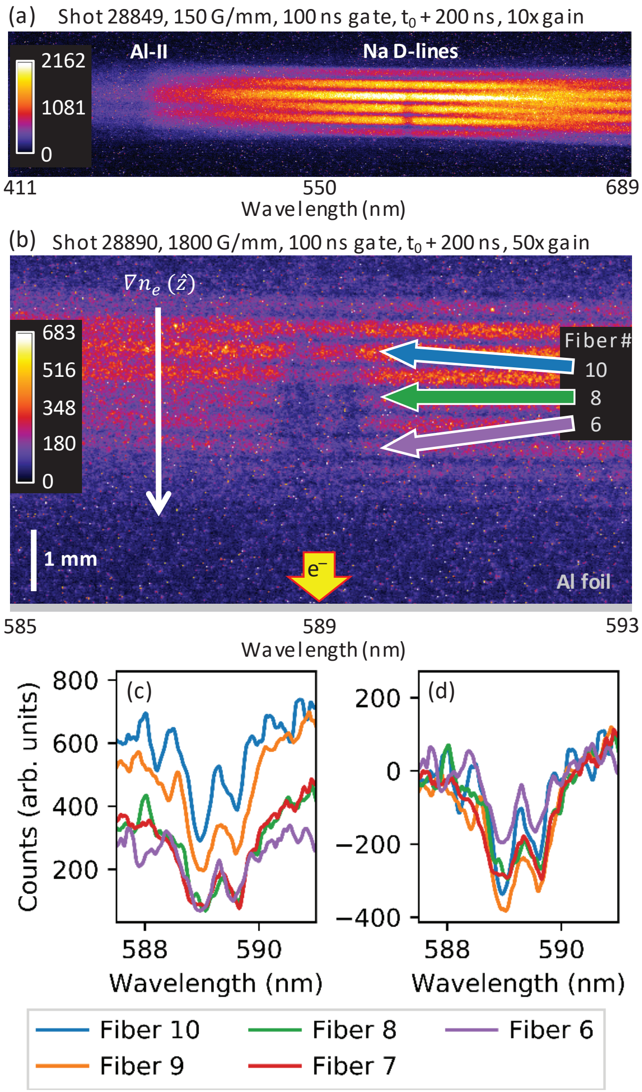

Figure 7.5: Measured spectra: (a) Low groove density (150 grooves/mm), spectral survey establishing the continuum within which the Na D-lines are absorbed. (b) High groove density (1800 grooves/mm) measurement focusing on the D-lines, both of which are clearly resolved. The time gate of both images is 200–300 ns after t_0. The aluminum foil surface and direction of the electron beam is also indicated. Lineouts of selected fibers indicate a significant variation in (c) the continuum intensity and (d) profiles of the absorbed D-lines. The peak line ratios for Fibers 6–10 are as follows: 1.17:1, 0.95:1, 1.06:1, 1.10:1, and 1.31:1.

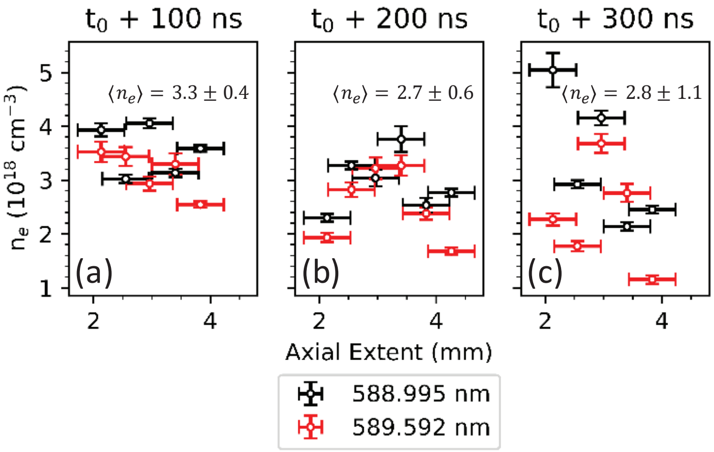

Figure 7.6: Calculated electron densities (inferred from Stark widths for the 588.995 and 589.592 nm lines) across several well-illuminated fibers and three different timeslices. The densities in (a) and (c) decrease as the distance from the foil surface increases, while (b) shows a maximum around 3.5 mm. The spatially-averaged electron density $\langle n_e \rangle$ trends to lower values at increasing times. The error bars shown for the inferred Stark electron densities are the standard errors from the Voigt fitting procedure. They do not include the 20% error bar from the documented Stark widths [7, 8] which are used to convert the FWHMs into electron densities.

time increases, the surface plasma density generally evolves to lower densities. However, the trends of the two lines do not agree completely. Averaging $\langle n_e \rangle$ across all three timeslices gives $3.0 \pm 0.8 \times 10^{18}$ cm^{-3}. We are not claiming that this density constitutes the bulk plasma; it is only representative of the outermost layer of the plasma from which the measured photons are able to escape and reach the detector.

While the plasma is in LTE [120, 129, 130], the absorbed D-lines are saturated due to the large density from which they originate, meaning the expected optically thin line ratio of 2:1 given by the Einstein coefficients no longer holds true. This behavior is exhibited by the spectra in Fig. 7.5 and will be further elaborated on in Sec. 7.3.2.

7.3 Spectral Modeling

A simplified spectroscopic-quality radiation transport model has been created to interpret the experimental spectra observed in Fig. 7.5. The model integrates several codes to accomplish this task, including radiation hydrodynamics (LASNEX [110]), radiation transfer (FESTR [6]), and the Los Alamos suite of atomic physics codes [117], which includes atomic structure (CATS), ionization (GIPPER), and atomic kinetics (ATOMIC). Previous aluminum-only runs using SESAME EOS 3715 [113] provided the basis for this model. While referred to as aluminum-only, they did in

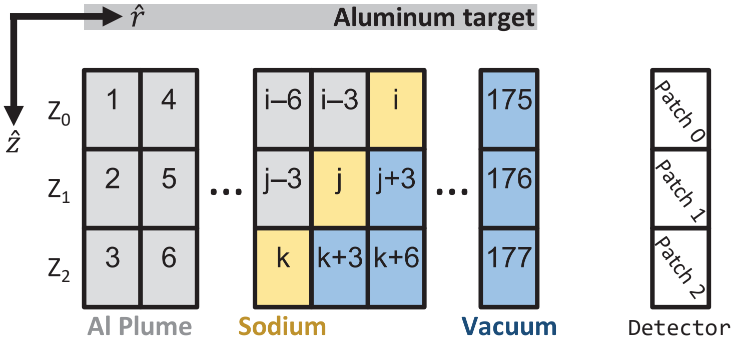

Figure 7.7: Illustration (not to scale) of the truncated hydro geometry used in FESTR with the zones numbered as shown. The foil is centered at $z = 0$. The IDL routine extracts the desired chordal lineouts (Z_0, Z_1, Z_2) from the full hydro output file. In this simplified model, the Na is placed at the outermost zone (maximum value of r) that contains aluminum, which borders the vacuum-containing zones. This distance is different for each lineout. The zones are revolved about the Z-axis to form toroids with quadrilateral cross-sections. The detector is constructed with three patches, which correspond to the chordal lineouts.

fact include a layer of water vapor on the foil surface, the presence of which is consistent with past experimental measurements [77]. An overview of how the LASNEX model is constructed is given in Sec. 6.1. For the analyses presented herein, we have found that it suffices to examine the individual axial slices immediately adjacent to the foil surface while hard-coding the sodium concentrations at each location. A full-scale 2-D cylindrically symmetric hydrodynamic model of the plume expansion after heating by the electron beam, including the sodium presence, would be the most accurate approach; however, this is not trivial and will take a significant number of iterations to ensure correct material evolution. Such a model is described in Chapter 8.

7.3.1 Model Description and Physics

The aluminum-only radiation hydrodynamics model is run in LASNEX to 400 ns with a 1-ns timestep containing >20,000 zones. The contents of these output files at each timestep include the electron temperature, ion temperature, electron density, elemental number densities, total mass density, and velocity at each node. An IDL script is used to extract the desired axial locations at a given timeslice from a hydro output file while interpolating the previously mentioned quantities along the radial extent [124]. This is required due to the evolution of the mesh as the simulation progresses in time.

Figure 7.7 illustrates the layout of the zones and detector used in FESTR, which employs a ray-trace method to sample the 2-D structure of the LASNEX simulation to generate synthetic spectra. The sodium is placed in zones *i*, *j*, and *k* for axial slices located at Z_0, Z_1, and Z_2, respectively.

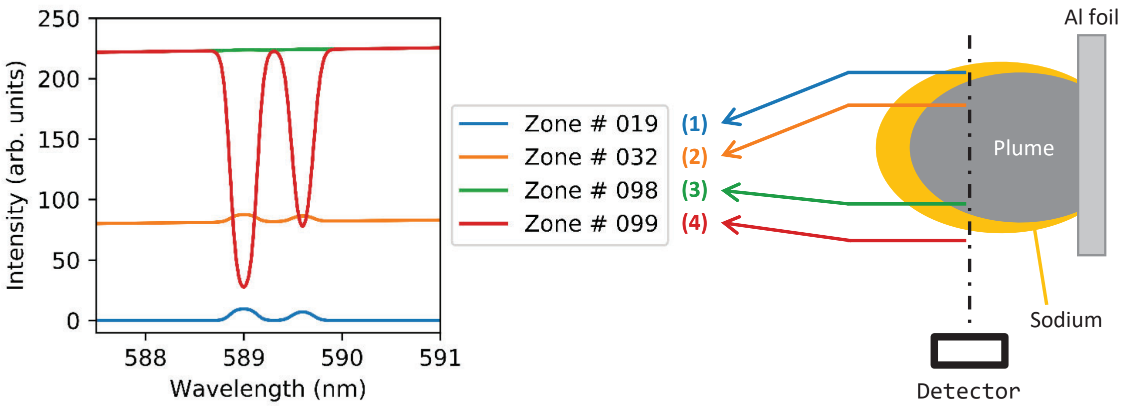

Figure 7.8: Physical description of how the Na absorption lines ($n_{\mathrm{Na}} = 10^{16}$ cm^{-3}) within the Al continuum are formed from the perspective of a photon traveling from top to bottom along the ray path (dash-dot line). (1) Optically thin emission of D-lines. (2) D-line emission on an increasing Al continuum. (3) Dominant Al continuum all but covers D-line emission. (4) Absorbed, saturated D-lines within a strong Al continuum. Note that these zone numbers are different than those shown in Fig. 7.7.

The detector is built with patches located at each axial slice at a radius beyond the radial extent of the plume. We run FESTR with its tracking feature enabled, which records local spectra at the position of every zone and in the direction of the traversing ray. This approach allows for a detailed understanding of how the spectra observed for each chord are built up and what parts of the plasma contribute significantly to the final measured spectra.

Spectral databases are generated using the ATOMIC code for both sodium and aluminum over the relevant temperature range (0.25–1.5 eV; 0.05-eV steps) and electron density range (10^{15}–10^{21} cm^{-3}; ten points per decade) from the hydro model. Note that CATS calculates the level energies and transitions *ab initio*, so these values will not identically match the NIST tables [107], but they are corrected by hand for experimental comparison. FESTR is then run to solve the radiation transport equation for photons as they pass through the simulated plasma plume. The current database is constructed by ATOMIC using no Stark broadening, so it is expected that the line widths produced by this model will not match experiment. However, the goal of this model is to match the line ratio and intensities, which are a direct function of the level populations that form the absorbed lines, in addition to any opacity effects that may impact the spectra formation. A good match of these quantities implies that the concentration of sodium atoms within the aluminum plasma plume is accurately captured.

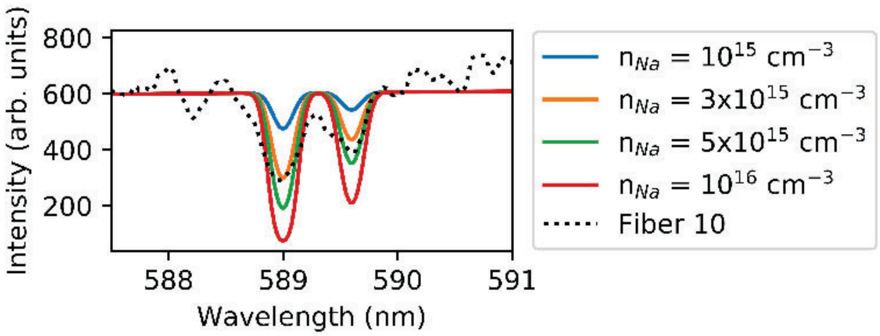

Figure 7.9: Comparison of experimental results from Fig. 7.5(c) with the 1-D radiation transport model. The most reasonable peak intensity comparison is obtained with a Na density of 3×10^{15} cm^{-3}. The line ratio calculated from the experimental data is 1.31:1. A density of 10^{16} cm^{-3} yields a simulated line ratio of 1.36:1, which best matches the measured line ratio.

7.3.2 Results and Comparison With Experimental Measurements

The tracking capability of FESTR is displayed in Figure 7.8, where we see how the spectra are formed as the ray passes from the far side (relative to the detector) to the near side of the plasma plume (transport from the top to the bottom of Fig. 7.8). At the outermost section of the plasma, the D-lines are observed in emission (blue trace, Fig. 7.8). When beginning to transit through the plasma, the lines are still being emitted but are superimposed on an increasing continuum due to the background aluminum plasma (orange trace, Fig. 7.8). Just before the ray exits the plasma, the continuum level is strong enough to dominate the D-line emissions (green trace, Fig. 7.8). Finally, once the ray escapes the plasma, the photons transit through the thin layer of sodium. The photons with energies corresponding to the D-line energies are absorbed, forming the final spectra observed by the detector (red trace, Fig. 7.8).

Figure 7.9 compares Fiber 10 from Fig. 7.5(c), located at an axial distance of 3.8 ± 0.4 mm from the foil surface, with four different sodium concentrations used in the radiation transport model. A sodium ion density of 3×10^{15} cm^{-3} shows the most reasonable agreement with the line intensities. However, a sodium ion density of 10^{16} cm^{-3} gives a line ratio of 1.36:1, which best matches the experimental line ratio of 1.31:1 with an error less than 4%. The line ratio, when further investigated using the radiation transport model, relaxes to the optically thin LTE ratio of 2:1 at sodium ion densities $\leq 10^{14}$ cm^{-3}. When the ion density is $\geq 5 \times 10^{16}$ cm^{-3}, the absorption lines are fully saturated, giving an effective ratio of 1:1. It is clear that the line profiles of the absorbed D-lines show a strong sensitivity to the concentration of sodium atoms present.

Calculated from the LASNEX results, the line-averaged ion density of the bulk aluminum plasma from 200–300 ns is 1.1×10^{21} cm^{-3} with an average ionization of $\overline{Z} = 0.48$. The temperature and density gradients seen at the given axial slice used to generate the synthetic spectra given in Fig. 7.9 remain relatively the same across the 100 ns window. In particular, the line-averaged electron (and ion) densities across three relevant timeslices (200, 250, and 300 ns) only vary by $< 10\%$, while the line-averaged electron temperatures are all within 3% of the time-averaged electron temperature of 0.37 eV. This demonstrates that the minimal error introduced by the time-integrated spectrometer measurement is negligible compared with uncertainties in the temperatures in Fig. 7.4(d) and electron densities in Fig. 7.6.

Note that the conditions of the bulk plasma satisfy the required conditions for LTE, despite the Na D-line ratio not appearing in the expected optically thin LTE ratio of 2:1. This is a result of the large level populations of the ground state Na-I atom, which result in the resonant D-lines being optically thick. However, collisional processes still regulate the level populations, justifying the LTE approximation [120, 129, 130]. Based on the time-averaged $\langle n_e \rangle$ from Sec. 7.2.1, and on the $\overline{Z}$ and best-fit $\mathrm{n_{Na}}$ from the model, we can infer locally the relative concentration of sodium atoms by dividing the sodium ion number density by the total ion number density. This yields an atomic concentration of $0.05 \pm 0.02\%$.

7.4 Sodium Contamination Quantification

After observing the Na lines experimentally from the electron energy deposition on the Al foils, we wish to understand the origin and the amount of Na in the Al foil. XPS and LIBS are used as complementary measurements to quantify the location and amount of the Na contaminant. XPS uses a source of monoenergetic X-rays incident upon the foil surface from which photoelectrons are emitted with energies characteristic of their originating atom's binding energy. By contrast, LIBS focuses a laser onto the foil surface, rapidly heating and ablating some of the material into a low-temperature plasma. This plasma acts as a source of emission lines from the atoms that make up the plasma. These diagnostic tools yield elemental composition information from two fundamentally different processes. XPS will be sensitive to all elements that have electron binding energies less than the incident X-ray energy. LIBS is more limited in that the temperature (and density) of the plasma generated will determine the type of emission lines to escape the plasma and ultimately be detected.

7.4.1 LIBS Measurements

LIBS is used to identify contaminants present on and within the aluminum foils. A 100-mJ, 8-ns Nd:YAG laser [131] operating at its fundamental frequency and rep-rated at 5 Hz is focused onto the sample material in a 300-μm spot. The resulting energy deposition results in material ablation and heating to approximately 1 eV. This plasma is generally optically thin and produces emission lines characteristic of its constituents. An Echelle spectrograph is paired with a Raptor Photonics Electron Multiplying CCD to record the spectra over a wavelength range of 200–1000 nm [132]. The detector delay relative to the laser pulse is 1 μs, while the gate width is 5 μs. The experimental configuration is nearly identical to the second setup described in Section 3 of Ref. [120].

Three different foil samples (100-μm-thick, 99.999% pure Al [133]; 50-μm-thick Anodized Al [134]; and 100-μm-thick Al 1100 alloy [127]) were prepared for analysis using identical methods. The 1100 alloy was used for the electron beam heating experiments described in Section 7.2.1, while the others are used as comparison for sodium quantification and documentation as potential future target materials. Note that an elemental analysis provided by the manufacturers of the Al 1100 alloy foils and 99.999% pure Al foils do not measure sodium as a trace element. An ethyl alcohol wipe-down was performed using Kimwipes [135] while wearing nitrile gloves [136]. Care was taken to handle the foils only by the edges and to not touch them in the middle of the surface where the analysis would be performed. Each sample was wrapped in Kimwipes and placed within plastic cases for transport to the LIBS laboratory. In the LIBS laboratory, the cases were opened, and the samples were unwrapped and placed on the substrate mount using cleaned metal tweezers to carefully grasp only the corners of the foils.

The resulting spectra were analyzed after multiple groupings of 10 laser shots. Based on the laser parameters and the reflectivity of aluminum, it is estimated that each laser pulse bores approximately 800 nm into the material. By taking many 10s of shots, an effective depth profile of the elements present can be determined. We expect to see the neutral aluminum lines corresponding to the 3p-4s doublet (394.401 nm, 396.152 nm) and 3p-3d triplet (308.215 nm, 309.271 nm, 309.284 nm) to dominate the spectra. We also expect contributions from sodium (principally the strong D-lines, based on measurements in Figs. 7.5 and 7.9), in addition to other vacuum surface impurities like carbon, nitrogen, and oxygen. The lines are identified and matched to the measured spectra using the NIST Atomic Spectra Database [107].

Figure 7.10 shows the results for two lines of interest: (a) Al 396.152 nm (3p-4s) and (b) Na-I 588.995 nm (3p-3s). The data were numerically integrated across the lines to investigate how the intensities varied as a function of depth into the material. As expected, across all three materials, the intensity of the Al line increases further into the sample. Although the trends are different, this behavior supports the argument that the bulk of the material is dominated by Al. This trend is followed by the other prominent Al-I lines at 394.401 nm, 308.215 nm, 309.271 nm, and 309.284 nm, with the only variation being in the relative amplitudes. Conversely, the Na D-line intensity decreases into the samples. Beyond 30 shots for the pure Al sample, the Na 588.995 nm line intensity was in the noise, so no further data were collected. This suggests that the Na contamination is limited to the surface for the pure Al foil. However, there is still significant

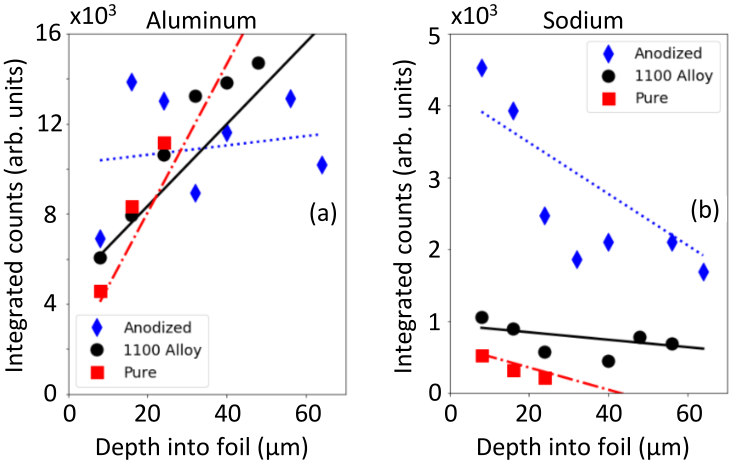

Figure 7.10: LIBS results for the three different Al foils. Plotted are the integrated line intensities and linear regressions as a function of foil depth for (a) the Al-I 396.152 nm line and (b) the Na-I 588.995 nm line. Note the scale difference. The line intensity is proportional to the amount of that element which is present. The Al linear fits show, as a function of increasing foil depth, an increase in the Al presence. The Na data show that the pure foil only has Na contamination on the surface, while the alloy and anodized foils still have a significant amount of Na well within the bulk of the material. This behavior indicates that the pure foil is indeed chemically pure through the bulk, whereas the alloy and anodized foils have Na as both a surface and a bulk impurity.

D-line intensity observed well into the alloy and anodized Al foils, potentially indicating that the Na contamination could be both a surface and a bulk contaminant.

Figure 7.11 shows an overlay for the three different samples of the 3p-4s Al doublet (a.1–3), 3p-3d Al triplet (b.1–3), and the Na D-lines (c.1–3) from selected groupings of 10 shots corresponding to depths of approximately 0–8 μm, 8–16 μm, and 32–40 μm into the material. These spectra were background-subtracted before analysis to remove the Echelle grating artifacts at longer wavelengths as well as the Hg-I lines from ambient light. Note that in (b.1–3) the 309.271 nm and 309.284 nm lines are not resolved and appear as a single broad line. Further inspection of the Al-I lines shows that the plasma created by the LIBS laser varies from sample to sample; the anodized Al foil shows lines with larger wings than both the pure and alloyed Al samples. This could be due to the laser coupling more energy into the foil during the ablation process. This hypothesis is supported by the qualitative observation during the experiments that the popping sound produced by the shockwave of the expanding plume is louder for the anodized foil compared with the pure and alloy foils.

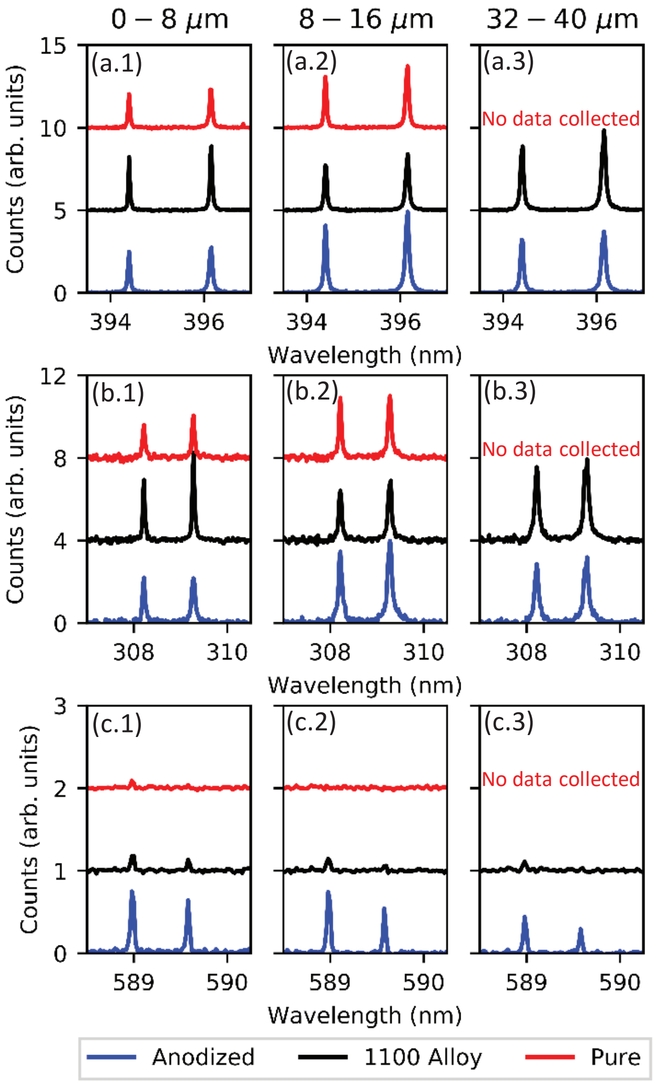

Figure 7.11: Measured line profiles for the Al-I 3p-4s doublet (top row), Al-I 3p-3d triplet (middle row), and Na 3s-3p doublet (bottom row) at depths of 0–8 μm, 8–16 μm, and 32–40 μm. The lines for the three foils are vertically shifted to better show the differences between the intensities. All plots are identically scaled showing the Al-I lines are approximately 5× more intense than the Na-I lines, and the Al-I 3p-4s lines are slightly stronger than the Al-I 3p-3d lines. Note that the pure Al sample had shots taken no further than 16–24 μm deep so the third column presents data only for the anodized and alloy samples.

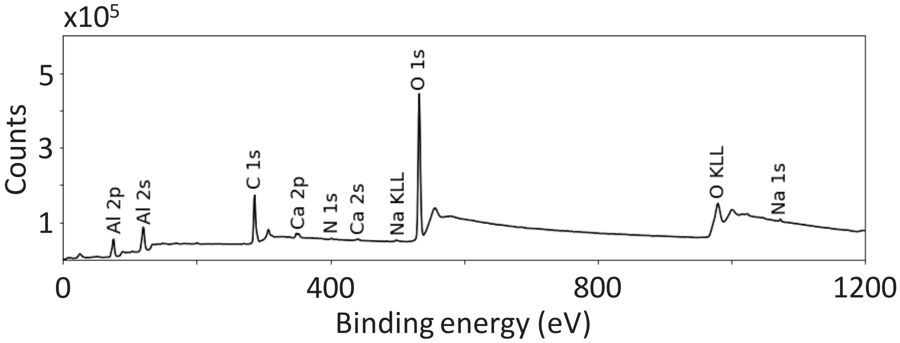

Figure 7.12: Example XPS spectra (corresponding to Case A in Table 7.1). Here, all peaks that could significantly be observed in the spectra are highlighted. Only the strongest peaks from each species are used to calculate the atomic percent concentration shown in Table 7.1.

7.4.2 XPS Measurements

XPS is used to provide a quantitative measurement of the surface contaminants present on the foils. The equipment used is a Kratos Axis Ultra XPS system located at the University of Michigan's Center for Materials Characterization [137]. This system has a sensitivity down to around one part per thousand, or 0.1 atomic percent. An electron beam operating at 15 kV and 10 mA is accelerated onto an aluminum anode to produce characteristic K_α X-rays. The X-rays are then monochromated and focused onto the sample in a small (<30 μm) spot, producing photoelectrons.

The electron emission occurs in a one- or two-step process. First, the X-ray transfers its energy to an inner shell electron (1s, 2s, 2p, etc.) to create a core hole. This photoelectron is ejected from the atom in this one step process of photoionization. Subsequently, an outer-shell electron can fill the core-hole vacancy via radiative or Auger decay. In the latter process, another electron is ejected, subject to energy conservation, via the process of autoionization. Both the Auger electrons and photoelectrons are passed through a hemispherical analyzer that retards the electron energies and focuses them onto a detector. While the X-rays may penetrate a few microns into the material, the electrons have a much shorter mean free path (λ_{mfp}) and only escape within roughly $3\lambda_{\mathrm{mfp}}$ of the surface. Therefore, the sampling depth for Al is limited to 8 nm, or 20 monolayers, so this is purely a surface interrogation technique.

The data collection was performed in survey mode over a bandwidth of 1200 eV to encompass the inner-shell and Auger peaks that could be produced by the various elements present on the sample surface. Figure 7.12 shows an example of the recorded spectra. Integrated peak counts are obtained by background-subtracting the continuum and then comparing these counts with the other peaks present. In this manner, XPS provides a quantitative measurement of the relative makeup of the material surface. All data processing was done using the CasaXPS software [138].

Element	Case A (at.%)	Case B (at.%)	Case C (at.%)
C 1s	$42 \pm 10\%$	83%	$66 \pm 5\%$
O 1s	$31 \pm 5\%$	12%	$19 \pm 2\%$
Al 2p	$25 \pm 6\%$	3.4%	$13 \pm 3\%$
Ca 2p	$1.0 \pm 0.0\%$	0.23%	$1.5 \pm 0.3\%$
N 1s	$0.43 \pm 0.26\%$	0.77%	$0.28 \pm 0.00\%$
Na 1s	$0.095 \pm 0.069\%$	0.39%	$0.075 \pm 0.010\%$

Table 7.1: XPS results given for three different test cases on a 100-μm-thick Al 1100 alloy foil. Both Case A and Case C were investigated at two different locations on the same foil, and the data presented are the mean and 95% confidence interval for each. Case B is the result of a single experiment at a single location. All data are given in terms of the atomic percent. Note that a confidence interval of 0% is an artifact of having only two data points.

XPS was performed on the Al 1100 alloy [127], which was prepared in three different manners. Table 7.1 shows the results for the test cases with all data given in terms of atomic percent. Case A was minimally handled with Fisherbrand nitrile gloves [139] and wiped down using Kimwipes [135] and a 90% isopropyl alcohol solution. Case B was handled with slightly sweaty bare hands and subjected to no wipedown. Case C was liberally handled and touched all over with the same set of Fisherbrand nitrile gloves [139], but no subsequent wipedown with isopropyl alcohol was performed.

The data clearly show, across all three cases, that aluminum, carbon, and oxygen dominate the elemental composition of the surface. However, there are also contributions from calcium, nitrogen, and sodium. Comparing Case C to Case A, when the foil was liberally handled with gloves and not wiped down, the carbon and calcium fractions increased along with a decrease in the aluminum and a slight decrease in the oxygen fractions. The sodium and nitrogen fractions cannot be said to have significantly changed, due to the larger error bars associated with these measurements. Now, considering Case B, where the foil was handled without gloves, the aluminum fraction dramatically decreases while the carbon fraction nearly doubles. Furthermore, the sodium fraction is now nearly 4 times larger. These trends support that handling materials with bare hands will introduce a significantly higher amount of carbon and sodium contaminants on the surface of the aluminum. The calculated sodium atomic concentrations for Case A and Case C agree within the error bars with the inferred concentration from Sec. 7.3.2.

7.4.3 Comparison of Results

The largest discrepancy between the XPS and LIBS results are the carbon lines. Carbon dominates the XPS spectra while it is virtually unobserved in the LIBS data. This is most likely due to the difference in the way each technique probes and then measures the samples. XPS can detect almost any element because there will always be some bound electron of that element that can be ejected and then detected. Conversely, LIBS spectra are determined by the plasma produced and the sensitivity of the spectrometer and detector. The majority of carbon's strong and prominent lines according to the NIST tables [107] lie $<$200 nm, and the detector used for the LIBS setup is only sensitive to wavelengths $>$200 nm, so it is likely that carbon lines are being produced given the plasma conditions, but the detector is simply not sensitive to them. This same argument holds true for the oxygen lines.

Nonetheless, both diagnostic techniques confirm the presence of sodium contamination. XPS initially demonstrated a measurable concentration of sodium atoms on the surface on the order of a few parts per thousand, but this small amount was not conclusive due to the diagnostic limitations. However, the LIBS results corroborate the XPS results by clearly measuring the spectral signature of the sodium D-lines.

7.5 Summary of Results

Sodium absorption lines have been observed on an expanding dense aluminum plasma plume heated by an intense, relativistic, monochromatic electron beam. The contamination location and amount was quantified using two fundamentally different techniques, XPS and LIBS. The sodium was determined primarily to be a surface contaminant across pure, anodized, and 1100 alloy aluminum, consisting of about 10 monolayers. This conclusion is supported by a decrease in the line intensity of the sodium D-lines when boring into the sample using LIBS. However, the alloy and anodized foils have a significant Na presence within the foils, suggesting that Na is an impurity embedded within the material lattices while the pure Al foil is indeed chemically pure.

These results motivated the construction of a spectroscopic-quality radiation transport model to interpret the plasma conditions using the profiles of the absorbed D-lines. The model shows an acute sensitivity to the sodium ion concentration with the best intensity match at $\mathrm{n_{Na}} = 3 \times 10^{15}$ cm^{-3}, and best line ratio match at $\mathrm{n_{Na}} = 10^{16}$ cm^{-3}. The unsaturated line ratio of 2:1 of the resonant Na D-lines requires $\mathrm{n_{Na}} < 10^{14}$ cm^{-3}. Stark broadening analysis of the experimental absorption spectra from the plasma plume gives an average electron density of $3.0 \pm 0.8 \times 10^{18}$ cm^{-3}. This, combined with the measured line ratios near 1:1, suggests that the saturated absorption lines originate from a dense, highly collisional outer layer of the plasma plume. The inferred sodium atomic concentration from both the simplified radiation transport model and the Stark broadening measurements agree with the XPS results from Case A and Case C, which justifies the use of the basic radiation transport model. Further experiments will be performed to improve and refine the modeling capability, including validation of the hydrodynamics model with time-resolved visible interferometry.

CHAPTER 8

Pure Al Measurements

8.1 Introduction

The measurements presented in this chapter were originally devised as a continuation of the experimental measurements and the modeling capabilities presented in Chapter 7. Beam-target interaction experiments of the different types of aluminum foils studied by XPS and LIBS (99.999% pure Al, 1100 Al, and anodized Al) were performed on the DARHT Axis-I accelerator and included 50, 100, and 200 μm thicknesses. The results from these more recent experiments with Al 1100 alloy foils on DARHT-I are now serving as a reference for the original set of measurements, which are presented in Chapter 7. The original goal of this new set of measurements was to observe the transition from absorption to emission of the sodium D-lines and the effect of different preparation techniques (Cases A–C shown in Tab. 7.1) on the resulting spectra. This effect is observed on anodized aluminum foils, but presently we are lacking the computational tools (e.g., the EOS for Al_2O_3) required to generate a hydrodynamic model of the plasma plume and corresponding synthetic spectra. This goal evolved into, instead, measuring and interpreting the Al-I 3p-4s doublet at 394/396 nm.

This chapter will present the spectroscopy and interferometry results of the three different thicknesses of the pure aluminum foils [133]. Initial Stark broadening calculations of the Al-I 3p-4s lines are performed and the effect of the self-absorption (SA) is discussed. The analysis of the interferometer results yields radial and axial density profiles to determine plasma plume extents and velocities. Spectra calculated by ATOMIC are used to threshold the plasma temperature in the optically thin approximation by matching line ratios. A simple model of the Al-I 3p-4s lines originating from a uniform slab of plasma is also created to better infer the effect of SA on line formation. These results complement the creation of a full scale radiation transport model using the hydro outputs from LASNEX to produce synthetic spectra and attempt to interpret the optical depth of the calculated Al-I 3p-4s lines. The SSI results are compared directly with the LASNEX radial and axial density profiles to both validate and improve the model.

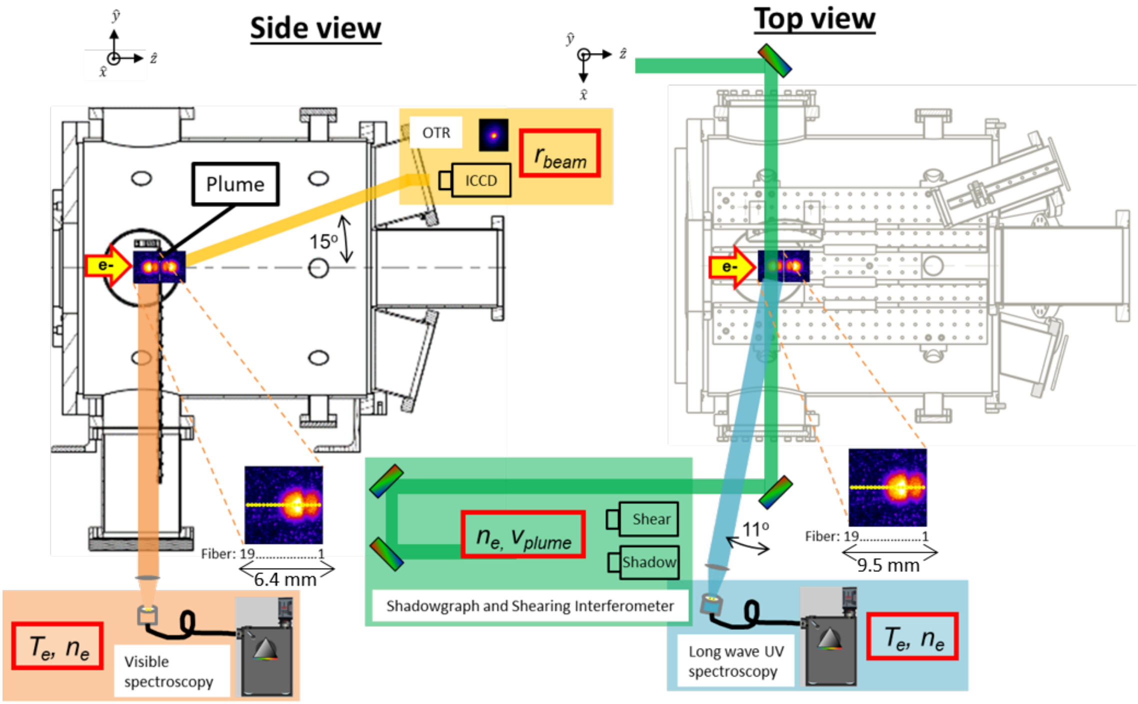

Figure 8.1: Present diagnostic configuration in the measurement region. This layout is representative of the measurements detailed in Chapter 8. Note that the side view described here is the same view displayed in Fig. 4.8. The plasma plume distribution shown for reference is an example measurement taken by the plume imaging diagnostic. This Figure is identical to Fig. 4.10 and is reproduced here for convenience.

8.1.1 Experimental Configuration

Two new diagnostics were deployed for these measurements: the long wave UV spectrometer (described in Sec. 4.2.3), and the SSI (described in Sec. 4.2.4). The SSI takes the place of the visible self-emission plume imaging diagnostic, while the long wave UV spectrometer ($M = 0.5\times$) supplements the visible spectrometer ($M = 0.7\times$, described in Sec. 4.2.2) to provide two separate chords of spectroscopy. Near-field OTR (described in Sec. 4.1.2) is used again to quantify beam energy density. The diagnostic setup is shown in Figure 8.1, which is identical to Fig. 4.10.

8.1.2 Data Collection

Datasets from the full diagnostics suite were collected for each of the three different thickness pure aluminum foils. Time-resolved near-field OTR measurements were made every 10 ns from $t_0 + 10$ ns to $t_0 + 90$ ns. Figure 8.2 shows the measurements of the beam spot size in $\hat{x}$ throughout the beam pulse, along with the current trace for reference. A consistent beam spot size is resolved

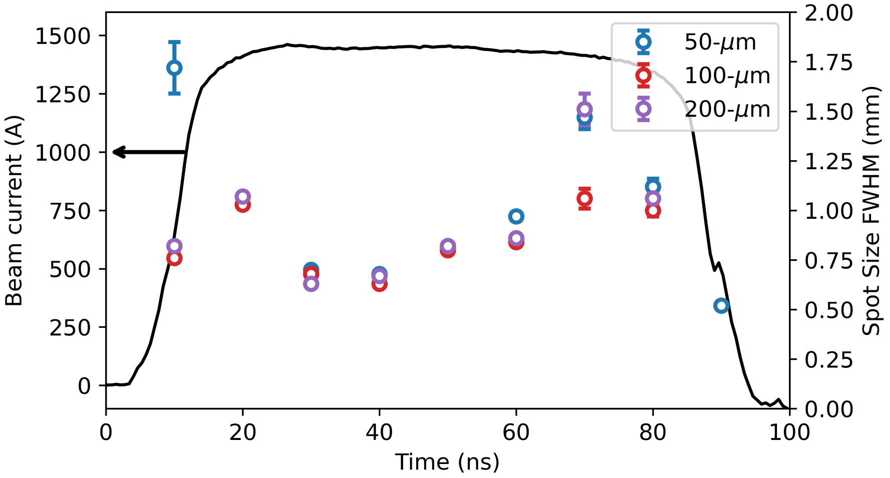

Figure 8.2: Time resolved near-field OTR measurements of the beam spot size in $\hat{x}$ for three different thicknesses of pure aluminum foils: 50 μm is shown in blue, 100 μm is shown in red, and 200 μm is shown in purple. The beam current is overlaid for reference. The time dependence of the spot size is most pronounced at the head and tail of the beam. The time averaged spot size in the middle of the pulse (from 20–60 ns) is used as the nominal spot size.

Target	20–60 ns FWHM
50-μm Al	0.84 ± 0.14 mm
100-μm Al	0.80 ± 0.14 mm
200-μm Al	0.81 ± 0.16 mm

Table 8.1: Calculated time averaged beam FWHM from 20–60 ns across all three pure aluminum foils. The data show a consistent beam spot size within the measured uncertainties.

across all aluminum target thicknesses, as demonstrated by the results in Table 8.1. The beam is not always axisymmetric (see Ref. [83]), but, to first approximation, it can be treated as such. Note that the time dependence of the beam spot size is well understood and can be described by the following: (1) the presence of off-energy electrons in the head and tail (rise and fall) of the electron beam pulse, which have different focal lengths compared with the nominal beam energy, and (2) the desorption and motion of ions upstream into the incoming electron beam that results in a time-dependent beam spot size (see Sec. 2.3 and [140]). The average beam spot size FWHM of 0.8 mm and the current profile shown in Fig. 8.2 are used to define the electron beam energy deposition in the LASNEX hydrodynamic model.

The SSI collected time-resolved measurements of the plasma plume density and extent from 100–500 ns. Measurements are made every 50 ns from 100 to 300 ns, and every 100 ns from 300 to 500 ns. This resolution early in time is adequate to compare with the LASNEX hydrodynamic model, which is run out to 400 ns. Similarly, the spectrometer measurements (both visible and long wave UV) use 200 ns gate widths and measure 100–300 ns and 300–500 ns for all foil thicknesses, with three shots averaged together at each time gate. The longer time gate and shot averaging are required to maximize S/N because the light output from the aluminum plasma plume is lower than other target materials like Ti, Cu, and Sn.

8.2 Spectroscopy of Optically Thick Al-I Resonance Lines

8.2.1 Measured Spectra

Similar to the sodium D-line measurements presented in Chapter 7, the Al-I 3p-4s doublet lines (396.152 and 394.401 nm) have a characteristic line ratio of 2:1 given by the Einstein coefficients of the transitions. The line ratio comes from the statistical weights of the atomic sublevels corresponding to the electronic transitions. This ratio holds true in LTE as long as the lines originate from an optically thin plasma.

Figures 8.3 and 8.4 show spatially-resolved spectra using the visible spectrometer (the line-of-sight is as shown in Fig. 8.1) from a 100-μm-thick pure aluminum foil at 100–300 ns and 300–500 ns, respectively. It is clear from all of these measured line profiles that the line ratios deviate significantly from the optically thin ratio of 2:1. The spatially-resolved spectra also exhibit a variation of the peak counts; further away from the foil surface (at greater axial extents), the counts are lower, while approaching toward the foil, the lines become brighter, up to the point where the opacity effects result in a blackbody-like continuum being produced, after which no visible light is detected on the spectrometers. This can be observed in Figure 8.5. A CCD image of the UV spectrometer that measures the Al-I 3p-4d lines at 308/309 nm is also shown for completeness in

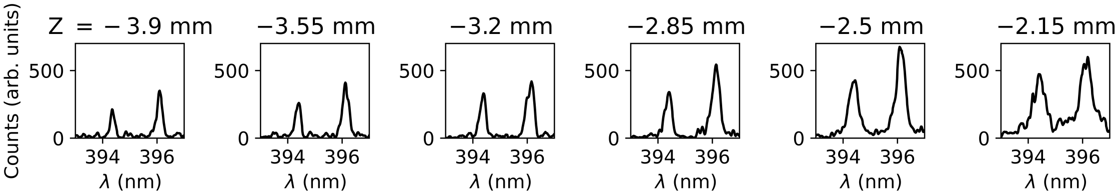

Figure 8.3: Measured Al-I 3p-4s spectral lines (average of shots 33898, 33909, and 33914) from an electron beam heated 100-μm-thick pure aluminum foil with a 100–300 ns gate. Each spectrum is from a fiber chord located at the specified axial (Z) distance given above each plot. Fig. 8.5 shows the corresponding CCD image from which these profiles are extracted.

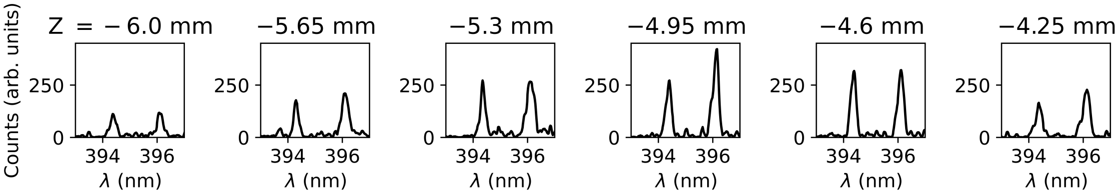

Figure 8.4: Measured Al-I 3p-4s spectral lines (average of shots 33897, 33910, 33915) from an electron beam heated 100-μm-thick pure aluminum foil with a 300–500 ns gate. Each spectrum is from a fiber chord located at the specified axial (Z) distance given above each plot. Note the different axial distances and count levels compared with Fig. 8.3.

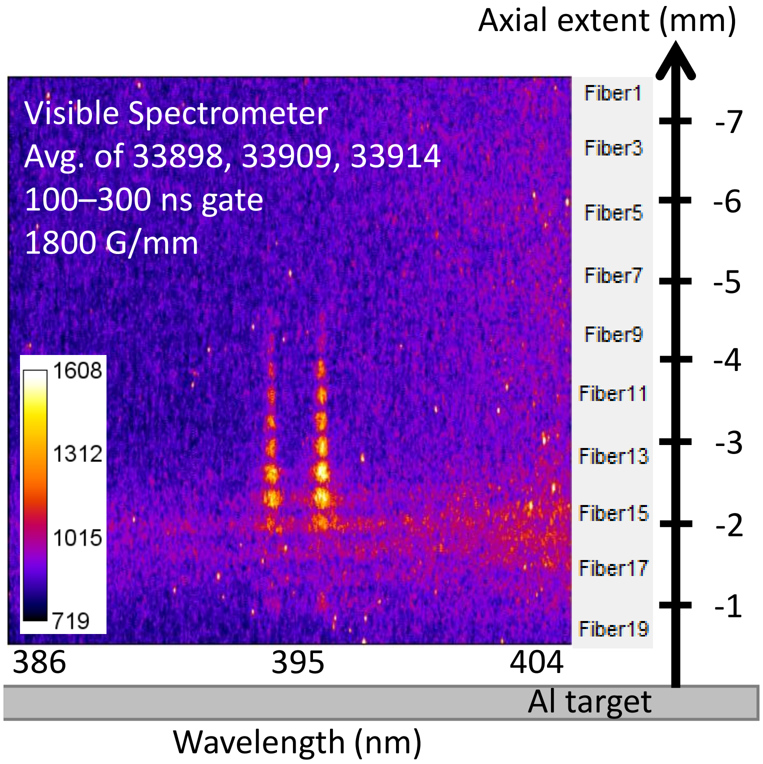

Figure 8.5: Example CCD image from the visible spectrometer used to obtain the data plotted in Fig. 8.3. The variation in line shape, intensity, and continuum with axial (Z) position is clearly observed.

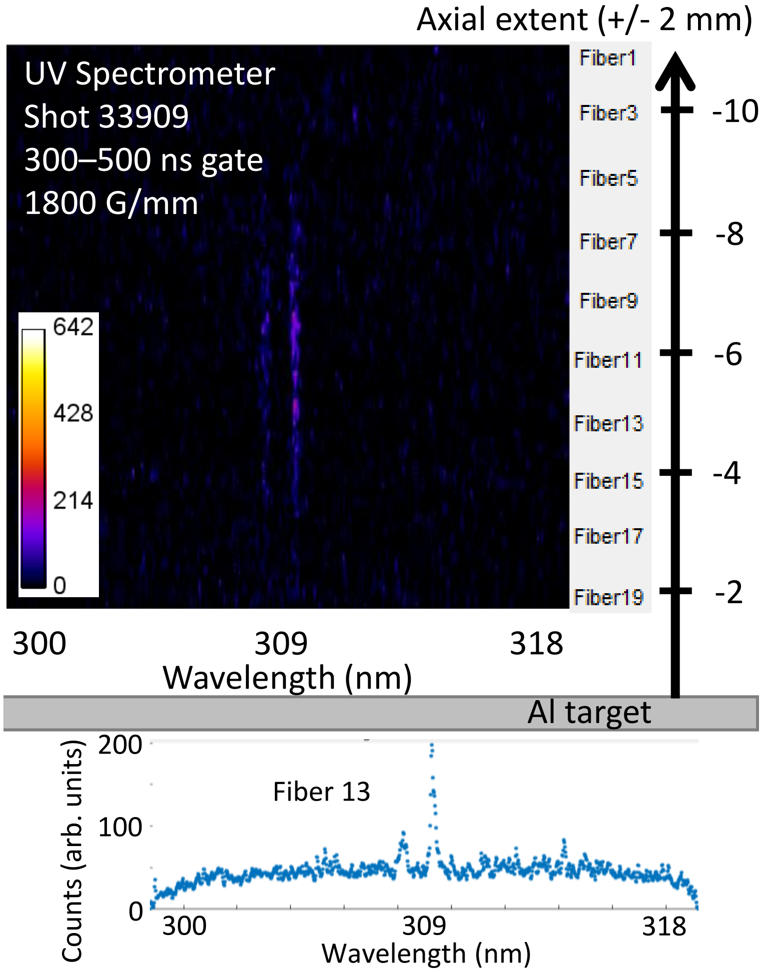

Figure 8.6: Example CCD image from the long wave UV spectrometer of the Al-I 3p-3d lines from 300–500 ns. The UV-sensitive CCD exhibits a well characterized leakage from bottom to top, resulting in a background gradient from ∼600 to ∼1000 counts. The variation in background intensity along increasing axial (Z) position is due to the reconstruction of the random packed linear fiber array from the CCD image.

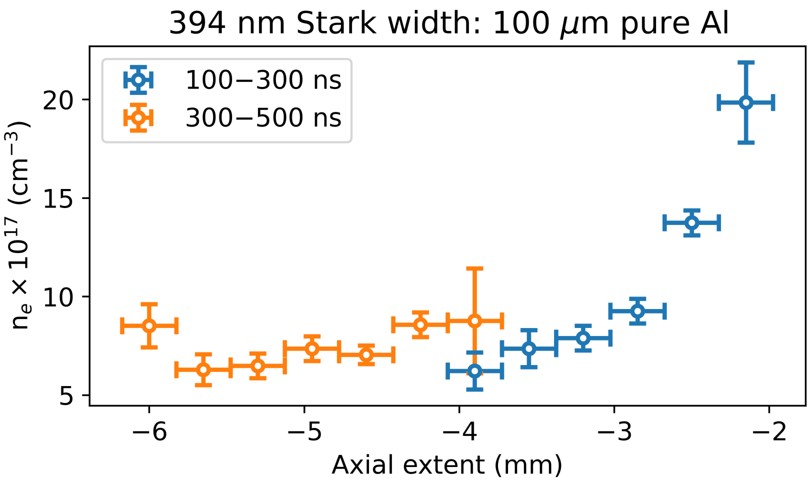

Figure 8.7: Calculated electron densities from a Stark broadening analysis of the Al-I 3p-4s 394.401 nm line from the measured spectra shown in Figs. 8.3–8.4. Early in time, a density gradient is observed for increasing axial extent. Later in time, the density appears to be relatively constant over > 2 mm.

Figure 8.6, but they are not analyzed due to the poor S/N compared with the Al-I 3p-4s lines. This demonstrates the capability of the long wave UV spectrometer measuring lines that were previously inaccessible by the visible spectrometer. Aluminum has proven to be a challenging material to measure spectroscopically when compared with spectrometer measurements of other materials like copper and tin, where many lines in the long wave UV (and visible) regimes are readily observed with 100 ns gate widths.

8.2.2 Stark Broadening

A Stark broadening analysis has been attempted to measure plasma densities from which the lines originate, but complications arise due to the SA nature of the Al-I 3p-4s lines. While still a valid analysis tool, the resonance lines will overbroaden and cause an overestimation of the electron density because of the reduction of the intensity at line center. This onset is more pronounced for the 396.152 nm line, as it has a higher opacity compared with the 394.401 nm line. So, the exponential factor in the radiation transfer equation, $e^{-\kappa(\lambda)x}$ (Eqs. 6.2–6.4), will more strongly affect the line shape of the 396.152 nm line before impacting the 394.401 nm line.

Plasma electron densities are calculated by a Stark analysis of the Al-I 3p-4s 394.401 nm line using the Stark widths from [141]. A value of 3.13×10^{17} cm^{-3}/Å is used to convert the Stark widths into electron densities. The Stark widths are obtained by fitting each individual line to a Voigt profile and then extracting out the FWHM.

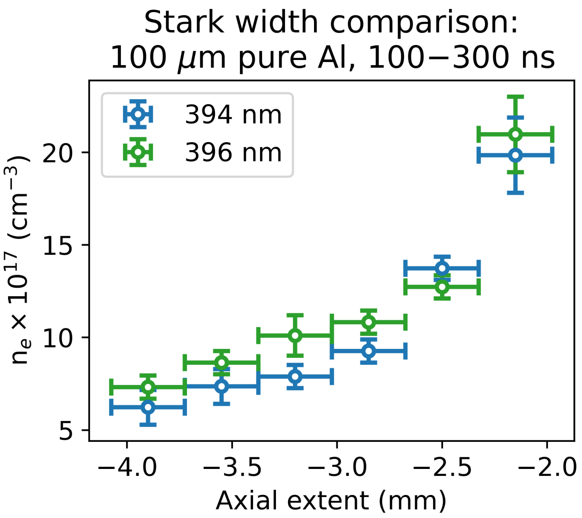

Figure 8.8: Comparison of the calculated electron densities from a Stark broadening analysis of the Al-I 3p-4s doublet lines from the measured spectra shown in Fig. 8.3. Across nearly all datapoints, the 396.152 nm line yields a higher electron density compared with the 394.401 nm line.

A plot of the electron density as a function of axial extent at two different time gates is shown in Figure 8.7. The density is observed early in time to show a mild gradient with increasing density approaching the target foil face. Later in time, the calculated densities appear to be relatively constant. This may be indicative of the limitations of the visible spectrometer as a density diagnostic; the lines are likely originating from an outer layer of the plasma plume and cannot escape from the higher density core of the plasma. It may also be an effect of self-absorption on the 3p-4s lines.

Figure 8.8 shows a comparison of the calculated electron densities from the 396.152 nm line and the 394.401 nm line. The 396.152 nm line shows a consistently higher electron density compared with the 394.401 nm line. This is likely a result of the stronger SA of the 396 nm line and will be explored in more detail in the next section.

8.2.3 Self-Absorption of the Al-I Lines

Evaluation of the SA of the Al-I 3p-4s lines is critical to interpreting the information the lines provide about the state of the plasma. Figure 8.9 assesses the level of SA for all the measurements made of the 3p-4s doublet, including the three different foil thicknesses and two sequential time gates. A linear regression of the data shows that, on average, 88% of the spectra observed exhibited a degree of SA that corresponds to an observed line ratio of 1.31:1. Almost all of the values exist with a line ratio between 2:1 (optically thin) and 1:1 (optically thick). The Al-I 3p-4s lines are never observed in experiment to undergo full self-reversal [125]. This fact will help to validate

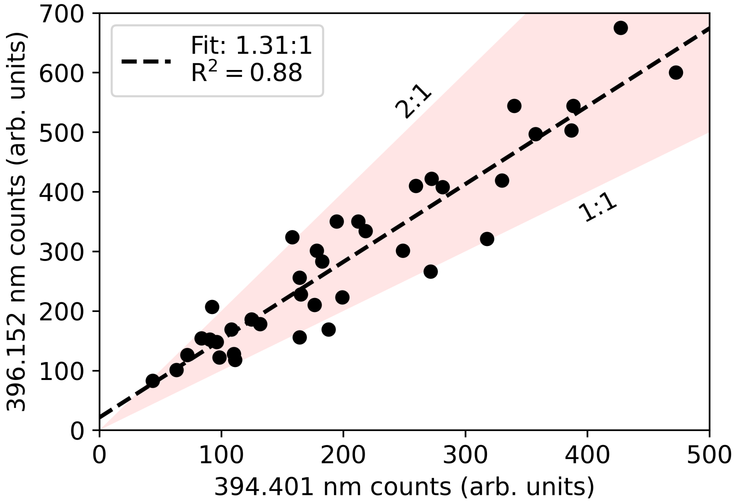

Figure 8.9: Plot of the Al-I 3p-4s doublet line counts across all pure aluminum foil thicknesses (50, 100, and 200 μm) and time gates (100–300 ns, 300–500 ns). A linear regression of the points yield a line ratio (slope) of 1.31 ± 0.08, with an $\mathrm{R}^2 = 0.88$. The shaded area in red encompasses both the optically thin 2:1 line ratio where SA is negligible, and an optically thick 1:1 line ratio.

the construction and implementation of the SA model presented in the following section, which will help narrow down the estimate of the temperature and density from which the spectral lines originate.

8.3 Spectral Modeling

This section details the modeling involved in interpreting and predicting the measured spectra. The tools used encompass the Los Alamos suite of atomic physics codes, LASNEX, FESTR, and include simple modeling that leverages the outputs from the ATOMIC code.

8.3.1 Self-Absorption Calculations

A simple model consisting of a uniform slab of temperature and density with a scale length Δx is constructed to show the effect of SA on line shape, line ratio, and Stark widths for the Al-I 3p-4s doublet. Simplifying Eqs. 6.2–6.4, the following can be written:

$$I(x) = I_B e^{-\tau(B,x)} + \int_B^x \epsilon(t) e^{-\tau(t,x)} dt, \tag{8.1}$$

where the optical depth terms $\tau(B, x)$ and $\tau(t, x)$ are defined as:

$$\tau(B, x) = \int_B^x \kappa(s) ds; \; \tau(t, x) = \int_t^x \kappa(s) ds. \tag{8.2}$$

The initial spectrum, I_B, is set equal to zero, which is equivalent to the assumption that only the spectrum from this slab of material contributes to the measurement. Since the slab is uniform in temperature and density, the emissivity, ϵ, and opacity, κ, are, by definition, constant over the length, Δx, of the slab. Transforming the integration bounds from (B, x) to $(0, \Delta x)$, the expression in Eq. 8.1 simplifies to:

$$I(\lambda) = \frac{\epsilon(\lambda)}{\kappa(\lambda)} \left(1 - e^{-\kappa(\lambda)\Delta x}\right), \tag{8.3}$$

Where the optical depth, $\tau(t, x)$, evaluates to the quantity $\kappa(\lambda)\Delta x$, and the emissivity, opacity, and specific intensity are written explicitly as functions of wavelength. The emissivity and opacity as a function of wavelength are evaluated using the Los Alamos suite of atomic physics codes.

The effect of varying slab thickness and plasma parameters (temperature, density) is explored using this model to identify threshold values where the line ratio of the Al-I 3p-4s doublet transitions from an optically thin condition (2:1) to an optically thick condition (1:1). Figure 8.10 shows a brief case study on the effect of varying one of these three parameters while holding the other two constant. The orange curves correspond to an optically thin calculation at the listed temperature and density pair. Note that all of these cases, if optically thin ($\tau \rightarrow 0$), have the expected 2:1 line ratio. The blue curves are the solutions of Eq. 8.3 given the parameters shown in each plot. Based on these results, the SA increases when the density increases, the temperature decreases, or the slab thickness increases.

Further studies are performed with this model, which include sweeping over the temperature/density parameter space and plotting the Al-I 3p-4s line ratio. Figures 8.11 and 8.12 show the effect of increasing temperature at a fixed slab thickness, and increasing slab thickness at a fixed temperature on the line ratio, respectively. For each case, at sufficiently low density, the lines are optically thin. Then, SA begins to play a dominant role in the line shape formation, resulting in a reduction of the line ratio, ultimately down to 1:1, at which point the line intensities saturate at a level corresponding to the blackbody emission intensity. Both of these figures demonstrate that the SA is less sensitive to slab thickness (Δx) at $T_e = 1$ eV; an order of magnitude change in Δx from 0.1 to 1 mm results in only about a 5× increase in the density where the onset of SA will be observed.. This is compared with the variation in T_e, where each 0.25 eV increase in T_e results in around a ∼5× higher density required to observe the onset of SA. Note that the calculations plotted in Fig. 8.11 break down for n_e above $\sim 3 \times 10^{18}$ cm^{-3}. This is a limitation of the collisional broadening model used in ATOMIC, which overestimates the broadened linewidths at these higher

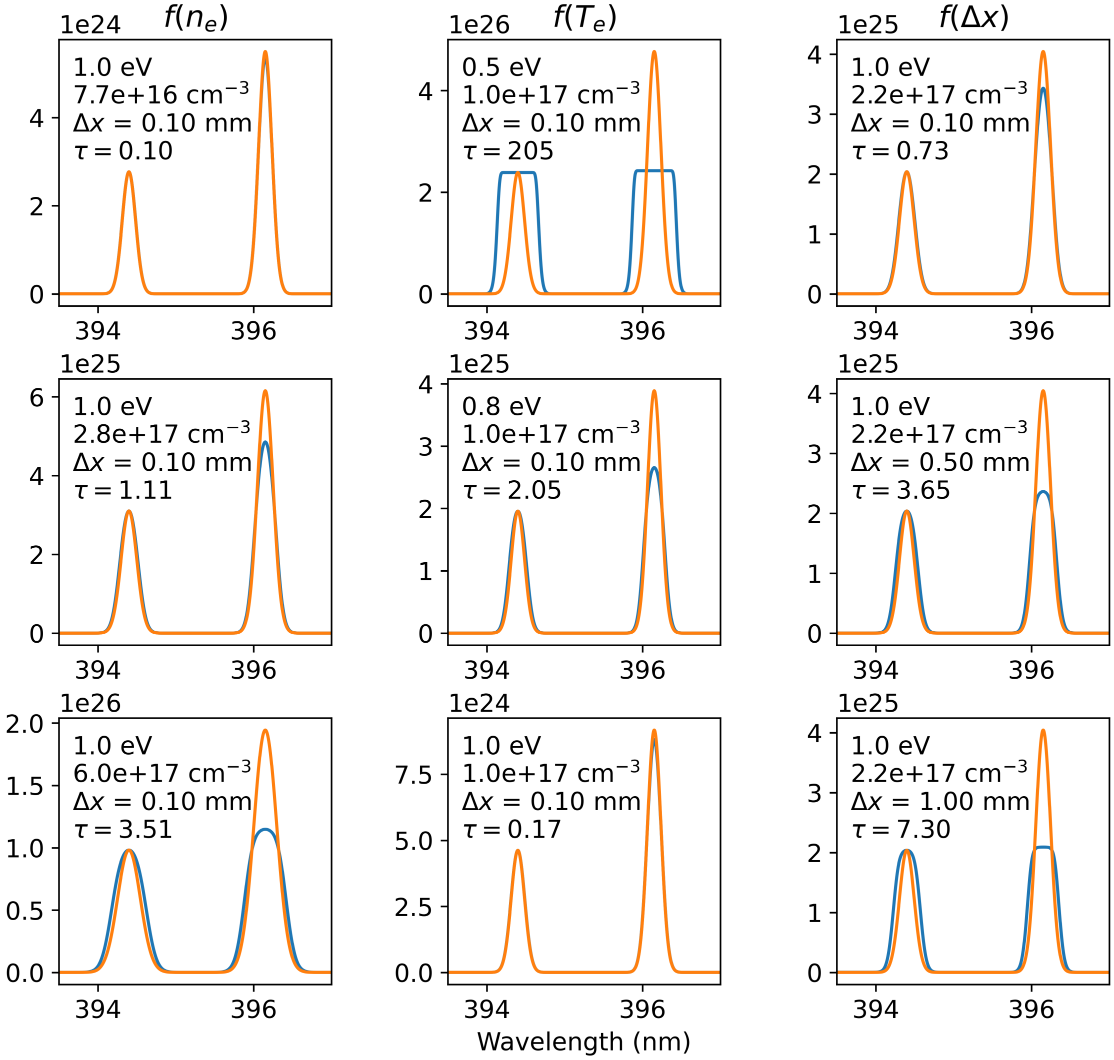

Figure 8.10: Plots showing the effect of n_e (left column), T_e (middle column), and Δx (right column) on the Al-I 3p-4s doublet. The optically thin calculation at each temperature/density pair is shown in orange. The blue trace corresponds to the SA results from Eq. 8.3. The value of the optical depth for each case is also displayed. The intensity of the SA profile is normalized to the optically thin profile at the 394 nm line center. For all plots, the x-axis units are (nm), and the y-axis units are (arb. units).

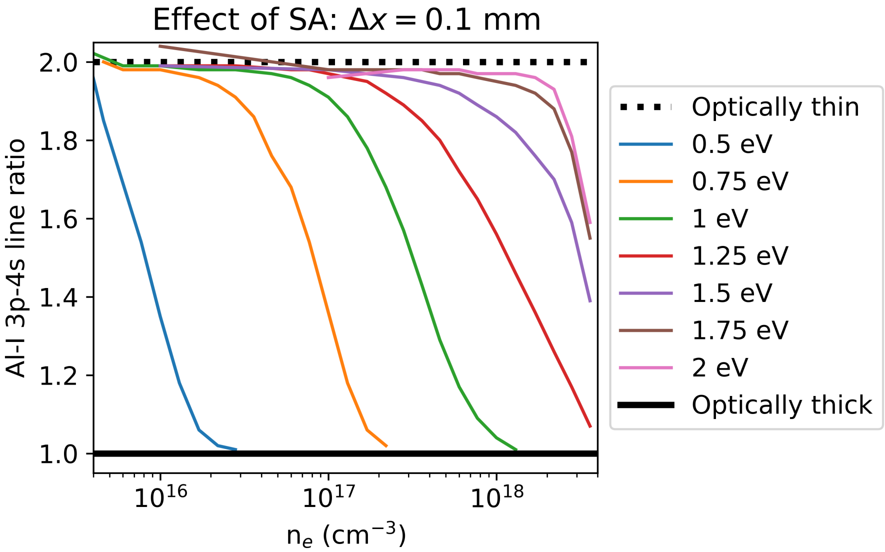

Figure 8.11: Plot of the density threshold for each given electron temperature which causes the Al-I 3p-4s doublet to experience SA at a fixed slab thickness of 0.1 mm. The dotted black line at a 2:1 ratio corresponds to the optically thin case. The solid black line at a 1:1 ratio corresponds to the optically thick limit.

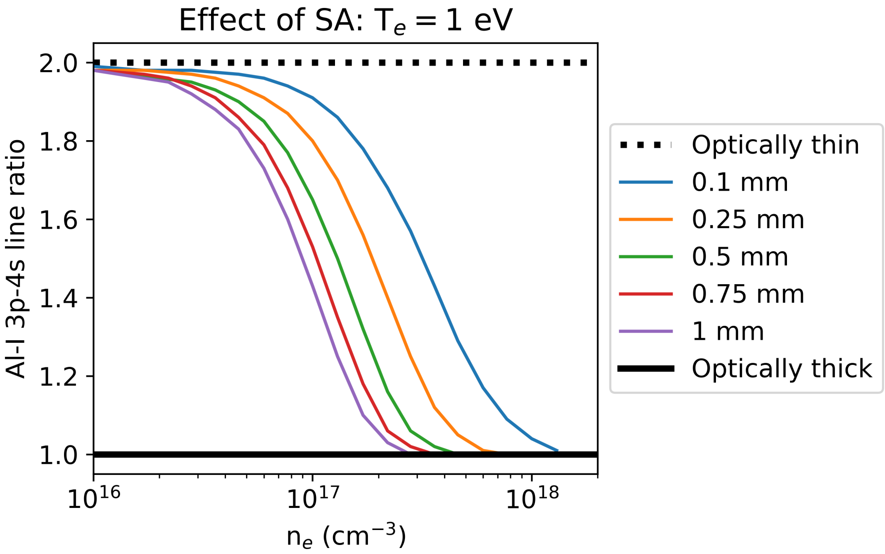

Figure 8.12: Plot of the density threshold for each given slab thickness which causes the Al-I 3p-4s doublet to experience SA at a fixed temperature of 1 eV. The dotted black line at a 2:1 ratio corresponds to the optically thin case. The solid black line at a 1:1 ratio corresponds to the optically thick limit.

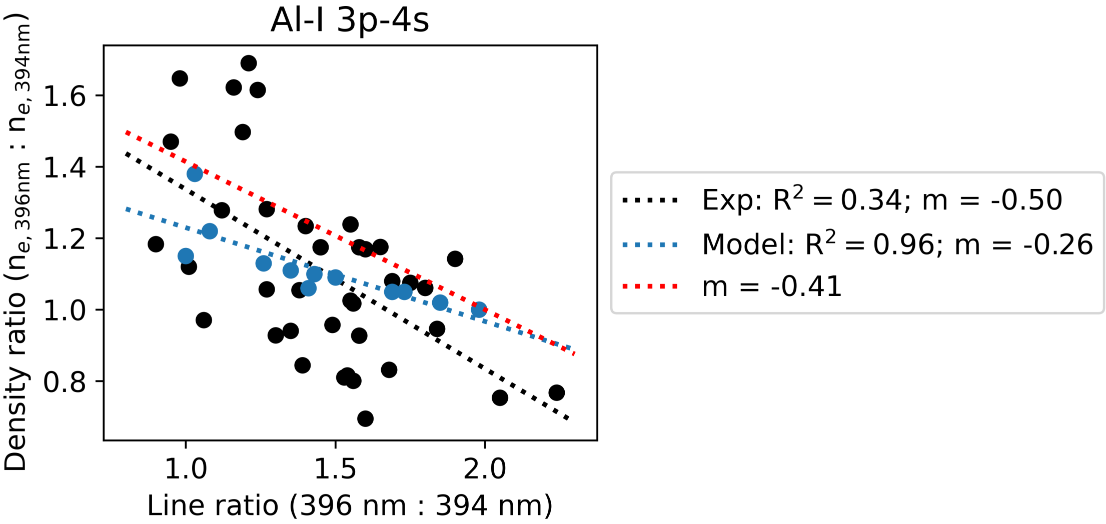

Figure 8.13: A plot of the Al-I 3p-4s line ratio against the density ratio. The black points and line represent the experimental data and linear regression. The blue points and line represent results from the SA model. The red line represents the theoretical value according to the simple optical depth model presented in Fig. 6.9.

densities.

Figure 8.13 plots the Al-I 3p-4s line ratio against the density ratio. The density ratio is defined as the ratio of the calculated widths of the 396 nm line to the 394 nm line as they undergo Stark broadening. This plot, similar to Fig. 8.9, includes all the measured Al-I 3p-4s lines, along with datapoints from the SA model, and highlights the non-uniform effect of SA on each line of the 3p-4s doublet. The experimental data tend to, in the optically thin case (line ratio of 2:1), produce similar Stark-calculated densities, which is to be expected, as each line of the 3p-4s doublet has the same Stark width [141]. The red dotted line corresponds to the simple optical depth model discussed in Fig. 6.9; when the optical depth reaches a value such that the line intensity is reduced by half, the line width increases by a factor of $\sqrt{2}$. The limitation of this model is that it does not predict self-reversal of the line shape. A spatial gradient in temperature or density is required to observe self-reversal effects [125]. So, at an optically thin line ratio of 2:1, the density ratio of the two lines should be identical ($= 1$). At the optically thick case of a 1:1 line ratio, the density ratio is $\sqrt{2} : 1$. The SA model underestimates this effect at increasing optical thickness, but matches relatively well near the ideal 2:1 line ratio.

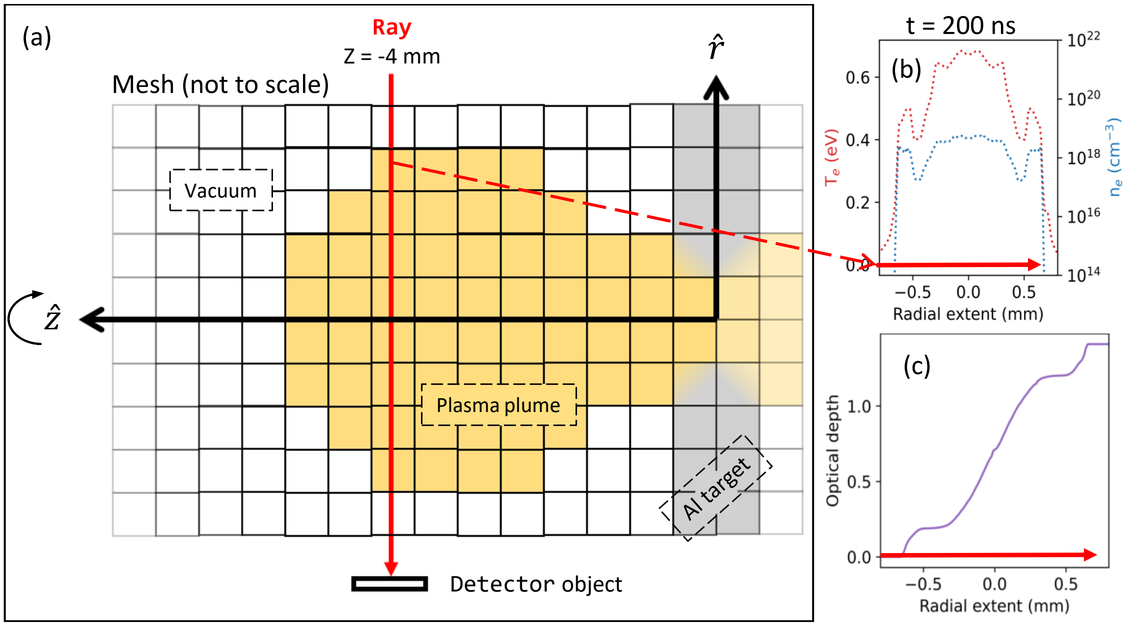

Figure 8.14: Cartoon illustration of the optical depth tracking modification to the FESTR code, which is run in tracking mode (discussed in Sec. 6.3). (a) The path of the `Ray` through the plasma plume defined by the outputs from LASNEX (recall these simulations are 2-D cylindrically symmetric). The `Ray` traverses the plume and solves the 1-D radiation transport equation upon crossing each `Zone`, along with accumulating the optical depth τ through each `Zone`. (b) Example spatial T_e and n_e profiles seen by the `Ray` as it crosses the `Mesh` at 200 ns. (c) Corresponding accumulated optical depth along the path of the `Ray`.

8.3.2 FESTR Optical Depth Tracking Calculations

The radiation transport model constructed for interpreting the Al-I 3p-4s lines is an extension of the model presented in Ch. 7. The spectral databases generated by the Los Alamos suite of atomic physics codes and used by FESTR span the temperature/density space covered by the LASNEX model and are described in Sec. 6.3.2. The photon energy grid from 390–400 nm has 501 points, which provides a spectral resolution of 0.02 nm. A series of four timeslices from the LASNEX model (100, 200, 300, and 400 ns) are formatted by Oz and passed to FESTR for spectroscopic quality radiation transport modeling. This allows for a reasonable comparison of the 100–300 ns and 300–500 ns spectrometer gates to the synthetic spectra while also minimizing computational time.

Figure 8.14 shows a cartoon illustration of how the optical depth tracking modification works within FESTR. As previously discussed in Sec. 6.3.4, FESTR is run in tracking mode which allows the `Ray`, as it crosses the `Mesh`, to record the spectrum accumulated through each `Zone` it traverses. In addition, these output files are modified to also contain the temperature and density

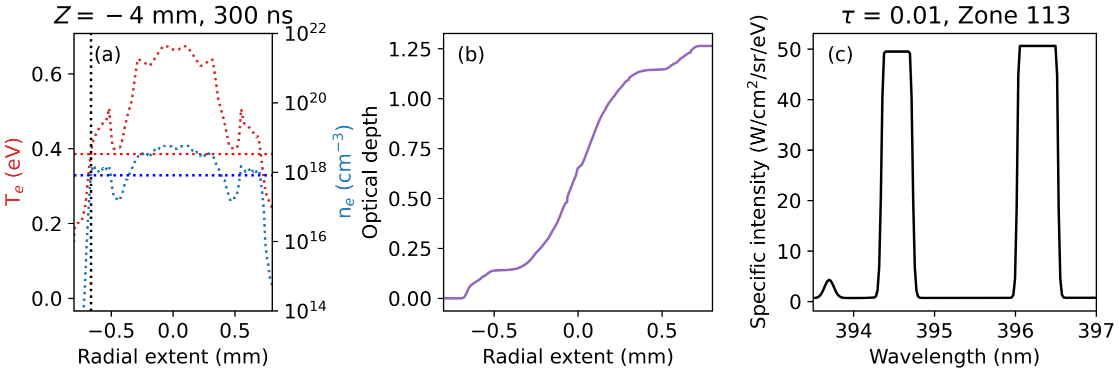

Figure 8.15: Radiation transport and threshold optical depth tracking results at 300 ns for a `Ray` launched along $Z = -4$ mm. (a) T_e (red) and n_e (blue) profiles as seen by the `Ray`, with the temperature and density point highlighted corresponding to the defined optical depth threshold of $\tau = 0.01$. (b) Accumulated optical depth along the path of the `Ray`. (c) Accumulated spectra at the the threshold optical depth of $\tau = 0.01$. The lines are observed in a saturated 1:1 ratio, where the flattop of each line corresponds to the blackbody emission intensity at the given wavelength.

of the `Zone`. Combined with the opacity tables (described in Appendix B, Table B.5) generated over a range of temperatures and densities at the center wavelengths of the Al-I 3p-4s doublet, the optical depth is evaluated at the line centers as a function of the spatial location of the `Ray`.

Figure 8.15 shows the results of the FESTR radiation transport model including optical depth tracking at 300 ns for a `Ray` located at an axial distance of $Z = -4$ mm. The radial T_e and n_e profiles traversed by the `Ray` result in an accumulated optical depth as shown in inset (b). Inset (c) displays the spectrum corresponding to a user-defined optical depth threshold of $\tau = 0.01$. The lines are observed in saturated emission, where the line ratio is 1:1 and the levels of the flattops correspond to the blackbody emission intensities at the given wavelengths. Note that this spectrum is originating from a `Zone` located at the outermost layer of the plasma with $T_e = 0.39$ eV and $n_e = 8.1 \times 10^{17}$ cm^{-3}.

Figure 8.16 further compares the line shapes given different conditions of optical thickness (a–c) with that shown in (d), which is the measured spectrum from Fig. 8.3 at $Z = -3.9$ mm. Inset (a) corresponds to the optically thin emission at the plasma parameters from the `Zone` at which $\tau = 0.01$. Inset (b) is the emission at an optical depth threshold of $\tau = 0.01$. Inset (c) shows the measured spectrum at the `Detector`, which corresponds to an accumulated optical depth of $\tau = 1.25$. None of the three synthetic spectrum cases match the experimental spectrum. The shortcoming here is reasoned to be the difference in the T_e and n_e profiles calculated by LASNEX compared with the n_e distributions measured by the SSI. This is discussed in the following section.

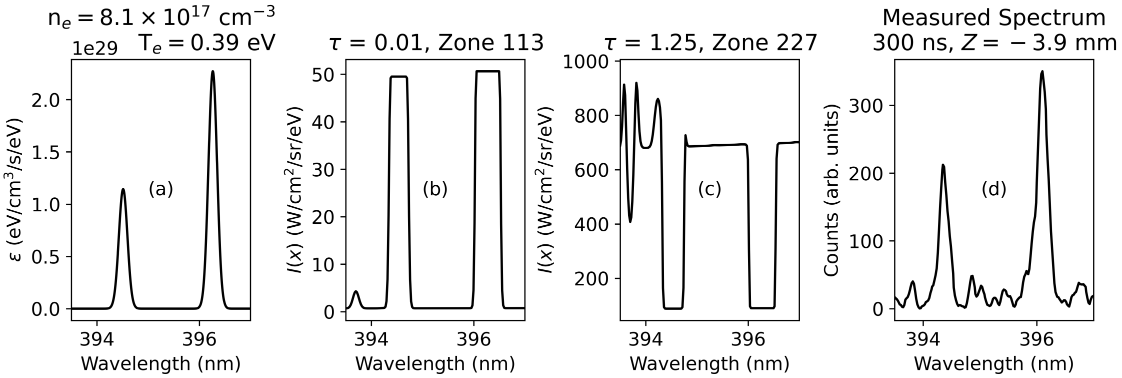

Figure 8.16: A series of plots of the Al-I 3p-4s doublet corresponding to different optical depths and spatial locations from the temperature and density profiles shown in Fig. 8.15(a). The `Zone` at which $\tau = 0.01$ has a $T_e = 0.39$ eV and $n_e = 8.1 \times 10^{17}$ cm^{-3}. (a) Optically thin ($\tau = 0$) spectrum at this plasma T_e and n_e. (b) Spectrum at $\tau = 0.01$, reproduced from Fig. 8.15(b). (c) Spectrum measured at the detector, corresponding to an accumulated optical depth of $\tau = 1.25$. (d) Measured spectrum at $Z = -4.25$ mm.

8.4 Analysis of SSI Plume Expansion Measurements

The SSI measures with a high degree of fidelity both the plasma plume extent and n_e profile, up to opacity limits [83]. Figure 8.17 shows the 2-D n_e profile of the plasma plume from an electron beam heated 100-μm-thick pure aluminum foil along with corresponding shadowgraphs. The n_e profiles are monotonically decreasing in both the radial and axial directions away from the center of the plasma plume. Limitations of the cutoff density are observed both early in time and later in time at the center of the plasma plume; it is an ongoing effort to improve the data analysis to better constrain n_e in this region. These n_e profile measurements are directly compared with the LASNEX radiation hydrodynamics model; this is discussed in Sec. 8.4.1.

Figure 8.18 shows a plot of the axial extent at $n_e = 10^{18}$ cm^{-3} for the three different thickness aluminum foils, along with the calculated velocity of this density profile as a function of time. The thicker foils, due to the increased pressure buildup within the material, disassemble with a higher sustained expansion velocity, which results in a larger plume extent later in time. This is in agreement with the formulations governing the plasma expansion discussed in Sec. 2.5. A plot of Eq. 2.8 is also shown in Fig. 8.18(b), which indicates that after the peak expansion velocity is achieved, the expansion is adiabatic.

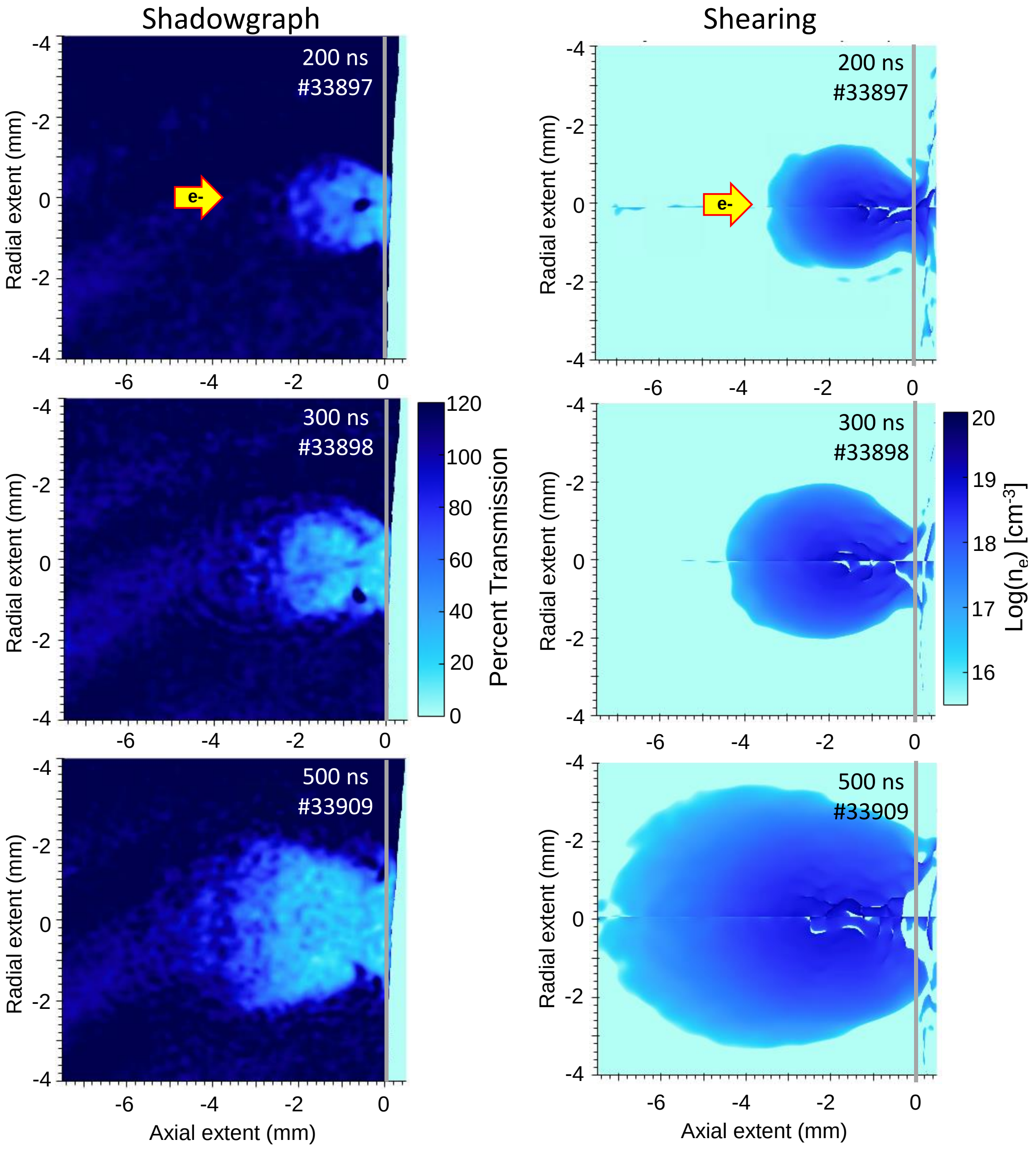

Figure 8.17: SSI n_e profiles of an electron beam heated 100-μm-thick pure aluminum foil at 200, 300, and 500 ns with the corresponding shot numbers indicated. The direction of the incoming electron beam is indicated in the 200 ns inset, and the gray bar in all insets represents the location of the aluminum foil.

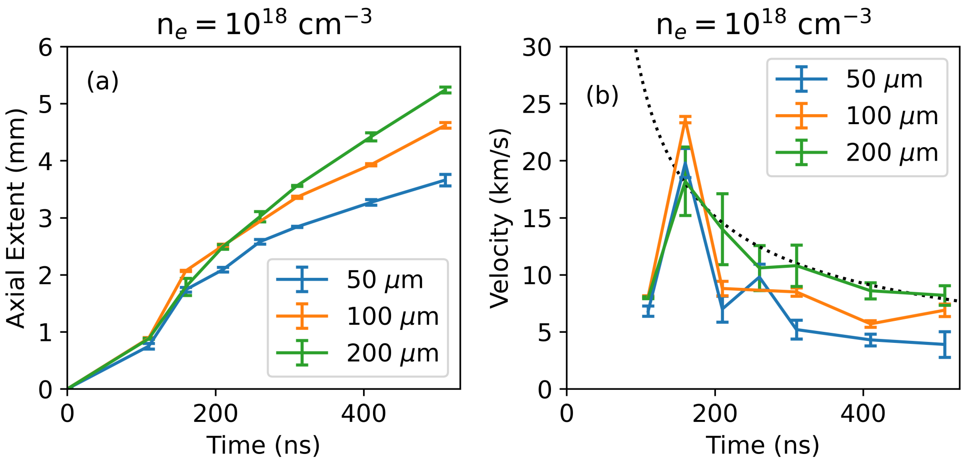

Figure 8.18: Comparison of (a) axial extents and (b) velocities for the three different thickness aluminum foils: 50 μm (blue), 100 μm (orange), and 200 μm (green). The thicker foils expand more rapidly and reach a larger extent compared with the thinner foils. The dashed line in (b) corresponds to the Taylor–von Neumann–Sedov point-source explosion solution given in Eq. 2.8 for the 200-μm-thick foil. A disassembly time of $t_0 = 42$ ns is assumed, and $\eta = 0.009$.

8.4.1 Comparison of SSI Measurements and LASNEX Calculations

This section focuses on the analysis of the measured SSI n_e profiles compared to the LASNEX radiation hydrodynamics modeling of the same foil with the measured beam parameters. Figure 8.19 shows the 2-D spatial profiles of T_e and n_e as calculated by the LASNEX model at 100 and 300 ns. Panels (c) and (d) of this figure will be compared directly with Fig. 8.17. Figure 8.20 plots the axial extents and velocities from the density profile, shadowgraph, and LASNEX model at an electron density of 10^{18} cm^{-3} and a shadowgraph transmission threshold of 70%, which roughly corresponds to the point at which the transmission of the laser light through the plasma plume is reduced by a factor of $1/e$. The LASNEX values are pulled directly from the dump files on axis ($R = 0$). The profiles from the SSI are integrated from $-0.5 < R < 0.5$ mm and have the associated error bars. In general, the LASNEX model slightly overpredicts both the plume extent and expansion velocity at this electron density contour.

Figures 8.21 and 8.22 plot axial and radial lineouts, respectively, of the measured and simulated n_e distributions, up to SSI opacity limitations denoted by the shaded regions. It is observed that, in fact, the agreement shown in Fig. 8.20 is the *only* point at which the measurement and the simulation are in agreement. These plots are sufficient to explain why the radiation transport optical depth tracking model described in the previous section does not replicate the lines measured in the experiment. Additionally, LASNEX predicts a much smaller plasma plume in the radial direction with sharper gradients in n_e. This is not a result of improper zoning—it is a consequence of how

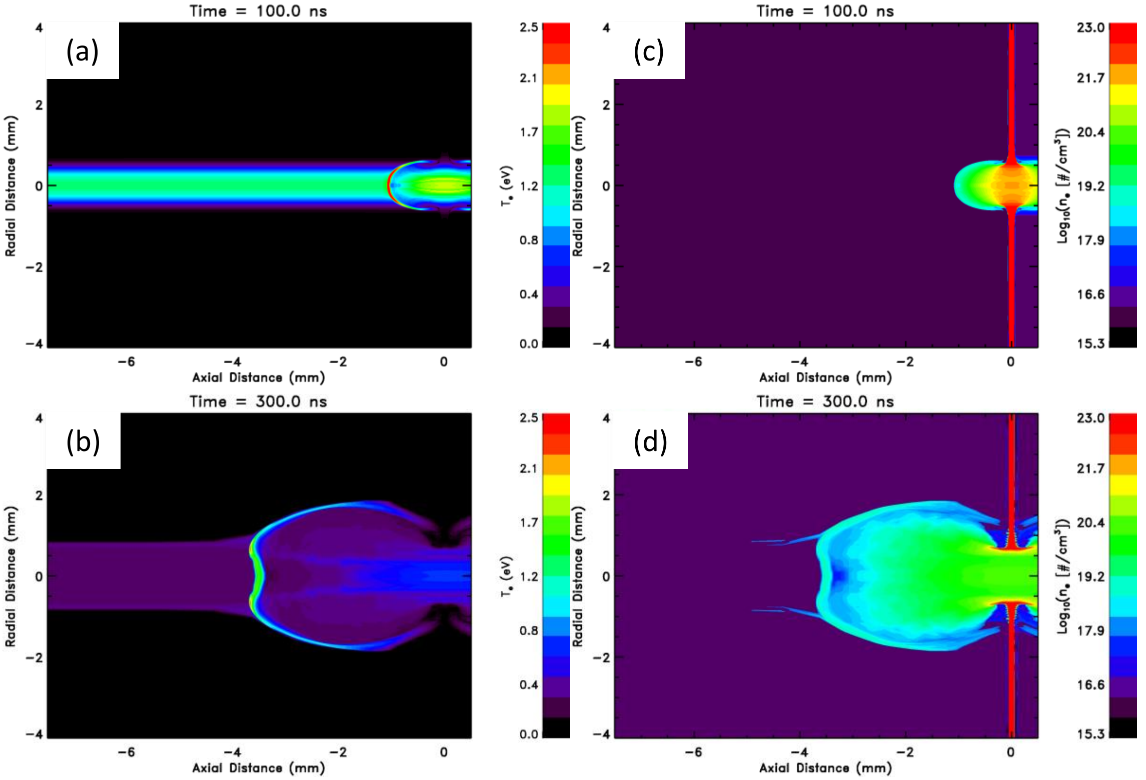

Figure 8.19: LASNEX-simulated T_e (left column) and n_e (right column) profiles for an electron beam heated 100-μm-thick pure aluminum foil at 100 and 300 ns. The electron beam profile used to heat the foil is from Fig. 8.2 and Tab. 8.1. The heated volume off of the foil surface observed on axis around $R = 0$ for (a) and (b) is a result of the electron beam passing through the foil and heating the background gas (water vapor) present in the simulation. The solid target foil is observed in (c) and (d) at $Z = 0$.

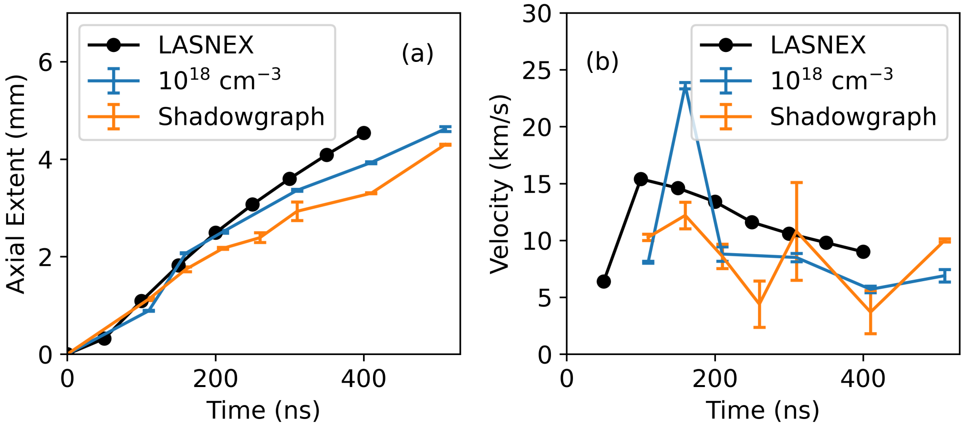

Figure 8.20: Comparison of (a) axial extents and (b) velocities between the LASNEX model (black), measured $n_e = 10^{18}$ cm^{-3} contour from Fig. 8.18 (blue), and shadowgraph (orange), for a 100 μm pure aluminum foil. The LASNEX model slightly overpredicts both the extent and velocity compared with the SSI measurements.

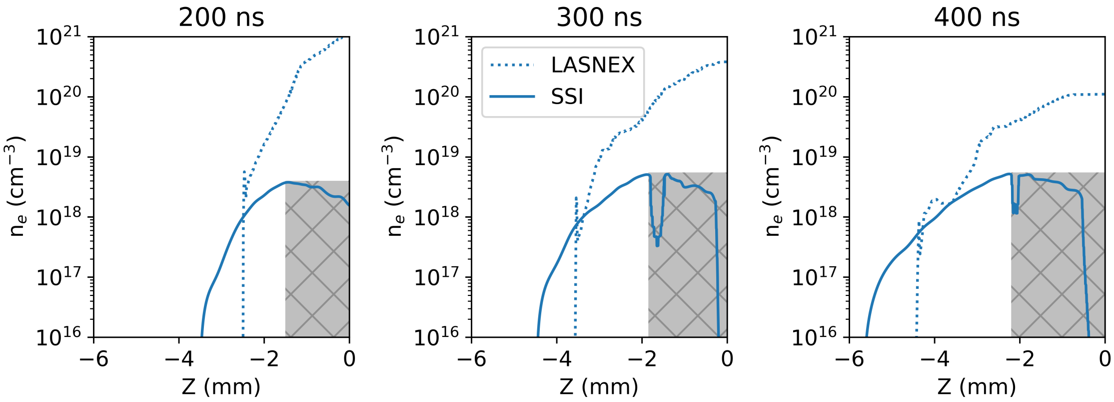

Figure 8.21: Comparison plots at three different timeslices (200 ns at left, 300 ns in the center, and 400 ns at right) of the axial extent on axis ($R = 0$) of the plasma plume from a 100 μm pure aluminum foil as measured with the SSI (solid line) and calculated by LASNEX (dotted line). The shaded regions correspond to where the n_e measurement is no longer accurate, due to the opacity effects on the transmission of the 532 nm light through the overdense plasma core.

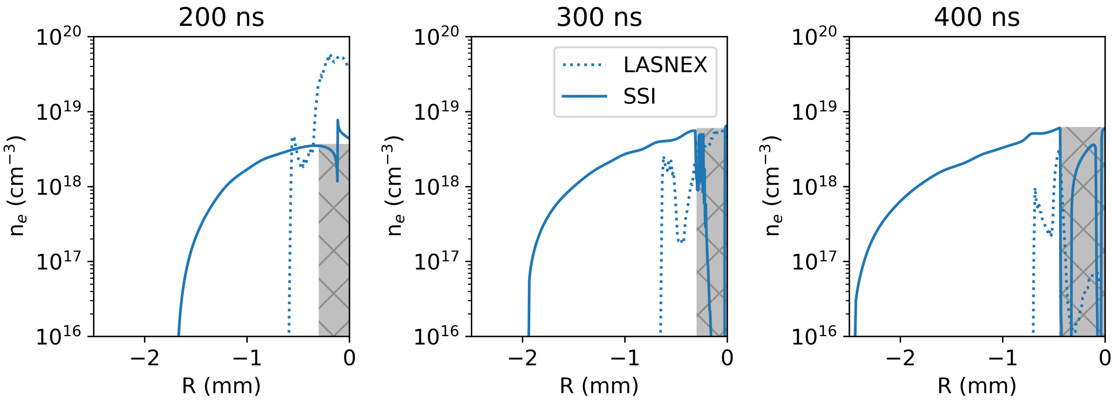

Figure 8.22: Comparison plots at three different timeslices (200 ns at left, 300 ns in the center, and 400 ns at right) of the radial extent at $Z = -2$ mm of the plasma plume from a 100 μm pure aluminum foil as measured with the SSI (solid line) and calculated by LASNEX (dotted line). The shaded regions correspond to where the n_e measurement is no longer accurate, due to the opacity effects on the transmission of the 532 nm light through the overdense plasma core. Note that these profiles are representative of the density profiles from which the spectroscopic lines originate.

LASNEX is handling the physics of the target hydrodynamic expansion. LASNEX determines the electron density from a Thomas-Fermi fit that is more applicable for higher temperature plasmas. However, this ionization calculation is independent of the opacity and pressure calculations, which may explain why the plume shape and hydrodynamic expansion match reasonably well with the SSI profiles, but the n_e distribution itself does not.

The value of this comparison is not lost, though; the SSI measurements serve as the first step toward benchmarking the EOS tables used within the LASNEX model. As noted in Fig. 6.2, the legacy Al EOS SESAME 3715 is used for all the hydrodynamics modeling results presented in this dissertation; the newer SESAME 3720 that includes the vapor dome physics has not yet been successfully run for the beam-target interaction modeling. This EOS comparison is left for future work.

The LASNEX radiation hydrodynamics model, while it matches the plume extent well, does not replicate the n_e gradient in the spectroscopically active region. LASNEX runs show much lower diffusion and preserve a sharp density gradient compared with the SSI measurements. This is not a resolution issue, as the average size of the LASNEX zones is < 10 μm. Furthermore, note that LASNEX uses Lagrangian hydrodynamics, so it will conserve mass in zones. A detailed assessment of this comparison for aluminum is given in [83].

Initial calculations of the optical depth using the measured SSI electron density distribution at a constant electron temperature suggest that the optical depth varies by 2–3× with this different n_e gradient, which is likely the reason why the synthetic spectra from FESTR do not fit well to

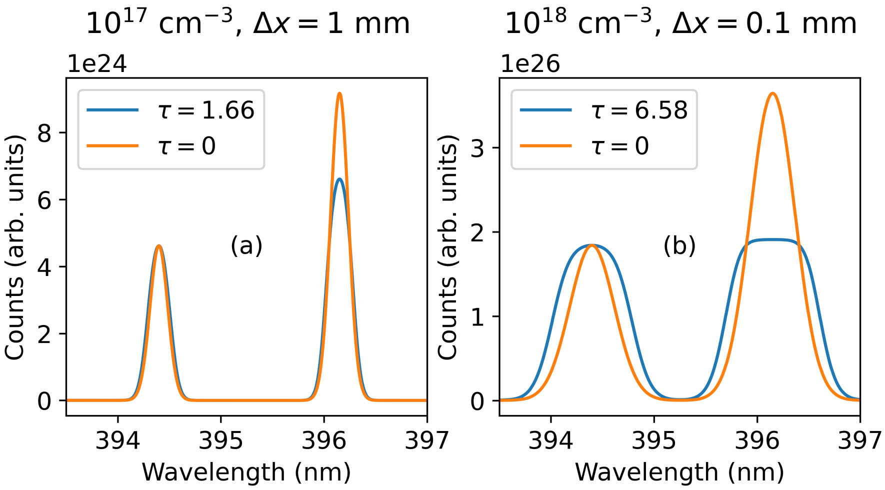

Figure 8.23: Plots of the Al-I 3p-4s doublet originating from a plasma with a temperature of 1 eV and a conserved areal density of 1.65×10^{-7} g/cm^2. (a) $n_e = 10^{17}$ cm^{-3} and $\Delta x = 1$ mm. (b) $n_e = 10^{18}$ cm^{-3} and $\Delta x = 0.1$ mm. The blue curve corresponds to the line shapes with SA, with the calculated optical depth at line center also shown. The orange curves correspond to the optically thin ($\tau = 0$) line shapes.

the measured line profiles of the Al-I 3p-4s doublet. Figure 8.23 roughly models this effect using the simple SA model based on the n_e contours from Fig. 8.22 and assuming a temperature of 1 eV. The outer part of the LASNEX plume, due to the sharp gradient below $n_e = 10^{18}$ cm^{-3}, is modeled at a density of $n + e = 10^{18}$ cm^{-3} with $\Delta x = 0.1$ mm. The SSI profile is very roughly mimicked with a density of $n_e = 10^{17}$ cm^{-3} and a longer path length of $\Delta x = 1$ mm, which matches the areal densities ($n_e \times \Delta x$) between the two models. These moderate changes result in a $4\times$ difference in the optical depth, τ, which significantly impacts the resulting line shapes. The lines for the lower density case appear in a 1.43:1 ratio. The higher density case shows both lines experiencing significant SA, appearing in a 1.04:1 ratio. The 396 nm line is also observed to be more significantly overbroadened as a result of this saturation.

8.5 Correction of Self-Absorbed Spectra

Figure 8.24 plots the Al-I 3p-4s line ratio as a function of the SA coefficient of both lines of the Al-I 3p-4s doublet from the SA model. These relationships are used to infer the SA coefficients from the experimentally measured spectral lines. This permits the calculation of the true electron density by taking into account the effect of SA on the calculated Stark width.

Figure 8.25 applies the self-absorption correction to the calculated Stark densities shown in Fig. 8.8. The outcome of the correction is that the Stark widths for both lines of the Al-I 3p-

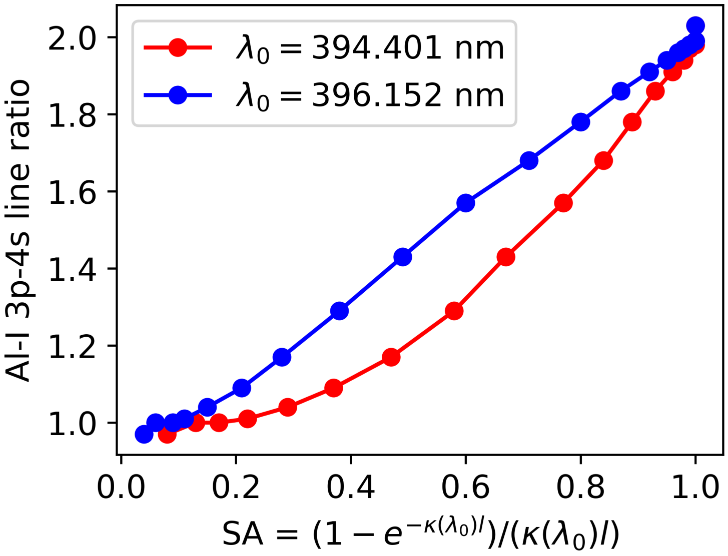

Figure 8.24: A plot of the Al-I 3p-4s line ratio as a function of the SA coefficient (Eq. 6.6) for the center wavelength of each line. The results shown are calculated by the SA model over a range of temperatures, densities, and slab thicknesses.

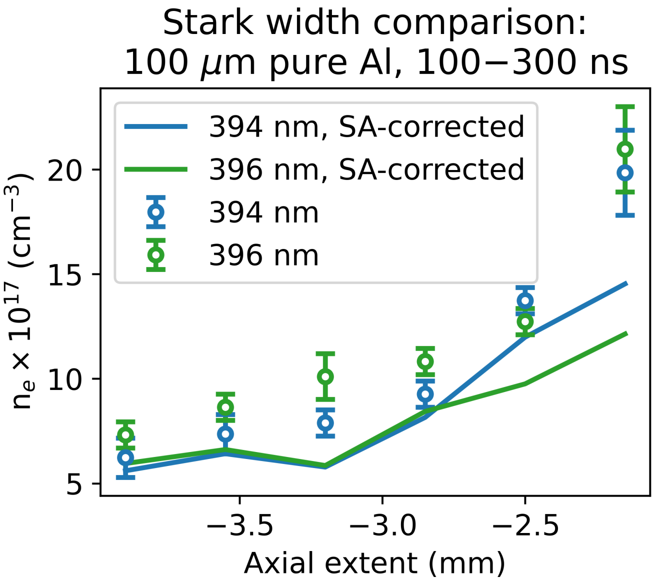

Figure 8.25: Comparison of the calculated electron densities from a Stark broadening analysis (shown in Fig. 8.8) combined with the SA-corrected densities using the relationship between the self-absorption coefficient and line ratio described in Fig. 8.24.

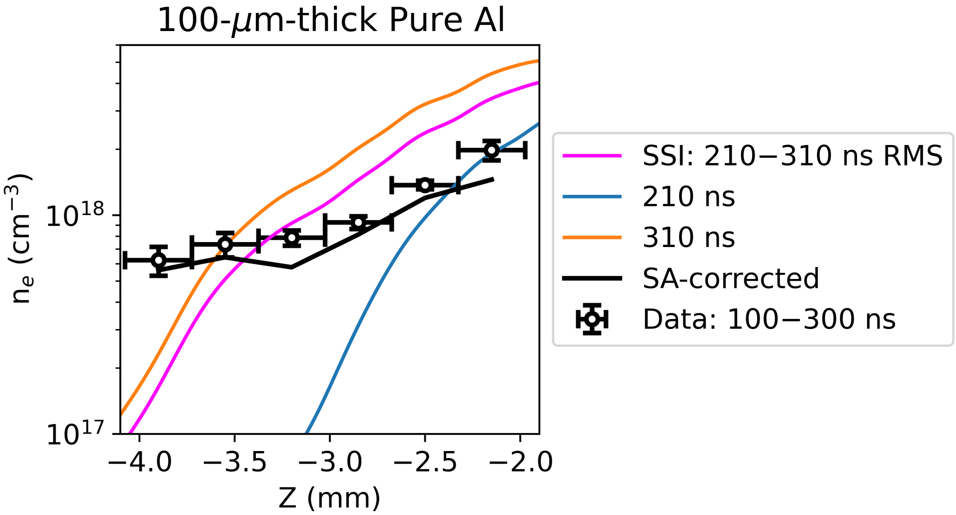

Figure 8.26: Overlay of the spatially resolved 394.401 nm Stark densities from Fig. 8.7 from 100–300 ns (the RMS density over 200–300 ns is shown in magenta) with the axial density profiles on axis at $R = 0$ (integrated from $R = -0.5$ to $R = +0.5$ mm) from the SSI measurements. The black line represents the SA-corrected densities. On average, they correspond to a 17% reduction from the uncorrected densities from Stark broadening. The density gradient observed from the spectroscopy measurements matches the SSI closer to the foil surface, but diverges at larger axial extents.

4s doublet now yield the same inferred electron densities across nearly all datapoints within their respective error bars. The average correction for the Stark densities calculated from the 394.401 nm line is 17%, and the average correction for the Stark densities calculated from the 396.152 nm line is 29%. This result confirms the validity of using the model-calculated SA coefficient to correct for self-absorption in the measured spectra, and also supports the observation that the higher-opacity 396.152 nm line experiences a higher degree of SA compared with the 394.401 nm line.

Spatial correlation of the spectroscopy measurements with the expanding plasma plume requires comparison with the SSI measurements. Figures 8.26 and 8.27 show the SSI n_e profile on axis from 100–300 ns and 300–500 ns, respectively, overlaid with the inferred densities from the Stark analysis of the spatially resolved spectrometer measurements of the Al-I 394.401 nm line. The SA correction is applied using Eq. 6.7 and the results from Fig. 8.24. For the 100–300 ns measurements, which are displayed in Fig. 8.25, the average SA correction is 17%, while for the 300–500 ns, the average SA correction is 35%. Both of these plots show that the densities calculated from the Stark broadening of the Al-I 3p-4s 394.401 nm line agree well with the expected density profile measured by the SSI at axial extents closer to the foil surface. However, the lack of universal agreement between the spectroscopy results and SSI measurements at larger axial extents cannot be solely explained by the presence of SA.

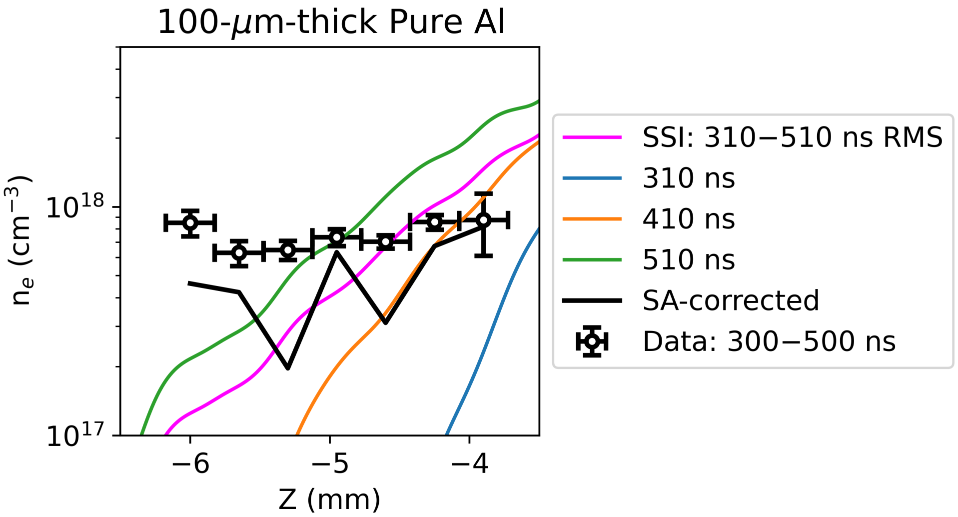

Figure 8.27: Overlay of the spatially resolved 394.401 nm Stark densities from Fig. 8.7 from 300–500 ns (the RMS density over 300–500 ns is shown in magenta) with the axial density profiles on axis at $R = 0$ (integrated from $R = -0.5$ to $R = +0.5$ mm) from the SSI measurements. The black line represents the SA-corrected densities. On average, they correspond to a 35% reduction from the uncorrected densities from Stark broadening. Similar to Fig. 8.26, the density gradient observed from the spectroscopy measurements matches the SSI nearer the foil surface, but tents to overestimate the density at larger axial extents.

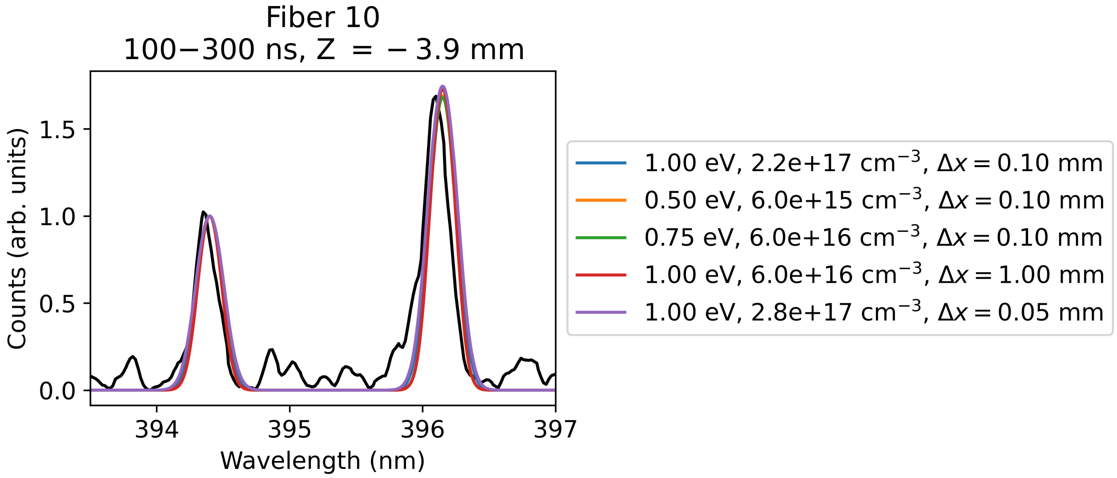

Figure 8.28: Overlay of Fiber 10, 100–300 ns, $Z = -3.9$ mm with the SA model using combinations of different temperatures, densities, and slab thicknesses. The line ratio of the measurement is 1.65:1. From this ratio, the inferred SA of the measured lines (black trace) is $\mathrm{SA}_{394\mathrm{nm}} = 0.82$ and $\mathrm{SA}_{396\mathrm{nm}} = 0.68$. The intensities are normalized to the 394 nm peak.

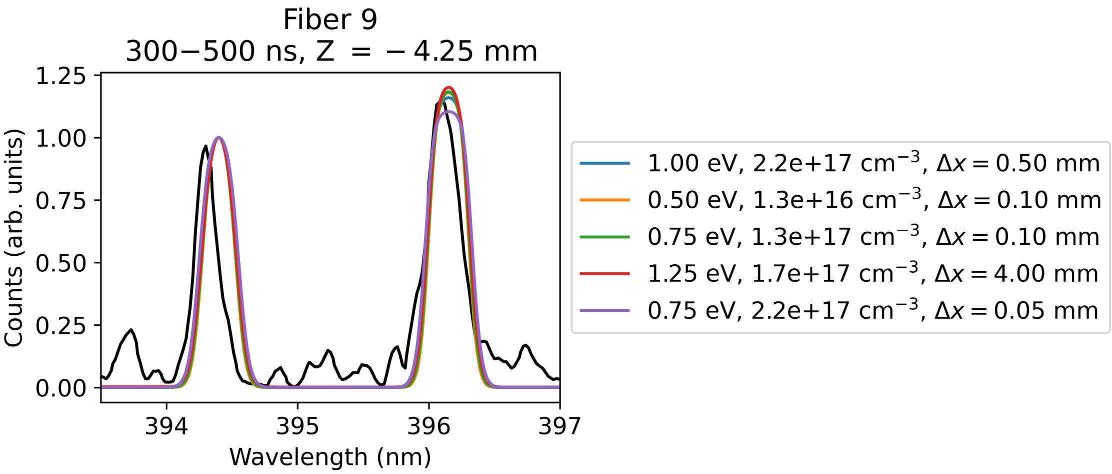

Figure 8.29: Overlay of Fiber 9, 300–500 ns, $Z = -4.25$ mm with the SA model using combinations of different temperatures, densities, and slab thicknesses. The line ratio of the measurement is 1.38:1. From this ratio, the inferred SA of the measured lines (black trace) is $\mathrm{SA}_{394\mathrm{nm}} = 0.64$ and $\mathrm{SA}_{396\mathrm{nm}} = 0.45$. The intensities are normalized to the 394 nm peak.

Using the simple SA model results in an under-constrained minimization problem, as three variables are being used to match a single quantity (the SA coefficient or, identically, the line ratio). Figures 8.28 and 8.29 plot the measured spectrum (black trace) from the fibers indicated along with overlays of the SA model calculations at selected T_e, n_e, and Δx combinations. The fitting procedure involves matching the line ratios, or the SA coefficient, for each of the lines. For the 100–300 ns gate, the curve corresponding to (1 eV, 2.2×10^{17} cm^{-3}, $\Delta x = 0.1$ mm) in Fig. 8.28 most reasonably matches the measured spectrum. Similarly, for the 300–500 ns gate, the curve corresponding to (1 eV, 2.2×10^{17} cm^{-3}, $\Delta x = 0.5$ mm) in Fig. 8.29 most reasonably matches the measured spectrum. The most clear example of this under-constraining of the fitting parameters is the red curve shown in Fig. 8.29, which corresponds to 1.25 eV, 1.7×10^{17} cm^{-3}, and $\Delta x = 4$ mm; the 4 mm slab thickness is nonphysically large compared to the SSI-measured n_e radial profiles shown in Fig. 8.22.

Comparing these inferred densities with the results shown in Figs. 8.26 and 8.27, it seems that the measurement earlier in time agrees well with the time-averaged density profile, while the measurement later in time underestimates the n_e. The early-time experimental measurement at a large axial extent ($Z = -3.9$ mm) yields a SA-corrected Stark width that overestimates the SSI-measured n_e, while the fit by the SA model infers a density that matches well with the SSI. This fact implies that the spectrometer resolution may be the limiting factor in the narrowest line width, and thus the smallest n_e, the spectrometer is able to measure.

For both cases, a better match of the line profiles can be obtained by generating the SA spectra over a finer range of electron temperatures and densities, e.g., 0.1 eV steps (instead of 0.25 eV steps) and more density points per decade. So, the SA model can be used to produce a surface in the 3-D phase space of (T_e, n_e, Δx) that corresponds to a specific value of the line ratio, or SA coefficient. From here, additional constraints can be placed to reduce the volume of the phase space by accounting for the measured n_e profiles, as shown in Figs. 8.26 and 8.27. This analysis will be repeated in the future for all of the measured line profiles shown in Figs. 8.3 and 8.4.

The synthetic spectra have been shifted in wavelength by -1.131Å to account for transmission through air. Note that the shift from the measured line centers with respect to the expected (modeled) line centers is not the result of a Doppler shift—instead, it is explained by the spectrometer calibration and the boxcar filter (five points wide) used to smooth the measured spectrum.

An unfolding of the 2-D electron temperature profile from the SSI shadowgraph measurement will help accurately assess the spatial origin of these spectral lines by allowing the construction of a radiation transport model using the experimentally measured temperature and density profiles of the plasma plume. This will be the subject of future work.

8.6 Summary of Results

Quantitative measurements of the plasma plume expansion for electron beam heated pure aluminum foils of varying thicknesses have been successfully performed. Near-field OTR resolved a consistent beam spot size across all foil thicknesses (50 μm, 100 μm, and 200 μm). Complementary spectroscopy chords successfully measured emission of both the Al-I 3p-4s lines at 394/396 nm and the Al-I 3p-3d lines at 308/309 nm. A comparison of the SSI n_e profiles confirms a slightly faster expansion and larger plume extent for thicker foils compared with thinner foils due to the increased pressure buildup. A simple SA model was created using calculations from the Los Alamos suite of atomic physics codes to interpret the plasma conditions that produced the measured spectra. Full scale spectroscopic-quality radiation transport calculations were also performed using the hydro outputs from LASNEX, but they are unable to replicate the experimental line shapes due to LASNEX calculating a n_e profile that differs significantly from the measured SSI density profile. Potential future improvements to this work include looking into using a modern aluminum EOS that incorporates vapor dome physics relevant for modeling dense plasmas, as well as advocating for development of a hydro code that includes the correct physics for modeling the beam-target interaction dynamics.

The simple SA model is able to reasonably replicate the measured spectra, and the inclusion of the SA correction helps bring the experimentally measured Stark widths from spectroscopy into agreement with the SSI-measured density profiles. However, the spectrometer resolution is still the limiting factor on how low of a density can be measured by Stark broadening. If the line widths are larger than the instrument response function (which is a function of the spectrometer slit width), then the convolution of these two profiles will result in a line shape corresponding to the instrument response, rather than the true line shape. Based on the narrowest line width of 1.99 $\AA$ measured in the experiments, this corresponds to a resolving power around $\lambda/\Delta\lambda \approx 2000$ for the 200 μm slit width used. However, this large slit width is required for the experimental measurements of the Al-I 3p-4s doublet, due to the low number of counts produced on the CCD, even with the long 200 ns gate widths.

In summary, the analyses presented within this chapter on the SA nature of the Al-I 3p-4s lines are valuable, as they can be applied to other spectral lines that have been observed to undergo self-reversal, which includes spectra from copper, titanium, and tin targets. Based on calibration measurements, an $8\times$ reduction in the spectrometer slit widths (200 μm to 25 μm) will only decrease the measured counts by $3\times$, while increasing the resolution by $\sim 3.3\times$. The use of X-ray probes is ultimately what will be needed to make higher density measurements earlier in time.

CHAPTER 9

Conclusions

9.1 Achievements

Substantial progress toward the development of a diagnostic platform for the DARHT electron beam-target interaction studies has been made over the course of this Ph.D. work. The results of these measurements on aluminum using this diagnostic platform are displayed in Figure 9.1. This plot shows the predicted peak T_e and n_e achieved as a function of time by a representative LASNEX simulation of an electron beam heated 100 μm pure aluminum foil using SESAME EOS 3715. These peak values correspond to the dense core of the plasma plume, which, due to opacity limitations of the existing diagnostic suite measuring only in the visible regime, has not been directly measured up to this point. The model predicts that the core of plasma plume may exist in the WDM state from 50–200 ns.

The region highlighted in magenta shows the region of phase space accessed by the experimental measurements presented in this dissertation, which includes both spectroscopy and interferometry. These measurements are representative of times from 100–500 ns, but are limited to measuring the outer, lower density layers of the plasma plume due to opacity effects. Future diagnostics, which are described in Section 9.2, will make higher density measurements earlier in time to corroborate the simulation results, and begin to probe the WDM state directly.

The following subsections describe chapter-by-chapter both the experimental and computational achievements.

9.1.1 Chapter 4

In Chapter 4, the construction, calibration, and fielding of a long wave UV spectrometer is discussed. This new capability permitted the measurements of spectral lines down to ~250 nm, which is a relevant spectral range for the transition metals used as targets in electron beam-target interaction experiments.

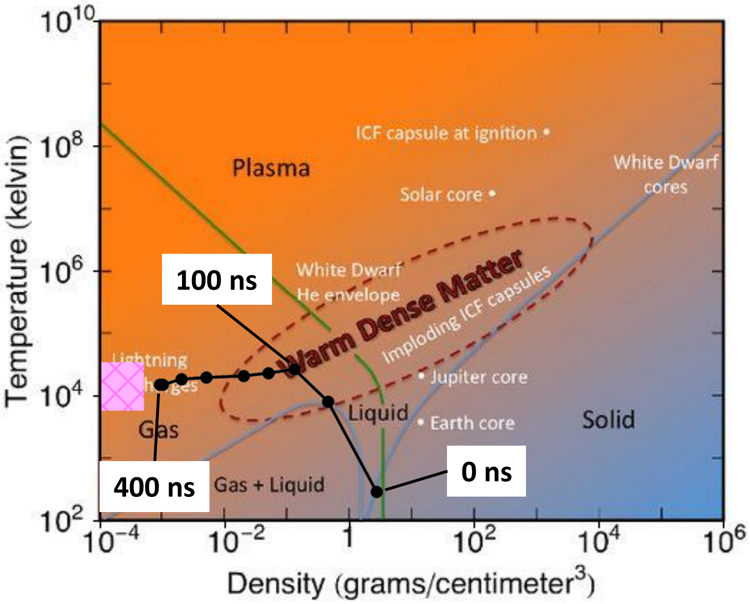

Figure 9.1: Temperature–density phase space plot which highlights the WDM regime situated among the four traditional states of matter. Figure from https://www.lanl.gov/. Overlaid on this plot in black points is the phase space trajectory of the peak T_e and n_e values from a representative LASNEX simulation of an electron beam heated 100 μm pure aluminum foil using SESAME EOS 3715. Also shown is a hashed magenta region which represents the region of phase space accessed by the set of measurements presented in this dissertation.

9.1.2 Chapter 5

In Chapter 5, a pulsed low-pressure hollow cathode has been fabricated and characterized for its potential as an EUV calibration source for next-generation DARHT beam-target interaction diagnostics. The spatial and temporal characteristics of the discharge with different background gases were diagnosed with self-emission imaging and long wave UV spectroscopy. The solid-state pulsed power system required to drive this source was also designed, modeled, built, and successfully employed to produce a discharge.

9.1.3 Chapter 6

In Chapter 6, the use of the Los Alamos suite of atomic physics codes along with a spectroscopic-quality radiation transport code to model emission and absorption lines from DARHT electron beam-target interaction plasma plumes is detailed. This capability to link the LASNEX radiation hydrodynamics model with the FESTR radiation transport code did not exist before this work. A preprocessor code was written that translates the LASNEX dump files into a FESTR-readable format. This capibility led to the improvement of the resolution in the LASNEX simulations in the lower density parts of the plasma plume, which is relevant for modeling the spectroscopic lines in the visible and long wave UV regimes. Modifications to the FESTR code to track the optical depth accumulated by the synthetic spectrum as it is built up enable a more accurate analysis of the plasma conditions from which optically thick lines originate. Additionally, proof-of-principle EUV calculations of L-shell emission lines from an aluminum warm dense plasma were performed, along with a parameter sensitivity study within the Los Alamos suite of atomic physics codes, to inform future diagnostic development.

9.1.4 Chapter 7

In Chapter 7, the first set of spatially and temporally resolved spectroscopic measurements of electron beam driven aluminum (1100 alloy) were made. Contamination quantification analyses performed with LIBS and XPS were used to understand the origin of the strong Na-I 3p-3s lines (D-lines) that were observed in absorption within an aluminum plasma continuum. These results informed the creation of the first spectroscopic-quality radiation transport model that linked together several different codes to interpret the conditions from which the sodium D-lines originated. A good agreement was found between the XPS results and the model, which confirmed the concentration of the sodium present within the aluminum alloy foil material, and which demonstrated, for the first time on an electron beam driven target experiment, the ability to interpret plasma conditions from measured absorption lines.

9.1.5 Chapter 8

In Chapter 8, the first measurements of beam-target interaction emission lines in the long wave UV regime are presented. The Al-I 3p-4s and 3p-3d doublets were both measured in emission. A detailed analysis of the Al-I 3p-4s doublet reveals that the lines undergo moderate self-absorption. The optical depth tracking modification was used with success to extract radial plasma temperature and density profiles from which the optical depth is evaluated. The full-scale spectroscopic-quality radiation transport model, however, was unable to replicate the line shapes measured in experiment because of the large discrepancy in the density profiles predicted by LASNEX verses those measured by the SSI. A simple model of the SA was used to successfully match the experimentally measured spectra with various combinations of temperature, density, and slab thickness in the model. These measurements led to the realization of the minimum density that can be resolved by the spectrometers for the Al-I 3p-4s lines due to the large slit width required to observe a signal on the CCD cameras. These measurements also demonstrate the sensitivity of visible and long wave UV spectroscopy to minor changes in both T_e and n_e. The simple SA model will be useful for analysis of other beam-target interaction experiments with spectra exhibiting either self-absorption or full self-reversal.

9.2 Future Recommendations

The motivation for diagnosing the DARHT electron beam-target interaction stems from DARHT's role in serving the Stockpile Stewardship Mission, which ensures the safety, reliability, and effectiveness of the U.S. nuclear deterrent. The DARHT accelerators are used for weapons radiography and produce these radiographs by converting the kinetic energy of the electron beam into bremsstrahlung X-rays using a high-Z converter target. While the current batch of studies has been performed on Axis-I, a single pulse LIA with a simple target geometry on low-Z materials, the ultimate goal is to move to diagnosing multi-pulse, high-Z bremsstrahlung converter target interactions that are found on DARHT Axis-II and future flash radiography machines based on an electron LIA. Understanding how the target plasma is produced and evolves in space and time is critical to ensuring the radiographic spot is well diagnosed. This enables comparisons to be made between experimental radiographs and synthetic radiographs from computer simulations. This also enables measurements of the WDM state and the benchmarking of hydrodynamics codes in general, including the benchmarking of the EOS tables used by the hydro codes to model material properties and transport in the WDM regime. To this end, the following recommendations for future work are suggested. The order of this list is a reflection of the author's thoughts on how a potential timeline might evolve.

1. Improve upon the simple self-absorption model by incorporating a finer resolution of temperatures and densities over which the spectral databases are generated. A fitting algorithm could be developed that automatically varies the independent variables (temperature, density, slab thickness) to match to a user-specified quantity (line ratio, line width, etc.).

2. Extract 2-D electron temperature profiles from the SSI shearing and shadowgraph datasets using existing single-point opacity databases at 532 nm. The opacity calculations combined with measured n_e from the sheared images and absorption from the shadowgraphs will provide 2-D n_e and T_e distributions. These resulting 2-D temperature and density profiles can then be directly imported into FESTR to produce synthetic spectra that can be compared directly with measured spectra.

3. Formalize the modifications to the FESTR code to permit optical depth tracking in any arbitrary 3-D geometry.

4. Continue to iterate on LASNEX runs with aluminum SESAME EOS 3720 to better understand the effect that the inclusion of the vapor dome has on the beam-target interaction and hydrodynamic expansion, compared with the legacy SESAME EOS 3715. In short, work to obtain a better match of the 2-D density profiles between LASNEX and the SSI.

5. Advocate for the development of a LANL-based code that includes the relevant physics required for modeling the electron beam-target interaction. No code at present has all of the correct physics packages required to model the collisional and radiative energy deposition by a relativistic electron beam.

6. Perform spectroscopic-quality radiation transport calculations of K- and L-shell (and possibly M-shell, depending on the target material) X-ray spectra from target materials of interest. To this end, the EUV decks for aluminum have already been generated.

7. Continue to improve upon full-scale spectroscopic-quality radiation transport modeling of spectral lines observed in the transition between emission and absorption, including self-reversal, for other target material of interest, including titanium, copper, tin, molybdenum, and tantalum. This analysis can be applied to already-existing datasets.

8. Extend the beam-target diagnostic capabilities to the X-ray regime to directly measure the target plasma density, temperature, and spatial extent early in time in the WDM phase. These techniques in the X-ray regime could include Thomson scattering, absorption spectroscopy, Talbot-Lau phase-contrast imaging, and radiography of the dense plasma plume early in time.

9. Ultimately, push to the high-Z materials used for bremsstrahlung converter targets on DARHT to directly probe the relevant physics regimes for Stockpile Stewardship radiography missions.

The nearest term items described by 1–3 represent the work that should have a quick completion time, perhaps under a year. Item 1 requires a simple increase in the range of temperatures and densities for which spectra are calculated. Item 2 utilizes existing datasets, so the proper analysis for the temperature unfolding along with the uncertainty quantification is all that is required. Item 3 involves modifying the FESTR code in the proper manner for the optical depth tracking; the present modification is only applicable to the 2-D cylindrically symmetric geometry used by LASNEX.

Items 4–5 are related and both are somewhat longer term, especially item 5. The EOS study should be relatively straightforward; however, the difficult part of performing this study is ensuring the ancillary knobs within LASNEX are appropriately set for the problem at hand. Going through these in detail may involve a large amount of work.

The additional computational items represented by 6–7 range from being very straightforward to much more involved. An example of the straightforward case would be extending the modeling already performed on aluminum, which has been presented in this dissertation. A framework currently exists for this material to perform L-shell calculations, so it could be pushed further to include K-shell spectra. A move involved example is the modeling of Sn, where much of the CATS and GIPPER calculations would need to be performed before moving onto the spectral calculations. A separate challenge is developing the radiation hydrodynamics model and using the appropriate EOS for this target material.

Finally, items 8–9 represent the next steps for the experimental platform used to study the electron beam-target interaction. The experimental results presented in this dissertation are limited in the peak densities measured by the diagnostics, so a push to higher energy diagnostics, which will make measurements in the X-ray regime, is required to measure the plasma plume early in time while it exists in the WDM phase. In Fig. 9.2, this corresponds to ultimately extending the range of the magenta box to higher densities. Item 9 represents the stretch goal in which the fully developed diagnostic suite described in item 8 is deployed on the bremsstrahlung converter target. This will require a substantial amount of effort and coordination among DARHT personnel and facility space, but will also provide critical measurements of the actual beam-target interaction physics in the actual radiographic configuration.

APPENDIX A

Beam Steering Algorithm

The steering algorithm described in Equations 3.10–3.12 was implemented into an IDL-based GUI, `vis_str`, for real-time beam tuning. The program interfaces with a separate IDL program, `wid_beam`, which acts as a self-contained Axis-I beam analysis toolkit.

Figure A.1 is displayed when `vis_str` is run. The user is prompted to select the date of the shots used for steering, along with the corresponding shot numbers that match up with the dipole iterations listed in the right-hand column. One limitation here is the shots used for steering must all be on the same date. This can be generalized in the future, if needed. The BPM for the steering correction is then selected. At present, the program will automatically select the next subsequent BPM after the chosen one for the calculations. The steering coils are then selected, along with the option to steer the beam either on-axis (normal mode of operations), or off-axis (implemented for future beam experiments).

The user can then choose to plot the selected centroids (*Plot Selected Centroids*) to verify the magnet iterations do not exceed the dynamic range of the BPM, as shown in Figure A.2. To analyze and correct the steering, the user selects *Calculate/Visualize Steered Centroids*, which will generate the plots shown in Fig. A.2 in addition to Figure A.3, providing the user with the new dipole settings by which to correct the centroid at the initial steering coil selected.

Figure A.4 shows plots of the beam centroid before and after the steering correction. This beam steering was used for the focused shot series that generated the data analyzed in Chapter 8. The time dependent motion of the beam centroid which is observed throughout the temporal duration of the pulse is known as corkscrew, and it is a result the chromaticity of the beam combined with cumulative misalignments of accelerator solenoids.

The current version of the `vis_str` program can be found at:

`\\darht-ops\Common\nramey\beam_str_4x4`

Note this is only available to internal LANL users that have access to the local DARHT network.

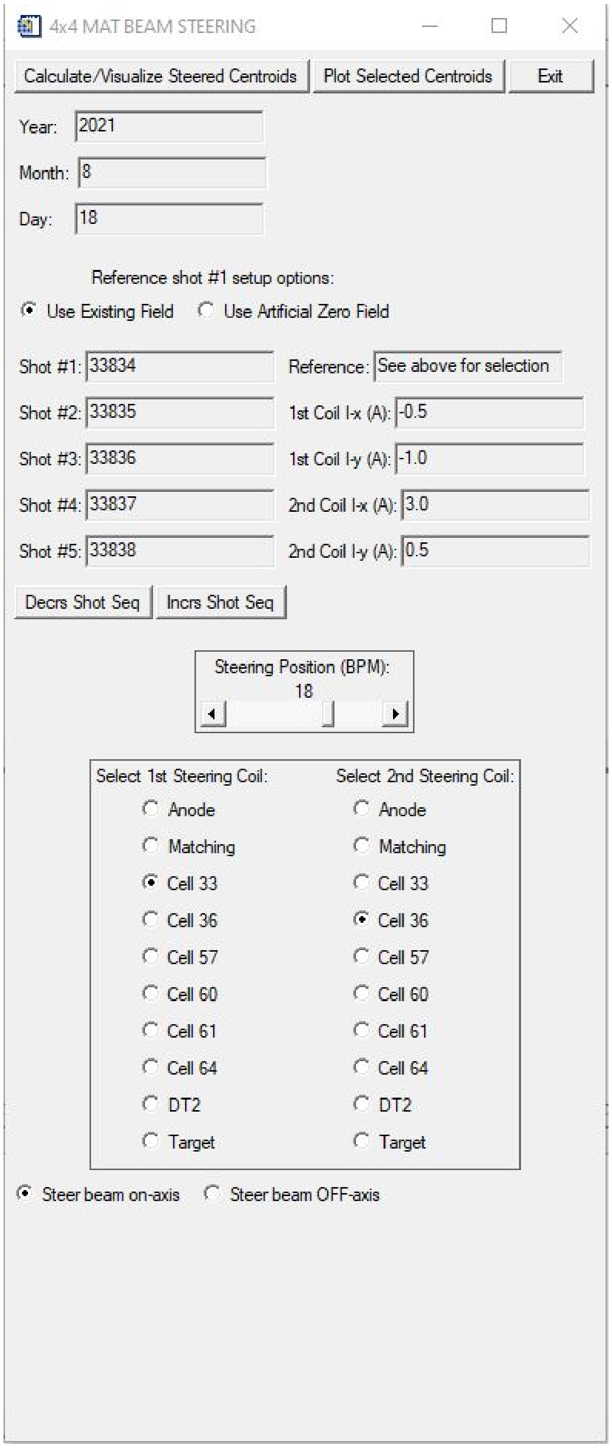

Year: 2021

Month: 8

Day: 18

Reference shot #1 setup options:

● Use Existing Field ○ Use Artificial Zero Field

Shot #1: 33834 Reference: See above for selection

Shot #2: 33835 1st Coil I-x (A): -0.5

Shot #3: 33836 1st Coil I-y (A): -1.0

Shot #4: 33837 2nd Coil I-x (A): 3.0

Shot #5: 33838 2nd Coil I-y (A): 0.5

Steering Position (BPM): 18

Select 1st Steering Coil:	Select 2nd Steering Coil:
○ Anode	○ Anode
○ Matching	○ Matching
● Cell 33	○ Cell 33
○ Cell 36	● Cell 36
○ Cell 57	○ Cell 57
○ Cell 60	○ Cell 60
○ Cell 61	○ Cell 61
○ Cell 64	○ Cell 64
○ DT2	○ DT2
○ Target	○ Target

● Steer beam on-axis ○ Steer beam OFF-axis

Figure A.1: Initial GUI for the 4x4 matrix beam steering.

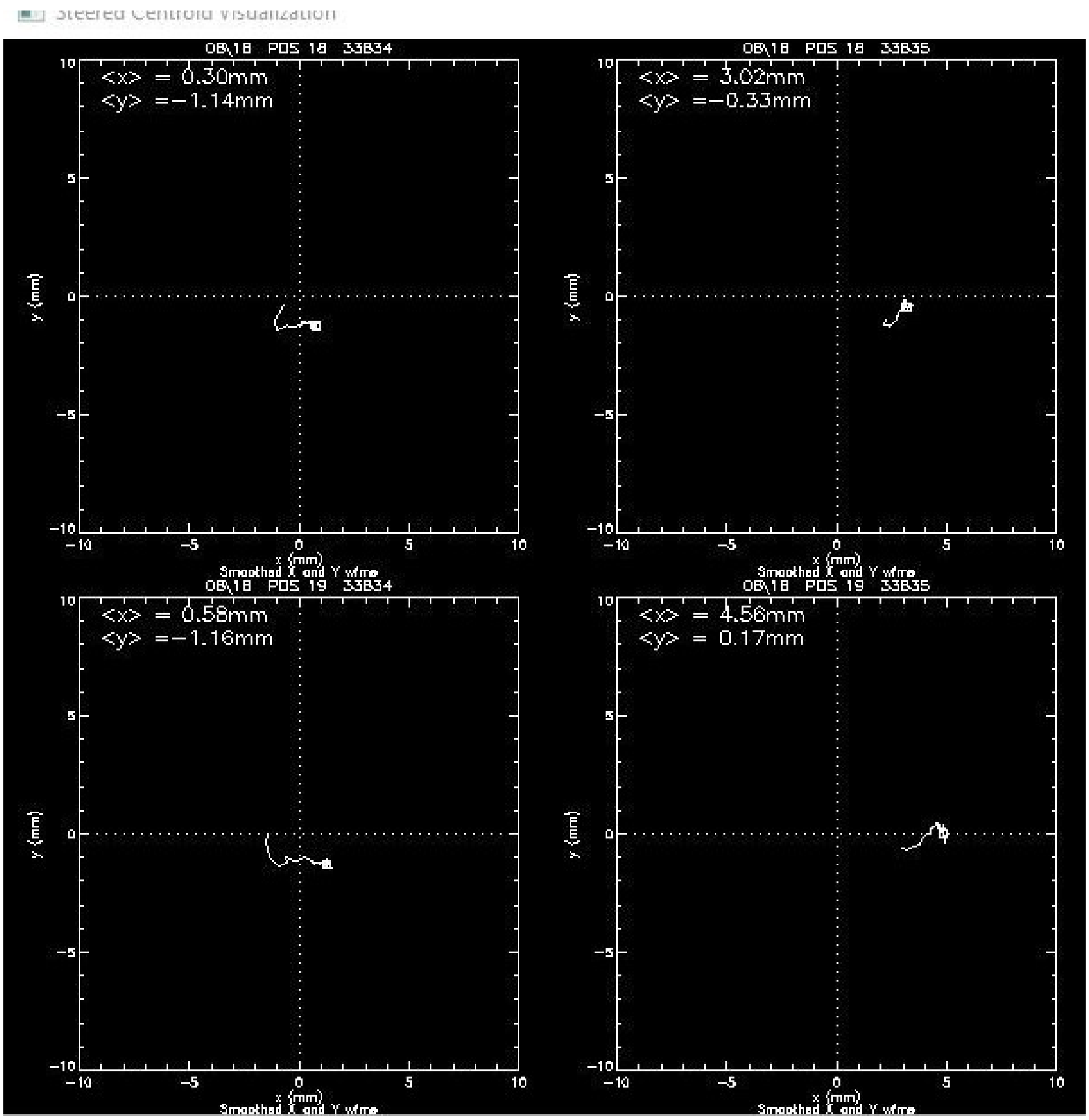

Figure A.2: Plots of the beam centroids for the selected shots at BPM 18 and 19 showing only the first two shots, consisting of the control shot and the 1st dipole kick in $\hat{x}$. Values of $\langle x\rangle$ and $\langle y\rangle$ are also displayed. Note that when the program is run, it plots the centroid of both BPMs for all five shots.

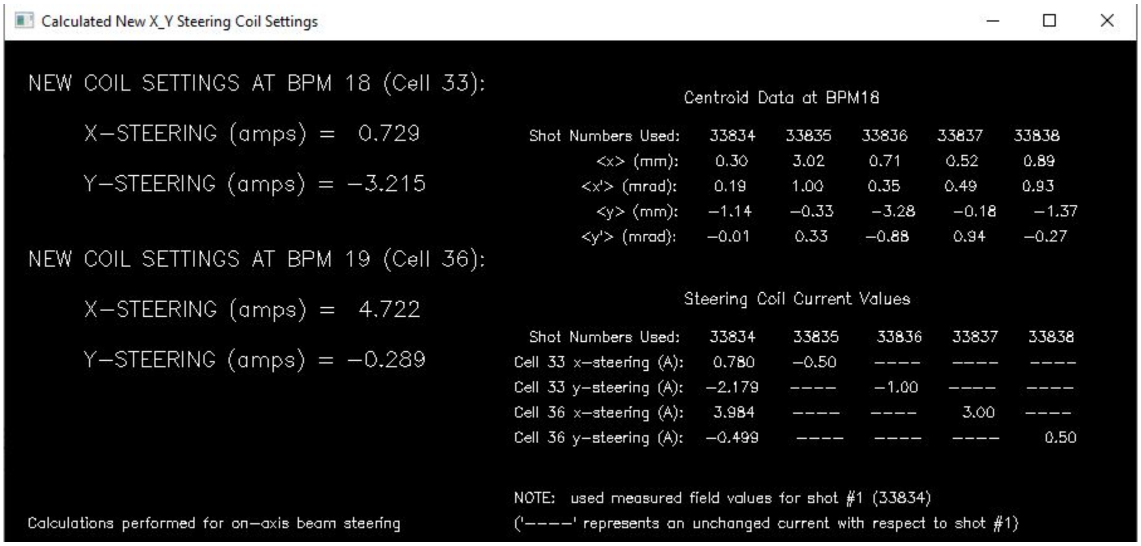

```
NEW COIL SETTINGS AT BPM 18 (Cell 33):                     Centroid Data at BPM18

     X-STEERING (amps) =  0.729            Shot Numbers Used:   33834   33835   33836   33837   33838
                                                    <x> (mm):    0.30    3.02    0.71    0.52    0.89
     Y-STEERING (amps) = -3.215                  <x'> (mrad):    0.19    1.00    0.35    0.49    0.93
                                                    <y> (mm):   -1.14   -0.33   -3.28   -0.18   -1.37
                                                 <y'> (mrad):   -0.01    0.33   -0.88    0.94   -0.27
NEW COIL SETTINGS AT BPM 19 (Cell 36):

     X-STEERING (amps) =  4.722                          Steering Coil Current Values

     Y-STEERING (amps) = -0.289            Shot Numbers Used:   33834   33835   33836   33837   33838
                                         Cell 33 x-steering (A):  0.780   -0.50    ----    ----    ----
                                         Cell 33 y-steering (A): -2.179    ----   -1.00    ----    ----
                                         Cell 36 x-steering (A):  3.984    ----    ----    3.00    ----
                                         Cell 36 y-steering (A): -0.499    ----    ----    ----    0.50

                                         NOTE:  used measured field values for shot #1 (33834)
Calculations performed for on-axis beam steering   ('----' represents an unchanged current with respect to shot #1)
```

Figure A.3: Results of the steering algorithm. The new dipole coil settings will center the beam at BPM 18.

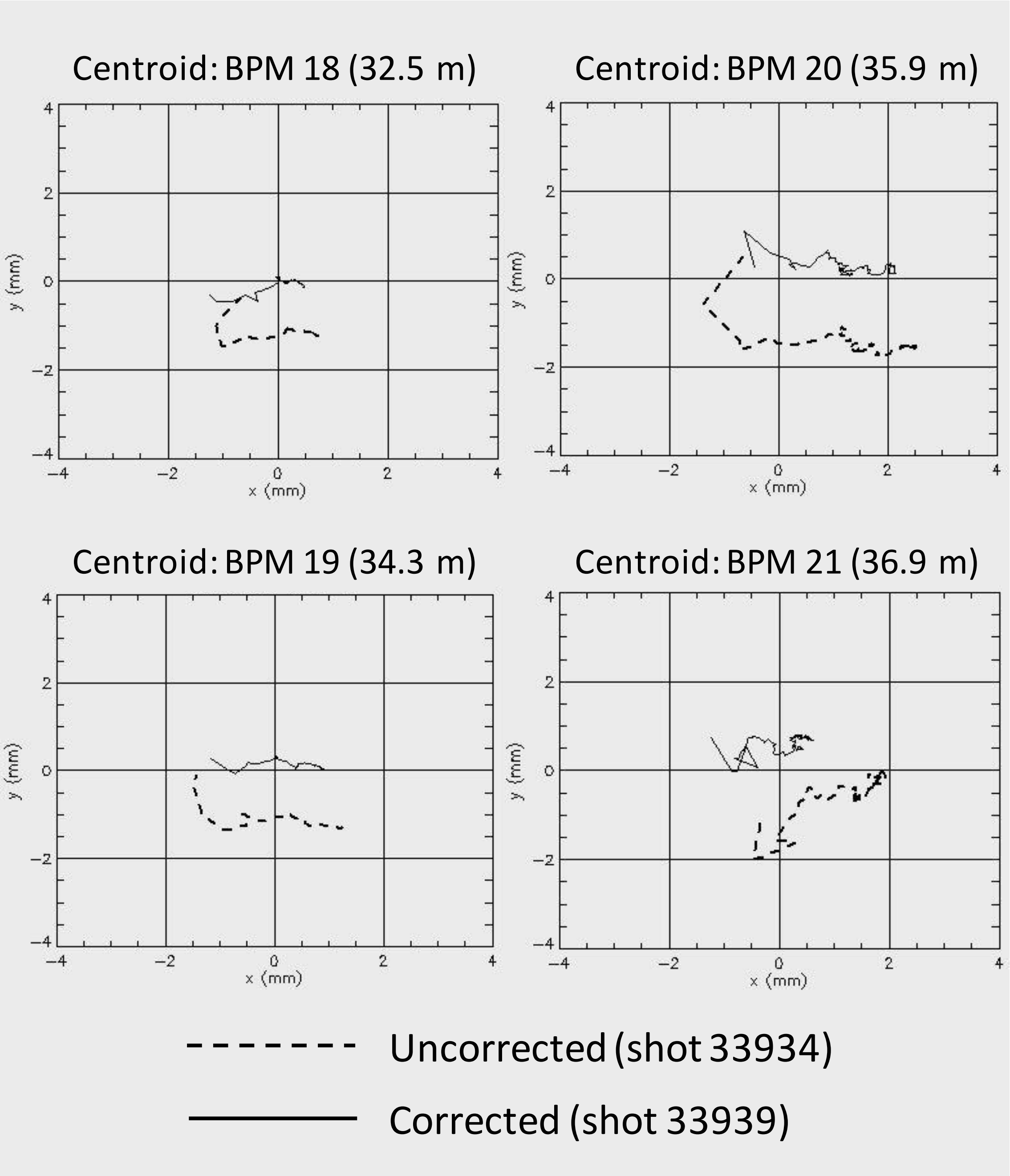

Figure A.4: Comparison of beam centroid location before and after applying the steering algorithm at BPMs 18–21. Before steering correction is shown as a dashed line, and after the steering correction is shown as a solid line.

APPENDIX B

Los Alamos Suite of Atomic Physics Codes Supplementary Information

This appendix discusses in more detail the specific usage of the Los Alamos suite of atomic physics codes at LANL. These details are relevant only for LANL employees as these codes, while unclassified, are not available to the public.

B.1 Useful Commands

This section defines many of the commonly used commands in the input decks for generating the relevant binary Independent of Platform and Can be Read by Existing Software Subroutines (IPCRESS) and ASCII p files produced and/or used by CATS, GIPPER, and ATOMIC, and also briefly touches on some useful commands within TAPS, which is a code that is used to interrogate the CATS and GIPPER IPCRESS files. Tables B.1–B.4 are provided for each code, defining the usage and required arguments for each specific command. Example input decks in the form of screenshots (Figures B.1–B.3) are also provided.

These codes are highly integrated with one another. A common use for the whole suite relevant to the applications contained within this dissertation is the following:

1. Build the CATS input decks (the configurations for each ion stage, typically I–IV for low-Z beam-target interaction plasmas). See Table B.1 and Figure B.1 for command descriptions and an example input deck, respectively.

2. (optional) Extract the relevant data from the NIST ASD Levels and Lines databases to generate the `nist.dat` and `nistgf.dat` files, respectively [142].

3. Proceed with CATS runs.

4. Use TAPS to interrogate CATS IPCRESS files to ensure that the NIST values (if used) are correctly matched. See Table B.2 for command descriptions.

5. Build the GIPPER input decks (typically, the number of GIPPER runs required is one less than the total number of CATS runs, i.e. the transitions for I–IV are I–II, II–III, and III–IV). See Table B.3 and Figure B.2 for command descriptions and an example input deck, respectively.
6. Proceed with GIPPER run(s).
7. Build the ATOMIC input deck. See Table B.4 and Figure B.3 for command descriptions and an example input deck, respectively.
8. Proceed with ATOMIC run(s).
9. Based on the `plt` output, ensure that the number of included stages results in a converged charged state distribution.
10. Identify line(s) of interest (wavelength or energy) in the output spectrum.
11. Use TAPS to identify the relevant transitions/levels/gf values for the above line(s). Again, refer to Table B.2 for command descriptions.

Command	Argument(s)	Description
`opend`	`<`c_i`>`	Writes result to an IPCRESS format output file with name c_i, overwriting any file that previously exists with the same name.
`ion`	`<Z> <i>`	Defines ion stage of interest, where `Z` is the atomic number and `i` is the ionization (1 = neutral, 2 = singly ionized, etc.).
`check_configs`	`<off/on>`	Removes duplicate configurations from the input list.
`exptl_energies`	`<off/on>`	Compares and corrects configuration energies to a user-supplied `nist.dat` file.
`exptl_gf`	`<off/on>`	Compares and corrects configuration gf values to a user-supplied `nistgf.dat` file.
`kcc`	`<#>`	Specifies the number of configurations in the file. Required if the number of configurations exceeds 200.
`rcf`	n/a	Specifies configurations. Configurations are listed one per line following this command.
`/`	n/a	Signifies end of configuration list.
`pwb`	n/a	Turns on plane-wave Born electron impact excitation cross section calculations. Required only for non-LTE runs in ATOMIC.
`run`	n/a	Begins fine-structure atomic structure calculations.
`rcn2n`	n/a	Begins configuration average atomic structure calculations.
`end`	n/a	Terminates CATS run and closes all files.

Table B.1: Common commands and descriptions for CATS input decks used to generate IPCRESS files. Note that the command arguments, when used in the input deck, are not actually contained within brackets, e.g. using the `opend <`c_i`>` command for naming the output IPCRESS-format CATS file `tal01` (Al-I) would read: `opend tal01`. More details on these commands (and additional commands not discussed) can be found in [10].

B.2 TaskPoolTupleAtomic

TaskPoolTupleAtomic is a program that uses the `TaskPoolTuple` class template to parallelize the running of the ATOMIC code over a grid of user-defined temperatures and densities [143]. Separate post-processing codes were written to extract and concatenate all the relevant information from the ASCII p files (T_e, n_e, $\overline{Z}$, $\kappa(\lambda)$, $\epsilon(\lambda)$, etc.) into a text file that can then be ported to a local machine for further data processing. This powerful addition to the capabilities of ATOMIC is illustrated by these next few examples:

1. Generation of single-point opacity databases at 532 nm, 355 nm, and 266 nm over a highly resolved range of temperatures and densities (see Fig. 4.25) to interpret the measured interferograms of the SSI diagnostic [83].

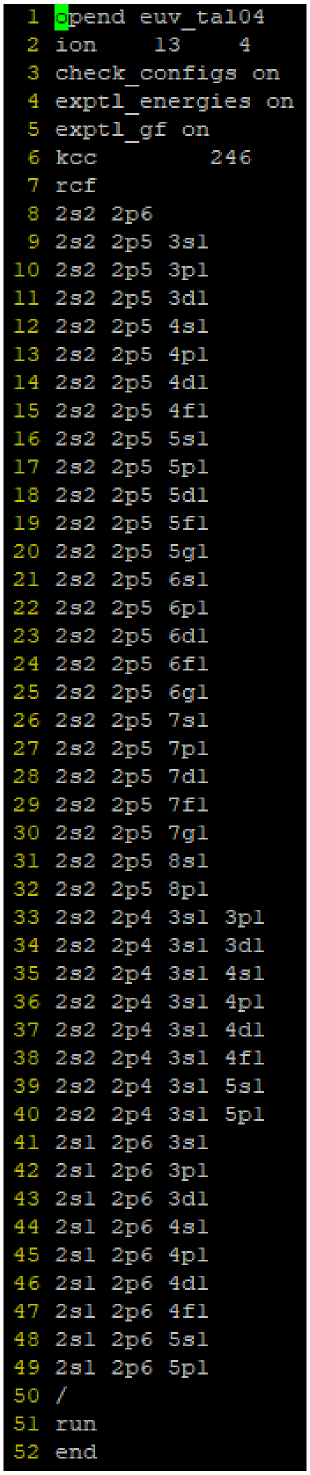

```
opend euv_tal04
ion     13    4
check_configs on
exptl_energies on
exptl_gf on
kcc         246
rcf
2s2 2p6
2s2 2p5 3s1
2s2 2p5 3p1
2s2 2p5 3d1
2s2 2p5 4s1
2s2 2p5 4p1
2s2 2p5 4d1
2s2 2p5 4f1
2s2 2p5 5s1
2s2 2p5 5p1
2s2 2p5 5d1
2s2 2p5 5f1
2s2 2p5 5g1
2s2 2p5 6s1
2s2 2p5 6p1
2s2 2p5 6d1
2s2 2p5 6f1
2s2 2p5 6g1
2s2 2p5 7s1
2s2 2p5 7p1
2s2 2p5 7d1
2s2 2p5 7f1
2s2 2p5 7g1
2s2 2p5 8s1
2s2 2p5 8p1
2s2 2p4 3s1 3p1
2s2 2p4 3s1 3d1
2s2 2p4 3s1 4s1
2s2 2p4 3s1 4p1
2s2 2p4 3s1 4d1
2s2 2p4 3s1 4f1
2s2 2p4 3s1 5s1
2s2 2p4 3s1 5p1
2s1 2p6 3s1
2s1 2p6 3p1
2s1 2p6 3d1
2s1 2p6 4s1
2s1 2p6 4p1
2s1 2p6 4d1
2s1 2p6 4f1
2s1 2p6 5s1
2s1 2p6 5p1
/
run
end
```

Figure B.1: Example CATS input deck. This file is built for an Al-IV ion with inner-shell vacancies corresponding to L-shell transitions.

Command	Argument(s)	Description
`file`	`<fname>`	Loads `fname`, an IPCRESS file generated by the CATS code.
`cfg`	n/a	Displays each configuration and total energy in eV.
`levels`	n/a	Displays a list of levels.
`floorgf`	`<#>`	Sets the smallest electric dipole gf value to be shown.
`angrng`	`<start> <stop>`	Sets the lower and upper bounds of the wavelength range (in Angstroms) to be displayed with `gf`.
`eprng`	`<start> <stop>`	Sets the lower and upper bounds of the wavelength range (in eV) to be displayed with `gf`.
`gf`	`<i1> <i2>`	Lists electric dipole gf values for level to level transitions. The wildcard $\star$ can be used in place of either `i1` or `i2` to go over all levels. If no arguments are provided, all transitions will be listed. These level (integer) indices correspond to the outputs of `levels`.
`end`	n/a	Closes files and exits TAPS.

Table B.2: Common commands and descriptions used in TAPS to interrogate CATS and GIPPER IPCRESS files. Note that the command arguments, when used in the input deck, are not actually contained within brackets, e.g. using the `file <fname>` command for loading the IPCRESS-format file `tal01` would read: `file tal01`. More details on these commands (and additional commands not discussed) can be found in [11].

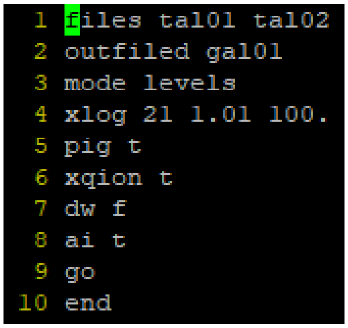

```
files tal01 tal02
outfiled gal01
mode levels
xlog 21 1.01 100.
pig t
xqion t
dw f
ai t
go
end
```

Figure B.2: Example GIPPER input deck. This file is built to calculate the cross sections for ionization transitions between Al-I and Al-II.

Command	Argument(s)	Description
`files`	<$\mathtt{c}_i$> <$\mathtt{c}_j$>	Read in atomic structure (CATS) data files $\mathtt{c}_i$ and $\mathtt{c}_j$, where i and j denote the ion stage. Typically, $j = i + 1$.
`outfiled`	<$\mathtt{g}_i$>	Write result to an IPCRESS-format output file with name $\mathtt{g}_i$, overwriting any file that previously exists with the same name.
`mode`	`<levels/cfg>`	Set the mode for calculating the cross section data: `levels` for fine-structure; `cfg` for configuration average.
`xlog`	`<#> <start> <stop>`	Set up a logarithmic grid of initial and final energies in threshold units.
`pig`	`<t/f>`	Perform photoionization calculation, if true.
`xqion`	`<t/f>`	Perform scaled-hydrogenic collisional ionization calculation, if true.
`dw`	`<t/f>`	Perform distorted-wave collisional ionization calculation, if true.
`ai`	`<t/f>`	Perform autoionization calculation, if true.
`epseig`	`<eps1> <eps2>`	Set a lower limit on the magnitude of the mixing coefficients of the initial (`eps1`) and final (`eps2`) level that will be retained. Can be used by only setting `eps1`, which automatically sets `eps2` = `eps1`. Default value for both is 0.001.
`go`	n/a	Begin ionization calculations.
`end`	n/a	Terminates GIPPER run and closes all files.

Table B.3: Common commands and descriptions for GIPPER input decks used to generate IPCRESS files. Note that the command arguments, when used in the input deck, are not actually contained within brackets, e.g. using the `files` <$\mathtt{c}_i$> <$\mathtt{c}_j$> command for CATS files named `tal01` (Al-I) and `tal02` (Al-II) would read: `files tal01 tal02`. More details on these commands (and additional commands not discussed) can be found in [12].

Command	Argument(s)	Description
`atom`	`<Z> <A>`	Set element used, with atomic number `Z` and atomic mass `A`.
`atmod`	`<cfg/f>`	Set atomic model: `cfg` for semi-relativistic configuration-average, or `f` for semi-relativistic fine-structure.
`mxpr`	`<#>`	Maximum number of pairs of temperature/density points ($= 1$ for all of these runs).
`nppr`	`<#>`	Number of pairs of temperature/density points actually used in the calculation ($= 1$ for all of these runs).
`ions`	<$\mathtt{i}_{min}$> <$\mathtt{i}_{max}$>	Lower ($\mathtt{i}_{min}$) and upper ($\mathtt{i}_{max}$) ion stages to be used in the calculation.
`load`	`<c> <g>`	Root names for CATS (`c`) and GIPPER (`g`) IPCRESS files.
`pfile`	`<pfile>`	Set output filename (default filename is "p").
`te`	`<te>`	Set electron temperature (in eV).
`dne`	`<ne>`	Set electron density (in electrons/cm^{-3}) using `lted` solver.
`anglin2`	`<#> <start> <stop>`	Set photon wavelength grid (linear in Angstroms).
`width`	`<dop/op>`	Set line broadening routine: `width dop` turns on Doppler (thermal) broadening; `width op` turns on collisional broadening with the Doppler broadening.
`idimi`	`<off/on>`	Turns on the improved D-K broadening routine (for use with `width op`).
`icnl`	`<off/on>`	Turns on continuum lowering (pressure ionization).
`sprpow`	<$\lambda/\Delta\lambda$>	Set synthetic spectrometer resolving power.
`lted`	n/a	Calculate LTE populations when n_e is provided via `dne` and solve for n_i. Use `lte` to solve for n_e when n_i is specified via`dn <ni>` (number density) or `dm <m>` (mass density).
`pzb`	n/a	Print Z-bar.
`pdl`	n/a	Print level populations (in ions/cm^{-3}).
`plt`	n/a	Print ion fractions.
`esptim`	n/a	Calculate and print emissivity (in 1/(cm^3 s)).
`abcoef`	n/a	Calculate and print opacity in units of cm^{-1}.
`kappa`	n/a	Calculate and print opacity in units of cm^2/g.
`sigma`	n/a	Calculate and print opacity in units of cm^2.

Table B.4: Common commands and descriptions for ATOMIC input decks used to generate outputs such as emissivity, opacity, and ionization balance. Note that the command arguments, when used in the input deck, are not actually contained within brackets, e.g. using the `atom <Z> <A>` command for aluminum would read: `atom 13 26.9815`.

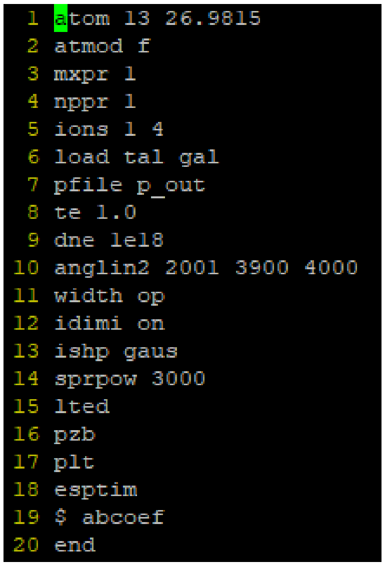

```
atom 13 26.9815
atmod f
mxpr 1
nppr 1
ions 1 4
load tal gal
pfile p_out
te 1.0
dne 1e18
anglin2 2001 3900 4000
width op
idimi on
ishp gaus
sprpow 3000
lted
pzb
plt
esptim
$ abcoef
end
```

Figure B.3: Example ATOMIC input deck. This run is for aluminum over the wavelength range of 390–400 nm, with the D-K collisional broadening routine turned on. Emissivity is being calculated, while the command to calculate opacity has been commented out using `$`.

2. Calculations of similar high resolution single-point opacity databases at the centers of the Al-I 3p-4s doublet to calculate the optical depth of these resonance lines (see Chapter 8, a summary of which is given in Table B.5).

3. Emissivity and opacity database generation (similar to those used by FESTR, with a photon energy grid of 500 points over a 10 nm bandwidth) for two separate Al-I doublets of interest (308/309 nm, grid center of 310 nm; and 394/396 nm, grid center of 395 nm) over 0.1–3 eV and 10^{15}–10^{22} cm^{-3} for a total of 930 runs.

A routine written in C++ called `op_tab_gen` extracts and generates the output files for items

T_e grid (eV)	0.05–3, 0.01 eV step
Total T_e points	295
n_e grid (cm^{-3})	10^{15}–10^{22}, 19 pts/decade
Total n_e points	144
Total combinations of T_e/n_e	42480
Nodes used on *Snow*	4 (×36 CPUs)
Total runtime	$\approx$ 30 minutes

Table B.5: Run summary on the LANL high performance supercomputer *Snow* of the single point opacity calculations for the Al-I 3p-4s doublet. The two energies used for the (separate) runs are 3.1427 eV and 3.1288 eV. A comparable serial run to complete this database generation, assuming 2 s per run, would have taken approximately 24 hours to complete.

1 and 2 above in a four-column format containing the following quantities: [T_e (eV), n_e (cm^{-3}), $\overline{Z}$, κ (cm^{-1})]. This routine can be obtained from the author upon request. Usage of this code is as follows:

```
./op_tab_gen <num_files> <ofile_name>,
```

where `<num_files>` represents the number of ASCII p files generated from the batch run, and `<ofile_name>` defines the output filename.

APPENDIX C

Oz README

Below is the README text file provided with the Oz code. This document explains all of the new routines and files used by Oz to perform its translator function.

README.txt

```
README.txt

Documentation for programs and routines unique to LASNEX_2Dcyl UniTest
        package and the FESTR to LASNEX translator code, known as Oz.

Nicholas Ramey
Los Alamos National Laboratory
J-6, DARHT Engineering, Operations, and Physics

Created on: 27 August 2019
Last modified: 5 May 2022

========================================================================

    NOTE: This document will not elaborate on files used by FESTR in
          its usual operation. In other words, files such as
          "times.txt", "materials.txt", "bounding_sphere.txt" etc. will
          not have their content explained. If they are created by a
          routine listed below, then that process will be explained.
          In addition, test_*.cpp files that have been modified to
          include new tests for these newly introduced capabilities
          will be referenced with the specific new routines that will
          be explained.

========================================================================

* * * * * * * * Step-by-step insctructions for using Oz * * * * * * * *
```

Syntax: braces {} denote variables, quotes "" denote scripts, *) denotes command line, and '\' indicates a line break in a file name, e.g. oz\
_main.cpp
would actually read:
oz_main.cpp
in its normal usage.

(1.a) Move the preliminary reformatter code "pyReadMulti.py" into the same directory containing all the LASNEX hydro dump files. Note the naming scheme that must be followed as stated in the header of "pyReadMulti.py".

(1.b) Ensure the hardcoded variables reqired at the beginning of "pyReadMulti.py" are correct, specficially, the variables {htype}, {nmat}, and {materialsList}.

(1.c) [optional] Modify the variable {printFrequency} for user feedback on preliminary reformatting progress.

(1.d) On LANL HPC machines, execute:

```
*) module load python
```

(1.e) Run "pyreadMulti.py" to generate "t" files:

```
*) python pyReadMulti.py
```

Note: this will also output "materials.txt" and "times.txt" files.

(2.a) In ./oz/src modify the options file "options.txt" to reflect the correct parameters.

```
    (2.b) Move the translated "t" files to the directory specified by
          {T_file_path}.


    (2.c) In the {Hydro_path} directory, create the
          "bounding_sphere.txt" file.


    (2.d) Ensure the {Material_table_path} directory containes the
          "Table.txt" file.


    (2.e) Return to ./oz/src and execute:

          *) make

          Which will compile and link the code to create the executable
          "oz".


    (3.a) Run Oz by executing:

          *) ./oz options.txt


    (3.b) [optional] If the user wishes to record the exact runtime of
          the code, he/she can execute:

          *) time ./oz options.txt


    (4.a) The top directory given by {Top_path} can now be moved to
          FESTR.

=======================================================================

File or routine name            Description
(routine location)



oz_main.cpp                     main() routine that is compiled into
                                the executable "oz" using the options
```

	specified in the file "options.txt". Proper syntax for (1) making then (2) running Oz is the following executed in the src/ directory: *) make *) ./oz options.txt The main() routine in Oz loops over all the timesteps provided in "options.txt" calling the Mesh constructor and creating the "mesh_*.txt", "grid_*.txt" and "time_*.txt" files in a directory defined in "options.txt".
Mesh.cpp	New constructor added that accepts four arguments: path: Direcotry path to "t" files. tlabel: Time-step index label in string form. htype: type of hydro data being read. material_of_interest_index: boolean-like int array that tells Oz which materials to include (1) or exclude (0) in the created "time_*.txt" files. This is called in the main() routine of "oz_main.cpp" and is looped over all timeslices provided in the file "options.txt".
options.txt	Contains all the hardcoded values needed to run Oz. Descriptions of each are included within the file. The

	directory names are such that they observe the reserved directory names to be used in the FESTR "options.txt" file so that the user can move the entire directory (Top_path) to FESTR without file relocation being required within the subdirectories.
OptionsParser.cpp	Called in "oz_main.cpp" to read in the contents of "options.txt". Its purpose is to simplify oz::main(). Includes warnings printed for the user if certain files that FESTR will expect are not in the right locations, specifically the following: "times.txt" not in Hydro/ subdirectory "materials.txt" not in Hydro/ subdirectory "Table.txt" not in Data/ subdirectory "bounding_sphere.txt" not in Hydro/ subdirectory** **this throws an error message because it is required by the Mesh constructor.
OptionsParser.h	Header file for "OptionsParser.cpp".
test_OptionsParser.cpp	Empty file required by the makefile. May fill with some unit tests, but they aren't necessarily required since "optionsParser.cpp" is a relatively simple class.

Foil2D_*.txt	Raw hydro dump from a 2D, cylindrically symmetric LASNEX simulation. The variable "htype" sets this, and is at present equal to "lasnex_2Dcyl". The values given are Zone-centered, and are listed under the top-left Node for each Zone.
Foil2D_020.txt	This dummy file includes the minimum grid required to be fully representative of a full mesh in the form mentioned above. The three other files (008, 050, and 061) only include 6 Zones, and do not include Zones that have Faces fully internal to the Mesh (i.e. not bordering the convex hull of the bounding sphere).
pyReadMulti.py	*** THIS CODE MUST BE RAN BEFORE RUNNING OZ *** Python translator code for converting files of type "Foil*.txt" to "Foil*.t". These "t" files are a simplified version of the LASNEX output files, with values such as the number of nodes, columns, rows, materials located at the header, and the stoichiometric data arranged such that is can be more easily parsed. The program uses the glob module to read in all text files of format "Foil*.txt" in the directory in which it is located. At present the code only writes the "t" files to the same directory. This code also creates

the "times.txt" file required by FESTR. If this is being run on a LANL HPC cluster, "module load python" is required.

```
NOTE: this program requires these hard-
      coded values located under the
      "Variable initialization" section
      (given for the above files):

htype = 'lasnex_2Dcyl' # hydro format
        # required for FESTR to properly
        # read

nmat = 5 # determine this from the
         # hydro file

materialsList = 'h c o al si' # this order
                # must match exactly the
                # hydro file
```

load_LASNEX_2Dcyl_Mesh020\ _Zone0_to_string > this is a unit test > in test_Zone.cpp	Create Zone 0 from "mesh_020.txt" (using FESTR routines) and compare with expected (hardcoded) values.
load_LASNEX_2Dcyl_Time020\ _Zone1_to_string_full > this is a unit test > in test_Zone.cpp	Create material values from Zone 1 of time_020.txt (using FESTR routines) and compare with expected (hardcoded) values. This #includes the "inc" file LASNEX_2Dcyl_time020_Zone1.inc.
bounding_sphere_hydro_size > this is a unit test > in test_Zone.cpp	Creates a bounding sphere and single Zone and compares the size from a Zone routine to the expected size. #includes: "cone_surface.cpp" "bounding_sphere_hydro.inc"

bounding_sphere_hydro\ _to_string > this is a unit test > in test_Zone.cpp	Creates the full string representation of the Mesh defined by #including "cone_surface.inc" and "bounding_sphere_hydro.inc" and compares to the hardcoded (expected) value.
LASNEX_2Dcyl_time020\ _Zone1.inc > this is located in > directory UniTest/	Creates Zone 1 from "time_020.txt" (using FESTR routines) and is based off of "hydro1_time0_Zone1.inc".
cone_grid.inc > this is located in > directory UniTest/	Builds Grid of Nodes defined in the files "Foil2D_008.t", "Foil2D_050.t", and "Foil2D_061.t" using the classes Vector3d, Node, and Grid. #included in: "cone_hydro.inc" "mesh_hydro_full.inc" "outer_Sphere_hydro.inc"
cone_surface.inc > this is located in > directory UniTest/	Builds the convex hull bordering a single Zone that has the coordinates (Nodes) of Zone 1 from "Foil2D_050.t". #included in "test_Zone.cpp"
bounding_sphere_hydro.inc > this is located in > directory UniTest/	Builds the outer surface of the bounding sphere. #included in "test_Zone.cpp"
outer_Sphere_hydro.inc	Builds the complete bounding sphere,

> this is located in > directory UniTest/	including both the outer surface and the convex hull bordering a single Zone that has the coordinates (Nodes) of Zone 1 from "Foil2D_050.t". This file is the cleaaner version of "cone_surface.inc". #includes "cone_grid.cpp" #included in "test_Zone.cpp"
cone_hydro.inc > this is located in > directory UniTest/	Builds the single Zone bounded by the convex hull that is built in "outer_Sphere_hydro.inc". #includes "cone_grid.cpp" #included in "test_Zone.cpp"

BIBLIOGRAPHY

[1] K. Falk, High Power Laser Science and Engineering **6**, e59 (2018).

[2] J. E. Coleman, 2019 USPAS, LA-UR-19-25377 (unpublished).

[3] J. E. Coleman and J. Colgan, Phys. Rev. E **96**, 013208 (2017).

[4] See https://www.thorlabs.com/thorproduct.cfm?partnumber=FGAP71 for more information about the GaP photodiode.

[5] See https://www.pasternack.com/images/ProductPDF/PE44118.pdf for more information about PE44118.

[6] P. Hakel, Comput. Phys. Commun. **207**, 415 (2016).

[7] J. Purić, J. Labat, S. Djenize, L. Ćirković, and I. Lakićević, Phys. Lett. **56A**, 83 (1976).

[8] J. F. Baur and J. Cooper, J. Quant. Spectrosc. Radiat. Transfer **17**, 311 (1977).

[9] C. J. Sansonetti, M. L. Salit, and J. Reader, Appl. Opt. **35**, 74 (1996).

[10] J. Abdallah, Jr., R. E. H. Clark, and R. D. Cowan, Technical Report No. LA-11436-M, Vol. I, Los Alamos National Laboratory, Los Alamos, NM, 1988.

[11] R. E. H. Clark, J. Abdallah, Jr., and S. P. Kramer, Technical Report No. LA-11436-M, Vol. III, Los Alamos National Laboratory, Los Alamos, NM, 1988, UC-705.

[12] B. J. Archer, R. E. H. Clark, C. J. Fontes, and H. Zhang, Technical Report No. LA-UR-02-1526, v1.7, Los Alamos National Laboratory, Los Alamos, NM, 2002.

[13] M. J. Burns, P. Allison, J. Downing, D. Moir, G. Caporaso, and Y.-J. Chen, *Technology Demonstration for the DARHT Linear Induction Accelerators* (NTIS, Washington, DC, 1992), pp. 283–290.

[14] M. J. Burns, P. W. Allison, R. L. Carlson, J. N. Downing, D. C. Moir, and R. P. Shurter, *Status of the Dual Axis Radiographic Hydrotest Facility* (CERN, Geneva, Switzerland, 1996), pp. 875–877.

[15] J. Fockler, B. Bowen, V. Carboni, P. Corcoran, J. Kishi, and R. Keunning, *A 4 MV ± 1% Flat-Top Electron Diode Driver* (IEEE, San Diego, CA, 1991), pp. 177–182.

[16] J. N. Downing, W. M. Parson, L. M. Earley, J. G. Melton, D. C. Moir, R. L. Carlson, G. A. Barnes, L. A. Builta, S. A. Eversole, G. Keel, D. C. Rader, J. A. Romero, and R. P. Shurter, *Pulsed Power Systems for the DARHT Accelerators* (IEEE, San Diego, CA, 1991), pp. 949–952.

[17] B. T. McCuistian, Technical Report No. SDD-DARHT-017 (U), Rev. A, Los Alamos National Laboratory, Los Alamos, NM, 2012.

[18] J. E. Coleman, D. C. Moir, M. T. Crawford, D. R. Welch, and D. T. Offermann, Physics of Plasmas **22**, 033508 (2015).

[19] J. N. Downing, W. M. Parsons, L. M. Earley, J. G. Melton, D. C. Moir, R. L. Carlson, G. A. Barnes, L. A. Builta, S. A. Eversole, G. Keel, D. C. Rader, J. A. Romero, and R. P. Shurter, Technical Report No. LA-UR-91-2089, Los Alamos National Laboratory, Los Alamos, NM, 1991, DARHT Technical Notes No. 15.

[20] M. J. Burns, B. E. Carlsten, T. J. T. Kwan, D. C. Moir, D. S. Prono, S. A. Watson, E. L. Burgess, H. L. Rutkowski, G. J. Caporaso, Y.-J. Chen, Y. J. Chen, S. Sampayan, and G. Westenskow, *DARHT Accelerators Update and Plans for Initial Operation* (IEEE, New York, 1999), pp. 617–621.

[21] M. Burns, K. Chellis, C. Mockler, T. Tucker, and G. Velesquez, Technical Report, Los Alamos National Laboratory, Los Alamos, NM, 1991, DARHT Technical Notes No. 7.

[22] C. Ekdahl, E. O. Abetya, R. Bartsch, L. Caudill, K. C. D. Chan, D. Dalmas, S. Eversole, R. Gallegos, J. Harrison, M. Holzscheiter, J. Johnson, E. Jacquez, B. T. McCuistian, N. Montoya, S. Nath, K. Nielsen, D. Oro, L. Rodriguez, P. Rodriguez, L. Rowton, M. Sanchez, R. Scarpetti, M. Schauer, D. Simmons, H. V. Smith, J. Studebaker, G. Sullivan, C. Swinney, R. Temple, Y. J. Chen, T. Houck, E. Henestroza, S. Eylon, W. Fawley, S. S. Yu, H. Bender, W. Broste, C. Carlson, G. Durtschi, D. Frayer, D. Johnson, K. Jones, A. Meidinger, K. Moy, R. Sturgess, A. Tipton, M. Tom, C. Y. amd Schulze, T. Hughes, C. Mostrom, and Y. Tang, (IEEE, Knoxville, TN, 2005), pp. 19–23.

[23] S. Nath, in Proc. 2010 Linear Accelerator Conference 750 (2010).

[24] K. Nielsen, Technical Report No. SDD-DARHT-009 (U), Rev. A, Los Alamos National Laboratory, Los Alamos, NM, 2012.

[25] R. D. Scarpetti, S. Nath, J. Barraza, C. A. Ekdahl, E. Jacquez, B. T. McCuistian, K. Nielsen, M. Schulze, J. Sietz, G. J. Caporaso, Y.-J. Chen, G. Logan, and F. Bieniosek, *Status of the DARHT 2nd Axis Accelerator at the Los Alamos National Laboratory* (IEEE, Albuquerque, NM, 2007), pp. 831–835.

[26] T. P. Hugues, D. P. Prono, W. M. Tuzel, and J. R. Vananne, Technical Report, Mission Research Corporation, Santa Barbara, CA, 2000, DARHT Technical Notes No. 188.

[27] C. R. Rose, S. Nath, and R. D. Temple.

[28] M. Schulze, E. O. Abetya, P. Aragon, R. Archuleta, J. Barraza, D. Dalmas, C. Ekdahl, K. Esquibel, S. Eversole, R. Gallegos, J. Harrison, J. Johnson, E. Jacquez, M. P., B. T. McCuistian, R. Mitchell, N. Montoya, S. Nath, L. Rowton, R. Scarpetti, M. Schauer, R. Anaya, G. Caporaso, F. Chambers, Y. J. Chen, S. Falabella, G. Guethlein, J. McCarrick, B. Raymond, R. Richardson, J. Watson, J. Weir, H. Bender, W. Broste, C. Carlson, D. Frayer, D. Johnson, A. Tipton, C. Y. Tom, T. C. Genoni, T. P. Hughes, and C. Thoma, *Commissioning the DARHT-II Scaled Accelerator Downstream Transport* (IEEE, Albuquerque, NM, 2007), pp. 2627–2629, THOBAB02.

[29] M. Schulze, E. O. Abetya, R. Archuleta, J. Barraza, D. Dalmas, C. Ekdahl, W. Gregory, J. Harrison, J. Johnson, E. Jacquez, M. P., B. T. McCuistian, R. Mitchell, N. Montoya, S. Nath, K. Nielsen, R. Ortiz, L. Rowton, R. Scarpetti, M. Schauer, R. Anaya, G. Caporaso, F. Chambers, Y. J. Chen, S. Falabella, G. Guethlein, B. Raymond, R. Richardson, J. Watson, J. Weir, H. Bender, W. Broste, C. Carlson, D. Frayer, D. Johnson, A. Tipton, C. Y. Tom, T. P. Hughes, and C. Thoma, *Commissioning the DARHT-II Accelerator Downstream Transport and Target* (IEEE, Victoria, BC, Canada, 2008), pp. 434–436, TUP020.

[30] H. Bethe and W. Heitler, Proc. R. Soc. Lond. A **146**, 83 (1934).

[31] M. J. Berger and S. M. Seltzer, Phys. Rev. C **2**, 621 (1970).

[32] N. B. Ramey, Bachelor's thesis, Case Western Reserve University, 2017, LA-UR-17-25600.

[33] T. J. T. Kwan and C. M. Snell, Technical Report No. XPA-RN (U)97-048, Los Alamos National Laboratory, Los Alamos, NM, 1997, DARHT Technical Notes No. 83.

[34] B. G. DeVolder and K. D. McLenithan, Technical Report No. XPA-RN (U)97-049, Los Alamos National Laboratory, Los Alamos, NM, 1997, DARHT Technical Notes No. 84.

[35] T. J. T. Kwan, Technical Report No. LA-UR-98-4802, Los Alamos National Laboratory, Los Alamos, NM, 1998, DARHT Technical Notes No. 103.

[36] T. Hughes, D. Welch, and R. Carlson, *Diode and final-focus simulations for DARHT* (IEEE, Vancouver, BC, Canada, 1997), pp. 1867–1869.

[37] T. J. T. Kwan, C. M. Snell, and P. J. Christenson, Physics of Plasmas **7**, 2215 (2000).

[38] A. Ng, in *2007 IEEE 34th International Conference on Plasma Science (ICOPS)* (IEEE, Albuquerque, NM, 2007), pp. 132–132.

[39] A. Saemann, K. Eidmann, I. E. Golovkin, R. C. Mancini, E. Andersson, E. Förster, and K. Witte, Phys. Rev. Lett. **82**, 4843 (1999).

[40] P. Audebert, P. Renaudin, S. Bastiani-Ceccotti, J.-P. Geindre, C. Chenais-Popovics, S. Tzortzakis, V. Nagels-Silvert, R. Shepherd, I. Matsushima, S. Gary, F. Girard, O. Peyrusse, and J.-C. Gauthier, Phys. Rev. Lett. **94**, 025004 (2005).

[41] Y. Ping, D. Hanson, I. Koslow, T. Ogitsu, D. Prendergast, E. Schwegler, G. Collins, and A. Ng, Phys. Rev. Lett. **96**, 255003 (2006).

[42] L. Lecherbourg, P. Renaudin, S. Bastiani-Ceccotti, J.-P. Geindre, C. Blancard, P. Cossé, G. Faussurier, R. Shepherd, and P. Audebert, High Energy Density Physics **3**, 175 (2007).

[43] B. I. Cho, K. Engelhorn, A. A. Correa, T. Ogitsu, C. P. Weber, H. J. Lee, J. Feng, P. A. Ni, Y. Ping, A. J. Nelson, D. Prendergast, R. W. Lee, R. W. Falcone, and P. A. Heimann, Phys. Rev. Lett. **106**, 167601 (2011).

[44] D. H. Kalantar, R. W. Lee, and J. D. Molitoris, Technical Report No. UCRL-TR-203844, Lawrence Livermore National Laboratory, Livermore, CA (2004).

[45] U. Zastrau, C. Fortmann, R. R. Fäustlin, L. F. Cao, T. Döppner, S. Düsterer, S. H. Glenzer, G. Gregori, T. Laarmann, H. J. Lee, A. Przystawik, P. Radcliffe, H. Reinholz, G. Röpke, R. Thiele, J. Tiggesbäumker, N. X. Truong, S. Toleikis, I. Uschmann, A. Wierling, T. Tschentscher, E. Förster, and R. Redmer, Phys. Rev. E **78**, 066406 (2008).

[46] J. Cihelka, L. Juha, J. Chalupský, F. B. Rosmej, O. Renner, K. Saksl, V. Hájková, L. Vyšin, E. Galtier, R. Schott, A. R. Khorsand, D. Riley, T. Dzelzainis, A. Nelson, R. W. Lee, P. Heimann, B. Nagler, S. Vinko, J. Wark, T. Whitcher, S. Toleikis, T. Tschentscher, R. Faustlin, H. Wabnitz, S. Bajt, H. Chapman, J. Krzywinski, R. Sobierajski, D. Klinger, M. Jurek, J. Pelka, S. Hau-Riege, R. A. London, J. Kuba, N. Stojanovic, K. Sokolowski-Tinten, A. J. Gleeson, M. Störmer, J. Andreasson, J. Hajdu, and N. Timneanu, in *Damage to VUV, EUV, and X-Ray Optics II*, International Society for Optics and Photonics, edited by L. Juha, S. Bajt, and R. Sobierajski (SPIE, Prague, Czech Republic, 2009), Vol. 7361, pp. 172–181.

[47] P. Sperling, E. J. Gamboa, H. J. Lee, H. K. Chung, E. Galtier, Y. Omarbakiyeva, H. Reinholz, G. Röpke, U. Zastrau, J. Hastings, L. B. Fletcher, and S. H. Glenzer, Phys. Rev. Lett. **115**, 115001 (2015).

[48] A. Lévy, P. Audebert, R. Shepherd, J. Dunn, M. Cammarata, O. Ciricosta, F. Deneuville, F. Dorchies, M. Fajardo, C. Fourment, D. Fritz, J. Fuchs, J. Gaudin, M. Gauthier, A. Graf, H. J. Lee, H. Lemke, B. Nagler, J. Park, O. Peyrusse, A. B. Steel, S. M. Vinko, J. S. Wark, G. O. Williams, D. Zhu, and R. W. Lee, Physics of Plasmas **22**, 030703 (2015).

[49] A. L. Kritcher, T. Doeppner, D. Swift, J. Hawreliak, J. Nilsen, J. Hammer, B. Bachmann, G. Collins, O. Landen, C. Keane, S. Glenzer, S. Rothman, D. Chapman, D. Kraus, and R. Falcone, Journal of Physics: Conference Series **688**, 012055 (2016).

[50] R. D. McBride, W. A. Stygar, M. E. Cuneo, D. B. Sinars, M. G. Mazarakis, J. J. Leckbee, M. E. Savage, B. T. Hutsel, J. D. Douglass, M. L. Kiefer, B. V. Oliver, G. R. Laity, M. R. Gomez, D. A. Yager-Elorriaga, S. G. Patel, B. M. Kovalchuk, A. A. Kim, P.-A. Gourdain, S. N. Bland, S. Portillo, S. C. Bott-Suzuki, F. N. Beg, Y. Maron, R. B. Spielman, D. V. Rose, D. R. Welch, J. C. Zier, J. W. Schumer, J. B. Greenly, A. M. Covington, A. M. Steiner, P. C. Campbell, S. M. Miller, J. M. Woolstrum, N. B. Ramey, A. P. Shah, B. J. Sporer, N. M. Jordan, Y. Y. Lau, and R. M. Gilgenbach, IEEE Transactions on Plasma Science **46**, 3928 (2018).

[51] D. B. Sinars, M. A. Sweeney, C. S. Alexander, D. J. Ampleford, T. Ao, J. P. Apruzese, C. Aragon, D. J. Armstrong, K. N. Austin, T. J. Awe, A. D. Baczewski, J. E. Bailey, K. L.

Baker, C. R. Ball, H. T. Barclay, S. Beatty, K. Beckwith, K. S. Bell, J. F. Benage, N. L. Bennett, K. Blaha, D. E. Bliss, J. J. Boerner, C. J. Bourdon, B. A. Branch, J. L. Brown, E. M. Campbell, R. B. Campbell, D. G. Chacon, G. A. Chandler, K. Chandler, P. J. Christenson, M. D. Christison, E. B. Christner, R. C. Clay, K. R. Cochrane, A. P. Colombo, B. M. Cook, C. A. Coverdale, M. E. Cuneo, J. S. Custer, A. Dasgupta, J.-P. Davis, M. P. Desjarlais, D. H. Dolan, J. D. Douglass, G. S. Dunham, S. Duwal, A. D. Edens, M. J. Edwards, E. G. Evstatiev, B. G. Farfan, J. R. Fein, E. S. Field, J. A. Fisher, T. M. Flanagan, D. G. Flicker, M. D. Furnish, B. R. Galloway, P. D. Gard, T. A. Gardiner, M. Geissel, J. L. Giuliani, M. E. Glinsky, M. R. Gomez, T. Gomez, G. P. Grim, K. D. Hahn, T. A. Haill, N. D. Hamlin, J. H. Hammer, S. B. Hansen, H. L. Hanshaw, E. C. Harding, A. J. Harvey-Thompson, D. Headley, M. C. Herrmann, M. H. Hess, C. Highstrete, O. A. Hurricane, B. T. Hutsel, C. A. Jennings, O. M. Johns, D. Johnson, M. D. Johnston, B. M. Jones, M. C. Jones, P. A. Jones, P. E. Kalita, R. J. Kamm, J. W. Kellogg, M. L. Kiefer, M. W. Kimmel, P. F. Knapp, M. D. Knudson, A. Kreft, G. R. Laity, P. W. Lake, D. C. Lamppa, W. L. Langston, J. S. Lash, K. R. LeChien, J. J. Leckbee, R. J. Leeper, G. T. Leifeste, R. W. Lemke, W. Lewis, S. A. Lewis, G. P. Loisel, Q. M. Looker, A. J. Lopez, D. J. Lucero, S. A. MacLaren, R. J. Magyar, M. A. Mangan, M. R. Martin, T. R. Mattsson, M. K. Matzen, A. J. Maurer, M. G. Mazarakis, R. D. McBride, H. S. McLean, C. A. McCoy, G. R. McKee, J. L. McKenney, A. R. Miles, J. A. Mills, M. D. Mitchell, N. W. Moore, C. E. Myers, T. Nagayama, G. Natoni, A. C. Owen, S. Patel, K. J. Peterson, T. D. Pointon, J. L. Porter, A. J. Porwitzky, S. Radovich, K. S. Raman, P. K. Rambo, W. D. Reinhart, G. K. Robertson, G. A. Rochau, S. Root, D. V. Rose, D. C. Rovang, C. L. Ruiz, D. E. Ruiz, D. Sandoval, M. E. Savage, M. E. Sceiford, M. A. Schaeuble, P. F. Schmit, M. S. Schollmeier, J. Schwarz, C. T. Seagle, A. B. Sefkow, D. B. Seidel, G. A. Shipley, J. Shores, L. Shulenburger, S. C. Simpson, S. A. Slutz, I. C. Smith, C. S. Speas, P. E. Specht, M. J. Speir, D. C. Spencer, P. T. Springer, A. M. Steiner, B. S. Stoltzfus, W. A. Stygar, J. Ward Thornhill, J. A. Torres, J. P. Townsend, C. Tyler, R. A. Vesey, P. E. Wakeland, T. J. Webb, E. A. Weinbrecht, M. R. Weis, D. R. Welch, J. L. Wise, M. Wu, D. A. Yager-Elorriaga, A. Yu, and E. P. Yu, Physics of Plasmas **27**, 070501 (2020).

[52] R. Reinovsky, in *2009 IEEE Pulsed Power Conference* (IEEE, Washington, DC, 2009), pp. 203–208.

[53] P. A. Gourdain, C. E. Seyler, and P. F. Knapp, in *APS Division of Plasma Physics Meeting Abstracts*, Vol. 2016 of *APS Meeting Abstracts* (APS, San Jose, CA, 2016), p. UO8.007.

[54] M. Evans, M. Adams, R. Shapovalov, P.-A. Gourdain, P. Campbell, J. Woolstrum, S. Miller, N. Ramey, N. Jordan, and R. McBride, in *2018 IEEE International Conference on Plasma Science (ICOPS)* (IEEE, Denver, CO, 2018), pp. 1–1.

[55] M. Evans, M. B. Adams, P. C. Campbell, N. M. Jordan, S. M. Miller, N. B. Ramey, R. V. Shapovalov, J. Young, I. West-Abdallah, J. M. Woolstrum, R. D. McBride, and P.-A. Gourdain, Physics of Plasmas **26**, 070704 (2019).

[56] T. Ao, E. Harding, J. Bailey, R. Lemke, M. Desjarlais, S. Hansen, I. Smith, M. Geissel, A. Maurer, J. Reneker, D. Romero, D. Sinars, G. Rochau, and J. Benage, High Energy Density Physics **18**, 26 (2016).

[57] F. M. Bieniosek, J. J. Barnard, A. Friedman, E. Henestroza, J. Y. Jung, M. A. Leitner, S. Lidia, B. G. Logan, R. M. More, P. A. Ni, P. K. Roy, P. A. Seidl, and W. L. Waldron, Journal of Physics: Conference Series **244**, 032028 (2010).

[58] P. Ni, F. Bieniosek, E. Henestroza, and S. Lidia, Nuclear Instruments and Methods in Physics Research Section A: Accelerators, Spectrometers, Detectors and Associated Equipment **733**, 12 (2014), 19th International Symposium on Heavy Ion Inertial Fusion.

[59] P. A. Seidl, A. Persaud, W. L. Waldron, J. J. Barnard, R. C. Davidson, A. Friedman, E. P. Gilson, W. G. Greenway, D. P. Grote, I. D. Kaganovich, S. M. Lidia, M. Stettler, J. H. Takakuwa, and T. Schenkel, Nuclear Instruments and Methods in Physics Research Section A: Accelerators, Spectrometers, Detectors and Associated Equipment **800**, 98 (2015).

[60] N. Tahir, S. Udrea, C. Deutsch, V. Fortov, N. Grandjouan, V. Gryaznov, D. Hoffmann, P. Hulsmann, M. Kirk, I. Lomonosov, A. R. Piriz, A. Shutov, P. Spiller, M. Temporal, and D. Varentsov, Laser and Particle Beams **22**, 485–493 (2004).

[61] A. Tauschwitz, J. A. Maruhn, D. Riley, F. B. Rosmej, S. Borneis, A. Tauschwitz, and K. Witte, Journal of Physics: Conference Series **112**, 032074 (2008).

[62] P. A. Ni, M. I. Kulish, V. Mintsev, D. N. Nikolaev, V. Y. Ternovoi, D. H. H. Hoffmann, S. Udrea, A. Hug, N. A. Tahir, and D. Varentsov, Laser Part. Beams **26**, 583 (2008).

[63] P. K. Patel, A. J. Mackinnon, M. H. Key, T. E. Cowan, M. E. Foord, M. Allen, D. F. Price, H. Ruhl, P. T. Springer, and R. Stephens, Phys. Rev. Lett. **91**, 125004 (2003).

[64] A. Pelka, G. Gregori, D. O. Gericke, J. Vorberger, S. H. Glenzer, M. M. Günther, K. Harres, R. Heathcote, A. L. Kritcher, N. L. Kugland, B. Li, M. Makita, J. Mithen, D. Neely, C. Niemann, A. Otten, D. Riley, G. Schaumann, M. Schollmeier, A. Tauschwitz, and M. Roth, Phys. Rev. Lett. **105**, 265701 (2010).

[65] W. Bang, B. J. Albright, P. A. Bradley, D. C. Gautier, S. Palaniyappan, E. L. Vold, M. A. S. Cordoba, C. E. Hamilton, and J. C. Fernández, Scientific Reports **5**, 1 (2015).

[66] W. Bang, B. J. Albright, P. A. Bradley, E. L. Vold, J. C. Boettger, and J. C. Fernández, Phys. Rev. E **92**, 063101 (2015).

[67] J. E. Coleman, Rev. Sci. Instrum. **87**, 123113 (2016).

[68] J. E. Coleman and J. Colgan, Phys. Plasmas **24**, 083302 (2017).

[69] N. B. Ramey, J. E. Coleman, P. Hakel, H. E. Morris, J. Colgan, J. E. Barefield, C. J. Fontes, R. M. Gilgenbach, and R. D. McBride, Physics of Plasmas **28**, 033301 (2021).

[70] H. Bethe, Zeitschrift für Physik **76**, 293 (1932).

[71] C. J. Fontes, C. J. Bostock, and K. Bartschat, European Physical Journal H **39**, 517 (2014).

[72] S. M. Seltzer and M. J. Berger, Nuclear Instruments and Methods in Physics Research B **12**, 95 (1985).

[73] See https://physics.nist.gov/PhysRefData/Star/Text/method.html.

[74] D. K. Brice, Nuclear Instruments & Methods in Physics Research Section B-beam Interactions With Materials and Atoms **12**, 187 (1985).

[75] P. Allison, Technical Report, Los Alamos National Laboratory, Los Alamos, NM, 1994, DARHT Technical Notes No. 49.

[76] H. A. Davis, R. T. Olson, and D. C. Moir, Physics of Plasmas **10**, 3351 (2003).

[77] C. Vermare, H. A. Davis, D. C. Moir, and T. P. Hughes, Phys. Plasmas **10**, 277 (2003).

[78] P. L. G. Ventzek, Ph.D. thesis, University of Michigan, 1991.

[79] J. E. Coleman, H. E. Morris, M. S. Jakulewicz, H. L. Andrews, and M. E. Briggs, Phys. Rev. E **98**, 043201 (2018).

[80] S. P. Marsh, *LASL Shock Hugoniot Data* (University of California Press, Berkeley and Los Angeles, CA, 1980), LA-UR-79-1019.

[81] P. C. Dieffenbach, Master's thesis, University of Tennessee, 2019, LA-UR-17-25600.

[82] J. E. Coleman, 2019 USPAS, LA-UR-19-25028 (unpublished).

[83] J. E. Coleman, J. E. Koglin, H. E. Morris, N. B. Ramey, and D. T. Offermann, Journal of Applied Physics **131**, 215901 (2022).

[84] H. A. Bethe, K. Fuchs, J. O. Hirschfelder, J. L. Magee, R. E. Peierls, and J. von Neumann, Technical Report No. LA-2000, Los Alamos Scientific Laboratory, Los Alamos, NM, 1947, Chap. 2.

[85] G. I. Taylor, Proc. R. Soc. A **201**, 159 (1950).

[86] G. I. Taylor, Proc. R. Soc. A **201**, 175 (1950).

[87] J. E. Coleman, Ph.D. thesis, University of California, 2008.

[88] S. Humphries Jr., *Charged Particle Beams* (John Wiley and Sons, New York, 1990), chapter 9.

[89] J. E. Coleman, D. C. Moir, C. A. Ekdahl, J. B. Johnson, B. T. McCuistian, G. W. Sullivan, and M. T. Crawford, Phys. Rev. ST Accel. Beams **17**, 030101 (2014).

[90] S. Humphries, AIP Conference Proceedings **297**, 597 (1993).

[91] P. Allison, Technical Report, Los Alamos National Laboratory, Los Alamos, NM, 1995, DARHT Technical Notes No. 50.

[92] P. W. Allison, Technical Report No. LA-UR-01-6585, Los Alamos National Laboratory, Los Alamos, NM, 2001.

[93] J. E. Coleman, C. A. Ekdahl, D. C. Moir, G. W. Sullivan, and M. T. Crawford, Phys. Rev. ST Accel. Beams **17**, 092802 (2014).

[94] S. M. Lund, C. J. Wootton, and E. P. Lee, Nuclear Instruments and Methods in Physics Research Section A: Accelerators, Spectrometers, Detectors and Associated Equipment **606**, 56 (2009), Heavy Ion Inertial Fusion.

[95] Y.-J. Chen, Nuclear Instruments and Methods in Physics Research Section A: Accelerators, Spectrometers, Detectors and Associated Equipment **292**, 455 (1990).

[96] Y.-J. Chen, Nuclear Instruments and Methods in Physics Research Section A: Accelerators, Spectrometers, Detectors and Associated Equipment **398**, 139 (1997).

[97] R. L. Carlson, R. N. Ridlon, and L. E. Stout, Review of Scientific Instruments **57**, 2471 (1986).

[98] L. Wartski, S. Roland, J. Lasalle, M. Bolore, and G. Filippi, Journal of Applied Physics **46**, 3644 (1975).

[99] C. B. Reid, Master's thesis, Naval Postgraduate School, 1990.

[100] P. Karataev, A. Aryshev, S. Boogert, D. Howell, N. Terunuma, and J. Urakawa, Phys. Rev. Lett. **107**, 174801 (2011).

[101] See https://www.princetoninstruments.com/products/pi-max-family for more information on PiMAX cameras.

[102] See https://www.princetoninstruments.com/products/spectrapro-family for more information on Acton spectrometers.

[103] J. E. Coleman, J. E. Koglin, J. P. Colgan, C. J. Fontes, P. Hakel, H. E. Morris, N. B. Ramey, and D. T. Offermann, in *63rd Annual Meeting of the APS Division of Plasma Physics* (APS, Pittsburgh, PA, 2021), No. 13, LA-UR-21-31095.

[104] J. Reader, C. J. Sansonetti, and J. M. Bridges, Appl. Opt. **35**, 78 (1996).

[105] See https://www.newport.com/f/pencil-style-calibration-lamps for information about Oriel pen lamps.

[106] See https://www.princetoninstruments.com/products/sophia-family/sophia for more information on SOPHIA cameras.

[107] A. Kramida, Y. Ralchenko, and J. Reader, NIST ASD Team 2014 NIST Atomic Spectra Database v. 5.2 (NIST, Gaithersburg, MD, 2014). See https://www.nist.gov/pml/atomic-spectra-database for more information about documented lines and levels.

[108] J. V. Sullivan and A. Walsh, Spectrochimica Acta **21**, 721 (1965).

[109] F. Paresce, S. Kumar, and C. S. Bowyer, Appl. Opt. **10**, 1904 (1971).

[110] G. B. Zimmerman and W. L. Kruer, Comments Plasma Phys. Controlled Fusion **2**, 51 (1975).

[111] The SESAME EOS library is a binary, tabular compendium of equations of state for numerous materials and is maintained and disseminated by Group T-1 at the Los Alamos National Laboratory (email: sesame@lanl.gov).

[112] K. S. Holian, Technical Report No. LA-10160-MS, Los Alamos National Laboratory, Los Alamos, NM, 1984.

[113] K. S. Trainor, Technical Report No. UCID-118574-82-2, Lawrence Livermore National Laboratoryx, Livermore, CA, 1982.

[114] S. Crockett, Technical Report No. LA-UR-04-6442, Los Alamos National Laboratory, Los Alamos, NM, 2004.

[115] T. Sjostrom, S. Crockett, and S. Rudin, Phys. Rev. B **94**, 144101 (2016).

[116] S. Crockett and T. Sjostrom, personal communication (2021).

[117] C. J. Fontes, H. L. Zhang, J. A. Jr, R. E. H. Clark, D. P. Kilcrease, J. Colgan, R. T. Cunningham, P. Hakel, N. H. Magee, and M. E. Sherrill, Journal of Physics B: Atomic, Molecular and Optical Physics **48**, 144014 (2015).

[118] N. H. Magee, J. Abdallah, J., R. E. H. Clark, J. S. Cohen, L. A. Collins, G. Csanak, C. J. Fontes, A. Gauger, J. J. Keady, D. P. Kilcrease, and A. L. Merts, in *Astrophysical Applications of Powerful New Databases*, Vol. 78 of *Astronomical Society of the Pacific Conference Series*, edited by S. J. Adelman and W. L. Wiese (Astronomical Society of the Pacific, San Fransisco, California, 1995), p. 51.

[119] P. Hakel, M. Sherrill, S. Mazevet, J. Abdallah, J. Colgan, D. Kilcrease, N. Magee, C. Fontes, and H. Zhang, Journal of Quantitative Spectroscopy and Radiative Transfer **99**, 265 (2006).

[120] J. Colgan, E. J. Judge, D. P. Kilcrease, and J. E. Barefield, Spectrochim. Acta, Part B **97**, 65 (2014).

[121] J. Colgan, personal communication (2018).

[122] C. J. Fontes, personal communication (2021).

[123] H. M. Johns, D. P. Kilcrease, J. Colgan, E. J. Judge, J. E. Barefield, II, R. C. Wiens, and S. M. Clegg, Journal of Physics B: Atomic, Molecular and Optical Physics **48**, 224009 (2014).

[124] H. E. Morris, personal communication (2019).

[125] R. D. Cowan, *The Theory of Atomic Structure and Spectra* (University of California Press, Berkeley, CA, 1981), pp. 22-23.

[126] A. El Sherbini, T. El Sherbini, H. Hegazy, G. Cristoforetti, S. Legnaioli, V. Palleschi, L. Pardini, A. Salvetti, and E. Tognoni, Spectrochimica Acta Part B: Atomic Spectroscopy **60**, 1573 (2005).

[127] See https://www.mcmaster.com/2471T94/ for more information on Al alloy foils.

[128] See https://www.princetoninstruments.com/learn/calculators/grating-dispersion for more information on grating disperson.

[129] R. W. P. McWhirter, *Plasma Diagnostic Techniques* (Academic Press, New York, 1965).

[130] H. R. Griem, J. Quant. Spectrosc. Radiat. Transfer **8**, 389 (1968).

[131] See https://www.quantel-laser.com/en/products/item/ultra-50-100-mj–134.html for information about the Quantel laser.

[132] See http://www.catalinasci.com/emu.cfm for more information about the EMU-65 UV/VIS/NIR spectrograph and EMCCD.

[133] See https://www.goodfellow.com/uk/en-us/displayitemdetails/p/al00-fl-000165/aluminum-foil for more information on pure Al foils (AL000565).

[134] See https://www.filmtools.com/blacstudfoil-5954.html and https://www.thorlabs.us/thorproduct.cfm?partnumber=BKF12 for more information on anodized Al foils.

[135] See https://www.kcprofessional.com/en-us/products/wipers/specialty-wipers/34155 for more information on Kimwipes.

[136] See https://www.ansell.com/us/en/products/touchntuff-92-600 for more information about Touchntuff gloves (NBR 92-600, lot 1503411905).

[137] See https://mc2.engin.umich.edu/techniques/kratos-axis-ultra-xps/ for more information about the Kratos Axis Ultra XPS.

[138] See http://www.casaxps.com/ for more information about CasaXPS software.

[139] See https://www.fishersci.com/shop/products/fisherbrand-powder-free-nitrile-exam-gloves-24/p-2826798 for more information about Fisherbrand gloves (Re-order # 19-130-1597D and 19-041-171D).

[140] S. Nath, in Proc. 2008 European Particle Accelerator Conference 1206 (2008).

[141] M. S. Dimitrijević and S. Sahal-Bréchot, Physica Scripta **49**, 34 (1994).

[142] J. Colgan and D. P. Kilcrease, Incorporating experimentally determined energy levels into the CATS atomic structure code, Memorandum T-1:14-001, Los Alamos National Laboratory, January 6, 2014.

[143] P. Hakel and C. J. Fontes, MPI-based management of parallel tasks with dynamic load balancing, Memorandum XCP-5:21-005, Los Alamos National Laboratory, July 27, 2021.